

Flow Convergence and Pressure Loss Characteristics in Viscous Flow through Rectangular Orifices with Applications in Porous Media

by

Yishak Abdulhafiz Yusuf

A thesis submitted in partial fulfillment of the requirements for the degree of

Doctor of Philosophy

Department of Mechanical Engineering
University of Alberta

© Yishak Abdulhafiz Yusuf, 2020

Abstract

The enhanced oil recovery process known as steam assisted gravity drainage (SAGD) uses horizontal wells with perforations on their lateral surfaces to inject steam into, and produce oil from, oilsand reserves. Slotted liners that are used external to these wells serve as screens to minimize sand production. The flow contraction caused by the presence of these slots leads to significant pressure loss in the flow increasing the probability of well failure due to plugging. Scrutinizing the underlying physics reveals a flow convergence phenomenon in the incoming flow of produced oil which is characterized by flow acceleration and streamline curvature.

The thesis considers the problem of flow into a single slot defining the geometry as a rectangular orifice of high aspect ratio, AR . The flow configuration in the SAGD flow scenario consists of the coupled regions of the porous media and the rectangular orifice. The research first investigates the flow through an open slot to model the pressure loss as a function of AR and the flow Reynolds number.

A semi-empirical model is developed for the pressure loss coefficient as a function of AR and flow convergence. The analytical modeling is based on the 1 dimensional Navier-Stokes equation and an asymptotic velocity transition model for a Gaussian velocity distribution. The loss coefficient decreased for increasing AR as per the model, agreeing with the hypothesized relationship regarding the streamline curvature and AR .

A large scale flow measurement facility is used to measure the pressure drop across rectangular orifices of various aspect ratio in the range $1 \leq AR \leq 250$. The orifices all have equal cross sectional area while the hydraulic diameters were varied to change AR . The flow rates in the experiments are selected to maintain the same Reynolds number across all orifices in the range

$0.05 \leq Re \leq 0.1$ which was selected based on field conditions in SAGD. The static pressure drop ΔP increased with increasing AR and Re . The effect of AR on the pressure drop was attributed to varying flow blockage and convergence effects which become apparent in their respective planes of investigation.

The changing flow convergence/blockage characteristics with changing AR is closely investigated by using particle image velocimetry (PIV) experiments to measure the velocity field from which the streamlines are determined. The streamlines for the flow through orifices having lower AR started to curve farther upstream than for higher AR . The trend in the axial distribution of streamline curvature were also reflected in the pressure gradients determined in both the streamwise and spanwise directions. Calculation of these pressure gradients is achieved by applying the equations of motion in streamline coordinates along the streamlines calculated using PIV data. The maximum streamwise pressure gradient occurred along the center streamline since the maximum velocity gradient also occurs along the centerline. The spanwise pressure gradient reached maximum wherever there is maximum curvature.

The study also considered the flow through the coupled media by including a representative porous region on the upstream side of the orifice using spherical glass beads with mean diameter of 1 mm. Modelling of the pressure loss through the coupled system developed a relation combining Ergun's equation for the porous bed and the model developed for the open-orifice scenario. The model described that higher AR leads to higher pressure drop across the coupled system due to dominating effect from flow blockage. Comparison of the pressure drop relation obtained from the model with that from experimental measurements showed that the flow convergence due to the orifice contributes more to the losses than the preceding porous region.

Preface

This thesis document presents the original work by Yishak Abdulhafiz Yusuf. The research work has been conducted at the Mechanical Engineering Department of the University of Alberta. All experimentations and development of the analytical model were performed using facilities of the Applied Thermo fluids Laboratory under the supervision of Prof. David S. Nobes. All the analytical modelling have been devised and developed by Yishak and he was responsible for setting up and running all experiments as well as collection and analysis of data. Yishak has also recommissioned the facility used for pressure measurement experiments which included re-instrumentation and development of software for monitoring and logging of data.

Prof. Nobes has been the supervisory author and has contributed to the manuscript edits of the thesis and publications. The thesis has produced the scientific articles for publications in peer reviewed journals and conference proceedings.

1. Yusuf, Y, Sabbagh, R, and Nobes, D.S. (2019) “Semi-empirical pressure loss model for low Reynolds number flow through slots”, *Physics of fluids*, 31(7), 073603;
2. Yusuf Y., Kinsale L., Ansari S., Nobes D. S. (2019) “*The convergent path of streamlines for the flow approaching a rectangular orifice through a porous region*” 4th Thermal and Fluids Engineering Conference (TFEC) April 14–17, 2019, Las Vegas, NV, USA;
3. Yusuf, Y., Ansari, S., Bayans, M., Sabbagh, R., El Hassan, M., and Nobes, D.S. (2018) “*Study of Flow Convergence in Rectangular Slots using Particle Shadowgraph Velocimetry*”, 5th International Conference on Experimental Fluid Mechanics – ICEFM 2018 Munich, Munich, Germany, July 2-4, 2018.
4. Yusuf, Y, Baldygin, A, Sabbagh, and Nobes, D.S. (2017) “*Flow of viscous fluid through rectangular orifice in the presence of porous media at the inlet section*”, 67th Canadian Chemical Engineering Conference, Edmonton, AB, Canada, October 22-25, 2017;

5. Yusuf, Y, Sabbagh, R, and Nobes, D.S. (2017) “*Flow convergence model for flow through long aspect ratio rectangular orifices*”, The Okanagan Fluid Dynamics Meeting, Kelowna, BC, Canada, August 21-24, 2017;
6. Yusuf, Y, Baldygin, A, Sabbagh, R, Leitch, M, Waghmare, P R., and Nobes, D.S. (2017) “*Effect of aspect ratio on pressure loss and characteristics of low Reynolds number flow through narrow slots*”, Proceedings of the 2nd Thermal and Fluid Engineering Conference, TFEC2017-18387, Las Vegas, USA, April 2-5, 2017; and
7. Yusuf, Y, (2016) “*Effect of Aspect Ratio and Boundary Conditions on Pressure Loss and Characteristics of Low Reynolds Number Flow through Narrow Slots*”, 2016 RGL Symposium on SAGD Near-Wellbore Physics and Design, University of Alberta, Edmonton, October 12, 2016

Yishak’s contributions as the lead author in the above publications were setting up experiments, developing software for data acquisition and processing, conducting experiments, analysing data, generating plots and preparing manuscripts. Yishak has also been involved in other research projects that have been published as:

1. Ansari, S., Yusuf Y.^a, Sabbagh R. and Nobes, D.S. (2019) “The Case for Emulsification in Steam Assisted Gravity Drainage (SAGD) Oil Production Process: A Review”, *SPE Journal*, (accepted for publication)
2. Ansari, S., Yusuf, Y.^b, Sabbagh, R., & Nobes, D. S. (2019). Determining the pressure distribution of a multi-phase flow through a pore space using velocity measurement and shape analysis. *Measurement Science and Technology*, 30(5), 054004.
3. Kinsale L., Yusuf Y.^c, Ansari S., Nobes D. S. (2019) “*Fines migration in the near-inlet region of a flow entering a narrow slot through a porous medium*” 4th Thermal and Fluids Engineering Conference (TFEC) April 14–17, 2019, Las Vegas, NV, USA

^a Contributions: Review of literature, preparation of manuscripts, analysis of mathematical models

^b Contributions: Review of literature, preparation of manuscripts, analysis and interpretation of data

^c Review of literature, design and manufacture flow channels for experiments, analysis and interpretation of data

4. Ansari S., Yusuf Y.^d, Kinsale L., Sabbagh R. and Nobes D. S. (2018) “*Visualization of fines migration in the flow entering apertures through the near-wellbore porous media*”, 2018 SPE Thermal Well Integrity and Design Symposium Banff |Canada, Nov 27–29 2018
5. S. Ansari, Y. Yusuf^e, R. Sabbagh, H. Soltani, L. Kinsale and D.S. Nobes (2018) “*An imaging derivation of the pressure field of a multi-phase flow in a porous media using μ -SPIV*”. In 19th International Symposium on the Application of Laser and Imaging Techniques to Fluid Mechanics, Lisbon, Portugal, July 16–19, 2018.
6. Leitch, M, Yusuf, Y^f, and Ma, Y (2017) “Interdisciplinary semantic model framework for complex SAGD production tooling system” *Journal of Computational Design and Engineering*, vol. 5, no. 1, pp 68-79, Elsevier
7. Yusuf, Y^g, and Ma, Y (2016) “Design of a simulation tool for steam assisted gravity drainage: Based on the concept of unified feature modeling scheme”, *Journal of Mechanics Engineering and Automation*, 6, pp 167-179, David Publishing
8. Yusuf, Y^g, and Ma, Y (2016) “*Design of a simulation tool for steam assisted gravity drainage: Based on the concept of unified feature modeling scheme*”, Proceedings of the Eleventh International Symposium on Tools and Methods of Competitive Engineering, TMCE2016-0014, Aix-en-Provence, France, 9-13 May 2016,

^d Contributions: Review of literature, preparation of manuscripts, analysis and interpretation of data

^e Contributions: Review of literature, manuscript edits, analysis and interpretation of data

^f Contributions: Initial development of idea and framework, review of literature, and preparation of manuscript

^g Contributions: Review of literature, development design of the model a simulation software, develop semantic representation of the model using unified modelling language (UML) scheme, preparation of manuscript

*To my wife, Hiwote Gebremichael, who walked the walk with me, and
To all my family and friends, who always stood by us.*

Acknowledgements

I sincerely appreciate the role of my supervisor Prof. David S. Nobes along the course of this thesis research. I cherish the endlessly supportive, encouraging, and humble advisor that he is for I have greatly benefitted from his mentorship. I am also thankful for members of my supervisory committee Profs. Carlos Lange and Sina Ghaemi for sharing their time to review my work and provide substantial comments and feedback. The financial supports rendered by the Natural Sciences and Engineering Research Council (NSERC) of Canada, Alberta Ingenuity Fund, Canadian Foundation for Innovation (CFI), and RGL Reservoir Management Inc. are also gratefully acknowledged here.

I have been fortunate to work with a number of highly skilled professionals in the Applied Thermofluids Lab. Especially, the close collaborations and comradery I enjoyed with Shadi Ansari, Reza Azadi, Aleksey Baldygin, Michael Bayans, Beatriz Bravo, Jake Hadeffield, Pavan Kamble, Lisa Kinsale, Carlos Mendez, Md Ashker Rashid, Reza Sabbagh, Gabriel Salata, Hiran Soltani, and Calynn Stumpf have all been great sources of strength and unforgettable experiences.

I remain indebted to my wife Hiwote Gebremichael who outstands as the strongest support since the beginning of my studies. My deep gratitude also goes to my parents Abdulhafiz Wober and Muluemebet Eshetu, my sister Azeb Yusuf, my mother in-law Meseret Abeje, and Abiy Wubneh who have all kept me showered with love and care. I extend special thanks to my sister Sarah Yusuf, and my brother in-law Addis Gebremichael for all their support, encouragement, and the ever delightfully insightful interactions they maintained.

Finally, let me take the opportunity to salute the PhD journey. I have learnt so much through the challenges involved which have also tested the limits of my perseverance. I am gratified to have overcome the process which often turned also into a quest of finding the higher self.

Table of contents

Abstract	ii
Preface	iv
Acknowledgements.....	viii
Table of contents	ix
List of Tables	xii
List of Figures.....	xiii
Chapter 1 Background	1
1.1. <i>Motivation</i>	<i>1</i>
1.2. <i>Hypothesis and Objectives.....</i>	<i>4</i>
Chapter 2 Literature Review	6
2.1. <i>Steam –assisted gravity drainage (SAGD).....</i>	<i>6</i>
2.2. <i>Pressure loss models for viscous flow through contractions.....</i>	<i>9</i>
2.3. <i>Equation of motion in streamline coordinates</i>	<i>14</i>
2.4. <i>Pressure loss models for porous media coupled with orifice.....</i>	<i>19</i>
2.5. <i>Summary.....</i>	<i>24</i>
2.6. <i>Organization of the thesis.....</i>	<i>25</i>
Chapter 3 Measurement Techniques and Facilities	28
3.1. <i>Pressure drop measurement experiments</i>	<i>28</i>

3.2.	<i>Velocimetry experiments</i>	41
3.3.	<i>Experiments with porous media</i>	51
Chapter 4 Semi-empirical pressure loss model for viscous flow through high aspect ratio rectangular orifices		56
4.1.	<i>Introduction</i>	56
4.2.	<i>Modeling of the pressure loss coefficient, K</i>	57
4.3.	<i>Results and discussion</i>	66
4.4.	<i>A re-statement of the model</i>	80
4.5.	<i>Modelling the loss coefficient using skew-Normal velocity distribution</i>	83
4.6.	<i>Conclusion</i>	87
Chapter 5 Effect of flow convergence on streamline behavior, velocity transition, and pressure loss characteristics		89
5.1.	<i>Introduction</i>	89
5.2.	<i>Streamline Calculation</i>	90
5.3.	<i>Calculation of the pressure gradients</i>	95
5.4.	<i>Results and discussion</i>	96
5.5.	<i>Conclusion</i>	105
Chapter 6 A Pressure drop relation for the viscous flow through a rectangular orifice with a porous upstream region		107
6.1.	<i>Introduction</i>	107
6.2.	<i>Pressure loss model for flow through the coupled media</i>	108
6.3.	<i>Results and discussion</i>	112

6.3.2	<i>Streamlines</i>	114
6.4.	<i>Conclusion</i>	119
Chapter 7	Conclusions and Recommendations	121
7.1.	<i>Conclusions</i>	121
7.2.	<i>Recommendations</i>	123
References		125
Appendices		141
A.	<i>Raw data for pressure measurement</i>	141
B.	<i>Codes for written programs</i>	145
C.	<i>Detail Drawings</i>	199

List of Tables

Table 1 – Dimensions of rectangular orifices used in the pressure measurement experiments	33
Table 2 – Data used to estimate the uncertainties of measured parameters for the case of $AR = 108$, and $Re = 0.05$	40
Table 3 –Uncertainty data for calculated results for $AR = 108$, and $Re = 0.05$	41
Table 4 – Dimensions of rectangular orifices used PIV experiments.....	44

List of Figures

Figure 1 – (a) Steam-assisted gravity drainage (SAGD) process of oil extraction; (b) definition of fundamental slotted liner geometry based on Yusuf et al. (2019) [59]	6
Figure 2 – A schematic showing the steam chamber in the SAGD process [59].....	7
Figure 3 – A conceptual representation of the radial flow into a section of a horizontal well (a) ideal flow where a homogeneous pressure difference is assumed between the inside of the well and the subcool region; and (b) a zoomed-in view to show the prominence of streamline curvature in the flow into the orifices on the pipe [59]	8
Figure 4 – Schematics showing (a) the definition of streamlines coordinates, and (b) the unit change in streamline position, from s to $s + ds$ <i>after</i> [102], [112]	15
Figure 5 – A sketch showing the effect of streamline curvature and the streamwise pressure distribution <i>after</i> [57].....	18
Figure 6 – (a) photograph of experimental facility; and (b) process flow diagram of the system	29
Figure 7 – (a) a solid model of the flow channel; and (b) annotated photograph of the test section prepared for an experiment	31
Figure 8 – Exploded views of the solid models showing the components in (a) method used to install the test coupons in the pipe, and (b) the shim-based approach devised to manufacturing test coupons of varying AR	33
Figure 9 – A screen shot of the graphical user interface of the data acquisition and monitoring software built for the experiment.....	35
Figure 10 – An example plot of the raw data for $AR = 108$ showing the averaging methods used for (a) Re and (b) ΔP	37
Figure 11 – A schematic representation of the experimental setup;	42

Figure 12 – The flow channel assembly consisting of laser-cut parts	43
Figure 13 – Sample images showing examples of (a) the raw image; and (b) the preprocessed inverted image for the sample channel	46
Figure 14 – Sample results for the orifice $AR = 2$ showing (a) the velocity vector map of the flow field with every 4 th and 2 nd vectors are shown in the x and y directions, respectively; (b) the centerline velocity and (c) the velocity profile at the entrance of the orifice	49
Figure 15 – Annotated photographs showing the upstream section with porous media filling for experiment	52
Figure 16 – Comparison of the pressure drop through the porous bed from experiment and theory for the case $AR = 37$ for a porous bed with particle size of 1.2 mm and porosity of 40%	53
Figure 17 – Annotated views of the solid model of the channel for PIV experiments with porous media [59]	55
Figure 18 – Schematics for (a) definition of the flow domain showing the different regions in the x - y and x - z planes; (b) defining the flow configuration in the x - y plane with the width, b magnified 30 \times	58
Figure 19 –Log-scale plot of the modeled Re -vs- K relationship as per Eq. (28) for all aspect ratios	65
Figure 20– Plot of changes in the static pressure drop as aspect ratio changes at different nominal Reynolds numbers	67
Figure 21– Plot showing the change in K as AR changes for the ranges (a) $1 \leq AR \leq 250$, and..	68
Figure 22– Plot of ϕ vs. AR from Eq(30) with non-linear least square fits	70

Figure 23– Plots of (a) wall pressure profile along axial direction, and (b) the measured pressure drop between transducers located upstream compared with theory72

Figure 24: K -vs- Re plots for experimental data (shown as points) and the developed model Eq. (28).....73

Figure 25– A plot showing values of the calculated angle, θ , for the orifice aspect ratios normalized by the maximum value, $\theta_{max} = 15.7215^\circ$. From the accompanying table showing actual values, it can be seen that $\theta_{max} = 15.7215^\circ$ occurs for $AR = 72$ 75

Figure 26– Re vs. K plots for experimental data (shown as points) and model rotated by multiplication by the rotation matrix76

Figure 27– Plots showing the velocity transition determined from Eq. (21) for all orifice aspect ratios for (a) $Re = 0.05$; (b) $Re = 0.075$; and (c) (a) $Re = 0.1$79

Figure 28 – Plots showing examples of (a) probability density function of the standard-Normal (black) and skewed-Normal distributions (red).....83

Figure 29 – Comparing the loss coefficient models developed assuming (a) standard Normal (Gaussian), and (b) skew-Normal velocity distributions86

Figure 30 –A schematic showing basic features of the streamline calculation scheme developed.91

Figure 31 – Examples showing results from calculations for (a) an individual streamline at $y/b = 2$, and (b) multiple streamlines at specified y/b locations in the flow field.....92

Figure 32 – Plots showing (a) the lines drawn from the center C to points along streamlines, (b) the calculated radii of curvature as a function of the streamwise coordinate x/b ...93

Figure 33 – The variation in the curvature angle $d\theta$ for orifice with $AR = 2$ 94

Figure 34 – Plots showing (a) $\partial p/\partial s^*$ and (b) $\partial p/\partial n^*$ along streamlines at the different locations from the centerline for $Re = 0.1$	95
Figure 35 – calculated streamlines for channels of (a) $AR = 1$; (b) $AR = 2$; (c) $AR = 3$	98
Figure 36 – The curvature angle $d\theta$ shown for (a) $AR = 1$; (b) $AR = 2$; and (c) $AR = 3$;.....	99
Figure 37 – axial velocity increase for channels of width, (a) $AR = 1$; (b) $AR = 2$; (c) $AR = 3$;	101
Figure 38 – Plots for normalized pressure gradient, (a)-(c) in the streamwise direction, $\partial p/\partial s^*$, and (d)-(f) in the span-wise direction, $\partial p/\partial n^*$, for (a),(d) $AR = 1$; (b),(e) $AR = 2$; and (c) (f) $AR = 3$	103
Figure 39 – The loss coefficient, K , calculated using Eq.(35) along the central streamlines for all aspect ratios for $Re = 0.1$	105
Figure 40 – ΔP as a function of Q plotted based on the developed relation given in Eq. (49) ...	111
Figure 41 – The change in ΔP as a function of Q plotted using the developed relation given in Eq. (49) and data from experiment	113
Figure 42 – The change in ΔP as a function of Q plotted using the developed relation given in Eq. (49) and data from experiment	114
Figure 43 – Streamlines in the pore matrix generated using data from PIV measurement of the flow through porous media	115
Figure 44 – Plots showing (a) streamlines at specified location in the flow field; and (b) the calculation of tortuosity demonstrated by the streamline at $y/b =$	117
Figure 45 – Plots showing the streamwise pressure gradient $\partial p/\partial s$ calculated along the corresponding streamlines as per Eq. (8).....	119
Figure 46 (i)–(ix) Raw data from the pressure measurement experiments in the open slot scenario for $AR = 1$ to $AR = 250$, correspondingly	144

Figure 47 – Screen captures showing the GUIs used in the software for (a) live monitoring and control, and supplementary panels for interfaces to configure (b) data acquisition, (c) plot settings, and (d) showing credits 147

Chapter 1 Background

1.1. Motivation

Production of heavy oil from oilsand reserves requires the application of enhanced recovery processes (EOR) [1]. Traditional extraction processes are not suitable for such reserves where the crude oil is found in the form of a mixture consisting of sand and bitumen [2], [3]. Bitumen is an extra heavy oil having density and viscosity in the ranges of $920 \leq \rho \leq 1000 \text{ kg/m}^3$ and $0.01 \leq \mu \leq 10 \text{ Pa s.}$, respectively, at temperatures between 100 and 250°C [3], [4]. Enhanced oil recovery processes produce oil by changing the thermodynamic equilibrium in the reservoir to cause the oil to flow. This objective is typically met by adding heat and/or other solvents that would increase the pressure and change the viscosity of the oil in the reservoir [5]–[8]. These types of oil recovery processes are generally more expensive than traditional ones because they have higher energy consumptions and require additional system components for sand- and flow control [9].

Steam-assisted gravity drainage (SAGD) is a type of enhanced recovery process which was developed in the 1970s [10]. It has become popular since recent years for extraction of oil from oilsand reserves [11]. In SAGD, two horizontal wells that are approximately 1 km long are drilled into the formation with a vertical distance of ~5m between them. The upper well, called the injection well, injects steam at 250 °C into the formation to increase the temperature of the bitumen and thus reduce its viscosity. The oil is then able to drain with the aid of gravity towards the lower well, known as the production well.

Alternative well completion methods are used to minimize the amount of sand produced with the oil and provide the structural integrity to the wellbore [9], [12], [13]. A completion refers to the external pipe casing used for the wells which creates a barrier between the formation sand and the

produced oil being pumped to the surface. Screens are included for sand/flow control by making axial and circumferential patterns of apertures (openings) on the lateral surfaces of the casings. The cross-section, size, and number of these apertures determines the total open area available to the flow. The variety of completion methods currently available to the industry include wire-wrap screens, precision punch screens and slotted liners [9], [14].

Slotted liners have been preferred amongst the industry because they offer the strongest mechanical integrity of the horizontal wells and also for their easier and cheaper manufacturing [1], [11]. They are produced mainly by forming narrow and long aspect ratio slots on the surface of a carbon steel pipe [15]. In the design of slotted liners, the size of the openings are selected to be smaller than the size of 90% of the sand particles in the formation [9].

The presence of these slots causes the flow of produced bitumen entering the production well to undergo a sudden contraction. A significant pressure loss hence results due to the transition from relatively-steady flow conditions farther upstream, to localized distributions of pressure and velocity in the near-entrance region [10], [14], [16]–[21]. The slots also induce acceleration and convergence in the flow [17], [19] due to the abrupt change in the cross-sectional area which leads to a significant velocity increase in this region. The convergence phenomena also has a strong attribute of streamline curvature which has a direct effect on local pressure distribution [22], [23].

The pressure distribution in the system in turn, affects the likelihood of well failure due to mechanisms leading to plugging of the slots [24]–[26]. Depending on local pressure gradients, different materials can be transported to the surfaces of the wells increasing the potential of the slots to plug [24]. These materials are commonly sand particles or fines, emulsions, or other hydrocarbons such as asphaltenes [26], [27]. The transport of solid particles and fines [24], [28], [29] is affected by flow convergence because of high-acceleration and low-pressure it creates [19],

[20], [30]. The chemical kinetics for the precipitation reaction of calcium carbonate is also a function of the pressure in the system whereby low pressure shifts the reaction equilibrium in favor of forming precipitates [24], [25], [31], [32].

Current knowledge of fundamental mechanics, can be used to relate the pressure loss in the formation to the inertial and viscous resistances of the porous medium [33]–[38]. Discounting the presence of the porous medium, the losses due the slot geometry can be modeled using theories developed for flows through sudden contraction [14], [39]. To describe the loss characteristics through the coupled media, there are models that have been developed to also account for the losses due to the interaction between the porous- and non-porous regions [19], [40]–[44]. The modeling of such systems included analytically describing the complex phenomenon for which solving different systems of partial differential equations of varying orders is required [34].

The mathematical modeling of similar problems typically defined the so-called Darcy and non-Darcy regions in the flow field [34], [40]–[44]. Classical models that apply to the corresponding regions are then used to express the pressure loss through each medium. It has been common to take the sum of the losses in each medium to calculate the total pressure drop across the entire domain [43], [44]. Darcy’s law for viscous loss through porous media [33] have been combined with the orifice flow equation [45]–[47] to yield analytical expression for the pressure loss in the coupled media.

The SAGD scenario brings more complexity to the problem not only because of the need to account for the interaction of the phenomena in the different media, but also due to the rectangular geometry of the contraction which has not been as widely studied as circular ones [48]. Therefore, even by excluding the porous medium, existing pressure loss models for viscous flow through circular contractions [45], [49]–[51] cannot be readily applied to model the flow through open

rectangular orifices having similar geometry to SAGD slots. Relevant theories such as the equations for orifice flow [52] apply for the circular geometry. The limited works on the rectangular geometry, consider flow conditions that significantly differ from those in SAGD to allow their use to approximate and/or predict the flow behavior [53]–[55]. The same works have nevertheless shown that a predictive pressure loss models can be developed by combining conservation laws with modified versions of theories for the circular geometry [54] [56].

1.2. Hypothesis and Objectives

The long aspect ratio rectangular orifices alone have strong effects on the overall pressure loss of in the entire SAGD system due to the flow convergence phenomenon they induce [19]. It has been shown that neighboring slots interact to influence the pressure and velocity distribution in the incoming flow hence affecting the flow acceleration and streamline curvature [57]. In a radial flow that is ideally symmetric, the effect of flow separation caused by adjacent slots can be imagined with a line that splits the streamlines directed towards the respective slots. As the flow enters the slots the extent of the streamline curvature is strongly influenced by the size of the slots due to its direct effect on the contraction geometry causing the convergence [19].

It is hypothesized here that the flow convergence induced by the rectangular orifices is a direct function the aspect ratio, AR , of the orifice. The study defines AR as the ratio of the axial length of the orifice to the size of the opening, or as it is referred here, its width. The near-entrance velocity distribution will hence be affected resulting in different behaviors of the velocity gradient for different slot geometry. The shape of the streamlines in this region is also expected to vary as a function of AR .

The general objective of this thesis is to investigate the pressure loss characteristics of the viscous flow through the coupled medium consisting of a porous region and a rectangular orifice. It aims

to develop a reliable model that can be used to further improve the design of slotted liners and other sand control and/or flow control devices. The research goal is to contribute to the fundamental knowledge of flow through rectangular orifices. Relating the pressure loss to the fundamental physics underlying the flow convergence and streamline behavior will also be among the novelties of the thesis.

The analysis of the problem seeks to formulate an expression for the loss coefficient as a function of orifice size and Reynolds number. The approach first isolates the flow through a single open slot to model the pressure loss behavior of a viscous flow. The expression developed for the pressure loss coefficient is to also account for the effect of convergence on the losses in the creeping flow regime. The analysis will apply the conservation equations to the flow field and a constitutive model to represent the localized phenomenon near the entrance.

Experimental measurement of the pressure drop across test coupons having different aspect ratios will be undertaken. Velocity measurement experiments are also conducted for a quantitative study of the behavior of the streamlines during the flow convergence. The tested flow cases include convergence scenarios in the presence and absence of a porous medium in the upstream region.

Relevant literature are reviewed in the next chapter. The survey of literature included topics regarding the SAGD process, fundamentals of pressure loss characteristics, and behaviour of streamlines in flows through contractions. The review also explored investigations of flow through coupled domains consisting of a porous region and an orifice.

Chapter 2 Literature Review

2.1. Steam –assisted gravity drainage (SAGD)

SAGD has become an increasingly popular method to recover oil from oilsand formations [11]. Basic components of the process are given in Figure 1(a). The figure shows the two horizontal wells that are drilled into the reservoir with a vertical distance of ~ 5 m [58]. The upper well injects steam at 250°C to increase the temperature of the bitumen and lower its viscosity. The heated bitumen is then able to flow towards the producer well passing through the openings found on the well completion method used. The method that uses devices called slotted liners is depicted in Figure 1(a) [9].

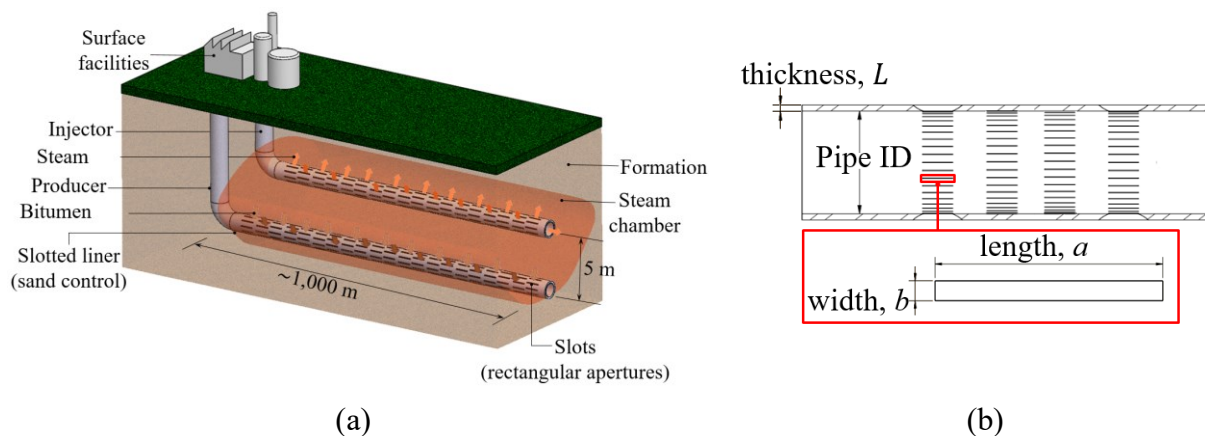


Figure 1 – (a) Steam-assisted gravity drainage (SAGD) process of oil extraction; (b) definition of fundamental slotted liner geometry based on Yusuf et al. (2019) [59]

The rectangular slots shown in Figure 1(b) are commonly manufactured using circular saw blades [39], lasers [60], or water jet [61]. The cross-section of the resulting slots can be defined using its length, a , and width, b . The dimension for the width, b , is selected based on the size of sand particles that make up greater than 90% of the particles in the reservoir formation, i.e. the D_{90} particle diameter used in literature [62] [9]. The length of the slot, a and the spacing between slots are specified based on the minimum open area that is to be provided to for the design production rate. The geometry of the apertures on lateral surfaces of the slotted liners are intended to provide

the required flow passage along the pipe thickness [19], [39], [63]. The sizing of these openings also considers preventing sand and other solids from entering the wells [24]. The design of SAGD system components therefore considers the effect flow through the geometries found in the sand control devices [18], [19], [21], [64], [65].

The schematic given in Figure 2 shows the primary part of SAGD transport phenomenon. The injection of steam forms a steam chamber as indicated in Figure 2. This is a steam-saturated region and it is the central part of the SAGD heat and mass transfer phenomena [3], [66]. The flow towards the production well primarily follows the edges of the steam chamber. Multiple phases flow along this path which include bitumen, steam-condensate, fine sand particles, and emulsions[3], [4].

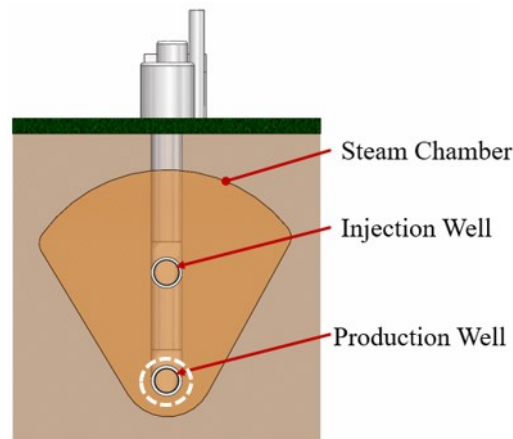


Figure 2 – A schematic showing the steam chamber in the SAGD process [59]

The produced oil enters the annular space between the inner well and the slotted liner casing to be pumped to the surface. As the flow reaches the slots, it conserves momentum by increasing its acceleration which causes the flow to converge, and hence the streamlines to undergo curvature [17], [19], [57]. Flow separation zones are created due to the interaction of the effects from adjacent slots [17], [19]. The size, geometry, and spacing of the rectangular orifices represented by the slot are thus strong factors affecting the curvature of streamlines.

The radial flow of produced oil into the orifices on the production well can be represented as in Figure 3 which shows a result from flow simulation which is conducted to visualize the prevalence of streamline curvature in the SAGD application [59]. The flow field shown in the figure was generated using a commercial flow simulation package (SolidWorks FlowSimulation2018, Dassault Systèmes) to provide a visual representation of the streamline curvature during the flow convergence phenomenon. The flow scenario depicts the condition where there is a uniform positive pressure gradient between annulus and the fluid surrounding the well, i.e. the sub-cool region[4].

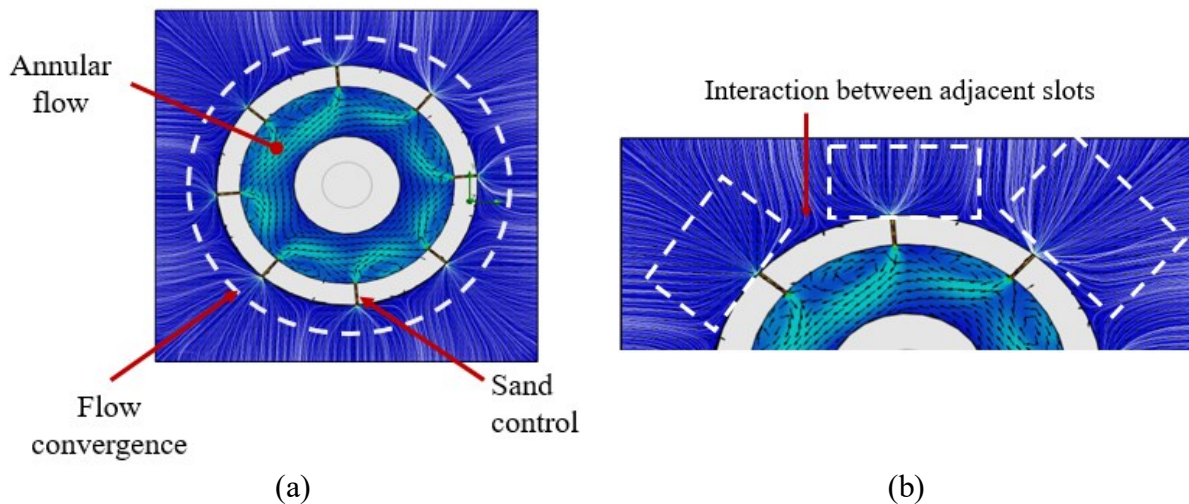


Figure 3 – A conceptual representation of the radial flow into a section of a horizontal well (a) ideal flow where a homogeneous pressure difference is assumed between the inside of the well and the subcool region; and (b) a zoomed-in view to show the prominence of streamline curvature in the flow into the orifices on the pipe [59]

Complex transport phenomena are involved in the SAGD process. The literature contains[3], [4], [7], [67]–[69] works that have treated the heat and mass transfer problems separately from the flow mechanics ones, and vice-versa. However, attaining a comprehensive model that describes the entire process with the precision and robustness required have proven to be far ahead. The rectangular geometry of the slots makes the modelling even more challenging as the literature on

orifice flow mostly contains works on the circular geometry with the rectangular ones receiving attention only recently.

In the following section, the review of relevant literature on pressure loss modeling for viscous flow through contractions is presented. In view of Figure 3 and its accompanying discussion, Section 2.3 reviews the theory regarding flow analysis using the behaviour of streamlines. Prior works related to the flow through the coupled media is given in Section 2.4 which also includes review of the fundamental theory on flow through porous media.

2.2. Pressure loss models for viscous flow through contractions

The flow of viscous fluid through contractions such as orifices and nozzles is a widely studied topic with, despite the efforts, much complexity that remains to be fully understood. Flows of this nature are commonly encountered in flow meters [70], [71], engines [72], [73], and processing plants [74]. While the development of a model that describes the flow characteristics has been extensively studied, there is still a continuing interest to model such systems as comprehensively as possible. The literature demonstrates various modelling approaches in different fields of application [45], [49], [55], [75]. A number of flow phenomena that are caused by the contraction geometry have been identified and described. Works have considered effects of the magnitude of the open area [50], [76], wall profiles and inlet geometry [77], and the axial length of the region of contraction [45], [78]. It is noticed that the majority of the studies in the literature have been mostly focused on contractions of the circular geometry. In recent years, however, non-circular geometries such as rectangular orifices are gaining attention because of the growing interest in their micro- and macro -scale applications for flow measurement and control devices [79]–[81].

The characteristic flow configuration can be explained by considering the flow scenario in a typical orifice plate flow meter [70]. Orifice plates typically contain round axisymmetric holes across

which the pressure drop is measured to determine the volumetric flow rate [82] The entire flow domain can be divided into three main regions – the upstream flow convergence region, the region inside the orifice (the contraction region), and the downstream region [45], [78] that returns to the bulk characteristics of a flow in a pipe. The planes at the inlet and exit faces of the orifice mark the respective interfaces between these regions.

The upstream region can thus be defined between regions in the far field ($x = -\infty$) where steady state conditions prevail, and the inlet face of the orifice at $x = 0$ for an axial coordinate, x , with the origin of the system placed at the orifice inlet. This region also includes the convergence zone which is measured from where the flow acceleration begins [52] to the inlet plane. If the entrance length, L_e , is considered [83], the convergence zone will cover the region $-\infty \leq x \leq L_e$ extending to where the orifice centerline velocity is reached. It can, however, be found to be appropriate to only consider up to $x \leq 0$ ensuring agreement between the physical and mathematical interpretations of the velocity distribution function [52], [84].

At steady conditions, Poiseuille flow characteristics will prevail in the upstream region [47] with a linear axial pressure gradient. However, in the near-inlet regions complex non-linear properties are often seen resulting in a range of flow events mainly formation of asymmetries and circulation regions due to shear- and inertia-related effects [22], [52], [81], [85]. The characteristics lengths of these regions can be described with respect to fluid, and geometric properties typically using expressions as a function of the Reynolds number, Re [54], [81].

For small circular orifices ($< 1\text{ mm}$), the resulting pressure loss is often characterized with respect to the diameter of the orifice and the total axial length of the contraction region [45], [52], [78], [86]–[88]. Investigations have also considered effects of small-scale geometric features such as the inlet wall profile [80] and surface roughness [89]. At these length-scales the influence from

micro- and nano-scale deformation properties of the fluid also becomes significant to affect the pressure distribution [81], [90]. For orifices with the rectangular geometry, studies consider the effect of a non-dimensional aspect ratio (AR) parameter often defined as the ratio of the dimensions of the area of the contraction on the inlet plane [16], [81], [91]. Typically, the lowest end in the range ($AR = 1$) represents an orifice with a square geometry while at the limiting end ($AR \gg 1$) is a Hele-Shaw-like flow [47], [81] between two walls separated by a very small distance.

Studies on rectangular orifices have shown that as AR increases, the static pressure drop, ΔP also increases [16], [81], [91]–[93] for all Reynolds numbers. The flow Reynolds number is commonly defined by using the hydraulic diameter as the length scale and the velocity through the contraction as the velocity scale. In creeping flow conditions ($Re \rightarrow 0$) the flow shows a viscosity-dominated streamlined pattern [81] while for higher Re , high inertia leads to asymmetries, down-stream flow axis switching [91], circulation and vortex generation. The effects of such Reynolds number-related variations often leads to regions of low pressure the attributes of which are of great modeling and experimentation interest due to the growing demand for predictive models in both the academic and industrial communities.

The development of pressure loss models for orifice flow has covered a wide range of flow conditions and configurations in the effort to analytically describe the flow phenomena in the various regions of flow domain [89], [94], [95]. There has been extensive work on circular orifices with publications commonly reporting effects of orifice size [45], [49], inlet velocity profile [96] and wall profile of the upstream region [80], [97], and effects of fluid rheology [81], [98]. The traditional modeling approach followed writing the momentum balance equation in non-dimensional form to obtain an expression for the loss coefficient as a function of Re and the orifice geometry [78], [87], [99]. A modeling approach to account for the physics of the contraction is

found in works by Grose in 1983 and 1985 [52], [97]. These works on circular orifices achieve their goal mainly by using the geometric characteristics of the control volume to include conditions for the conservation equations. Researchers have, foremost, not treated the flow through long aspect ratio rectangular orifices in as much dedication as to circular geometries [54]. With respect to the flow-related factors, the effect of flow convergence on the pressure loss is not yet described in terms of purely physical analysis. The focus has been on obtaining an empirical parameter by fitting a known theory to data from experiments measuring pressure drop [78], [87], [99]. Most studies on flow convergence have only focused on qualitatively describing the shape profile of the convergence zone mostly defined in terms of constant region of pressure [17] or proximal velocity gradient [52], [100].

The Bernoulli equation can be used to discuss the balance of the loss in hydrostatic pressure to the gain in kinetic energy for flow through a sudden contraction. An empirically determined term for the discharge coefficient, C_d , is typically used to account for the deviation due to assuming negligible viscosity effect in Bernoulli's equation [52], [101]. This coefficient is defined as the ratio of the actual discharge to the theoretical discharge and is given by:

$$C_d = \frac{\dot{m}}{A\sqrt{2\rho\Delta P}} \quad (1)$$

where \dot{m} is the mass flow rate, ΔP is the static pressure drop across the orifice, ρ is the density of the fluid and A is the constriction area.

In a series of continuing works on flow through circular orifice, Grose [52], [97] has shown that the orifice discharge coefficient (C_d) can be described as the product of three coefficients each accounting for a factor in a pressure loss. These are coefficients for contraction, velocity profile and for viscous effects. The development of an experimentally verified representation of the viscous effect coefficient for flow through circular orifice at low Reynolds numbers ($Re < 1$) has been presented [52] by assuming an asymptotic velocity transition in 1D flow.

A dimensionless pressure loss coefficient, K , can be obtained by taking the square of C_d , rewriting the expression in terms of volume flow and taking its inverse, the coefficient can also be calculated by taking the ratio of the static pressure drop to the kinetic energy. At creeping flow conditions ($Re \ll 1$) through circular orifices, the loss coefficient through a finite thickness is given by [78]:

$$K = \frac{12\pi}{Re} + \frac{64}{Re} \frac{L}{d_o} \quad (2)$$

where L is the orifice length along the flow direction; and d_o is the orifice diameter. The first term follows the analytical solution for orifice of zero thickness while the second term is the common Darcy friction factor [78]. In general, the relationship between Re and K can be generalized as:

$$K = A + \frac{B}{Re} \quad (3)$$

where A and B are empirical constants. A summary of the different suggestions for the numerical values of the constants in Eq. (3) can be found in the literature [78].

For a rectangular orifice inside a similarly shaped microchannel, developed correlations [54], [81] showed that the pressure drop is a function of the average velocity through the orifice, and geometric factors such as the contraction ratio and aspect ratio. Zivkovic et al. [54] and Oliveira et al. [81] used a Couette coefficient, K_L , which is defined as the excess pressure drop normalized by that average wall shear stress across the sudden contraction and sudden expansion regions in upstream and downstream the orifice, respectively. The use of this coefficient also avoided the non-linearity due to the inverse relation seen in Eq. (3) where Re_w is the Reynolds number defined based on the width (w) of the rectangular orifice.

The effect of orifice aspect ratio on the normalized pressure loss has been reported by Oliveira et al. [81] where higher aspect ratios led to pressure loss. The axial pressure loss was normalized by the product of the velocity and the square of the smaller orifice dimension. Considering the ratio of the static pressure loss to the kinetic energy gain as the loss coefficient, however, would result

in an inverse relationship because a direct relationship can be formed between orifice aspect ratio and flow acceleration, strain rate, and, hence, streamline curvature. The change in the pressure loss for varying aspect ratio would hence be mainly due to streamline curvature when compared to the acceleration and strain rate as the findings by Oliveira et al. also indicate [81].

2.3. Equation of motion in streamline coordinates

Investigating curvature phenomena in orifice flow using analytical techniques requires working in streamline coordinates [57]. For creeping flow at steady state conditions, the streamlines and pathlines are the same which helps by making the analysis less challenging. Application of fundamental theory regarding the behaviour of streamlines to arrive at analytical relations between the velocity and pressure gradients is reviewed in this section [102]. The discussion also includes relations between streamline curvature and the major field parameters.

Important flow characteristics can be described in reference to streamlines which reflect the spatial distribution of the flow [47], [84]. Streamlines can be used to identify and classify regions in the flow field and characterize their behaviors. Analysis of streamlines is commonly used in investigations related to extensional flow [81], turbomachinery [103] and hydrology [104]. Aerodynamic researches are also popular for making extensive use of streamlines [105]–[107].

Irrespective of the relative dominance of shear and inertial forces, the change in the shape of the streamline is always common to the flow convergence phenomenon in orifice flow. The curvature of streamlines in the near-orifice region is a 2D phenomenon that is one of the basic features defining the convergence [19]. In streamlines, the curvature is primarily associated with acceleration and hence the pressure field in the corresponding local regions [57] but with the effect extending to pressure loss across the entire system [108].

In general, the relationship that has been established is such that when there is streamline curvature, the pressure increases along the axis, n , normal to a streamline in the direction away from the center of curvature [57], [102], [108]. The concavity of a curved streamline therefore gives the first indication for the direction of pressure gradient. In the streamwise direction, s , the pressure gradient is directly associated with the corresponding change in velocity along a streamline. From this perspective, streamline curvature generally results from an increase in dynamic pressure while the static pressure decreases along a streamline [84], [57]. In the case of orifice flow, the region of acceleration is also where streamline curvature is maximum as well as the pressure and velocity gradients [22], [109], [110].

Analytical approaches commonly solve Euler's equation of motion in streamline coordinates to relate the velocity and pressure distributions along both s , and n directions [102], [108]. The radius of curvature, R , is defined parallel to the positive n -vector which also signifies its strong influence on the pressure gradient in the transverse direction [57], [84], [102]. The curvature of the streamlines can be determined from the velocity or pressure field or both to ultimately calculate the radius, R [108], [111].

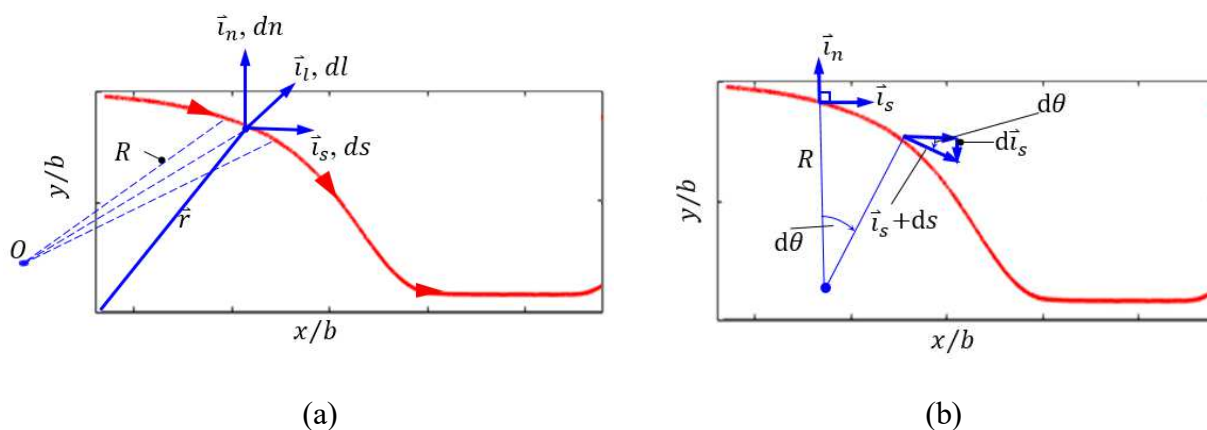


Figure 4 – Schematics showing (a) the definition of streamlines coordinates, and (b) the unit change in streamline position, from s to $s + ds$ after [102], [112]

Definition of the streamline coordinate system is given in Figure 4. In Figure 4(a), the basic geometric attributes that describe a point on a streamline are shown. Primarily, a trio of unit vectors are used to locate a point in the system from the view of an external observer at center O outside the xy -plane. The flow direction is denoted by the vector, \vec{l}_s , while the unit vectors, \vec{l}_n and \vec{l}_l point towards the normal direction and the bi-normal direction, respectively. Defining these vectors and the radius of curvature, R , enables the measurement of the unit streamwise increments ds and $d\theta$ as shown in Figure 4(b) [102], [112].

The unit vectors, the local radius of curvature, R , and the center, C shown in Figure 4(b) are all unique to every point along a streamline. The radius of curvature takes positive value when the normal vector, \vec{l}_n , is pointed away from the center of curvature. The bi-normal direction vector satisfies the relationship $\vec{l}_l = \vec{l}_s \times \vec{l}_n$.

By definition, the velocity in the direction of flow is tangent to a streamline at all points [47], [84]. This property can be used to extract the curvature information of the streamline. It allows to determine the change in radius of curvature for a unit increment along a streamline. Euler's equations of motion are written to relate the velocity and pressure fields in both coordinates. The equations essentially represent the balance of mechanical energy in the system. Neglecting body forces, Euler's equation in the s -direction is written as:

$$\frac{\partial}{\partial s} \left(\frac{v^2}{2} \right) = -\frac{1}{\rho} \frac{\partial p}{\partial s} \quad (4)$$

where v is the velocity at a point on a streamline. The negative sign indicates that a pressure decrease will always result from a velocity increase and vice-versa [57], [84], [102]. In the n – direction, the equation becomes:

$$-\left(\frac{v^2}{R}\right) = -\frac{1}{\rho} \frac{\partial p}{\partial n} \quad (5)$$

where R is the local radius of curvature of the streamline. The dominant effect of the radius of curvature on the pressure variation the n direction is noticed from the equation. It can be seen that that as the curvature of a streamline increases, pressure increases in the direction away from the centre of curvature [57], [102].

Shapiro (1963) compared the flows through straight and curved channels to show the relationship between streamline curvature and the pressure as shown in Figure 5 [57]. Considering 1D flow, the average pressure on AB is lower but closely comparable to the pressure far upstream. However, the streamline curvature leads to increasing pressure from A to B resulting in the pressure at B to be significantly higher than the upstream pressure. Similarly, the average pressure along CD is higher than but comparable to the downstream pressure but with the pressure at D higher than at C due to curvature effects. Referring to the accompanying pressure profile, it becomes apparent that streamline curvature represents the pressure rise to the maximum at point B and fall to the minimum point C, rather than follow the steady decrease profile from A to D shown for flow along a straight wall.

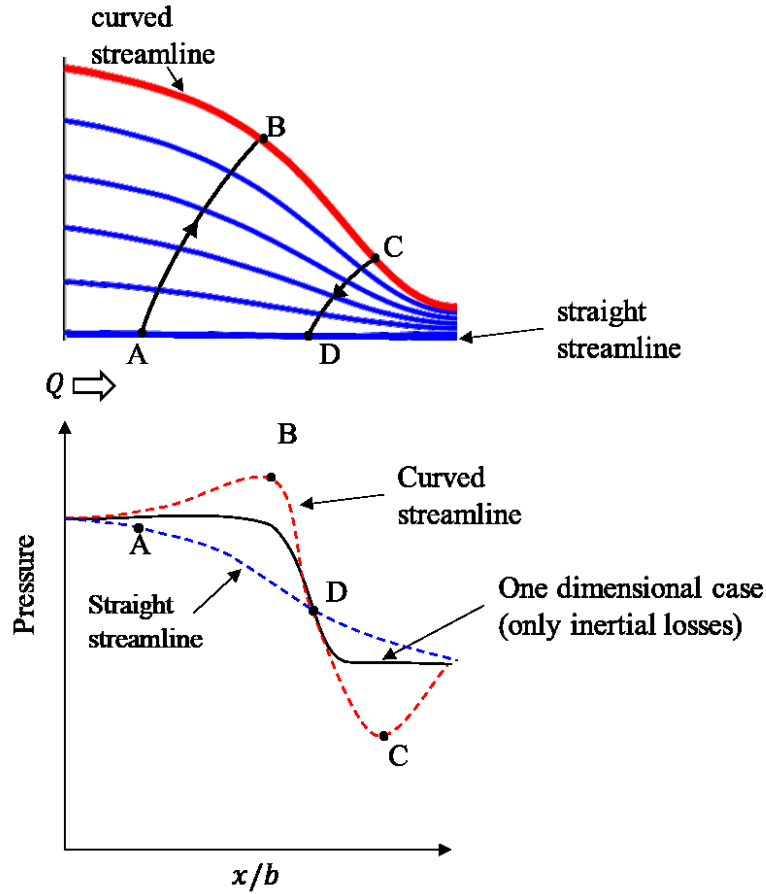


Figure 5 – A sketch showing the effect of streamline curvature and the streamwise pressure distribution *after* [57]

To represent the conservation of momentum along individual streamlines in Eulerian reference, the Navier-Stokes equation can be written in the streamwise direction. When the streamline coordinate system is used to write the momentum balance equation, the Lagrangian version of the momentum equation in the s -direction reads [84]:

$$\rho \vec{v} \frac{\partial \vec{v}}{\partial s} = \frac{\partial}{\partial s} \left((2\mu + \lambda)(\vec{\nabla} \cdot \vec{v}) - p \right) - \mu \frac{\vec{v}}{|\vec{v}|} \left(\vec{\nabla} \times (\vec{\nabla} \times \vec{v}) \right) \quad (6)$$

where μ and λ are the first and second Lamé parameters as defined in the strain-stress relationship given by classical continuum mechanics [113]. It is to be noticed that the first Lamé constant μ is equivalent to the dynamic viscosity coefficient for Newtonian fluids.

It is interesting to note that Eq. (6) implies that Bernoulli's equation applies if a flow is either incompressible where $(\vec{\nabla} \cdot \vec{v}) = 0$ or for an irrotational flow for which $(\vec{\nabla} \times \vec{v}) = 0$, with an emphasis in the either-or condition [84]. Under this condition both viscous terms on the right side of Eq. (6) disappear and the equations in streamline coordinates take the form of Eq. (4).

2.4. Pressure loss models for porous media coupled with orifice

It is known that the behaviour of streamlines changes [114] when there is a porous region upstream the orifice. With the coupling of the two media – orifice and porous bed – playing a significant role in determining the pressure distribution [34], [40], [42], [115]–[118]. The topic of streamline behaviour in porous media inevitably raises a discussion of the parameter tortuosity which describes the elongated distance travelled by the fluid due to the presence of the obstacles of the pore matrix [59], [119]–[123]. The review of studies that investigated the flow through the coupled media is presented in this section.

Pressure drop due to a porous bed is commonly calculated to determine the energy input required by the system [36]. The energy requirement is related to the inertial and viscous resistances to the flow caused by the pore matrix [33], [37]. The most widely used relation for the pressure drop through porous media is Darcy's law developed in 1856 [33], [36]. The law describes the pressure drop in one-dimensional laminar flow of a Newtonian fluid [33]. It expresses the pressure drop, ΔP , across a porous media of length, L , as a function of the volume flow rate, the fluid viscosity, μ , and an intrinsic property of the porous medium, κ , as:

$$\frac{\Delta P}{L} = q \frac{\mu}{\kappa} \quad (7)$$

where the flux q is for the volume flow per unit area. The area here refers to the total cross sectional area of the porous region rather than the area at the pore-scale [43]. The primary statement of Darcy's law is that, as the viscous resistance across the porous medium increases, and permeability

decreases, a greater pressure loss along the length of the porous bed results. The parameter κ , is the permeability of the porous medium and its fundamental definition is given by Eq.(7) [36]. The permeability, as its name implies, represents the ability of the flow to permeate through the flow passage provided by the pore matrix.

Along an individual streamline, Darcy's law may also be written as [117]:

$$\frac{\partial p}{\partial s} = A \cdot q(s) \quad (8)$$

where, in this form, A is termed the coefficient of viscous resistance which is equivalent to $\frac{\mu}{\kappa}$ according to Eq. (7). The equation is applicable for flows at $Re < 10$ with the particle size of the porous media used as the length scale to calculate the Reynolds number [117], [124]. To account for inertial effects, Forchheimer in 1901 [36] gave an equation adding a term to Eq.(8) such that:

$$\frac{\partial p}{\partial s} = A \cdot q(s) + B \cdot |q(s)|q(s) \quad (9)$$

where B is the coefficient of inertial resistance in the porous region. The expressions for the coefficients A and B been given by Ergun (1952) as a function of fluid viscosity and properties of porous media [36] such that:

$$A = \frac{150}{\psi^2 d^2 \rho g} \frac{(1 - \varepsilon)^2}{\varepsilon^3} \quad (10)$$

$$B = \frac{1.75}{\psi d g} \frac{(1 - \varepsilon)}{\varepsilon^3}$$

where ρ is the fluid density, g is gravitational acceleration; ε is the porosity of the medium; ψ is a particle shape parameter (1 for spherical particles), and d is the mean particle diameter [36].

The derivations of the coefficients have been based on the general physical principle which argues that the total flow resistance is the combination of the viscous and inertial resistances. In Eq.(9), it

is also noticed that the viscous resistance is represented as a linear function while inertial effects are accounted for by the direction preserving square term of the flux [117], [125].

Modelling the pressure distribution in flow through the coupled media has been investigated to solve problems in the oil and gas [21], [126], filtration and hydrology [40], [44], [117], medicine [34], and automotive [34]. Analytical approaches have typically classified the flow regions into the subdomains to write the corresponding pressure loss from the respective theories and couple the resulting equations [34], [117]. Pure mathematical modeling of the problem have mainly focused on describing the phenomena at the interface to model the local change in the pressure distribution [34], [40], [41], [127], whereas in engineering analyses considering global changes in the bulk scale distributions of the pressure and velocity sufficed [34], [38], [43], [128].

For flow domains consisting of an orifice and a porous region, studies have coupled the orifice equation given in Eq.(2) with either Darcy's law or Forchheimer's equation [117], [126]. The corresponding pressure drops due to each medium were calculated to determine the total pressure loss through the system. To obtain the final expression for the pressure loss, the sum of the losses through each medium has been commonly used [44], [117], [126].

Collins et al. [43] developed model for the problem of groundwater contamination due to intrusion to an underground distribution pipe through an aperture on its surface . The derivation combined analytical models for the flow through porous media with models for losses through an orifice. A quadratic equation of the volumetric flow rate, Q , is solved in the final step to describe the relationship between the pressure loss and volume flow. In this work, however, the geometry of the opening on the pipe surface was assumed to be circular which might not apply as suitably to different cases.

For the assumed circular geometry of the crack on a pipe at depth, D , the total head loss, Δh , has been given as:

$$\Delta h = h_p - D = h_o + h_{pm} \quad (11)$$

where h_p is the pressure head in the pipe, and h_o and h_{pm} are the losses through the orifice and the porous media, respectively. By using the orifice equation and Darcy's law, the final model given by Collins et al. is [117, p. 1055]:

$$Q = \frac{1}{\sqrt{k' + \frac{d_o g \sqrt{GB}}{6}}} \frac{\pi d_o^2}{4} \sqrt{2g\Delta h} \quad (12)$$

where Q is the volumetric flow rate; d_o is the diameter of the orifice; g is gravitational acceleration; Δh is the difference in the static head between the pipe and the head of groundwater external to the pipe; k' is a constant representing the friction loss through the pipe thickness; G is a factor that defines geometric constraints; and B is the inertial resistance coefficient given in Eq. (10). The expression has replaced the coefficient of discharge by the denominator term under the square root. It is noticed that this term is also function of the orifice size, inertial resistance in the porous media, losses due to friction in the orifice, and the overall shape of the radial flow.

Collins et al. (2013) compared the effect of porous media properties and orifice size on the pressure drop across the coupled domain [117]. Experimental and numerical investigations have verified the model shown in Eq. (12) by studying the flow of water through three kinds of porous media and three sizes of a circular orifice. The results showed that the porous region had stronger effects on the flow rate-pressure relationship for larger orifice diameters. The results pertaining to the effect from the properties of the particles of the media showed that the effect of the region is less pronounced for a porous bed of plastic particles than those of gravel packs. This was attributed to the effects from surface roughness where the smoother particles led to less resistance to flow.

The effect of the streamline behaviour on flow retardation as described by the permeability is commonly represented by the Kozeny-Carman relation which states [119], [120], [123]:

$$\kappa = \frac{\varepsilon^3}{\psi \tau^2 S^2} \quad (13)$$

where κ is the permeability coefficient, ε is the porosity of the medium; ψ is the shape factor which depends on the granular properties of the porous bed ($= 1$ for spherical particles), τ is the hydraulic tortuosity, and S is the specific surface area. The equation provides a semi-empirical relationship between the properties of the pore structure and the geometry of streamlines the latter represented by τ [119].

The coefficient τ is defined as the ratio of the effective length, L_{eff} , travelled by the fluid particle along the tortuous path in the pore matrix, to the distance, L , the fluid covers along the straight line in the macroscopic flow direction. It represents the factor by which the straight-line path is elongated. In the calculation, the effective length travelled by the fluid can be determined by taking the arc length of the streamlines along the path [119].

The streamlines through the complex geometry of the pore matrix can be obtained by determining the velocity field using either experimental [59] or numerical techniques [119], [120], [123]. Duda et al. [120] have showed that the tortuosity factor can be determined from the ratio of the average intrinsic velocity to the macroscopic-scale one. Theoretically, this approach requires to solving the Navier-Stokes equations in all pore spaces of the medium to obtain the velocity distribution.

Analytical investigations of the problem have also modeled the porosity-tortuosity relation system by using statistical approaches to describe the flow along differential paths defined in the pore geometry [122]. Numerical investigations, have showed the application of lattice Boltzmann method to approximate the tortuous path over a cubic grid representing the pore structure [119],

[120], [123]. Reported results showed that tortuosity can be used to derive different parameters describing the transport phenomena in addition to fluid path. The literature also contains tortuosity parameters defined in problems of diffusion [129], [130], and electricity [131]

2.5. Summary

The flow configuration in the SAGD case is made up of a coupled flow domain containing the porous region and the orifice [132]. The respective flows through each of the subdomains alone are widely studied. The modelling of similar flow configuration has also been the focus of research in the field of hydrology and ground water distribution in relation to the intrusion of contaminants through cracks on the pipe surfaces [117]. The review has in general shown that there is still the need to model the flow through rectangular orifices of the SAGD geometry to represent the effect of the slots on the pressure loss characteristics, hence, failure of wells due to plugging.

In their modelling studies have separately represented the losses through each media and took the total pressure drop across the entire system as the summation of the respective losses [21], [43], [44], [126], [128]. Darcy's law and Forchheimer's relation have been famously applied to write the losses through the porous region, whereas the orifice equation provided the relationship between the flow rate and pressure drop. The geometries of the orifices considered in the literature are all approximated by the circular geometry making the existing models inapplicable to model the SAGD scenario.

The review has not found any work that described the flow convergence phenomenon in orifice flow with respect to streamline curvature which is an essential property that has to be considered in the flow of produced bitumen into the production well [19], [126]. The prominent works on flow convergence have addressed their issues by defining a region of constant pressure [126] and proximal iso-velocity surfaces in the near entrance region [22], [23], [100], [109], [110], [133].

The investigation of flow convergence also covered geometries different from the rectangular orifice geometry found in SAGD slotted liners [23], [110], [133].

In general, the literature review highlighted the possibility to separately model the flow through the coupled flow domain in SAGD. It has also shown the knowledge gap in relation to the role of flow convergence in the loss characteristics of the viscous flow through rectangular orifice in both the presence and absence of a porous upstream region. The capability of combined pressure and velocity measurements to obtain reliable data to model the loss coefficient and streamline curvature as a function of orifice geometry is also learnt.

2.6. Organization of the thesis

The thesis is organized in the remaining five chapters. Chapter 3, describes the techniques employed for pressure and velocity measurement. The facilities used for the experiments are also explained. A description of the methods used to manufacture the test coupons containing the orifice geometries is provided. The methods applied in processing the data such as averaging and uncertainty calculations are also explained.

The development of a semi-empirical pressure loss model for the viscous flow through the rectangular orifices having high aspect ratio, as in SAGD slots, is the topic of Chapter 4. The hypothesized effect from orifice aspect ratio on the flow convergence and hence the resulting pressure loss is formally presented in this chapter. The developed model is based on the conservation of momentum equations and a localized velocity transition model. The approach is described by showing the derivation using the 1D Navier-Stokes equations and a Gaussian model for a unique asymptotic velocity transition in the convergence zone. The results from experiments showing the effect of aspect ratio on the pressure loss and velocity transition behaviors are also discussed in the chapter.

Chapter 5 strengthens the physical argument presented in Chapter 4 by using results from velocimetry experiments to show the difference in the curvature properties of streamlines for changing aspect ratio. The calculation scheme developed to obtain streamlines from the velocity data is discussed. The discussion of results includes the curvature properties, pressure gradients, and velocity transition as a function of orifice geometry. The relationship between the loss coefficient and orifice aspect ratio is verified.

In Chapter 6, the case where a porous region is present in the upstream region of the orifice is considered. The semi-empirical model developed in Chapter 4 is coupled with Ergun's model for porous media to yield a model for the flow rate-pressure drop relationship. The results from pressure measurement experiments are also used to show the pressure drop for different aspect ratio of the orifices tested. A closer view of the behaviour of the streamlines in the tortuous path of the coupled medium is also provided.

The major conclusions drawn and recommendations for future research are presented in Chapter 7. This chapter is mainly a collection of the conclusions and remarks stated in the respective chapters with some additional ones that are more comprehensible for the broader view. The chapter concludes the thesis by forwarding recommendations points for future work with respect to the major lessons learnt and the research questions that follow.

The last chapter provides the appendices to the thesis. Included in the appendices are the raw data from the pressure drop experiments, drawing package, and programming scripts. The drawing package provides details of the components designed and manufactured for the experiments. The scripts provided were written to (1) develop the data acquisition and monitoring software for the pressure measurement experiments; (2) read and process logged data for data analysis and plotting;

and (3) implementation of the streamline calculation algorithm to determine the streamlines in the flow field and streamwise calculation and plotting of parameters.

Chapter 3 Measurement Techniques and Facilities

The experiments conducted for the study consisted of pressure and velocimetry measurements. Each measurement includes the two scenarios where a porous medium is present and absent in the upstream region. The pressure measurement are conducted in a large scale flow facility whereas the velocimetry experiments used a conventional bench scale setup allowing for the use of the optical diagnostic technique, particle image velocimetry (PIV). The upstream side in the orifice flow configuration is modified to include a porous region for experiments in that scenario.

In this chapter, the respective measurement facilities used for the experiments are presented. The design and manufacturing techniques used to make the corresponding test coupons for the orifice geometry are also included in the discussion. Data collection and processing methods including averaging and uncertainty calculation are also explained using example sets of data from the pressure measurement and velocimetry experiments.

3.1. Pressure drop measurement experiments

A flow measurement facility has been instrumented and programmed for experiments to measure the pressure drop across rectangular orifices at different flow rates. The temperature controlled system handles and transports viscous fluid through a flow loop that has two main sections. The test section is where the main flow pipe containing the orifice plate is placed whereas a separate fluid handling section consists of the reservoir for the working fluid, pumps, flow meter, and the pipe network. Experiments conducted for this study use a commercially available viscous liquid with $\mu = 1.80 \text{ Pa}\cdot\text{s}$, and $\rho = 884 \text{ kg/m}^3$ at $45 \text{ }^\circ\text{C}$ (Brightstock Oil, Fuchs Lubricants Canada Ltd.).

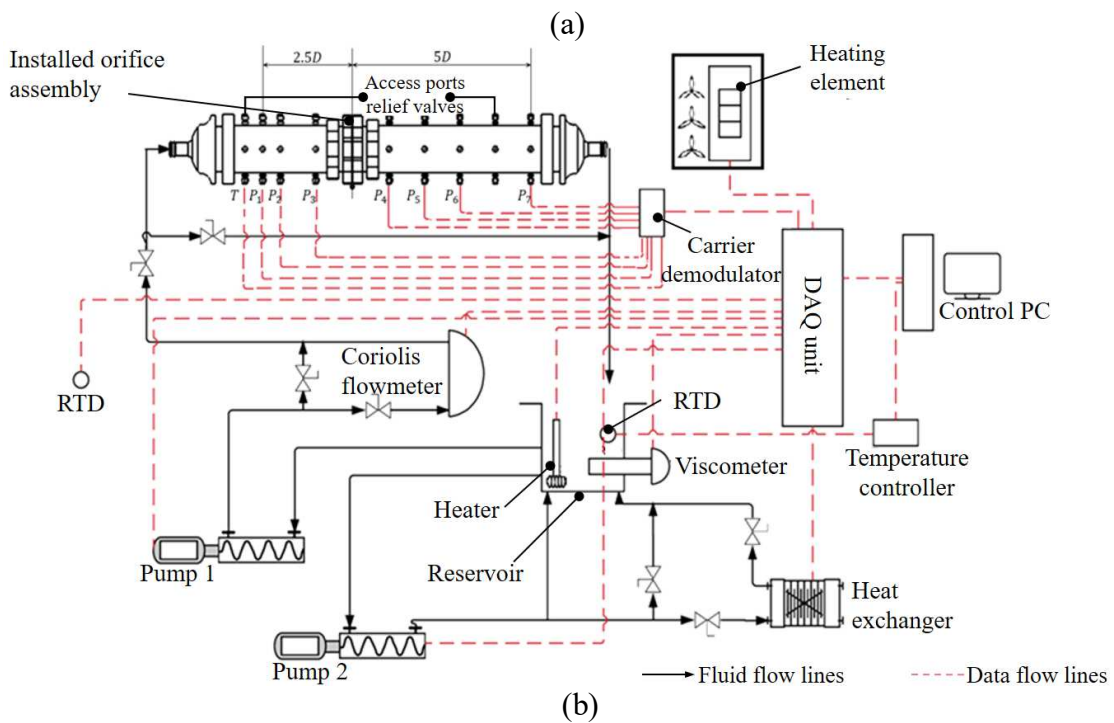
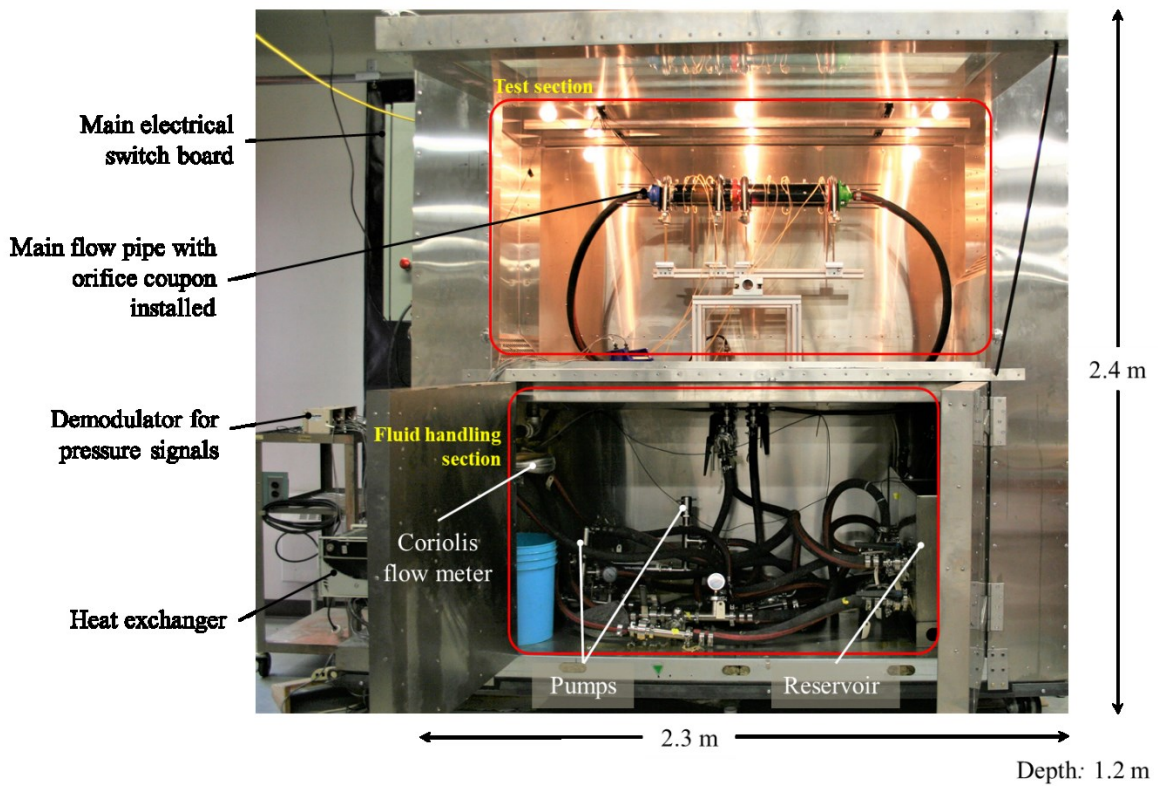


Figure 6 – (a) photograph of experimental facility; and (b) process flow diagram of the system

The process flow diagram of the experimental setup is shown in Figure 6. Two progressive cavity pumps (MD 012-12, and BN 1-6L, Seepex Inc.) were used to withdraw the viscous oil from the reservoir and circulate it either through the main flow loop (Pump 1), or through a heat exchanger (Pump 2). A submersible electric heater (TLCP303053, WATTCO™) was used to heat the oil in the reservoir to lower its viscosity to ensure minimized resistance to pumping. A commercial temperature controller (CNPT series, OMEGA Engineering, Inc.) was used to maintain the temperature of the oil in the reservoir at a pre-set value. Temperature in the flow pipe is also monitored using a resistance temperature detector (RTD) (TR40, WIKA Instruments Canada Ltd.) to identify any deviations in viscosity. A Coriolis flow meter (CMFS025, Micro Motion Elite series, Micro Motion, Inc.) was used to measure the mass flow rate of the oil pumped to the upper (test) section. The oil viscosity in the experiment was monitored with a viscometer (7827 High performance viscosity meter, Micro Motion Inc.) installed in the reservoir.

The main flow pipe used for the experiments is shown in Figure 7. The pipe was made from commercially available transparent acrylic tubes having a wall thickness of 9.5 mm and had an internal diameter of 76.2 mm. The lengths of the pipes used for the upstream and downstream sections were 203 mm, and 330 mm, respectively. As indicated in Figure 7(b), the fittings were manufactured from acrylonitrile butadiene styrene (ABS) polymer by fused deposition modeling technique of additive manufacturing using a commercial 3D printer (Ultimaker 2, Ultimaker BV). ABS was selected for its thermal resistance property (glass transition temperature = 105°C) which was found sufficient to withstand the experiment conditions in the test section of the facility. The fittings used include the reducers at either ends to connect the rubber hoses; and the flanges used to connect the two pipe section which also sandwiches the test coupon assembly. The details of the design and dimensions of the test section are provided in Appendix C.

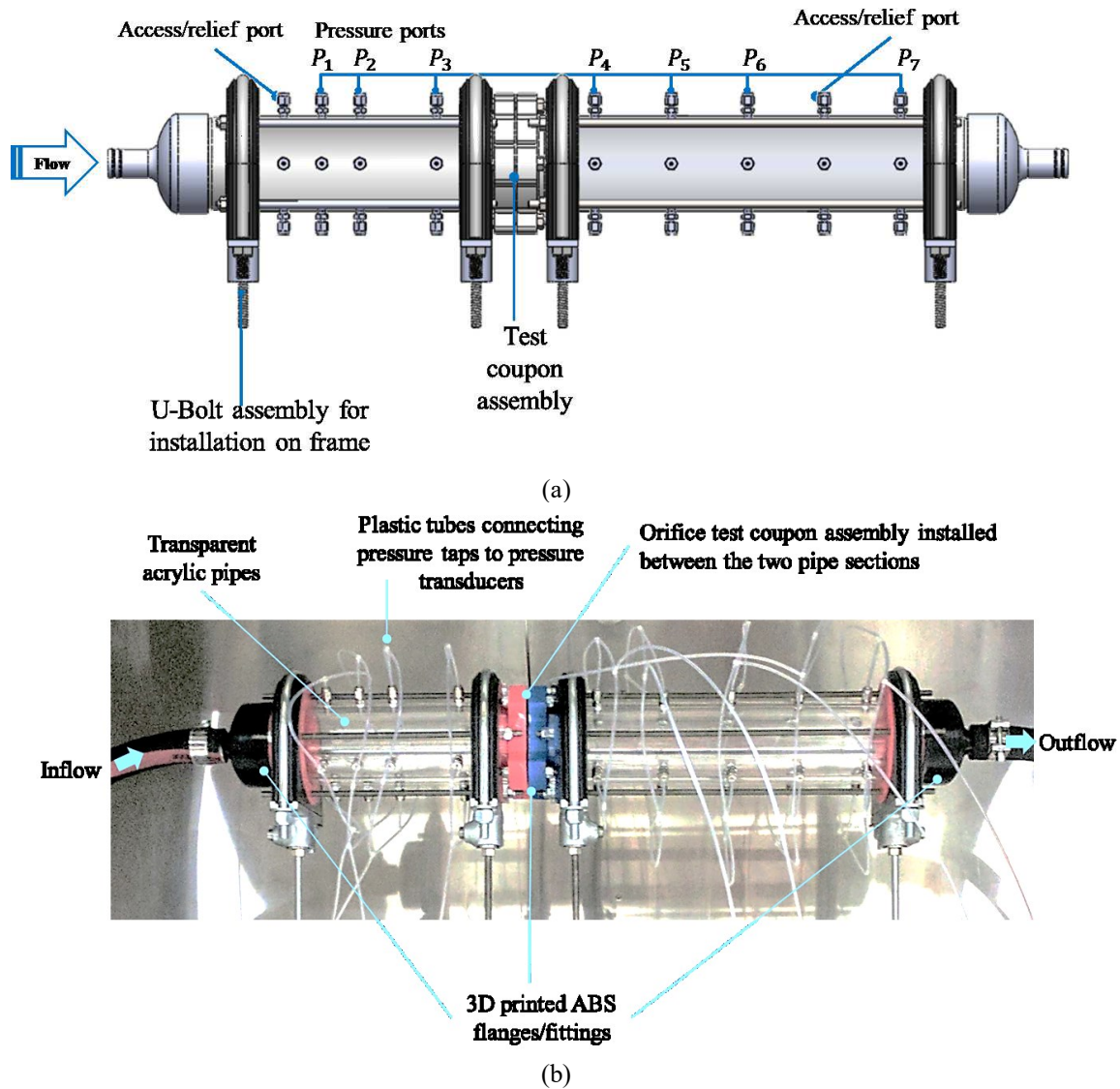


Figure 7 – (a) a solid model of the flow channel; and (b) annotated photograph of the test section prepared for an experiment

The pipe was designed to measure pressure at multiple wall locations so that the flow was not disturbed by other techniques such as probes or pitot tubes [16], [134]. The holes used as pressure taps had a diameter of 6 mm. The pressure measurement taps were equally spaced along axial direction at a distance equal to D_{pipe} . At each axial location, four taps that are symmetrically placed along the pipe circumference are also found. The pressure taps at every radial location were connected to each other using 3.18 mm plastic tubing (PFA-T2-030-100, Swagelok Company) and the cumulative flow from the four taps was connected to a single pressure transducer (DP15,

Validyne Engineering) using commercially available stainless steel tube fittings (SS-200-1-1, Swagelok Company) for the connections.

It should be noted that one set of the pressure taps in the upstream side were placed at a distance of $2.5 D_{pipe}$ from the orifice. It was made to match the protocols for orifice plate flow meters [70] that dictate pressure tap locations of $2.5 D_{pipe}$ and $5 D_{pipe}$, for upstream and downstream pressure measurements, respectively, labeled as P_1 and P_7 on Figure 7(a). The pressure measurement scheme described enables determination of the pressure gradient between different selected regions of the flow domain.

There were seven pressure measurement locations along the test section. The upstream and downstream pressures measured at the locations labeled as P_1 and P_7 in Figure 6 were used in the calculation of the static pressure drop across the orifice as:

$$\Delta P = P_1 - P_7 \quad (14)$$

The experiments conducted were all in the creeping flow regime ($0.01 \leq Re \leq 1$) and the volumetric flow rate provided by the pump was manipulated so that Re was kept constant for flows through the orifices with different aspect ratios. Each run began by heating the reservoir until the temperature in the reservoir reaches 45°C ($\mu = 1.8 \text{ Pa}\cdot\text{s}$; and $\rho = 884 \text{ kg/m}^3$). The heated oil was then pumped to fill the main flow pipe in the upper section.

3.1.1 Test coupons

The approach used to make the test coupons is depicted in Figure 8. Plastic shim materials were placed between stainless bars to make the rectangular orifices for the experiments as shown in Figure 8(a). A commercial knife cutting machine (Cricut Explore Air™ 2, Provo Craft & Novelty, Inc.) was used to make the plastic shim materials in the required shapes. Manufacturing of orifices

having widths as low as 0.01 mm could be achieved by using this approach. As the shim stock materials had controlled thicknesses, it ensured uniform width among all orifices.

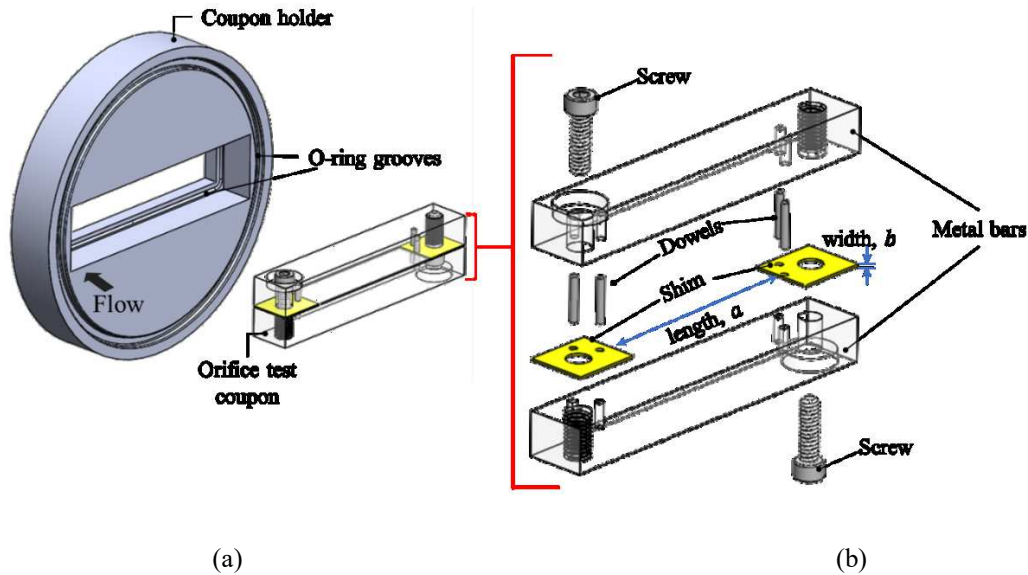


Figure 8 – Exploded views of the solid models showing the components in (a) method used to install the test coupons in the pipe, and (b) the shim-based approach devised to manufacturing test coupons of varying AR

The different dimensions of the rectangular orifices used for the experiments are listed in Table 1. A constant area of 9 mm^2 is maintained for all orifice aspect ratios while the aspect ratio, AR , is varied in the range from $1 \leq AR \leq 250$ which can be seen from the first column of the table. The square orifice with $AR = 1$ is a $3 \times 3 \text{ mm}^2$ whereas for higher AR , the length, a , increases and its width, b , decreases as shown in the second and third columns of Table 1, respectively. The hydraulic diameter, D_h , given under the fourth column, decreases as AR increases for constant cross sectional area. The column in Table 1 which corresponds to the cross sectional area, shows that there were some deviations from the intended value of 9 mm^2 due to the combination of the dimensions a and b selected. The last column of the table provides the number and sizes of shim stock materials used to make the orifices. It can be seen that the majority of the orifices required multiple shims to be stacked to obtain the specific width.

Table 1 – Dimensions of rectangular orifices used in the pressure measurement experiments

<i>AR</i> (-)	Length, <i>a</i> (mm)	Width, <i>b</i> (mm)	Hydraulic diameter, D_h , (mm)	Area (mm ²)	Shim(s), <i>b</i> = total thickness (mm)
1	3.00	3.00	3.00	9.00	(0.75)(×4)
37	18.25	0.5	0.97	9.25	(0.50)
50	21.21	0.42	0.83	8.99	(0.40) + (0.02)
72	25.46	0.35	0.69	8.93	(0.31) + (0.04)
108	31.18	0.29	0.57	9.02	(0.10) + (0.19)
143	35.87	0.25	0.50	8.98	(0.25)
179	40.14	0.22	0.44	8.82	(0.19)+(0.025)
214	43.89	0.20	0.40	8.78	(0.19)+(0.01)
250	47.37	0.19	0.38	9.03	(0.19)

3.1.2 Processing and averaging of data

The experimentation began by heating the oil to ~ 45 °C to reduce its viscosity for easier pumping. The main flow pipe is then filled with the oil which normally took around 45 minutes. The two access ports on the pipe were used as vents to release air during the filling. Data logging began when a steady stream of the liquid was observed through these vents indicating the absence of any trapped gas bubbles. The flow loop was then run for 6-10 minutes at each flow rate while corresponding data is recorded at a rate of 1 Hz. This allowed to investigate a range of flow rates in one setup of the experiment for each *AR*. The experiments for each *AR* were repeated for the same range of flow rates. After the end of each experiments the system was fully drained and partially disassembled when coupon changing is required. With three repeats, the experiment for one particular *AR* was setup and data collected over an average of a three-day period.

As *AR* increased, maintaining the same ranges of *Re* had more difficulty during the experiments due to decreasing hydraulic diameters. This led to significant flow blockage in the *x-y* plane increasing the respective minimum flow rate that could be achieved. Therefore, more emphasis was given to cover as wide of a range of *Re* as possible within $0.01 \leq Re \leq 0.1$, than to get the exact same *Re* distribution for all aspect ratios. Three nominal Reynolds numbers, namely, $Re_{nom} = 0.05, 0.075, \text{ and } 0.1$ were defined for the averaging. The main reason behind selecting

these specific numbers was in reference to actual SAGD conditions which have typically values of $Re = 0.06$ across a single slot [16]. Upon calculation of the Reynolds number corresponding to each data point, the data lying between the nominal values of Reynolds number were averaged. For example, the average values of the parameters at $Re_{nom} = 0.05$, are obtained by averaging the data for Reynolds numbers less or equal to 0.05. Similarly, the data for $Re_{nom} = 0.075$ are determined by taking the average for $0.05 \leq Re \leq 0.075$.

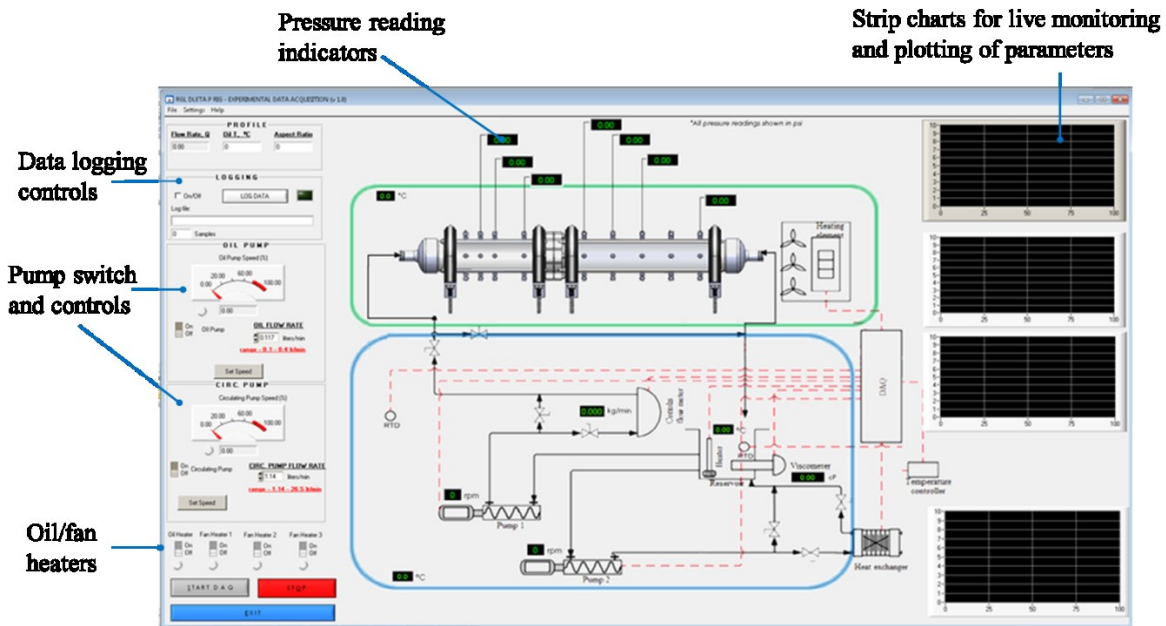
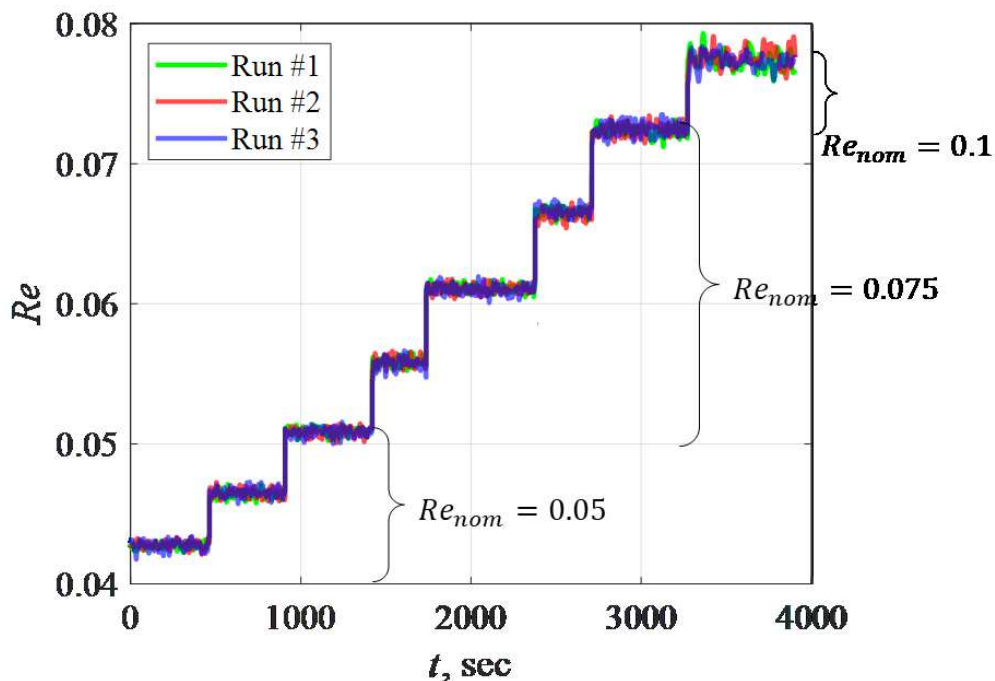


Figure 9 – A screen shot of the graphical user interface of the data acquisition and monitoring software built for the experiment

An in-house software with graphical user interface was written in a commercial integrated development environment (LabWindows™/CVI, National Instruments) for data logging and monitoring parameters. The graphical user interface shown in Figure 9 shows that the software enabled full control of the pumps, the oil heater, and the fan heaters. Indicators and strip charts were also included for live display of measurement readings and plots of specified parameters. The user also has the control of turning data logging on or off as well as specifying the path for the log file. The detailed description of the developed software is given in section (i) of Appendix B.

The averaging method is described in Figure 10 using the data for $AR = 108$ as an example. The plots in Figure 10(a) and (b) respectively show the raw data for Re and ΔP for one of the three runs conducted while the remaining two runs are represented by the average lines indicating the mean values in the respective ranges. The stepwise change seen in the plots reflect the change in pump speed used to control general flow rate. The value of Re was determined by using the mass flow rate from the Coriolis flow meter, and the orifice dimensions to calculate the velocity and the hydraulic diameter.

It can be seen that, for $AR = 108$, eight different Re values were covered. In each run, the step change in the values of Re are used to identify the range covered. As indicated in Figure 10, mean values of ΔP and Re are calculated by averaging the values for the three runs. The data for the different runs also shows the repeatability of the experiment with the maximum difference of $\leq 5\%$ between runs for both Re and ΔP . The raw data for the rest of the aspect ratios are given in Appendix A.



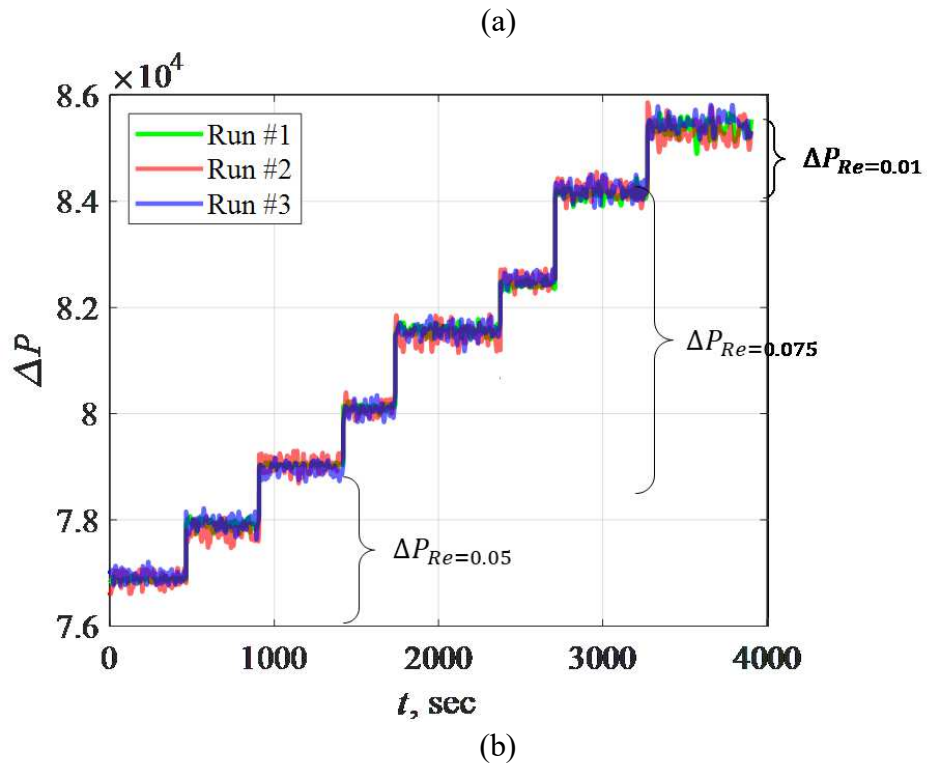


Figure 10 – An example plot of the raw data for $AR = 108$ showing the averaging methods used for (a) Re and (b) ΔP

3.1.3 Uncertainty calculations

Both random (precision) and bias (systematic) errors were considered to estimate the levels of uncertainties in the reported data [135]–[137]. The uncertainty ranges which are calculated for a 95% confidence represent the combined effect of these error sources. For random uncertainties, the standard deviation in the data for a parameter was used. Specified accuracies the instruments were referred to calculate the bias uncertainties. The reference data for the bias errors in the instruments came from the manufacturer specification and/or calibration data.

If an average of N measurements are used to calculate the parameter, \bar{X} , the combination of the standard random uncertainty, $s_{\bar{X}}$, and the bias uncertainty, $b_{\bar{X}}$, is calculated as:

$$u_{\bar{X}} = \sqrt{(s_{\bar{X}})^2 + (b_{\bar{X}})^2} \quad (15)$$

where $u_{\bar{X}}$ is called the combined standard uncertainty of a measurement. The individual levels of the random and bias uncertainties depend of the number of respective error sources identified. For a total of K sources, the elemental contributions from random and bias errors to their respective levels of uncertainties are calculated such that:

$$s_{\bar{X}} = \frac{1}{\sqrt{N}} \left[\sum_{k=1}^K (s_{\bar{X}_k})^2 \right]^{1/2} \quad (16)$$
$$b_{\bar{X}} = \left[\sum_{k=1}^K (b_{\bar{X}_k})^2 \right]^{1/2}$$

where $s_{\bar{X}_k}$ is the elemental random standard uncertainty of the k^{th} source; and $b_{\bar{X}_k}$ is the bias uncertainty due to the k^{th} source. To report the final result in the form of the expanded uncertainty level $\bar{X} \pm U_{\bar{X}}$, the result from Eq. (15) is multiplied by the Student's t value [135] appropriate to the desired confidence level which gives $t = 1.96$ for a 95% confidence [135], [137]. In

engineering analysis, this t -value is typically rounded up to calculate the combined level of uncertainty such that, $U_{95} = 2u_{\bar{x}}$, [137, pp. 19–20].

The propagation of uncertainty method is used to determine the uncertainty level of an experimental result, R , which is not directly measured but instead obtained from manipulating one or more of other independent parameters, $\bar{X}_1, \bar{X}_2, \dots, \bar{X}_I$, [136], [137]. In this technique, the level of uncertainty in R is determined by using the Taylor series approximation based on the functional relationship between the dependent and independent parameters, i.e. $R = f(\bar{X}_1, \bar{X}_2, \dots, \bar{X}_I)$ for a total of I parameters involved. The change of R that resulted due to a change in a parameter, \bar{X}_i , is determined by estimating the respective sensitivity coefficient, θ_i [136], [137] which is given in the form of a differential equation. For a known mathematical relationship between R and its parameters, the absolute sensitivity coefficient is given by the partial differential equation:

$$\theta_i = \frac{\partial R}{\partial \bar{X}_i} \quad (17)$$

If the relative sensitivity coefficient is desired, the result can be multiplied by the ratio \bar{X}_i/R which yields non-dimensional values of the coefficient [137].

Analogous to Eq. (15), the combined standard uncertainty of a result, u_R , is estimated as:

$$u_R = \sqrt{(s_R)^2 + (b_R)^2} \quad (18)$$

where, according to the propagation equation, the random and bias uncertainties of the result become:

$$s_R = \left[\sum_{i=1}^I (\theta_i s_{\bar{X}_i})^2 \right]^{1/2}$$

$$b_R = \left[\sum_{i=1}^I (\theta_i b_{\bar{X}_i})^2 \right]^{1/2} \quad (19)$$

where s_R is random uncertainty, and b_R is the bias uncertainty in the result R . The final expanded uncertainty can be given as $\bar{R} \pm 2u_R$, where, here again, the t -value is rounded to 2 for 95% confidence limit.

For the experiments in the study, the ultimate goal of the error analysis was to determine the level of uncertainty in the reported values of the loss coefficient K . Values of K were calculated using the ratio of the static pressure drop to the kinetic energy written in terms of the mass flow rate instead of the velocity. The propagation of uncertainty method was used which also required the uncertainties in ΔP to be determined beforehand. Data pertaining to the uncertainty calculations for an example set of data for $AR = 108$ at $Re = 0.05$ is provided in Table 2 and Table 3 below. The corresponding raw data can be seen in Figure 10 for the duration $0 \leq t \leq 1871$.

Table 2 – Data used to estimate the uncertainties of measured parameters for the case of $AR = 108$, and $Re = 0.05$

Measured Parameter	Units	N_i	\bar{X}	$b_{\bar{X}_i}$	$s_{\bar{X}_i}$	$u_{\bar{X}}$	$U_{\bar{X},95}$
Upstream pressure, P_1	Pa	1872	7.89×10^4	1.7	0.007	1.7	3.4
Downstream pressure, P_7	Pa	1872	721.81	29.6	0.1	29.8	59.6
Mass flow rate, \dot{m}	$\frac{\text{kg}}{\text{sec}}$	1872	0.08	1.25	1.12	1.75	3.37
Orifice length, a	m	5	31.18	-	0.003	0.003	0.006

Table 2 shows the data for independent parameters whose measurements are used to calculate ΔP and the loss coefficient, K . The main sources identified can be seen in the first column including the orifice length, a which is required to calculate the orifice area in the estimation of the uncertainty in K . The error in the orifice width, b , is assumed to be negligible considering the controlled thickness of the shim materials used. The random standard uncertainty, $s_{\bar{X}_i}$, is

determined from the standard deviation of the length for 5 samples of the shim material cut in dimensions corresponding to the given AR . Larger number of data is used to estimate the uncertainties due to the other sources shown.

The estimated uncertainties in ΔP and K for the same data set are summarized in Table 3. The values were calculated following the propagation equations by using respective sensitivity coefficients as defined in Eq. (17)–(19). A 95% confidence limit is maintained in all of the final uncertainty ranges reported.

Table 3 –Uncertainty data for calculated results for $AR = 108$, and $Re = 0.05$

Result	units	R	$b_R, \%$	$s_R, \%$	$u_R, \%$	$U_{R,95}, \%$
Pressure drop, ΔP	Pa	7.82×10^4	1.7	0.003	1.7	3.5
Loss coefficient, K	-	5.82×10^4	2.3	0.005	2.3	4.6

3.2. Velocimetry experiments

Non-invasive measurements of the flow velocity are often desired to investigate fluid dynamics problems that involve flow through internal cavities and/or complex channel geometries. Optical diagnoses techniques such as particle image velocimetry (PIV), and particle tracking velocimetry (PTV) are thus widely used among researches in academics and industry [138]. These techniques not only allow measurements without interfering the flow field but can also yield 2D and 3D vector fields of the flow as opposed to invasive techniques such as hot wire anemometry that measure the pointwise velocity.

In PIV and PTV, captured images of the flow field are processed using cross-correlation algorithms to obtain the vector field. The sensors in the imaging devices capture the light that is scattered off of solid particles that are used to seed the flow. The seeding particles, typically glass spheres, have comparable density with the fluid so that they faithfully follow the flow to represent its motion.

The flow field is illuminated by using a light source such as a laser or light emitting diodes [138], [139].

The setup used to conduct the PIV experiments in this study is shown in Figure 11. The components include a flow channel assembly; a syringe pump (PHD 2000, Harvard Apparatus); a camera (SP-5000M-PMCL-CX; JAI Inc.) coupled with 50 mm lens (AF NIKKOR 50 mm 1:1.4D; Nikon); a light emitting diode (LED) light source (BX0404-520 nm; Advanced Illumination); and a function generator for controlling the camera frame rate. The syringe pump was used to drive the flow of glycerol ($\mu = 1.4138$ Pa.s, and $\rho = 1260$ kg/m³ at 20°C) which was seeded with 40 μ m glass sphere particles having a density of 1050 kg/cm³(Dynoseeds ® TS 40, Microbeads). The camera was run at 45 frames per second to capture images of the center plane of the flow field. Setting the required frame rate for the camera was achieved by the function generator. The flow field was back-illuminated by the LED panel located behind the flow channel. The optical access to the flow cell containing the orifice geometry is provided by using transparent material poly-methyl methacrylate (PMMA) for the channel walls.

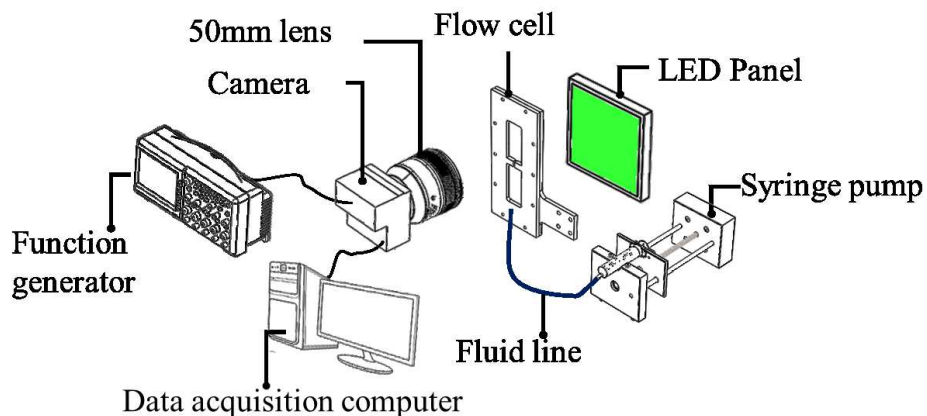


Figure 11 – A schematic representation of the experimental setup;

3.2.1 Flow channels

The flow channel assembly, shown in Figure 12, consists of three laser-cut parts made from 6.35 mm thick acrylic sheets. The two outer parts were windows that provided optical access for imaging whereas the middle part was the main flow cell containing the geometry being experimented. The wall distance, D , and the orifice width, b , could be varied to make orifices of different geometries. The field of view of the experiments was also chosen to cover more of the region upstream the orifice than downstream because of the emphasis on investigating flow convergence.

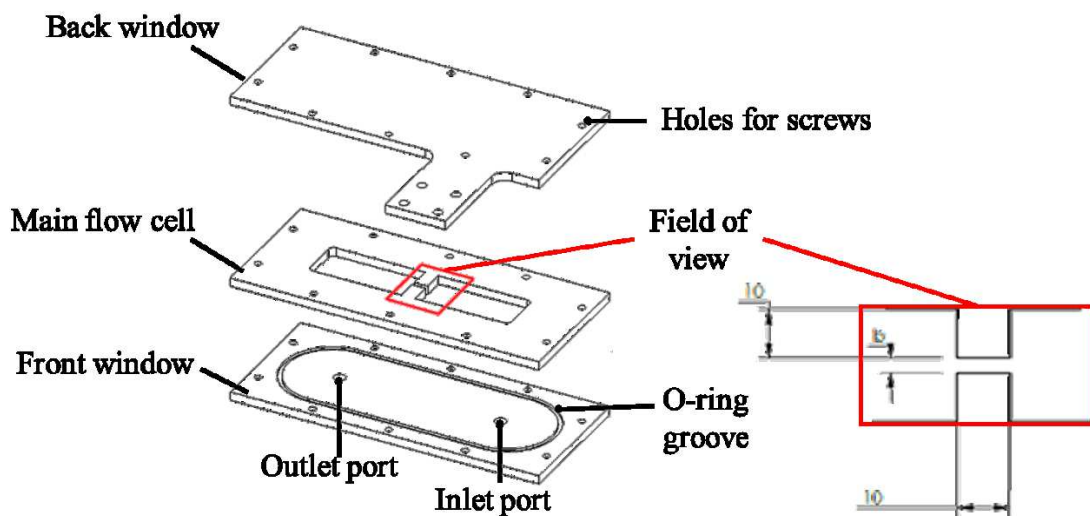


Figure 12 – The flow channel assembly consisting of laser-cut parts

The effect of orifice geometry is studied by changing the aspect ratio. The number of orifice aspect ratios matching those covered in the pressure measurement experiments had to be minimized. Conducting the velocimetry experiments for channels having the same dimensions would have otherwise been challenging due to the need to image excessively large or insufficiently small fields of view especially for higher AR s with $b \leq 1$ mm

The orifice AR is varied by changing the width, b , while keeping the wall distance, D constant. The list of orifice dimensions used in the experiments are given in Table 4. It can be seen that the

hydraulic diameters and the aspect ratios lied in the ranges of $1.5 \leq D_h \leq 5.6$ mm and $1 \leq AR \leq 3$, respectively.

Table 4 – Dimensions of rectangular orifices used PIV experiments

Aspect ratio AR , (-)	Width, b (mm)	Length, a (mm)	Wall distance, D (mm)	Hydraulic diameter, D_h , (mm)	Area (mm^2)	Area ratio, α (%)
1.27	5.00	6.35	10	5.6	31.75	20
2.12	3.00	6.35	10	4.1	19	13
3	1.00	3.00	10	1.5	3	5

Flow cells for the $AR = 1$ and $AR = 2$ orifices were manufactured by laser-cutting transparent acrylic sheets whereas for $AR = 3$, additive manufacturing using stereolithographic 3D printing (Form2, FormLabs) was used. When the x - y plane is parallel and coincident with the build plate of the 3D printer, the dimension a in Figure 18(b) translates to the thickness in the z -direction. This puts a restriction on the length a of the orifices manufactured especially for dimensions less than 1 mm. The minimum length that could be achieved for the prints with the acceptable qualities is 3 mm which is used as the length for the $AR = 3$ orifice. It is seen from Table 4 that the $AR = 1$ and $AR = 2$ have their length at $a = 6.35$ mm.

Comparing the flow configurations used for the pressure measurement and PIV experiments shows that the planes of investigation are different. The domain for the flow through a pipe-installed rectangular orifice can be observed from two planes of investigation corresponding to the two mid planes sectioning the pipe. As shown in [48], analysis in these planes also allow the application of the Cartesian coordinate to study the flow.

The flow scenario during pressure measurement experiments involve flow contraction in both planes, whereas the flow configuration in the PIV scenario only has contraction in one of the planes. It follows that the parameter AR has a dominating effect on flow convergence during

pressure measurement experiments while the orifice width b directs flow convergence in the velocimetry experiments. 2D velocity measurement on either of the plane will produce similar results pertaining to flow convergence and velocity transition. The behaviour of streamlines studied on these planes will also produce similar observation. Conducting velocimetry experiments with configurations matching those of the pressure measurement would require performing simultaneous measurement of the velocity on both planes of investigation.

3.2.2 Image processing

Software built in-house using a commercial development environment (CVI LabWindows, National Instruments Inc.) was used for image acquisition. A different commercially available software (DaVis 10, LaVision GmbH) was used to process the raw images to ultimately calculate the velocity field. The cross-correlation to produce the vector field, and some common pre- and post-processing are the three stages involved in the image processing described in the following section.

3.2.2.1 Pre-processing

Pre-processing of raw images is used to identify limitations in the data and apply the appropriate transformation to avoid any challenges in the vector calculation stage. Techniques commonly applied in this stage include: inverting, masking and rotation in the case of misalignments [138]. As the name implies, inverting operations transform the images by applying a different intensity function to change the contrast so that the particles are distinctly trackable. Unnecessary parts of images that are to be excluded from the calculation region are defined in the masking stage of the pre-processing. These regions are usually captured images of solid parts in the flow channel, or other moving boundaries which are typical in studies of multiphase flows [140]. Both operations

are part of the pre-processing stage done for the images from the experiments conducted in this study.

The before and after examples of a pre-processed image are shown in Figure 13. The annotated image of the raw data can be seen in Figure 13(a). The dimensions of the flow cell are indicated along with the directions of flow and the gravity vector. The image contrast enables the detection of the tracer particles which for all experiments were hollow glass spheres that are $40\ \mu\text{m}$ ($2 - 4$ pixels) in size. The camera has a resolution of (2560×2048) pixel² with a pixel size of $5\ \mu\text{m} \times 5\ \mu\text{m}$.

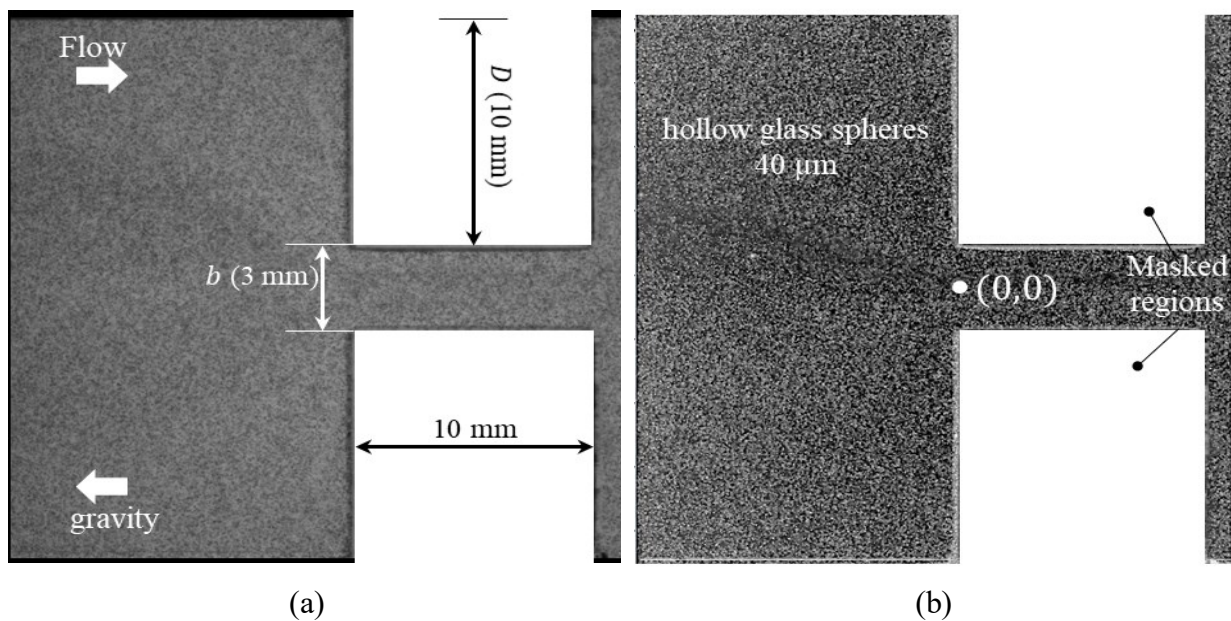


Figure 13 – Sample images of the center plane of the flow field showing examples of (a) the raw image; and (b) the preprocessed inverted image for the sample channel

The significant improvement as the result of the pre-processing can be seen in Figure 13(b). The inversion of images in the pre-processing stage used in this subtracted the maximum intensity count and applied normalized particle intensity. Since shadowgraph imaging is used in the experiments, pre-processing was essential to make sure the particle images are distinctly detected

in the vector calculation. The ultimate goal of these experiments was to plot the streamlines in the flow which necessitates having the proper contrast.

The images shown in Figure 13 also define the regions masked out to be omitted from the vector calculation. The rectangular geometries of the walls were defined on both sides of the channel based on the dimensions of the channel. To verify if the appropriate masking was defined, the processed vector field can be examined to see if it shows the no-slip boundary condition of zero velocity at the solid wall. If a velocity significantly greater than zero is observed at the solid boundary, it indicates that geometric mask covers part of the flow field far enough from the wall. It is also seen that the origin of the coordinate system, O , was placed at the intersection of entrance plane of the channel and the centerline.

3.2.2.2 Cross-Correlation of images

During the processing stage, images of the flow field are divided into small regions known as interrogation windows. The size of these windows is chosen based on the flow properties and the size of the seeding particles which is often suggested to be around 2 pixels [138]. Common practices recommend that one interrogation window fits between 5 – 10 particles.

The cross-correlation technique is applied to determine the displacement vector corresponding to the movement of particles from one interrogation window to another between frames [138]. The displacement and the time interval between frames are then used to calculate the velocity vector. The velocity field is obtained when the vectors corresponding to each interrogation window are determined across the entire series of images.

Smaller window sizes are used when increased resolution is sought from the final result. Reducing the size of the windows, however, risks having a smaller number of particles per window. The common remedy for this is to use an overlap between adjacent windows in the gridded flow field,

and/or apply the cross-correlation more than once using different windows sizes for each pass [138].

The processing scheme applied in this research were specified based on the channel dimensions [139]. The window sizes used to process images were 96×96 , 24×24 , and 12×12 (pixel)² for the channels with $AR = 1, 2$, and 3 respectively. The number of acquired images for all experiments was 500, which were all recorded at 45 frames-per-second. The processing of the collected images was conducted using the sum of correlations technique of vector calculation [141].

The velocity field corresponding to the sample data is shown in Figure 14. The width of the channel, b , was used to normalize the length scales in both directions while the global maximum velocity, U_{max} , normalized the velocity, U . Background noise in the data were removed in the post processing stage by applying smoothing kernels of size 4×4 . The kernel sizes used were different for different sizes of the orifice ranging from 2×2 to 6×6 for the smallest and largest orifice widths, respectively. The primary goal was to ensure a smooth velocity field that clearly shows the flow convergence behaviour in the upstream region.

From the colormap in Figure 14 (a), the expected flow phenomena such as the convergence [139] and the growth of shear layer as a function of the axial distance can be observed. The zero velocities at the solid-fluid interfaces verify the physics and that the masks are applied properly. The change in the velocity in the transverse direction can be traced to notice the parabolic shape of the velocity profile.

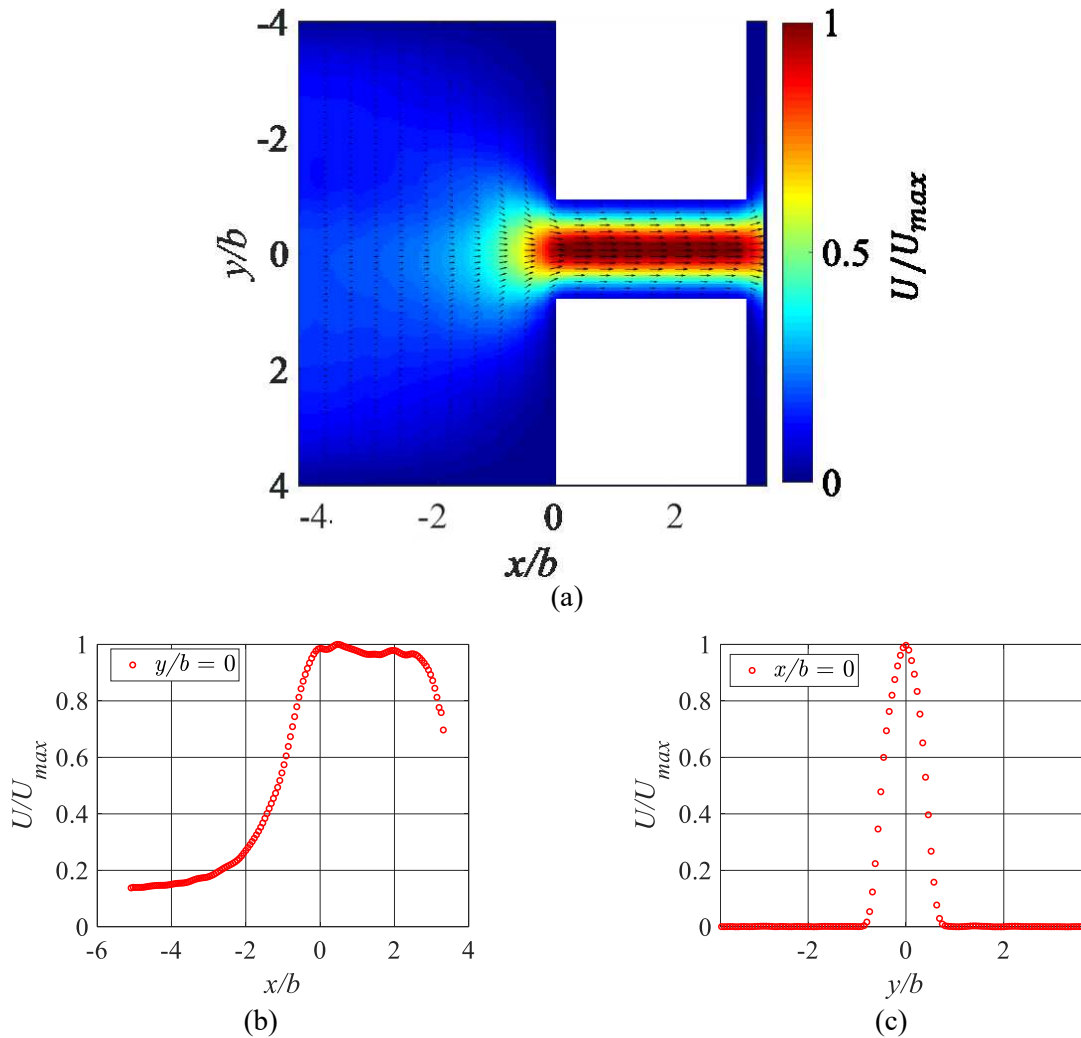


Figure 14 – Sample results for the orifice $AR = 2$ showing (a) the velocity vector map of the flow field with every 4th and 2nd vectors are shown in the x and y directions, respectively; (b) the centerline velocity and (c) the velocity profile at the entrance of the orifice

The velocity vectors in the far upstream region ($-2.25 \leq x/b$) are parallel which implies that there is no streamline curvature. The flow acceleration is seen for $x/b \geq -2.25$ with the velocity increasing to reach its maximum at $x/b = 0.25$ making evident the effect of entrance length by reaching the maximum velocity past the inlet plane at $x/b = 0$. Inside the channel, the flow continues with the expected parabolic velocity profile [47]. The Newtonian behaviour of the flow is better seen from Figure 14 (b) which shows the normalized centerline velocity plotted against

the axial distance [47]. From the figure it can be seen that the flow reaches its maximum velocity at entrance plane at $x/b = 0$.

3.2.2.3 Post-processing

In post processing of PIV data, the obtained result from the vector calculation stage are taken through some steps to correct outliers. Outlier detection methods are applied to the data to identify erroneous vectors that are to be removed/replaced. Detection algorithms mostly apply the global histogram operator, the dynamic mean value operator, or normalized median tests to validate the detected flaws in the data [138]. The replacement of data is commonly achieved by applying the linear, bilinear, median, or spline type of interpolation techniques. The next step in the post-processing is typically smoothening of the data field to remove noise by applying a kernel of size 2×2 , or larger [138]. The application of any differential operator on the velocity field data generally follows the smoothening stage [142].

The primary interest of the data processing stage that followed lied in calculating the streamlines to investigate their curvature behaviour. Obtaining a smooth velocity field data was therefore essential to assure the velocity transition behavior in the convergence zone is represented with adequate accuracy. The creeping Reynolds number and steady state flow conditions covered by the experiments were advantageous in the processing since more focus is on obtaining spatial information of the flow field.

3.2.2.4 Uncertainty considerations for PIV measurements

A number of sources contribute to errors in the results gathered from PIV experiments. The main one are the precision errors inherent to the instruments whereas random errors also play significant role in determining the uncertainty levels of results. The performance of the software package used for the processing also has the potential to add to the random errors in the velocity [138]. The

cross-correlation peaks are also influenced by the errors due to the size of the interrogation windows and other features of the processing scheme applied [143]. The effect of uncertainty on the cross-correlation is indicated by an asymmetry in the shape of the peak which is expected to be perfectly symmetric under ideal conditions [144].

The uncertainty estimate for the data in this study is determined using a commercial software (DaVis 10, LaVision GmbH). The calculation determined the uncertainty in the average velocity \bar{U} , by taking the ratio of the standard deviation to the square root of the number of vectors [144]. The maximum uncertainty was $< 2\%$ in the data for all aspect ratios.

3.3. Experiments with porous media

3.3.1 Pressure measurement

The upstream section of the main pipe in the flow facility was packed with spherical glass particles with an average particle size of 1.2 mm. The reason behind the selection of these particles is using particles of known and constant property to simplify the case for the analytical investigation. Only a portion of the upstream section was packed with the particles covering the region from the location of the first pressure transducer to face of the orifice i.e. $-2.5 D_{pipe} \leq x \leq 0$.

Photographs of the upstream section taken while packing with porous media and after it has assembled for experiment are shown in Figure 15(a) and (b), respectively. The pipe section was turned upside down with the test coupon assembly that has been installed on the lower side. The porous media particles were then poured while manually shaking the pipe section to obtain a packed porous bed with the average porosity of $\varepsilon \leq 40\%$. The pore volume of the packed bed is determined using the direct method. In this method, the known volume of the oil used to fill the pack ($3.5 \times 10^{-4} \text{ m}^3$) is subtracted from total volume of the cylinder representing the upstream section ($8.7 \times 10^{-4} \text{ m}^3$). The relatively loosely packed bed was intended to eliminate concerns

regarding the accumulation of back pressure due to flow blockage. There was also no possibility for fluidization since the flow rate was at creeping Reynolds numbers.

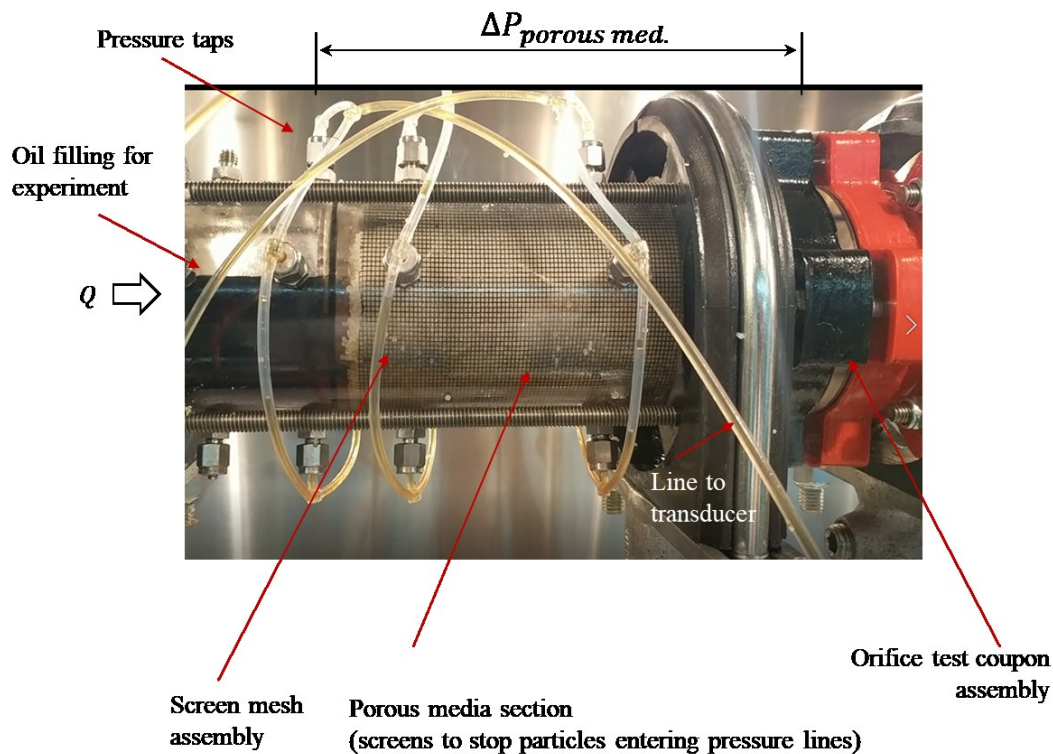


Figure 15 – Annotated photographs showing the upstream section with porous media filling for experiment

The upstream part of the installed flow pipe containing the porous region can be seen in Figure 15(b). Additional components were added to form the structure that supports the porous bed and keep it stationary. The design of the structure also allowed to line the internal wall of the pipe with a flexible mesh screen to prevent particles from entering the pressure taps. The primary part in the packing assembly is also an assembly of 3D printed perforated screen with the wire mesh sandwiched in between to avoid flow of particles back to the circulating pump while draining and filling stages.

The benefit of having multiple pressure measurement locations along the porous bed allowed the verification of the pressure drop measurements across a known length using theoretical equations such as Darcy's relation [33]. Three transducers could measure the pressure along the porous

media at the distances equal to $1 D_{pipe}$, $2 D_{pipe}$, and $2.5 D_{pipe}$. The final pressure drop across the coupled media is taken as the difference between the readings from the transducers at $2.5 D_{pipe}$ upstream and $5 D_{pipe}$ downstream similar to the open slot scenario as given in Eq. (14). The measured pressure drop across the length of the porous region between the transducers was used to verify the measurements by determining the permeability coefficient discussed in Section 2.4.

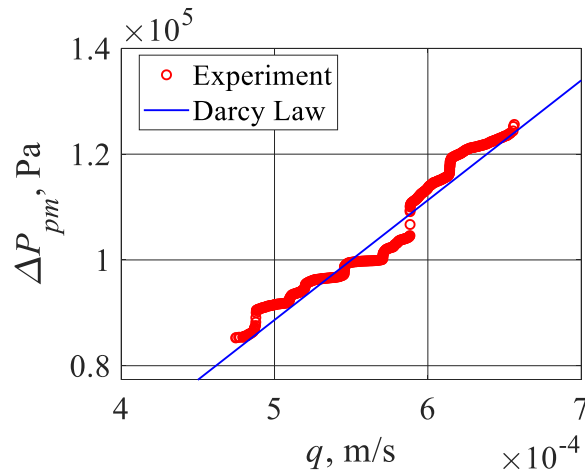


Figure 16 – Comparison of the pressure drop through the porous bed from experiment and theory for the case $AR = 37$ for a porous bed with particle size of 1.2 mm and porosity of 40%.

The pressure drops across the porous media obtained from the measurements are compared to Darcy’s law in Figure 16. The plot shown is for the flow through the orifice with $AR = 37$ at $Re = 0.075$. The plots display the measurement data fits the expected linear relationship between the Darcy flux, q , and the pressure drop due to porous media, ΔP_{pm} , for laminar flow through packed beds [33]. The coefficient of permeability was also used to check the match between the results. The results from experiments deviated from those calculated using the Darcy’s model by errors amounting to less than 5%.

The experiments included three aspect ratios, namely, $AR = 37$, $AR = 108$, and $AR = 214$. The lowest aspect ratio that could be included was, $AR = 37$. As it can be referred from Table 1 that the dimensions of the coupon for $AR = 1$ would have led to the particles from the porous bed

passing through the orifice due to the difference in their size. The selection of the remaining two orifice aspect ratios was justified by covering the same range of aspect ratio as the open slot experiments. Since the results from this part of the experimentation are compared with those from the open slot scenario, considering only three AR s for the coupled domain has been found sufficient.

3.3.2 *PIV experiments*

Investigation of the streamlines in the flow through the coupled domain was also conducted by measuring the velocity field using shadowgraph PIV. The same setup described in Section 3.2 was used to measure the velocity field. The working fluid and the seeding particles were also kept the same. The modified component out of the setup shown in Figure 11 is the flow channel. Views of the assembly are provided in Figure 17 [59].

An arrangement of cylindrical pillars was used to form the tortuous path representing the pore matrix. Images captured in 2D thus represent a section of the flow field with the circles signifying spherical particles sectioned across the mid-plane. The geometry is described in the annotated solid models given in Figure 17. The pillars in the pore matrix had a diameter of 1 mm with the spacing between each particle at 1.5 times the diameter. The channel tested had the width of, $b = 1$ mm representing an orifice of $AR = 3$. The shortest distance between the channel entrance and the pore matrix was also kept at 1 mm.

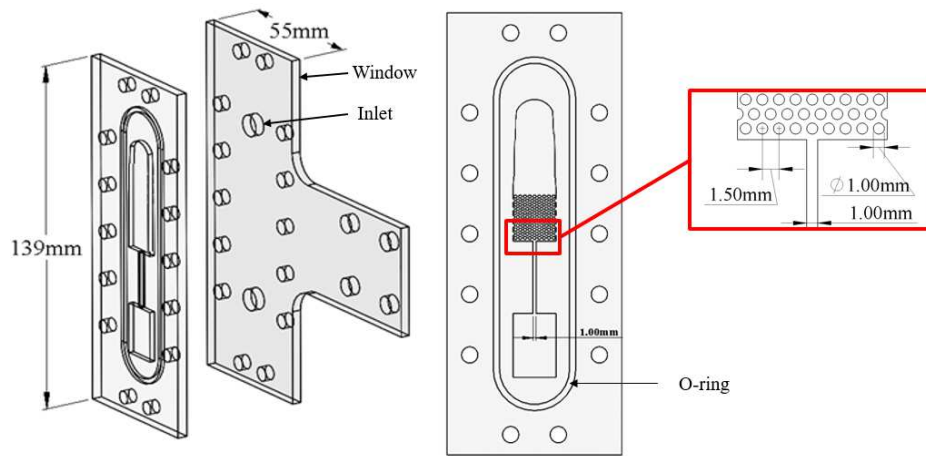


Figure 17 – Annotated views of the solid model of the channel for PIV experiments with porous media [59]

The flow cell was made by additive manufacturing technique using a commercial 3D printer whereas the transparent window was made from laser-cut acrylic. The sealing in the assembly was ensured by using a commercially available 2.38 mm o-ring. The parts were firmly held together using 10×M3 hex bolts. The torque applied to the screws was strong enough to avoid leakage between the window and the flow cell. The material used for the flow cell is a commercially available clear photopolymer resin (FLGPCL02, Formlabs, Inc), which is cured to form a translucent wall. The transparency of the printed part can be increased by gradually sanding the flat side of the wall to ensure enough light passes for the shadowgraph imaging. The depth of the cavity that represents the fluid domain is made as small as possible to allow considering a purely 2D flow [140].

A single orifice size ($b = 1 \text{ mm}$, $AR = 3$) is considered in the velocimetry experiments for the flow through the coupled domain. Since the objective of the experiments was to elaborate the effect of convergence in the presence of porous media, the primary flow characteristic studied was the tortuosity [119]. The change in the distance from the centerline of the flow field was sufficient to provide data for varying tortuosity which eliminated the need to obtain data for varying orifice size.

Chapter 4 Semi-empirical pressure loss model for viscous flow through high aspect ratio rectangular orifices¹

4.1. Introduction

In this chapter, a semi-empirical model for a non-dimensional pressure loss coefficient for viscous flow through rectangular orifices is developed. The aspect ratio of the orifices is varied in the range $1 \leq AR \leq 250$. The coefficient, K , is defined as the ratio of the static pressure loss to the kinetic energy gain. The analytical modeling uses a unique definition of a flow convergence parameter, ϕ , which is defined in the asymptotic velocity transition model. The flow measurement method employed to obtain data for the pressure drop across the rectangular orifices is explained in Section 3.1. The data is analysed to determine the relationship between AR and non-dimensional pressure loss coefficient, K [78], [145]. A wider range of AR is covered in this study as compared to studies in the literature that gave the same definition to the parameter.

The information presented in this chapter is organized in 4 sections. Section 4.2 discusses and presents the derivation in the development of the analytical model. Section 4.3 presents the results obtained from the experiments and discusses the analysis that followed the comparison of the loss coefficient data from the experiment to the model developed. Section 4.4 re-states the model with comments pertaining to the discussion of results. In Section 4.5, a highlights of modifying the

¹ Components of this chapter have been published as:

- Yusuf, Y, Sabbagh, R, and Nobes, D.S. (2019) “Semi-empirical pressure loss model for low Reynolds number flow through slots”, *Physics of fluids*, **31**(7), 073603;
- Yusuf, Y, Sabbagh, R, and Nobes, D.S. (2017) “Flow convergence model for flow through long aspect ratio rectangular orifices”, *Proceedings of the Okanagan Fluid Dynamics Meeting*, Kelowna, BC, Canada, August 21-24, 2017; and
- Yusuf, Y, Baldygin, A, Sabbagh, R, Leitch, M, Waghmare, P R., and Nobes, D.S. (2017) “Effect of aspect ratio on pressure loss and characteristics of low Reynolds number flow through narrow slots”, *Proceedings of the 2nd Thermal and Fluid Engineering Conference*, TFEC2017-18387, Las Vegas, USA, April 2-5, 2017;

modelling approach by using the skew-Normal distribution for the near-inlet velocity is given to demonstrate potential improvement of the model that can be achieved. The major conclusions drawn are finally summarized in Section 4.6 which also forwards suggestions for future work aiming to arrive at a more comprehensive model.

4.2. Modeling of the pressure loss coefficient, K

The modeling in this study aims to relate the convergence phenomenon in the upstream region to the orifice aspect ratio. The definition of the domain for the 1D modelling of the flow through a rectangular orifice is given in the schematic shown in Figure 18. Figure 18(a), shows a rectangular orifice of thickness, Th , installed in a pipe of diameter, D_{pipe} . For a volume flow rate, Q , the velocities \bar{u}_u and \bar{u}_o are defined as the mean upstream velocity in the pipe, and mean velocity through the orifice, respectively.

As the flow approaches the orifice it undergoes convergence in two planes as indicated in Figure 18(a). This region is characterized by flow acceleration and curvature of streamlines as the flow enters the orifice. The length of the convergence region, L_c , can be affected by the distance between the edges of the orifice and the pipe wall on both the planes. In the x - z plane the distance between the edge of the orifice and the pipe wall changes as the orifice length, a , changes. In the x - y plane given in Figure 18(b) the other wall distance D_y is determined by as the orifice width, b . Conceptually, the main variation between the convergence conditions for different aspect ratio orifices can be associated to the variation of these wall distances. The aspect ratio of the rectangular orifice is defined as, $AR = a/b$, where orifice length, a , and its width, b , are defined in Figure 18. For $AR = 1$, the flow will have equal extent of streamline curvature as its convergence properties are the same in both planes. The sketches of streamlines in Figure 18(a) indicate that for the flow through long aspect ratio orifices ($AR \gg 1$), increased contraction effects can be expected in the

x - y plane. For long aspect ratios, the convergence in the x - z plane is thus minimal since the edges of the orifice are closer to the pipe wall. As AR increases, the associated decrease in b can be expected to lead the effects related to the back pressure and flow convergence. However, effects from the increase in the length a is mainly related to interaction between the pipe wall and the orifice edge.

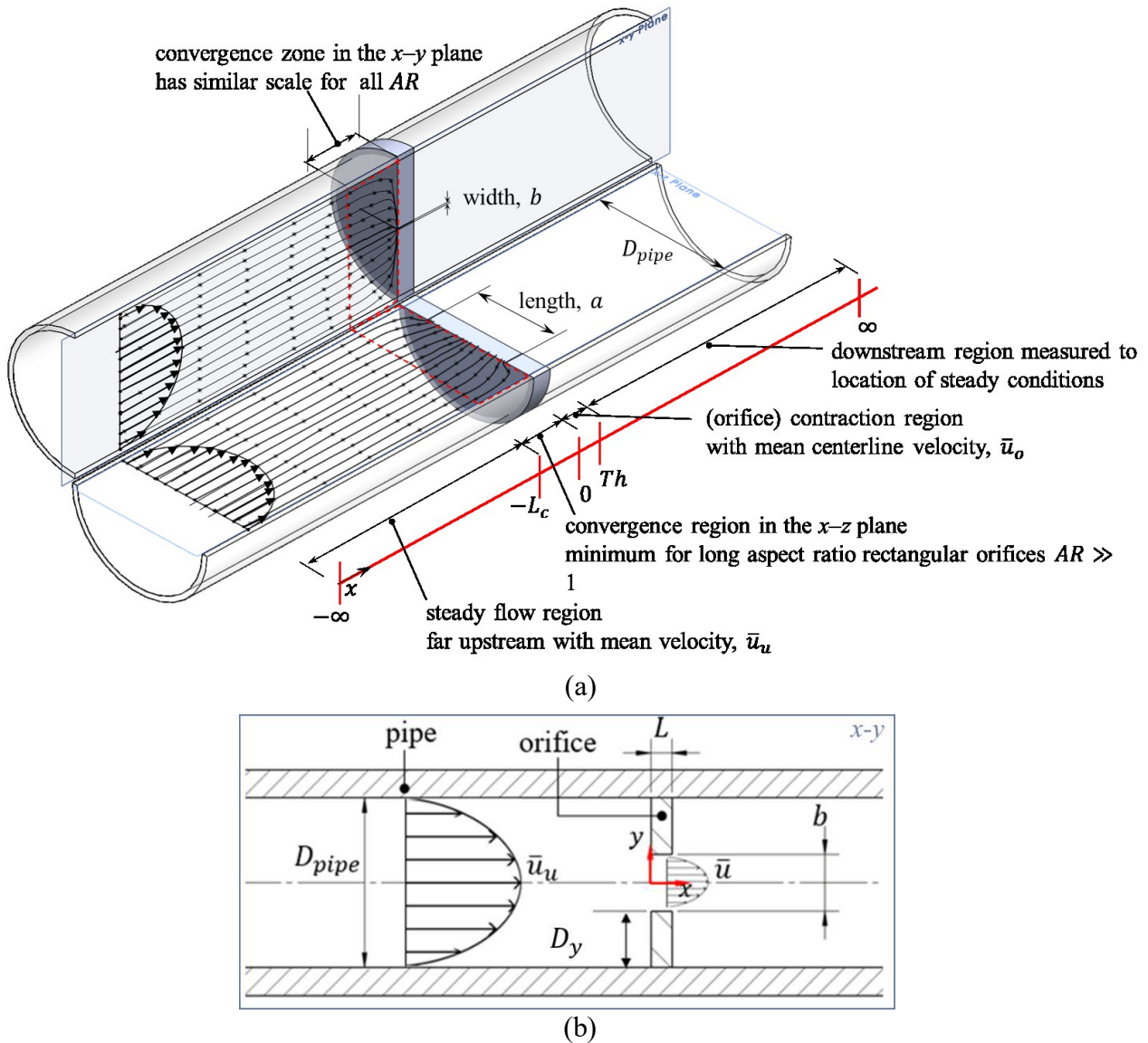


Figure 18 – Schematics for (a) definition of the flow domain showing the different regions in the x - y and x - z planes; (b) defining the flow configuration in the x - y plane with the width, b magnified 30 \times

The primary relevance of defining the two planes of investigation in Figure 18 is to ensure consistency in using Cartesian coordinates for the length scales in both the orifice and pipe regions. It is critical to note that the only valid condition to write the momentum balance equation in the x - y coordinates is when, in cylindrical coordinates, $\theta = 0$ or $-\pi$ which is equivalent to the planes defined.

On either of the planes of investigation defined, the general 1D form of the steady state Navier-Stokes equation in the x -direction after neglecting the effect of gravity can be written as:

$$\left(u \frac{du}{dx}\right) = -\frac{1}{\rho} \frac{dp}{dx} + \nu \left(\frac{d^2u}{dx^2}\right) \quad (20)$$

where, u is the velocity of the flow, p is the pressure and ν is the kinematic viscosity of the fluid.

The description of the flow field by using Eq. (20) shows the balance of the forces due to acceleration and those due to viscosity. The 1D assumption implies that radial and circumferential gradients are considered to be negligible. This assumption is more rational for flows in the creeping flow regime. However, at high Re , inertial effects from phenomena such as vena-contracta or radial variations are too significant to be ignored.

Assuming the direction of acceleration to be parallel to the streamlines [97] the integral form of Eq. (20) can be solved if the axial pressure distribution is known. It is also noted here that taking the differential form of Eq. (20) with respect to x results in an equation that describes the flow behavior along individual streamlines. The velocity increase from upstream conditions in the pipe, \bar{u}_u , to the mean velocity through the orifice, \bar{u}_o , is taken to occur along a distance in the convergence zone close enough to the inlet plane to neglect effects from shear forces due to effects from the pipe wall.

If the standard normal (Gaussian) distribution is assumed for the mean velocity, its gradient is expected to show an asymptotic behavior[146]. Therefore, the integral of the gradient function, in

this case taking the Gaussian integral, can be used to model the velocity distribution in the acceleration region such that:

$$\bar{u} = \bar{u}_u + \bar{u}_i \text{erf}(\epsilon) \quad (21)$$

where \bar{u}_i is the difference between the orifice velocity, \bar{u}_o , and upstream velocity, \bar{u}_u ; $\text{erf}(\cdot)$ is the error function operator; and ϵ is the non-dimensional axial distance between the two asymptotic conditions. For circular orifices, ϵ is defined as the ratio of the horizontal distance, x , to the diameter of the orifice [52]. From the dimensions defined in Figure 18, the smallest length-scale of the rectangular orifice, b , is selected for having the most profound effect on both flow convergence and pressure loss phenomena. Accordingly, the normalized axial distance is given as, $\epsilon = \phi x/b$ where the parameter ϕ is defined as the flow convergence factor.

The error function, $\text{erf}(\epsilon)$, represents the transition of velocity from \bar{u}_u to \bar{u}_o between the steady flow region far upstream locations, $\epsilon = -\infty$, and the inlet plane at $\epsilon = 0$. If the centerline velocity is assumed to follow a symmetric Gaussian distribution between these locations, the nature of $\text{erf}(\epsilon)$, will force the maximum velocity to be at $x = 0$ which will fail to account for an entrance length [83] into the rectangular orifice. On the other hand, considering the region $-\infty \leq x \leq \infty$ will result in major theoretical challenges [84] because the integral of the second derivative term vanishes and the viscous term disappears [52]. These difficulties can be avoided by using only the positive/negative portion of the error function. When there is an increase in velocity by multiple orders of magnitude, however, it will collapse the neglected region into a vanishingly small region which makes it difficult to extract information.

The negative part of the function is considered here because it represents the upstream convergence region [97]. Replacing ϵ in Eq. (21) with $\phi(-x)/b$ and differentiating with respect to the axial coordinate x gives:

$$\frac{d\bar{u}}{dx} = \frac{2\bar{u}_i \phi}{\sqrt{\pi} b} \exp\left(\frac{\phi x}{b}\right)^2 \quad (22)$$

where, ϕ , the convergence factor, represents effects from the upstream flow convergence that contribute to the pressure loss. This equation describes the axial velocity gradient in the near orifice region representing the asymptotic velocity increase both physically and mathematically through the error function.

In this work it is argued that, in view of the underlying concept relating the pressure gradient and the behavior of streamlines, the convergence zone can also be fundamentally characterized by the prevalence of change in the shape of the streamlines (curvature) as the flow accelerates into the orifice. The curvature of the flow streamline is a function of flow characteristics that are in general related to the inertial and viscous properties [139]. Its effects on the velocity distribution can be seen to ultimately change the transition from steady to localized conditions that respectively occur in the far- and near-field relative to the width, b .

Substituting du from Eq. (22) into the integral of Eq. (20) and once again taking the integral of the resulting equation between upstream limits ($\epsilon \rightarrow -\infty$) and inlet plane of the orifice ($\epsilon = 0$) yields:

$$\int_{\bar{u}_u}^{\bar{u}_o} \bar{u} d\bar{u} = -\frac{1}{\rho} \int_{p_u}^{p_d} dp + \nu \int_{\frac{2u_i\phi}{\sqrt{\pi}b}}^0 \frac{\partial^2 u}{\partial x^2} dx \quad (23)$$

where the subscripts u and d indicate upstream and downstream pressure conditions, respectively.

The actual locations for the pressures are determined based on regions of steady conditions both upstream and downstream. It should be noted that the integration limits for the second integral on the right side of Eq. (23) represent the velocity gradient from the first asymptotic value at the beginning of the convergence region $\left(\frac{d\bar{u}}{dx} = 0\right)$ to the second at the inlet plane of the orifice $\left(\frac{d\bar{u}}{dx} = \frac{2u_i\phi}{\sqrt{\pi}b}\right)$. Undertaking the integration and rearranging the terms gives:

$$\frac{\bar{u}^2 - \bar{u}_u^2}{2} + \frac{2\phi v \bar{u}_i}{\sqrt{\pi} b} = \frac{\Delta p}{\rho} \quad (24)$$

where Δp is $p_u - p_d$. The velocity \bar{u}_i , is substituted as a function of \bar{u} by evaluating Eq. (21) at $\epsilon = 0$ which gives $\bar{u}_i = \bar{u} - \bar{u}_u$; whereas \bar{u}_u is substituted using the volume flow rate, Q , and cross sectional area of the upstream region (pipe) to give $\bar{u}_u = Q / \left(\frac{\pi D_{pipe}^2}{4} \right)$. After the substitutions,

Eq. (25) reads:

$$\bar{u}^2 [1 - \alpha^2] - \frac{2\Delta p}{\rho} + \frac{4\phi v \bar{u}}{\sqrt{\pi} \cdot b} - \frac{16\phi v \bar{u} \beta^2}{\pi^{\frac{3}{2}} \cdot D_h^2} = 0 \quad (25)$$

where D_h is the hydraulic diameter of the orifice, and three geometric ratios, β (diameter ratio), AR (aspect ratio) and α (area ratio) are defined as part of the derivation. The parameter β , is defined as the ratio of the hydraulic diameter of the orifice to the pipe diameter, while the ratio of the orifice-to-pipe cross sectional areas are given by α , such that:

$$(a) \beta = \frac{D_h}{D_{pipe}} \quad (b) AR = \frac{a}{b} \quad (c) \alpha = \frac{a \cdot b}{\pi D_{pipe}^2 / 4} \quad (26)$$

The definition of the flow Reynolds number for this flow geometry is given as:

$$Re = \frac{\bar{u}_o \cdot D_h}{\nu} \quad (27)$$

which uses the mean streamwise velocity through the orifice and the hydraulic diameter as the velocity and length scales, respectively. Since it is the smallest length in the system, the use of the width, b , might be suggested as an alternative length scale. However, using this length scale does not include the corresponding change in the orifice perimeter as AR changes. The hydraulic diameter, on the other hand, has a definition that reflects changes in both the cross-sectional area of the rectangular orifice as well as its perimeter. Therefore, for a constant cross-sectional, D_h also represents the change in the perimeter of an orifice when AR is varied, which can be considered

as a strong benefit for the study of rectangular orifices. After substituting for Re , Eq. (25) can be factored and rearranged to give the pressure loss coefficient, K , as a function of AR as:

$$K = \frac{\Delta P}{\frac{1}{2}\rho\bar{u}^2} = [1 - \alpha^2] + \left[\frac{4\phi}{\sqrt{\pi} \cdot Re} \right] \left[\frac{2AR}{AR + 1} \right] (1 - \alpha) \quad (28)$$

At low Re , the dominance of viscous losses will lead to an increase in the loss coefficient that can be seen from the second term on the left side of Eq. (28). The effect, however, cannot be expected to be direct since the convergence parameter ϕ is also a function of Re . At relatively higher Re , the contraction effect will become the lead contributor to the pressure loss coefficient since the second term on the left will approach to zero leaving only $(1 - \alpha^2)$. This implies that, for the same cross sectional area or constant α , the loss coefficient will tend towards a constant value for increasing Reynolds number.

The AR -term reflects effects related to the relative change in flow convergence in the x - y and x - z planes (Figure 18) as the orifice aspect ratio increases. For the aspect ratio range of $1 \leq AR \leq \infty$, the corresponding range of the AR -term is $1 \leq \left[\frac{2AR}{AR+1} \right] \leq 2$. The lower range ($AR \rightarrow 1$) represents the flow through a square orifice where the flow undergoes maximized convergence in both planes. In this scenario, the convergence in both planes is also 2-D as the shape of the streamlines become a function of position in the convergence region. Therefore, it can be expected that, at constant Re , the loss coefficient will have greater values for lower aspect ratio than higher ones. At higher aspect ratios ($AR \rightarrow \infty; \left[\frac{2AR}{AR+1} \right] \rightarrow 2$) the limiting case of a Hele-Shaw flow is reached [47], [81]. The convergence phenomenon in this case is more pronounced in the x - y plane (Figure 18a) due to the relative reduction in effects from wall interactions in the x - z plane.

To obtain the analytical relationship between K and Re as a function of AR , data needs to be available to estimate the relationship between ϕ and AR . However, with no indication at this stage regarding how ϕ changes with AR , the integrated form of Eq. (20) can be used in combination with Eq. (21) to provide an analytical description of ϕ as:

$$\phi = \frac{b}{x} \operatorname{erf}^{-1} \left[1 - \frac{\bar{u}_u}{\bar{u}} \left(\frac{-2\Delta p}{\rho} - 2\nu \left(\frac{\bar{u}_u - \bar{u}}{x} \right) \right)^{-\frac{1}{2}} \right] \quad (29)$$

as a function of, x , the length of a the velocity transition measured from the onset of the velocity increase where the local velocity is greater than the upstream velocity ($u > \bar{u}_u$) to the plane of the orifice where the velocity reaches the mean velocity through the orifice ($u = \bar{u}$). The pressure gradient on the right represents the loss across the convergence zone which is also a function of the fluid density and viscosity. The effect of AR on the convergence, however, is not clearly reflected in this equation. For a constant pipe diameter and orifice area, the change in orifice AR is mainly by changing the length, a than its width, b .

A discussion pertaining to the quantitative estimation of ϕ for circular orifices is given by Grose (1983) who modeled and experimented the flow through pipe-installed circular orifices [52, p. 213]. In that study, the error function asymptotic definition has shown that a “viscosity parameter, ϕ_v ” has a constant value of 33 which indicates a zone of influence having length equal to 20% of the orifice diameter. With an initial assumption of a convergence zone having a length equal to 20% of the orifice width, it is predicted in this work that the aspect ratio and convergence parameter have an inverse relationship of the second order, i.e. $\phi = f(AR^{-2})$. It also allows the change in the relative extents of convergence given the wide range of AR that extends from the square geometry to long aspect ratio narrow orifices.

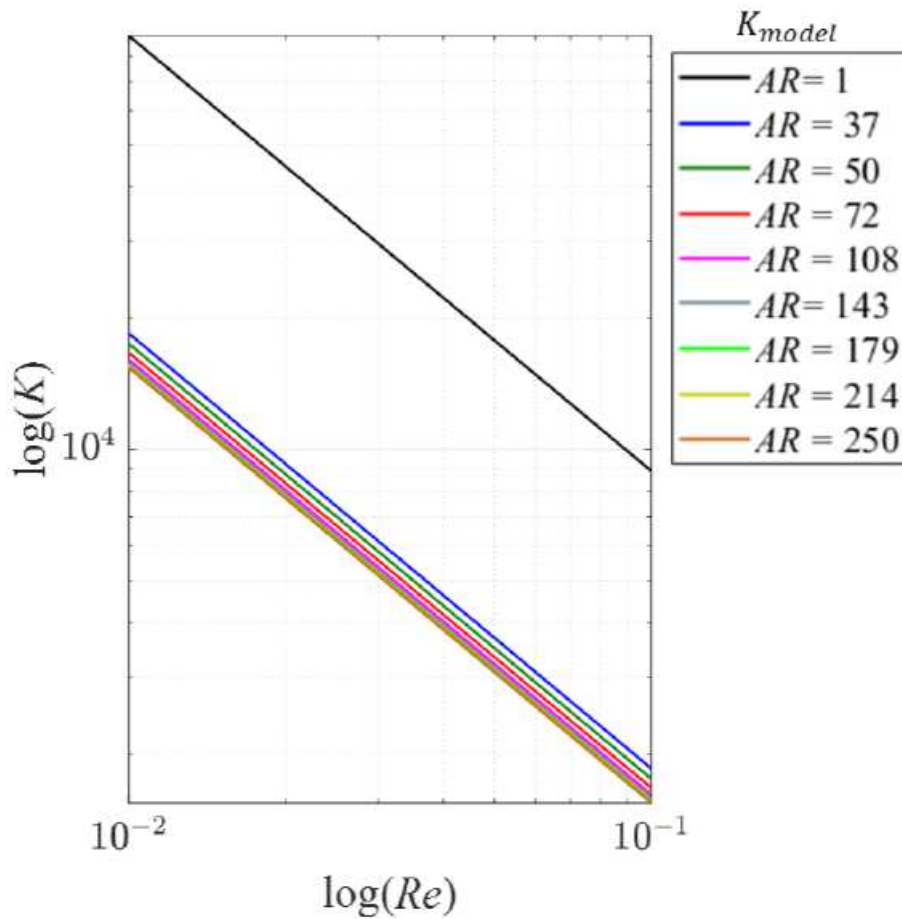


Figure 19 –Log-scale plot of the modeled Re -vs- K relationship as per Eq. (28) for all aspect ratios

Using the developed model, Figure 19 shows the changes in K with respect to changes in Re and AR obtained from Eq. (28). The model generally shows that K decreases as AR increases which agrees with the hypothesized behavior of flow convergence. The overall trend of all plots shows an inverse relationship between the loss coefficient and Reynolds number where higher Re leads to lower K which is also generically reflected in Eq. (3)[78], [145]. The difference seen between the loss coefficient values for the square orifice and the high aspect ratio orifices indicates significant variation in the flow phenomenon when AR changes. The change in K decreases as AR increases shown in Figure 19 are attributed to the progressively minimal change in the hydraulic diameter of the orifice as the AR increases. As the orifice aspect ratio, AR , keeps on increasing, the difference between the velocities through the orifices for a common Re decreases.

The assumption of the asymptotic velocity transition for rectangular orifices has led to the convergence-based loss coefficient model described in Eq. (28). The parameter ϕ represents the upstream flow convergence phenomenon that is directly related to the distance taken by the velocity transition which is given by Eq. (21). The results from experimental measurements are expected to verify the modeled relationship between pressure loss and orifice aspect ratio. A form of Eq. (28) can be used to calculate ϕ from experimental data to be used in Eq.(21) to determine the velocity gradient as a function of the near-entrance distance, x/b .

4.3. Results and discussion

The processing and analysis of data is ultimately aimed at determining the $Re - K$ relationship from the measurements. Experimental data containing the measurements directly logged from the readings are used to calculate the Re as per the definition given in Eq.(27). The data from measurements at a value of Re corresponding to a duration of the set pump speed is averaged to give the effects of AR for equal Re . Results pertaining to the effects of AR on ΔP , K and ϕ are presented in this section. Before comparing experimental data to the model given in Eq.(28), the respective pressure loss characteristics described by these parameters are presented. The codes used to perform the required calculation and generate the plots given in this section are provided in section (ii) of Appendix B.

4.3.1 Static pressure drop, ΔP and loss coefficient, K from experiments

The effect of AR on the static pressure drop, ΔP , is shown in Figure 20 for different Re . It can be seen that the pressure drop generally increases as AR increases. At constant AR , an increase in ΔP is also seen for increasing Re . The constant area maintained for all AR shall not imply equal velocity through the orifices for the same Re . Since the hydraulic diameter D_h is the length scale used to calculate Re , higher volume flow rate must be used for increasing AR to match Re because

D_h decreases as AR increases. The resulting increase in velocity has to be balanced by an increase in the pressure drop for momentum of the fluid to be conserved. In the experiments of this study, the change in cross sectional area from the pipe section to the orifice is from $4.5 \times 10^{-3} \text{ m}^2$ to $0.009 \times 10^{-3} \text{ m}^2$ for all aspect ratios which results in an area reduction of 99.8 %.

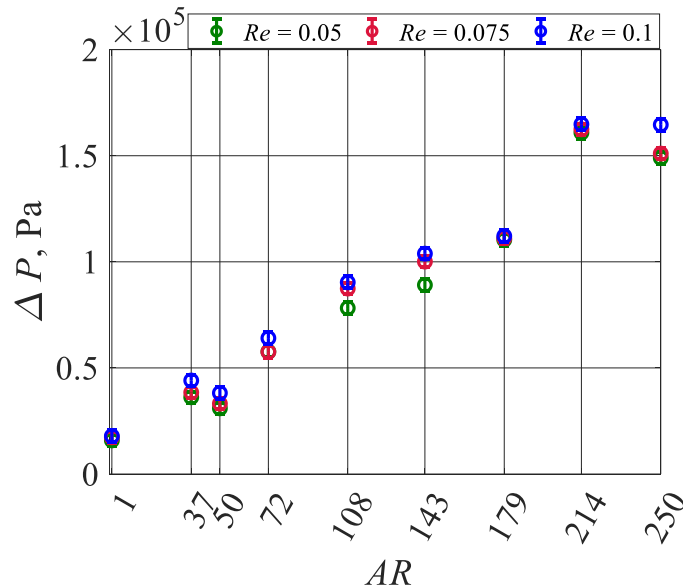


Figure 20– Plot of changes in the static pressure drop as aspect ratio changes at different nominal Reynolds numbers

The mean velocity through the orifice is determined by dividing the volume flow rate by the orifice area to be used in the calculation of the loss coefficient, K . For the experiments that are considered in this study, the velocity varies between 0.02 m/s at the minimum Re for $AR = 1$ to 0.43 m/s at the maximum Re for $AR = 250$ which is an order of magnitude change. A dominant effect of the downstream velocity on K has been expected as ΔP is divided by the square of the velocity.

The change in K as AR changes can be seen in Figure 21(a). In general, as AR increases, K shows an asymptotic behavior for all Re considered. The loss coefficient, K , for the square orifice ($AR = 1$) is greater than the other orifices by a minimum of 25%. This is directly attributed to the required increase in the velocity through the orifice as AR increases to maintain a constant Re . For

an increase in Re , however, K decreases for a given AR due to not only increasing loss in static pressure but also an increase in velocity.

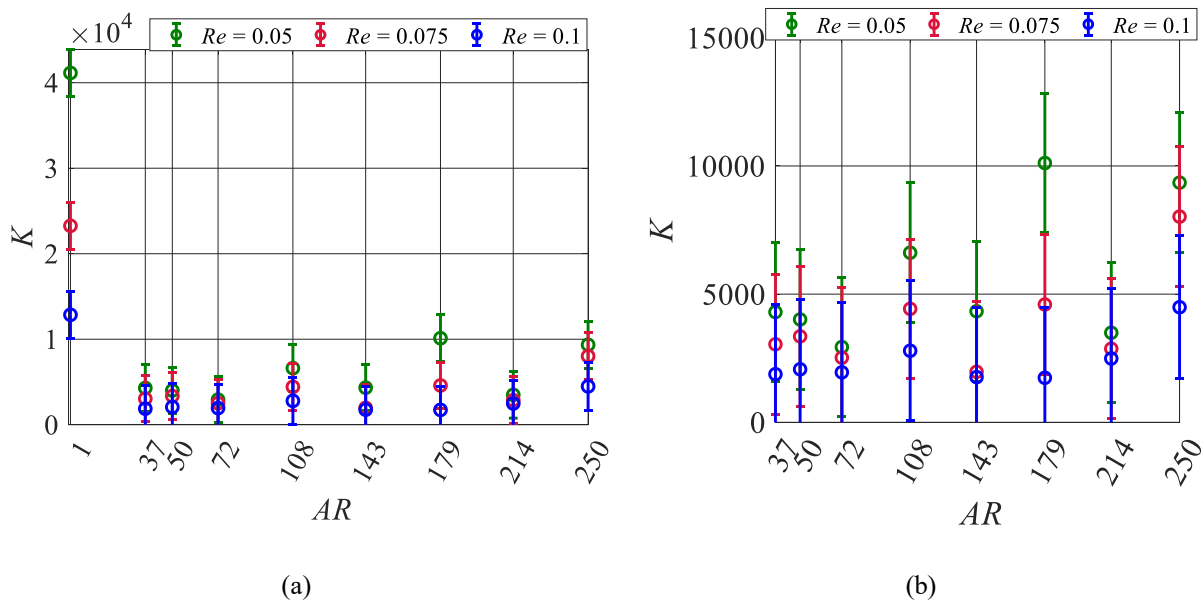


Figure 21– Plot showing the change in K as AR changes for the ranges (a) $1 \leq AR \leq 250$, and (b) the $37 \leq AR \leq 250$

In Figure 21(b) a portion of the plot for $37 \leq AR \leq 250$ is given for a better look at the flow blockage effects as AR increases. Increasing blockage effects lead to higher ΔP due to decreasing width, decreasing hydraulic diameter, and increasing perimeter of the orifice. The loss coefficient, however, decreases as AR increases due to the higher velocities through the orifice. At the same Re as, AR increases the velocity through the orifice also increases since the experiments maintained the same Re which is defined using the hydraulic diameter as the length scale. As Re increases, the loss coefficient decreases because the increase in velocity leads to higher gain in kinetic energy.

The uncertainty ranges given in Figure 20 and Figure 21 are calculated only based on error sources identified for the measurement in ΔP . Since the loss coefficient K and the convergence parameter ϕ are themselves calculated, but not measured, a propagation of uncertainty method [137] was used. As a result since the loss coefficient K includes the velocity term in its calculation the random

and bias errors from the mass flow meter will propagate. Referring to Eq. (30) the uncertainty in ϕ will include the square of the errors due to the mass flow meter since both Re and K are present in its calculation. This leads to the larger uncertainties observed in Figure 21 and Figure 22.

To relate the flow convergence factor, ϕ , with AR Eq. (28) can be rearranged to read:

$$\phi = \frac{\sqrt{\pi} \cdot Re}{4} \left[\frac{K - (1 - \alpha^2)}{\frac{2AR}{AR + 1} (1 - \alpha)} \right] \quad (30)$$

With experimental data available for the loss coefficient the equation can be used to determine the change in convergence as AR changes. The results obtained from Eq. (30) are plotted in Figure 22.

The data follow a second order non-linear fit in the form of $\phi = f(AR^{-2})$, which is shown in the figure to describe the relation between ϕ and AR . Values for ϕ from Eq. (30) and the non-linear fit generally show that ϕ decreases as AR increases. The greatest deviation is seen for $1 \leq AR \leq 37$ whereas for $37 \leq AR \leq 250$, the change in ϕ is nearly insignificant. The steep decrease in ϕ for $1 \leq AR \leq 37$ also indicates that ϕ strongly depends on the convergence phenomenon. This relationship can also be physically interpreted by referring to the orifice width, b , which significantly decreases as AR increases. It can then be inferred that as AR increases the flow requires less distance to reach the asymptotic velocity through the orifice. This concept matches with the theory regarding the dominance of contraction effect on the pressure distribution when other flow conditions remain constant [52].

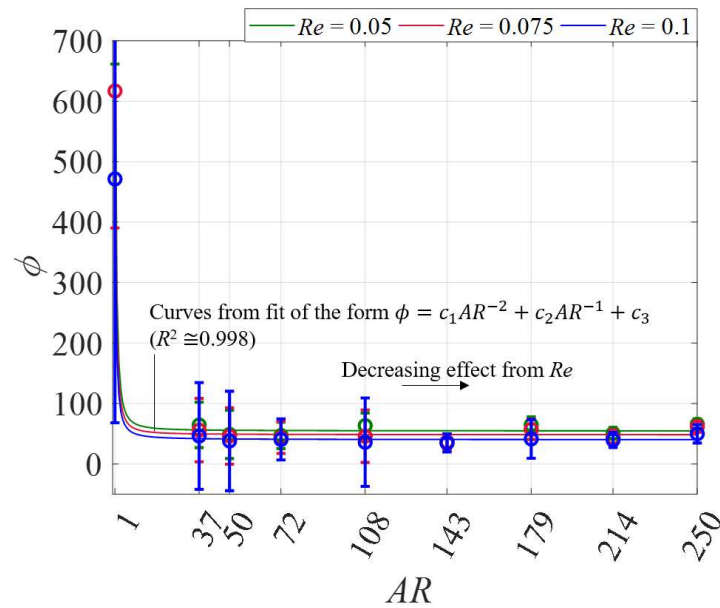


Figure 22– Plot of ϕ vs. AR from Eq(30) with non-linear least square fits

An alternative view of Eq.(22) and Eq.(29) is with respect to the effect of the rate of strain [81], [94] considering the relationship between the flow convergence phenomenon and AR seen in Figure 22. As such it can be interpreted that at lower aspect ratios, greater convergence leads to higher shear rate which translates to increased pressure loss coefficient due to an extra strain. This is caused by the change in the balance of viscous stresses as the flow accelerates near the orifice inlet. Therefore, ϕ , would represent the viscosity-related convergence phenomenon which affects the extent of streamline curvature. Its original appearance in the constitutive equation of the velocity distribution shown in Eq. (21) also indicates its direct relation with the strain rate tensor [47]. This also supports the hypothesis and the modeling approach employed.

4.3.2 Wall pressure profile

The axial distribution of the wall pressure can be used to indicate the significance of the phenomena expected upstream. Major consequences of the contraction can be inferred from the change in wall pressure as the flow approaches the orifice. An increase in the wall pressure may indicate of flow blockage or flow convergence based on the fundamental description of these

phenomena [57]. The flow blockage leads to back pressure development resulting in increased static pressure at the walls. Flow convergence relates to the development of shear dominated regions as the streamlines converge to the entrance. The relative size of these regions such as recirculation zones depend on the Reynolds number [81]. The trend that has been shown is that as Re increases the size of these regions also increases. The particular nature of these flow structures has been described as circulation zones and Moffatt vortices [147] at both turbulent and laminar conditions [81].

Measurements from the multiple set of transducers along the axis of the main flow pipe used in the experiments are used to plot the axial profile of the wall pressure. The results are plotted in Figure 23 which shows the average measurement for $Re = 0.1$. The axial distribution of wall pressure in the pipe is also compared with theory. The theoretical pressure distribution is calculated using the relationship for a laminar flow in a circular pipe given by the Hagen – Poiseuille equation as:

$$\frac{\Delta P}{L} = \frac{8\mu Q}{\pi \left(\frac{D_{pipe}}{2}\right)^4} \quad (31)$$

The effect of AR on the pressure loss is accounted through the volume flow term, Q , which varies with aspect ratio for experiments at constant Re . From Figure 23(a) it can be seen that for the range $1 \leq AR \leq 72$ the upstream pressure increases as it approaches the orifice. For the remaining range of aspect ratio, however, the wall pressure remains relatively constant for the upstream region covered by the transducers. The indication of this is that the effect of convergence for higher AR is apparent in the region $0 \leq x/D_{pipe} \leq -1$. This observation is obviously subjected to further validation due to the absence of pressure measurement in this region. Nonetheless, it would not be plausible to assume the upstream pressure for higher AR s began its increase before $x/D_{pipe} \leq -2.5$. The comparison with theory in Figure 23(b) shows that the results the experiments have

yielded reliable data that come well in agreement within the uncertainty ranges to verify that the expected physics is measured.

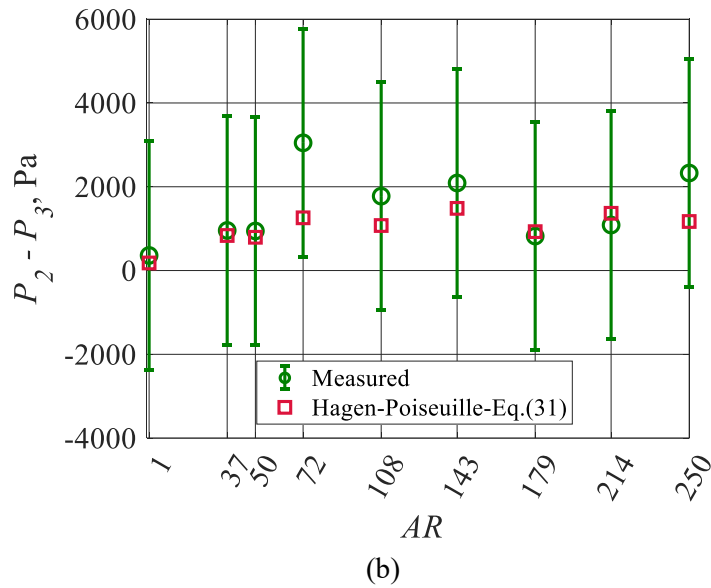
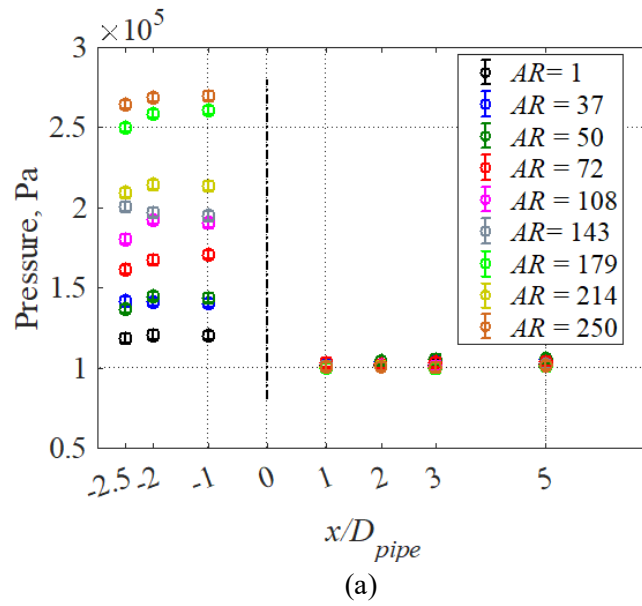


Figure 23– Plots of (a) wall pressure profile along axial direction, and (b) the measured pressure drop between transducers located upstream compared with theory

4.3.3 Model verification

4.3.3.1 Pressure loss coefficient, Eq. (28)

The log-log plot of Re against loss coefficient data from the experiment, K_{exp} , and from the developed model shown in Eq. (28), K_{model} , is shown in Figure 24. A common angular deviation was observed between the slopes of the model curves and the line, L_e , drawn through, K_{exp} data for corresponding AR . It is expected that calculating the angle, θ , could quantify the observed deviation between the loss coefficient predicted by the 1D model and obtained from experiments. The mismatch also highlights the possibility that the employed pressure measurement technique was highly 1D in nature which could not capture the change due to varying relative dominance of flow convergence in the two planes as AR changed.

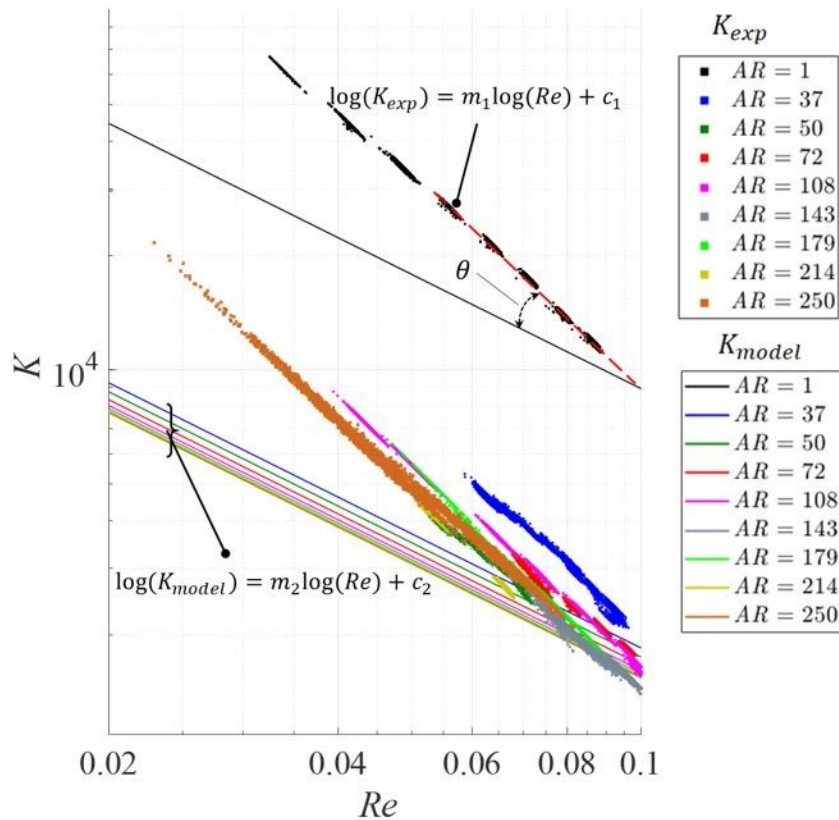


Figure 24: K -vs- Re plots for experimental data (shown as points) and the developed model Eq. (28)

It is hence important to obtain a clearer understanding of the relationships between the combination of the pressure measurement experiment data and the 1D model developed. This is undertaken here using statistical approach through factor analysis [148]. In factor analysis, it is possible to investigate variables which have effects that are not observable [148]. Relationships between the variables that make interpretation of the results difficult can be resolved by applying various analysis techniques depending on the intended simplification and/or clarity [148]–[150]. Such application of factor analysis and the interpretation methods therein is common in the fields of medicine and social sciences [148], [151] and has been used in engineering applications related to flow mechanics [152]. The relationship between the model data and the experiments indicate a potential application of a technique similar to factor rotation [151]. Factor rotation refers to repositioning of the distributed the data points, or the coordinate axes, in the plotted space. The main objective is to obtain a clearer view of the relationships between variables that could not be directly captured by the collected data, in the case here, the combination of the pressure measurement experiment and the 1D model. Rotation of the model line, L_m , about the AR -axis is therefore proposed to enable a clearer view of the effect of AR on the flow convergence phenomenon that could not be directly captured by the experiments and the 1D model.

The angle θ between the two intersecting lines, L_m and L_e , can be calculated as:

$$\theta = \tan^{-1} \left[\frac{m_e - m_m}{(1 - m_e m_m)} \right] \quad (32)$$

where m is the slope of the line and the subscripts m and e indicate the line of the model data, L_m , and that of the experiment, L_e . For each AR , the respective linear fit of $\log(K)$ vs. $\log(Re)$ is used to generate the lines in the linear scale corresponding to the ones shown in Figure 24.

The plot of the calculated values of the respective angles normalized by the maximum calculated angle, θ/θ_{max} , is given in Figure 25. Distribution of the values of θ over the range of AR covered

$(\theta/\theta_{max}\sim 1)$, indicates that the angle separating the intersecting lines might potentially be a constant. This strongly suggests the rotation of the axes themselves rather than individual $\log(K)$ vs. $\log(Re)$ lines for each aspect ratio.

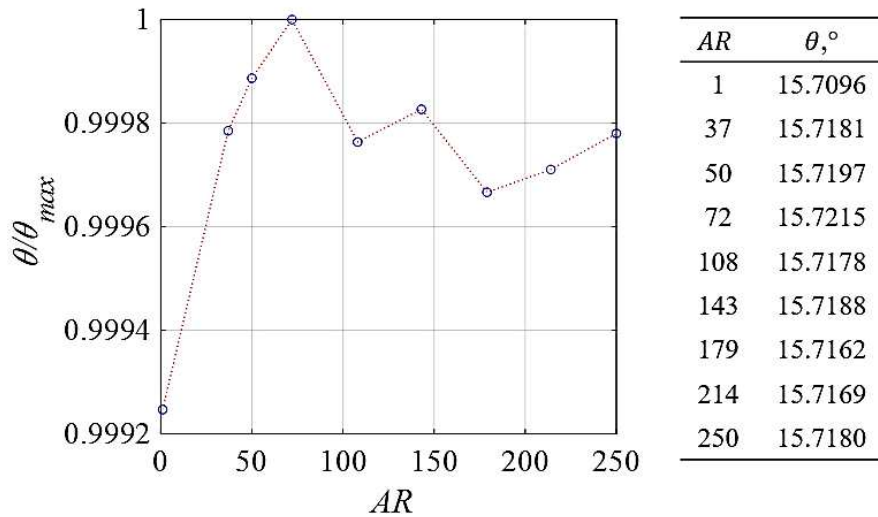


Figure 25– A plot showing values of the calculated angle, θ , for the orifice aspect ratios normalized by the maximum value, $\theta_{max} = 15.7215^\circ$. From the accompanying table showing actual values, it can be seen that $\theta_{max} = 15.7215^\circ$ occurs for $AR = 72$

The challenge of accurately locating a center of rotation for each AR that is both physically and analytically sensible could be avoided by rotating the model data about a point in reference to the origin of the coordinate system. The resulting post-rotation variations in the values of $\log(K)$, the dependent variable in this case, can be reduced by introducing an offset factor to account for the deviations caused by shifting the rotated line back to its original location could thereby be accounted for. In this study, the rotation has been made about the point $(10^{-2}, 10^{-3})$ on the $\log(Re)$ -vs- $\log(K)$ plots. The definition of a center of rotation is required as the range of Re covered in the study does not start from 0 and the location of the origin has been shifted from $(0,0)$ to the respective centers of rotation.

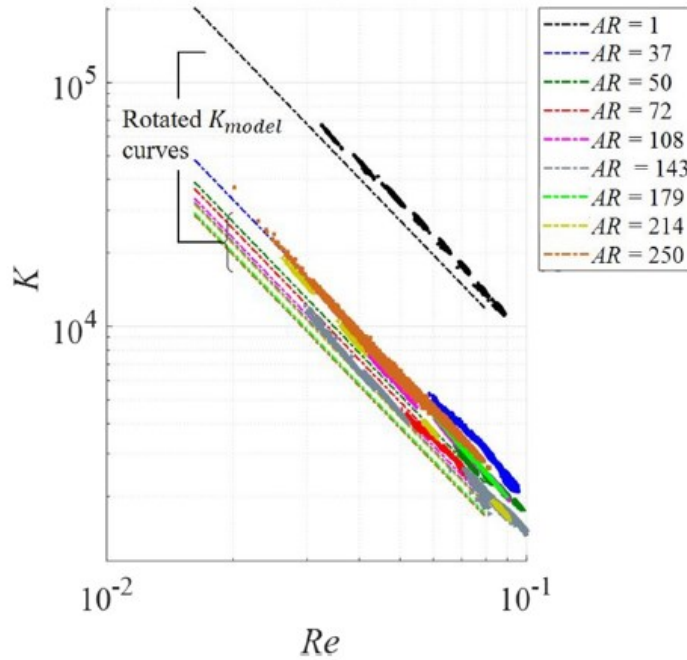


Figure 26— Re vs. K plots for experimental data (shown as points) and model rotated by multiplication by the rotation matrix

The plot showing the experimental data together with the rotated version of Eq. (28) is given in Figure 26. The rotation has been able to account for the estimated deviation between the data sets that resulted from the strong 1D nature of both the pressure measurement technique and the modeling approach. The usage of the arithmetic mean as the center of rotation resulted in mean deviations in K that are exaggerated due to the influence from the data at the asymptotic ends of the spectrum based on the Re range. Before the rotation, the data in Figure 24 can be used to calculate the relative logarithmic error to determine the percentage deviations. The error ranged from 36% to 70% across all AR at $Re = 0.01$, to less than 30% at $Re = 0.1$. With rotation applied, Figure 26 shows improved agreement between model and experiment results. After the rotation, the relative percentage error ranged from 14% to 32% at the lowest Re to less-than-6% at $Re = 0.1$.

To address the mismatch due to attempting to model a 2-D phenomenon with a 1D flow model, θ can be expressed (parameterized) as a function of AR which can be used to construct the matrix

that will rotate Eq.(28) in the $Re - K$ space. The parametrization can be achieved by making use of the relation known as the Rodrigues formula [153] which gives a single equation that can be used to obtain the rotation matrix from an axis-angle representation such that the norm of the direction vector returns the rotation angle θ . However, the change in the angle θ shown in Figure 25 suggests that the angle between the model and experiment lines corresponding to each AR is nearly a constant value. This also indicates that the employed exploratory method of factor rotation is appropriate with the perception that the effects of behavior of the unobservable parameter is more or less inherent to the model.

4.3.3.2 Velocity transition

From the observations so far and discussion of the results, it can be seen that the constitutive velocity transition equation shown in Eq. (21) takes a crucial role in determining the validity of the model equation. It is, therefore, necessary to consider the velocity transition behavior for the flow through each rectangular orifice. To achieve this, a length of the convergence region as a factor of the orifice width b is considered. The choice of b is based on the same rationale as described in the definition of the axial length for velocity transition in Section 4.2. Considering the initial definition of ϵ , for a value of Re in the range $0.05 \leq Re \leq 0.1$, the value of ϕ can be averaged and used together with the length of the convergence region, x , such that:

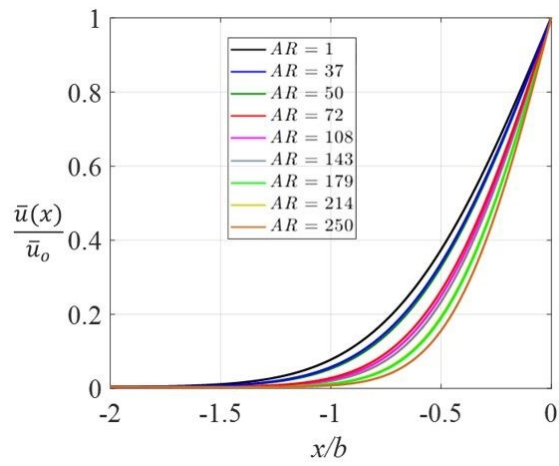
$$\epsilon = \frac{\bar{\phi}_{Re} x}{b} \quad (33)$$

where $\bar{\phi}_{Re}$ is the averaged convergence factor for the considered range of Re ; b is the width of the orifice; and x the axial distance in the upstream convergence region. Calculated values of ϵ are then used in Eq. (21), along with the corresponding values for the mean velocities to plot the velocity distribution $\bar{u}(x)$ in the convergence region. The mean velocity $\bar{u}(x)$ is then normalized by the orifice velocity, \bar{u}_o , to yield:

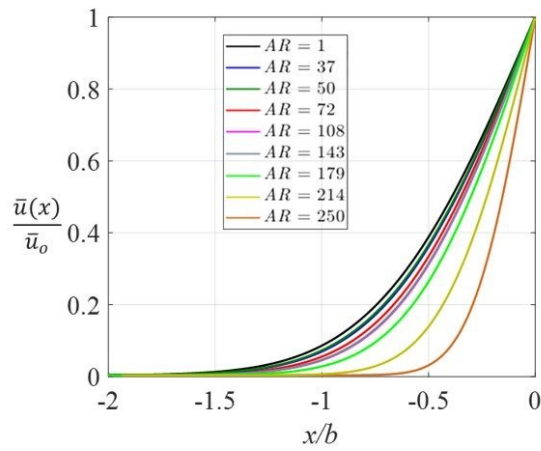
$$\frac{\bar{u}(x)}{\bar{u}_o} = \frac{\bar{u}_u}{\bar{u}_o} + \frac{\bar{u}_i}{\bar{u}_o} \operatorname{erf}\left(\frac{\bar{\phi}_{Re}x}{b}\right) \quad (34)$$

where each of the required variables can be used from experimental data to plot $\bar{u}(x)$ as a function of AR and Re in the convergence zone. In view of the discussion given in Section II regarding Eq. (21), only the region $x \leq 0$ which includes the convergence zone is considered. If the entire region of $-\infty \leq x \leq \infty$ was instead considered, the results would show values of normalized velocity greater than 1 occurring at the entrance of the orifice. This is due to the symmetric nature of the error function $\operatorname{erf}(x)$ in the range. An alternative way to deal with this issue and ensure that both mathematical and physical principles are obeyed is to model the velocity distribution as skewed-Gaussian [146]. Although this approach provides increased robustness by allowing an additional a parameter to that regulates skewness, it comes at the cost of significant increase in the complexity and tediousness of the model derivation.

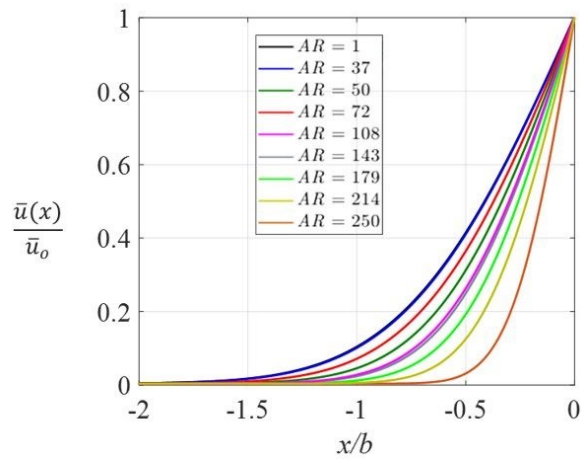
Plots of the velocity transitions in the convergence zone are shown in Figure 27 as a function of AR and Re . The velocity plotted is normalized by orifice velocity \bar{u}_o which is assumed to occur at $x = 0$, or, if the entrance length for full development is considered [83] then the maximum velocity occurs at $x \geq 0$. There is minimal effect of this assumption on the results since the only change will be on the horizontal axis while the relative spacing between the plots remains the same.



(a)



(b)



(c)

Figure 27– Plots showing the velocity transition determined from Eq. (21) for all orifice aspect ratios for (a) $Re = 0.05$; (b) $Re = 0.075$; and (c) (a) $Re = 0.1$

All the plots in Figure 27 commonly show that as the AR increases the flow takes longer to start its acceleration. For smaller AR however, the change in velocity starts farther upstream. The convergence zone for all aspect ratios in general lies within $-2 \leq x/b \leq 0$. The maximum length of convergence is seen for $AR = 1$ in the order of $x/b = -1.5$, whereas the minimum length, and minimum convergence, is for $AR = 250$ for $x/b \cong -0.5$.

As Re increases the velocity increase begins closer to the inlet face of the orifice and the gradient is more sudden than for lower Re due to the increased flow acceleration for higher Re . The concept of maximum extent of convergence in the square orifice leading to longer distance of velocity transition is thus confirmed. Referring to the developed loss coefficient model in Eq. (28), it can be seen that at all Re , the contribution from the flow convergence factor ϕ is significant. The factor ϕ quantifies the relationship between the flow convergence length and AR also as a function of Re .

4.4. A re-statement of the model

The analysis of experimental measurements and the comparison with the model developed based on momentum conservation, affirmed the capability of describing the viscous flow through rectangular orifices as a function of AR . The results showed that inclusion of the convergence parameter ϕ in the definition of the independent variable, in this case the non-dimensional axial distance ϵ , was a key step in representing the flow convergence phenomenon quantitatively. There was, however, a deviation between the loss coefficient data from experiment and model which was notably angular in nature. Comparing the angle, θ , corresponding to each AR showed that it could be considered to be a constant value. This suggests that an effect that is inherent to the measurement, the analysis, or their combination has not been captured. The results from this study strongly indicates that such a mismatch can be the 1D-nature of the employed analytical and

pressure measurement method, while the flow convergence is predominantly 2D. This can be verified by using an approach that combines velocity and pressure measurement allowing a better agreement between analytical and physical descriptions of the flow, particularly in the convergence region.

The possibility to adapt to this limitation by using a factor rotation approach was also shown for the loss coefficient, K , allowing the model to be re-stated as:

$$K = \frac{\Delta P}{\frac{1}{2}\rho\bar{u}_o^2} = [1 - \alpha^2] + \left[\frac{4\phi}{\sqrt{\pi} \cdot Re} \right] \left[\frac{2AR}{AR + 1} \right] (1 - \alpha) \quad (35)$$

a) $\phi = f(AR^{-2})$

b) $\bar{u}(\epsilon) = \bar{u}_u + \bar{u}_i \text{erf}(\epsilon)$

The flow convergence parameter ϕ and velocity gradient in the convergence zone $-\infty \leq x \leq 0$ shall, respectively, obey the relations in Eq. (35a) and (35b) where $\epsilon = \frac{\phi}{b} x$. It should be noted that Eq. (35a) can be used to obtain an initial estimate for the relationship between ϕ and AR especially in the absence of any prior data for the estimation.

If the correction to the angular deviation is considered, the rotated version of the loss coefficient model, K' , can be given as[153]:

$$K' = K \times R$$

a) $R(\theta) = I_3 + \frac{\sin\theta}{\theta} [n]_x + \frac{1-\cos\theta}{\theta^2} (nn^T + I_3)$

b) $I_3 = \begin{bmatrix} 1 & 0 & 0 \\ 0 & 1 & 0 \\ 0 & 0 & 1 \end{bmatrix} \quad (36)$

c) $[n]_x = \begin{bmatrix} 0 & -\theta & 0 \\ \theta & 0 & 0 \\ 0 & 0 & 0 \end{bmatrix}$

where $R(\theta)$ is the rotation matrix for an angle θ ; I_3 is the identity matrix given in Eq. (36b); and $[n]_x$ the cross-product matrix for rotation along the AR -axis defined in (36c) for the direction vector $n = [0 \ 0 \ \theta]$. The representation given in Eq. (36a) is known as the Rodrigues formula which is used to give the angle-axis representation of the rotation matrix[153].

It is worth noting that the approaches applied in both modeling and experimentation had gone through significant refinement to develop with the model discussed in in this chapter. Earlier approaches included a measurement method which used pitot-tube-like probes to measure the pressure rather intrusively [16]. The loss coefficient obtained from these measurements described the opposite relationship between K and AR which is believed to be due to the measurement of the dynamic pressure rather than the static pressure. This motivated upgrading the measurement facility to the one described in Section 3.1.

The formulation of the physical and mathematical properties of the convergence phenomenon through using the concept of streamline curvature and parameter, ϕ , has also gone through some development. Previous attempts inclined towards assuming that the convergence phenomenon will mainly be dictated by the width, b , of the orifice. This has led to consider the maximum convergence to be for higher AR because of the narrower width [16], [134]. This would have led to higher values of ϕ for higher AR which conflicts with the streamline behavior as illustrated in Figure 18 and the mathematical role expected from convergence in the Gaussian transition.

4.5. Modelling the loss coefficient using skew-Normal velocity distribution

If the distribution of the mean velocity is assumed to follow the standard normal (Gaussian) distribution, the function forces the location of the maximum value to be at the inlet of the orifice ($x = 0$). However, the concept of hydraulic entrance length dictates that this does not fully represent the actual physics since the flow requires the distance, L_e , to fully develop after entering the orifice. In order to account for this deviation, it can be expected that a skewness can be introduced to the distribution so that it is no longer symmetric and with its maximum velocity occurring at ($x \geq L_e$).

The probability density functions following the standard- and skew-normal distributions are shown in Figure 28(a). From the respective curves it can be seen that the skewed Gaussian distribution allows to account for the entrance length which is known to occur at $x > 0$ whereas using the symmetric Gaussian distribution requires the entrance length to be neglected. The same effect is noticed in the corresponding cumulative distribution functions shown in

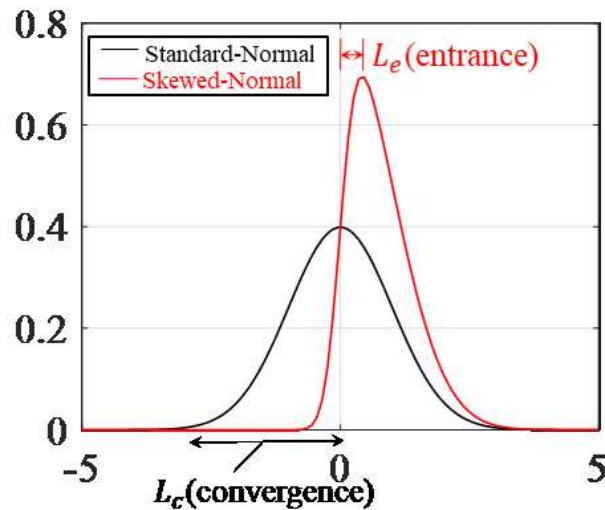


Figure 28 – Plots showing the probability density function of the standard-Normal (black) and skewed-Normal distributions (red)

One way to avoid this problem has been found by partially considering the flow field to focus on either the upstream region, the contraction region, or the downstream region [48], [52]. However,

this method will cause the portion of the region which is not considered to reduce to a vanishingly small region. Modeling the velocity gradient between the convergence region and the location of the full development in the channel as per skewed Gaussian distribution may allow the relative lengths of the convergence region and the entrance regions to be estimated.

The skewed normal distribution can be defined as a class of distributions whose special case results in the normal distribution [146]. For a continuous and random distribution X that has the probability density function of the form:

$$f(x) = 2\gamma(x)\Phi(\delta x) \quad (37)$$

where the standard normal (Gaussian) density function, and its distribution evaluated at δx are, respectively, given by:

$$\gamma(x) = \frac{\exp\left(\frac{-x^2}{2}\right)}{\sqrt{2\pi}} \quad \Phi(\delta x) = \int_{-\infty}^{\delta x} \gamma(t) dt \quad (38)$$

where δ is a fixed arbitrary number known as the shape parameter; and t denotes an arbitrary random variable. The shape parameter regulates the shape of the density function where at $\alpha = 0$ the standard normal density is obtained.

When the velocity is assumed to rather follow the skew-normal distribution, the corresponding model for the velocity transition becomes:

$$\bar{u}(\epsilon) = \bar{u}_u + \bar{u}_i \operatorname{erf}\left(-\frac{\epsilon - \mu_{SN}}{\sqrt{2}\sigma_{SN}}\right) \quad (39)$$

where μ_{SN} and σ_{SN} are the statistical mean and standard deviation of the skew-normal velocity distribution, respectively. The velocity increase along the axial direction is thus written as.

$$\frac{du}{dx} = \frac{\bar{u}_i}{\sigma_{SN}} \frac{\phi}{b} \sqrt{\frac{2}{\pi}} \exp\left(-\frac{\left(\frac{\phi x}{b} - \mu_{SN}\right)^2}{2\sigma_{SN}^2}\right) \quad (40)$$

The principal idea behind this modeling approach is to obtain a differentiable expression for the velocity so that its derivative can be used in the momentum equation to express the pressure along a streamlines. The resulting equation can then be manipulated to give a mathematical expression for the dimensionless pressure loss coefficient, K_{SN} , for the assumed skew-normal (SN) velocity distribution.

The final model for K_{SN} is given by:

$$K_{SN} = [1 - \alpha^2] - \left[\frac{4\phi}{\sqrt{\pi} \cdot Re} \right] \left[\frac{AR}{AR + 1} \right] (1 - \alpha) \sqrt{\frac{2}{\sigma_{SN}^2}} \exp\left(-\frac{\frac{\phi x}{b} - \mu_{SN}}{\sqrt{2}\sigma_{SN}}\right)^2 \quad (41)$$

The definitions given in [146] can be used to substitute for μ_{SN} and σ_{SN} such that:

$$\mu_{SN} = \bar{u}_u + \bar{u}_i \sqrt{\frac{2}{\pi}} \frac{\phi}{\sqrt{1 + \phi^2}} \quad (42)$$

$$\sigma_{SN} = \bar{u}_i \sqrt{1 - \frac{2\phi^2}{1 + \phi^2}} \quad (43)$$

Comparing the plots in Figure 29(a) and (b), the application of the skew-Normal distribution provided results that better show the loss coefficient as a function of AR . The overall trend in the relationship between Re and K reflected is the same as the one seen in Figure 29(a) with the effect of AR also remaining the same. The spacing between that plots, however, have increased significantly which can be seen from the plots for $AR > 1$ in Figure 29(b) as compared to the results from the Gaussian assumption. The angular deviation also remained in the new plots from the skewed-Normal distribution. It is also noted that the curves for the loss coefficient model based on the skewed-Normal distribution lied mostly above the experimental values whereas the opposite is true for the standard-Normal case.

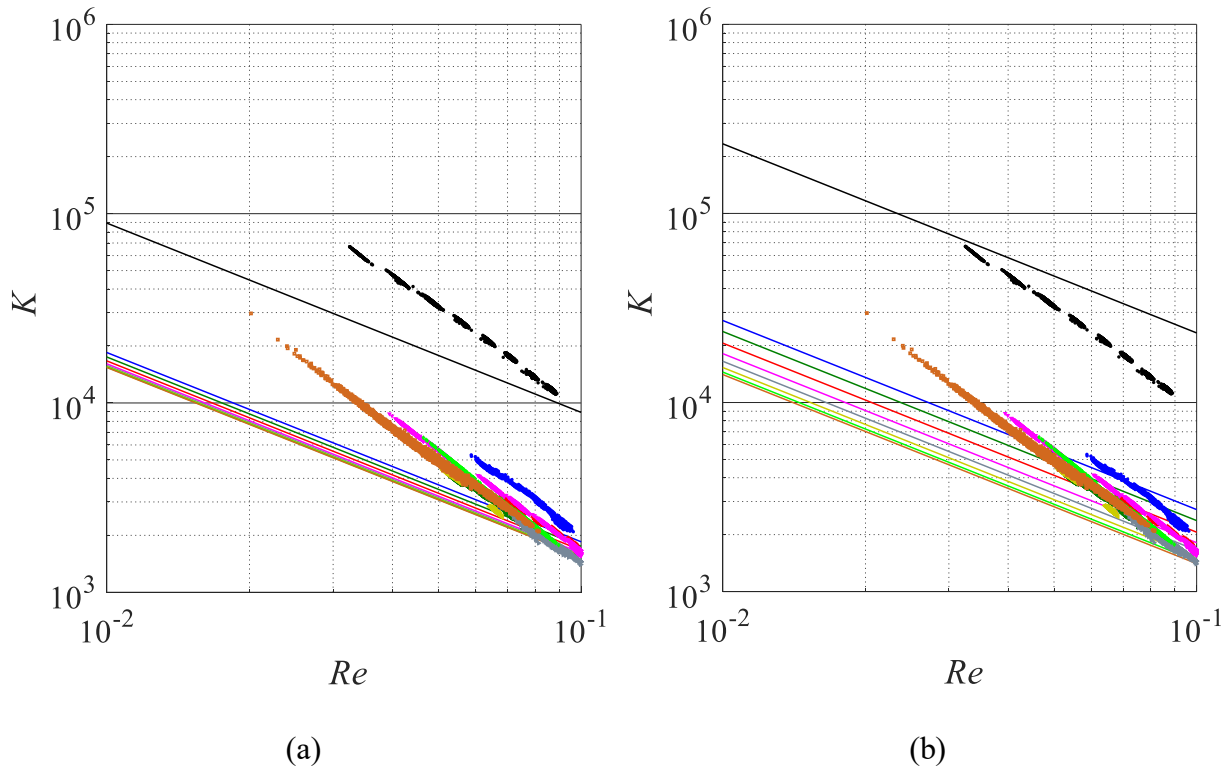


Figure 29 – Comparing the loss coefficient models developed assuming (a) standard Normal (Gaussian), and (b) skew-Normal velocity distributions

There is less motivation to pursuing the analysis to incorporate the skew-Normal distribution to replot the velocity transition curves. This is mainly because of the emphasis on the flow convergence phenomenon in the region $x/b \leq 0$. The main objective of this section was to document the foundation work and demonstrate the possibility for model refinement if the interest arises.

4.6. Conclusion

The study has developed a predictive model for the flow of viscous fluid through rectangular orifices. The model is developed based on the 1D Navier-Stokes equation and a constitutive equation for the unique velocity transition behavior that is directly related to flow convergence. The flow convergence is defined as the 2-D phenomenon that is essentially described by the curvature of the streamlines as the flow approaches the region near the entrance of the orifice measured from where its velocity begins to change. The length of this convergence zone is a function of the inlet geometry of the rectangular orifice that can be varied by changing its hydraulic diameter. The relative dominance of the 2-D convergence phenomenon is affected by the orifice aspect ratio, AR . The maximum convergence is for the orifice of the square shape, $AR = 1$, because the streamlines merge towards the orifice inlet from all directions. As the orifice hydraulic diameter is changed to increase AR , one of the distances between the edge of the orifice and the wall of the pipe will decrease. 2-D phenomenon will therefore become less dominant as the AR increase which leads to relatively less flow convergence.

The convergence parameter, ϕ , has been defined as part of the velocity transition behavior, which also dictates the behavior of the streamlines in the convergence zone. The theoretical analysis developed a non-dimensional expression for a pressure loss coefficient which is mainly a function of the flow Reynolds number in the creeping regime $0.01 \leq Re \leq 0.1$. The model is also heavily influenced by the properties of ϕ which is as strong a function of AR itself.

For a flow of viscous fluid at equal Re , the pressure loss coefficient, K increases as AR decreases supporting the idea of dominating contribution from upstream 2-D effects. Experiments measured the static pressure loss, ΔP , and the calculated the pressure loss coefficient, K , to verify the model. Experiments showed that a higher aspect ratio generally leads to higher ΔP due to the flow

blockage. For a given AR , an increase in Re leads to an increase in ΔP as result of the directly proportional relation between the flow rate and ΔP generally for viscous flows through contractions. Higher Re leads to lower values K for due to increased gain in inertia compared to loss in static pressure.

Comparing the K data from experiment to the model showed it had a significantly higher than expected slope in the response of $\log(K)$ to $\log(Re)$. A unique angular relationship between lines representing the experiment and model data was also observed. This deviation is attributed to the strong 1D nature of both the experimentation and modeling techniques which fails to fully capture the convergence phenomenon through ϕ . The investigation further led to multiplication of the model line by the rotation matrix which resulted in data with closely matching slopes and better agreement. The rotation was made from the exploratory standpoint which also follows the concept of factor analysis.

The model was used also verified by plotting the velocity transition in the convergence zone as a function of AR and Re . It has thereby been shown that ϕ from experiment can be used to describe not only the axial velocity gradient in the near inlet region but also the relative length of the convergence region. The strong influence of flow convergence as described by ϕ and its direct relation with AR indicates a promising success from future complementary investigations such as velocity measurement of the flow field.

Chapter 5 Effect of flow convergence on streamline behavior, velocity transition, and pressure loss characteristics²

5.1. Introduction

The previous chapter presented the change in velocity transition in the region $-2 \leq x/b \leq -0.5$ for all AR s. The relative distance covered in the region was also comparable to the ranges reported in [49], [52], [97]. The prevalence of streamline curvature and the strong effect of AR in the near-entrance region has thereby been asserted given the different distances of velocity transition for the various AR s. The discussion regarding the role of 2D convergence effects which were seen when initially comparing experimental measurements with the model has also related the length of the convergence zone to AR and hence to the curvature of streamlines.

Data regarding the curvature of streamlines can be used to closely study the effect due to flow convergence. The analysis of measurement data yields quantitative information regarding the curvature of streamlines as a function of axial distance and orifice size. This chapter applies the results of PIV experiments described in Section 3.2 to measure the 2D velocity field. The experiments measure the flow of glycerol ($\mu = 1.4138$ Pa.s, and $\rho = 1260$ kg/m³ at 20°C) at $Re = 0.1$.

The flow convergence phenomenon in the upstream region is investigated by focusing more on streamline properties. The pressure gradients in the streamwise, s and span wise, n directions are determined following the fundamental relations in streamline coordinates as reviewed in

² A version of this chapter has been published as Yusuf, Y., Ansari, S., Bayans, M., Sabbagh, R., El Hassan, M., and Nobes, D.S. (2018) "Study of Flow Convergence in Rectangular Slots using Particle Shadowgraph Velocimetry", *5th International Conference on Experimental Fluid Mechanics – ICEFM 2018*, Munich, Germany, July 2-4, 2018

Section 2.3. A unique approach is used to calculate the streamlines from 2D velocity data. The data analysis describes the behaviour of streamlines in the convergence zone quantitatively.

Sections, 5.2 and 5.3, discuss the approaches used to calculate the streamlines and the pressure gradients, respectively. The elaborations in these sections use the data for $AR = 2$ as a sample. The effect of AR on the behavior of streamlines, and the velocity and pressure distributions is discussed in section 5.4. The effect of AR on the pressure loss coefficient is also described. The chapter closes by drawing major conclusions in section 5.5.

5.2. Streamline Calculation

The input data taken is in the form of a structured grid of velocity which corresponds to the location of the interrogation windows used for velocity vector calculation. The calculation of streamlines transforms the field into an unstructured, i.e. Lagrangian, form, It is therefore critical to obtain the correct transformation of the spatial coordinates when values from the gridded data are directly used in the calculation. However, it has to be expected that the calculated points along a streamline seldom coincide with grid nodes which calls for an interpolation step to be added [154][155].

The streamlines in the flow field are determined from the velocity data using the calculation scheme shown in Figure 30. This describes how the sets of s and n coordinates for each streamline are obtained by calculating the path of a particle from velocity and position data at each grid point. It is important to note that the streamlines and pathlines coincide for steady state flow conditions [47]. The input parameters to the calculation process are the x , and y coordinates of the gridded data and the corresponding velocity vectors components, \vec{v}_x and \vec{v}_y . A starting point (x_i, y_j) is specified as indicated on top left corner of Figure 30 at $i = j = 0$.

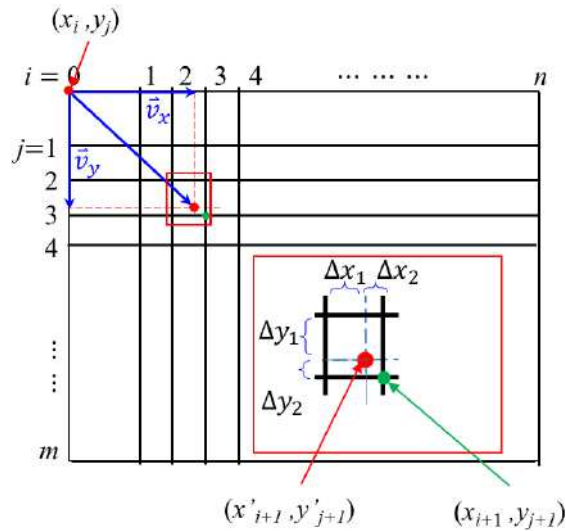


Figure 30 –A schematic showing basic features of the streamline calculation scheme developed.

The coordinates for subsequent points on the streamline (x'_{i+1}, y'_{j+1}) are then calculated as:

$$\begin{aligned} x'_{i+1} &= x_i + v_{x(x_i, y_j)} \times \Delta t \\ y'_{j+1} &= y_j + v_{y(x_i, y_j)} \times \Delta t \end{aligned} \quad (44)$$

where $v_{x(x_i, y_j)}$ and $v_{y(x_i, y_j)}$ are the velocity vectors at (i, j) , and Δt is the time between frames.

The distances Δx and Δy defined in the zoomed-in portion of the figure represent the case where the position of a calculated point along a streamline does not overlap with a grid point in the input data. This scenario indicates that an approximation step is necessary in order to obtain the position and velocity vectors to be used in the next step of the calculation sequence. The algorithm determines the closest node on the grid by selecting the minimum distances Δx and Δy . The coordinates required to calculate the next point on the streamline (x_{i+1}, y_{j+1}) are then obtained.

This process is repeated until all the points along a streamline are calculated.

Representative results from the streamline calculation are shown in Figure 31. The method allows direct control over specifying the number of streamlines to be calculated, their position and spacing in the flow field, and the number of points per streamline. Figure 31(a) demonstrates this capability by showing a plot of a single streamline initiating from a specified location ($y/b = 2$). This feature has significant benefits for an analysis approach that wishes to calculate parameters like the local

velocity and pressure along individual streamlines. It also permits the calculation of geometric parameters such as the radius of curvature and local angle of curvature [102]. The programming script which implemented the streamline calculation algorithm is written in a multi-paradigm computing environment (Matlab 2019, MathWorks). The full code is provided in section (iii) of Appendix B.

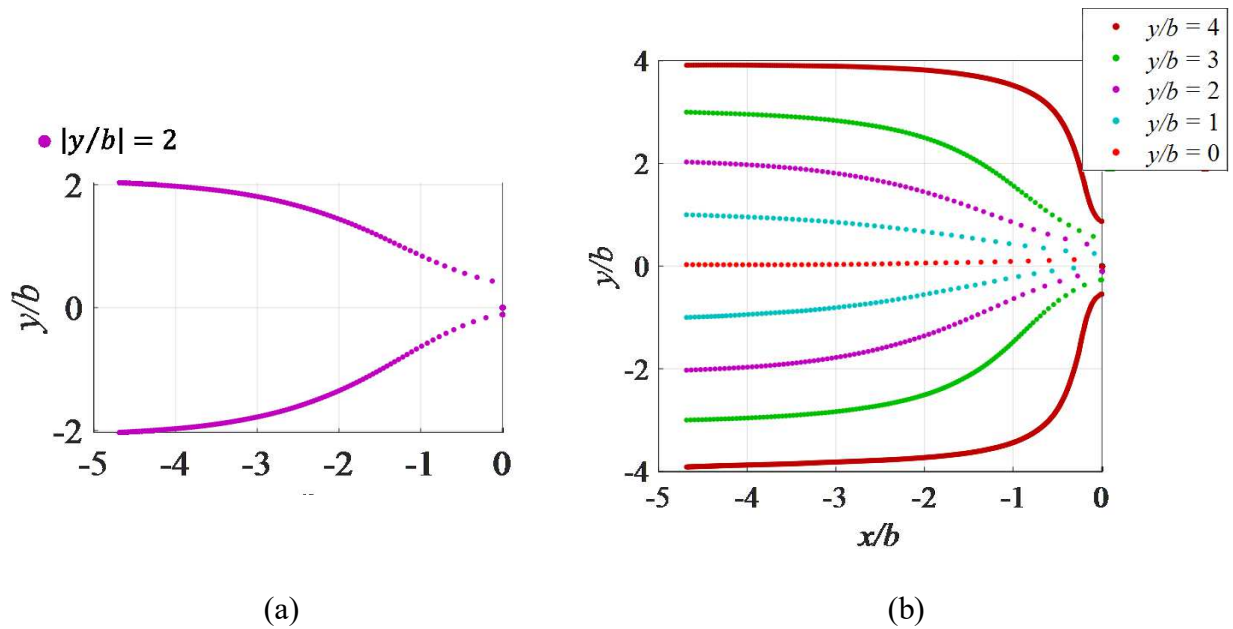


Figure 31 – Examples showing results from calculations for (a) an individual streamline at $y/b = 2$, and (b) multiple streamlines at specified y/b locations in the flow field. In Figure 31(b) it is shown that multiple locations can be simultaneously defined to define the respective starting points of the streamlines plotted across the flow field. Such plots allow the comparison of streamline curvature as a function of the position, y/b . The calculation scheme does not require specifying solid boundaries in the flow field. The presence of any confinement and/or obstacle in the flow field, however, can be clearly communicated through the shape of the calculated streamlines. The reduction in the number of parameters that have to be defined for the calculation of streamlines is also significant advantage here.

The curvature property of streamlines can be studied by calculating the local radius of curvature. As per the definition given in Figure 4 the radius is part of the parameters that are unique to all

points on a streamline. The radius, R_{ij} , corresponding to a point (x_i, y_j) along a streamline can be determined after defining the center of curvature C at (x_c, y_c) , such that:

$$R_{ij} = \sqrt{(x_i - x_c)^2 + (y_j - y_c)^2} \quad (45)$$

There is an inverse relationship between streamline curvature and the radius, where curvature is minimum for maximum R_{ij} and vice-versa. The relative distance between the center point, C , and a point on a streamline therefore determines the relationship between streamline curvature and the axial location which is extracted from the distribution of R_{ij} as a function of axial position.

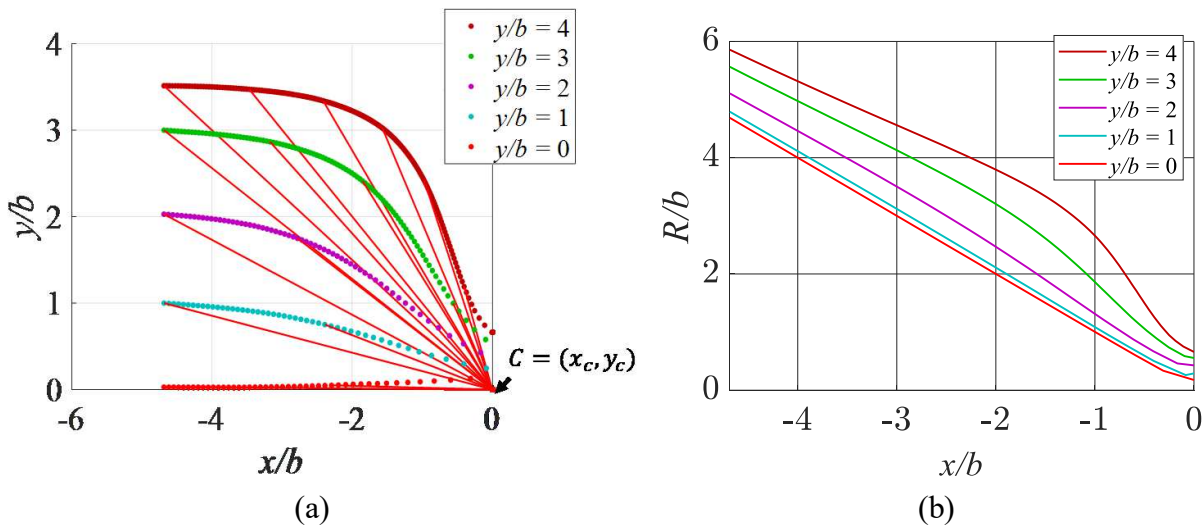


Figure 32 – Plots showing (a) the lines drawn from the center C to points along streamlines, (b) the calculated radii of curvature as a function of the streamwise coordinate x/b

Plots showing the calculation of the radii of curvature along the points on the streamlines are given in Figure 32. From Figure 32(a), it can be seen that the center, C , is selected to coincide with the origin defined at the inlet of the channel. The streamline curvature is plotted in Figure 32(b) as a function of position. It is clear from the curves that R_{ij} decreases with decreasing distance to the center, C .

It is implied that maximum curvature of streamlines occurs in the near-entrance region. Maximum values of R_{ij} upstream the orifice indicate minimum curvature in the region which correspond to

straight streamlines. The radii of curvature along the centerline remains at the maximum since the streamline along the central axis of has the minimum curvature.

The progression of streamline curvature in the direction of flow is determined by calculating the streamwise change in the angle, $d\theta$, according to the definition of the streamline coordinate system given in Figure 4. Figure 33 shows the change in angle $d\theta$ as a function of x/b for each streamline. The plots show that $d\theta$ starts to increase as the flow approaches the inlet and the streamlines start to converge. The constant increase in $d\theta$ reflects the continuous increase in the curvature in the convergence zone. The location where $d\theta$ is maximum indicates the inflection point which marks where the concavity of the curvature changes. Near the entrance, the curvature continues with $d\theta$ approaching zero as the streamlines return to become parallel.

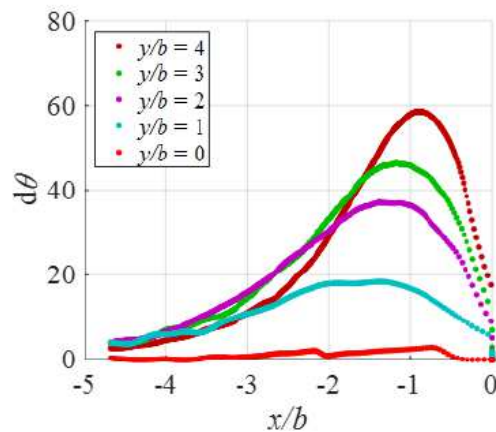


Figure 33 – The variation in the curvature angle $d\theta$ for orifice with $AR = 2$

5.3. Calculation of the pressure gradients

The streamwise and spanwise pressure gradients for each point along the streamlines, i.e.

$\frac{\partial p}{\partial s}$ and $\frac{\partial p}{\partial n}$, respectively, are calculated using the equations of motion in streamline coordinates

given in Eq. (6). The results plotted in Figure 34 show the gradients, $\frac{\partial p^*}{\partial s}$ and $\frac{\partial p^*}{\partial n}$, for the channel

with $AR = 2$. The pressure gradients are normalized by the maximum along the corresponding streamline.

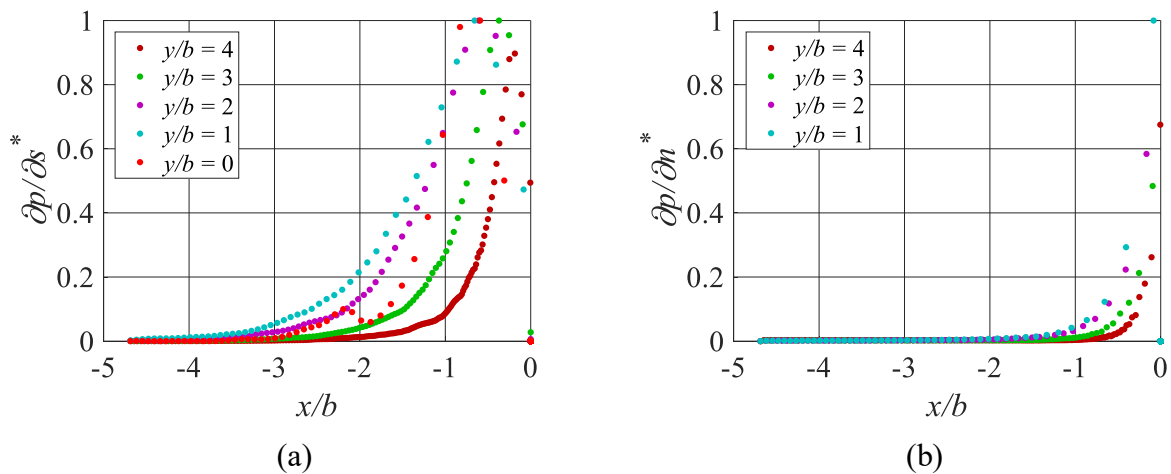


Figure 34 – Plots showing (a) $\frac{\partial p^*}{\partial s}$ and (b) $\frac{\partial p^*}{\partial n}$ along streamlines at the different locations from the centerline for $Re = 0.1$

The maximum pressure gradient in both the s and n directions generally occurs near the entrance. This meets the expectation since, along the streamwise direction, the flow velocity is significantly higher in near-entrance while, in the transverse direction, maximum pressure gradient in this region is caused by maximum streamline curvature. The trends in the plots shown in Figure 34(a) hence closely resemble the axial velocity transition profile along corresponding streamlines. From the location for the onset of velocity increase that can be seen from the curves, an estimate for the size of the convergence region can be obtained. The difference in the pressure distribution along the streamlines at different transverse locations can be seen from both plots provided in Figure 34.

The effect of streamline curvature on the pressure gradient in the n direction is seen in Figure 34(b) which shows maximum pressure gradient in the region of maximum curvature $-1 \leq x/b \leq 0$.

For the streamwise pressure gradient, the streamline closest to the center line begins its increase relatively farther upstream than the streamlines at other locations. The plots also reflect that, as the distance between the streamlines and the centerline increases, the velocity decreases which leads to an increase in pressure. In physical terms, this can be translated as the effect of the shear dominance at locations closer to the channel wall [57], [81].

5.4. Results and discussion

5.4.1 Streamline behavior

The streamlines for the different channels at a common Reynolds number of $Re = 0.1$ are shown in Figure 35(a) – (c). It should be noted that the field of view covered only the upstream region following the objective of investigating the convergence phenomenon in this near-entrance region. Accordingly, streamlines in the region $-5 \leq x/b \leq 0$ are shown for $AR = 1$ and 2 while for $AR = 3$, the region $-15 \leq x/b \leq 0$ is shown. A larger section is chosen for $AR = 3$ to include respective regions in the upstream section and in the orifice entrance.

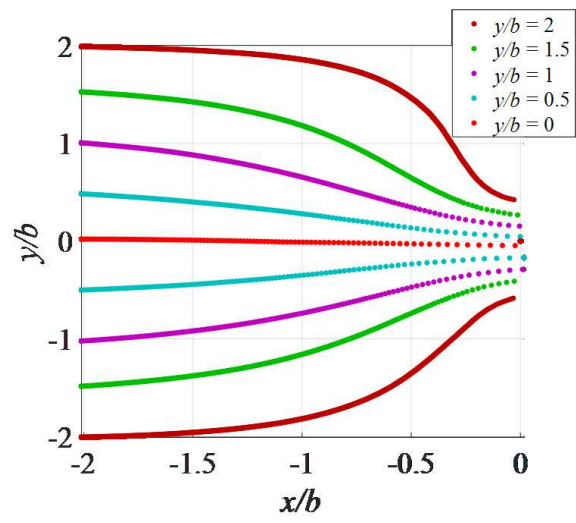
The locations in the transverse direction which were specified to plot the streamlines are also indicated. The locations were specified to cover the range of $-4 \leq y/b \leq 4$, $-3 \leq y/b \leq 3$, and $-5 \leq y/b \leq 5$ for $AR = 1, 2$ and 3 , respectively. The spacing between the streamlines is kept constant at a unit distance along the normalized position, y/b to assist the comparison.

It is apparent that the location where streamline curvature begins is different for the various aspect ratios. The results show that for $AR = 3$, the streamlines begin to curve at $x/b = -10$ whereas for $AR = 1$ and 2 the curvature started at $x/b = -1.5$ and $x/b = -3$, respectively. The extent of

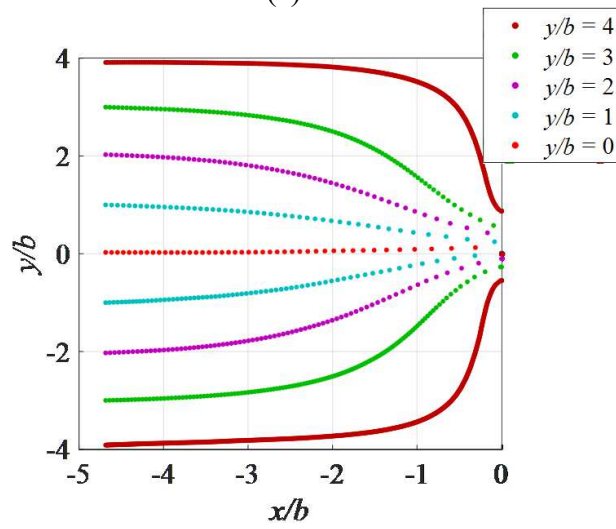
curvature increased at locations on the streamlines farther away from the centerline. The plots also show the symmetry about the central axis which follows expectations based on the nature of viscous flows in the creeping regime ($Re \leq 1$) [81].

The difference in the curvature undergone by the streamlines during convergence is compared by calculating the angle $d\theta$ defined in Figure 4(b). This parameter represents the local angle between the velocity vector at the corresponding point on a streamline and the horizontal axis. For straight streamlines, $d\theta$ will have a value close to zero while for increased convergence it will tend towards $\pm 90^\circ$ depending on the direction of curvature.

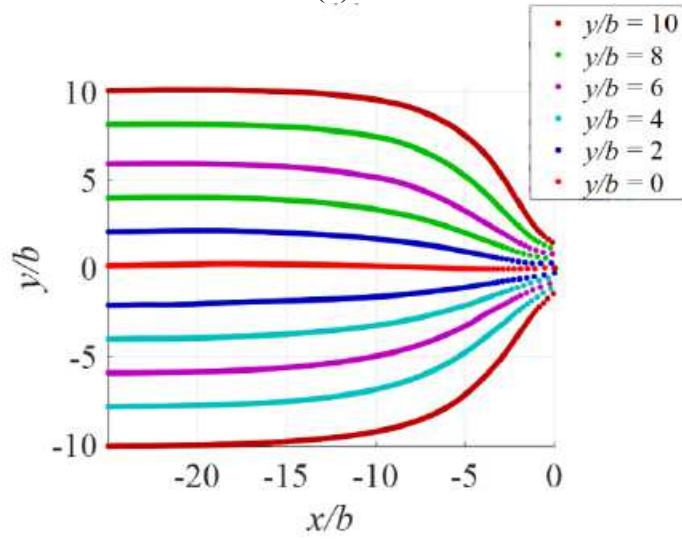
The plots in Figure 36(a) – (c) show values of $d\theta$ calculated for the corresponding streamlines shown in Figure 35(a) – (c). Significant increase in $d\theta$ is seen in the region $-2 \leq y/b \leq 0$ and $-4 \leq y/b \leq 0$ for $AR = 1$ and 2 , respectively. The region for $AR = 3$, however, covers the $-10 \leq x/b \leq 0$ extending further upstream. It is also implied that the streamlines undergo curvature for a larger non-dimensional distance as AR increased. The curvature phenomenon for the streamlines, however, covers the entire upstream region for lower AR . The center streamlines in all cases remained straight but with non-zero values of $d\theta$ which are ignored since it is to be expected that in actual flow conditions the center streamlines do not follow perfect straight line. It is also seen from the plots in Figure 36(a)–(c) that the maximum streamline curvature occurs for streamlines closer to the wall.



(a)

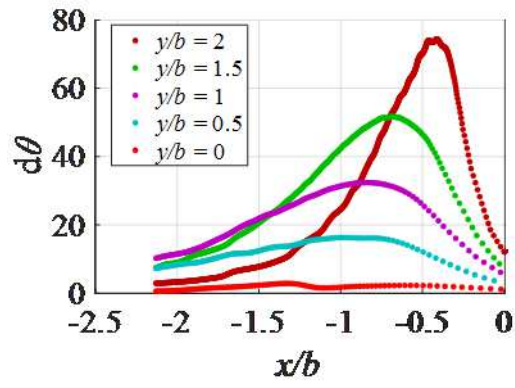


(b)

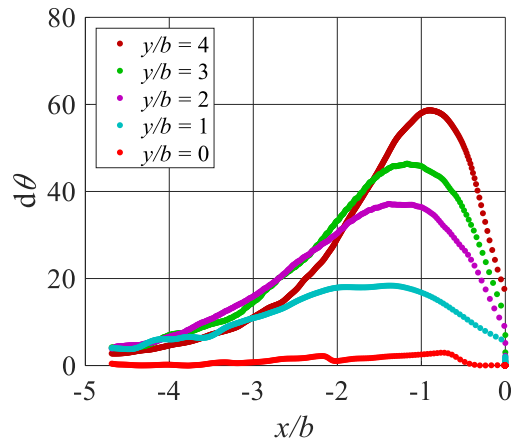


(c)

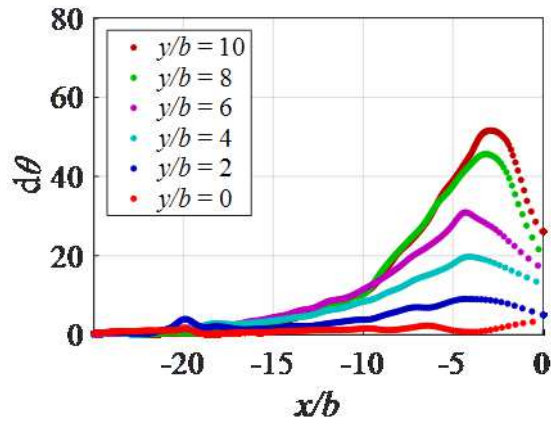
Figure 35 – calculated streamlines for channels of (a) $AR = 1$; (b) $AR = 2$; (c) $AR = 3$



(a)



(b)



(c)

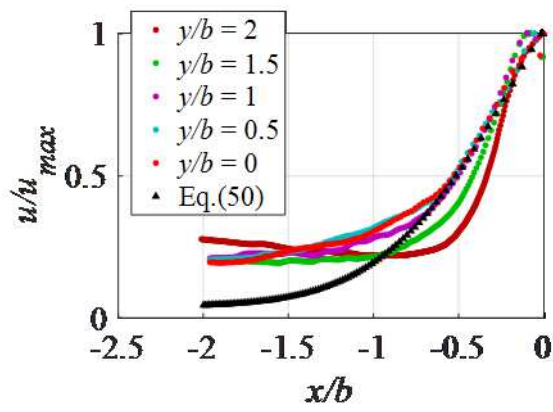
Figure 36 – The curvature angle $d\theta$ shown for (a) $AR = 1$; (b) $AR = 2$; and (c) $AR = 3$;

5.4.2 Velocity transition

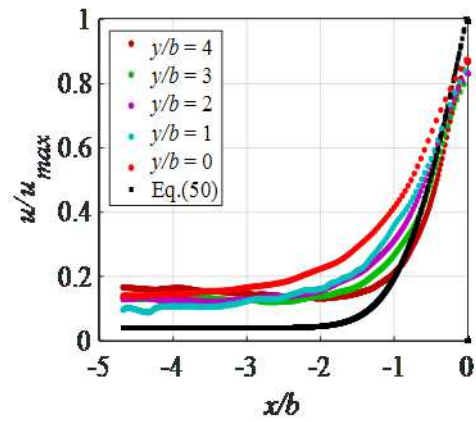
The axial velocity distributions respective to the streamlines are also compared with the analytical Gaussian model. Referring to Eq.(34), the value of the flow convergence factor, $\bar{\phi}_{Re}$, is estimated from least square fit which is shown in Figure 22. The results are shown in Figure 37(a)–(c) where the velocity distributions for individual streamlines are plotted. Figure 37(d) shows only the plots for the central streamlines for each AR . The velocity transition analytically determined as per Eq.(34) is included in each plot for comparison.

Within a flow channel, significant differences are seen between the axial velocity distributions along the streamlines at different y/b locations. Especially for $AR = 1$ and $AR = 2$, the plots in Figure 37(a) and (b) are relatively more spread out signifying this effect. For $AR = 3$, however, there is less difference in the axial velocity variation along the different streamlines. For fully developed flow, the parabolic profile of the velocity distribution in Newtonian flows suggests, it is expected that, at constant x/b , locations are farthest from the centerline, or closer to the wall of the upstream region, have the minimum velocity.

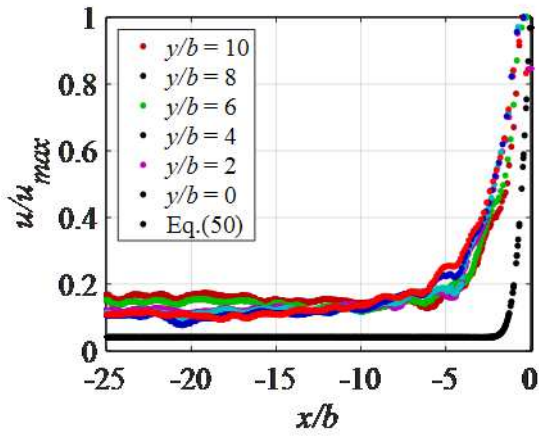
The effect of AR on the length of convergence is also observed from Figure 37(a)-(c). The plots for the lower AR in Figure 37(a) show that the flow reaches the orifice velocity in longer distance than the higher aspect ratio orifices. The plots given in Figure 37(b) and (c) can be compared to see that as AR increases the velocity transition takes shorter distance. Comparing the increase in velocity along the center streamlines for all the aspect ratios, Figure 37(d), shows the same effect where the maximum entrance distance taken is by the orifice of $AR = 1$ with $AR = 3$ taking the shortest entrance distance for the velocity transition. This provides a stronger validation than what is discussed in sub-section 4.3.3.2.



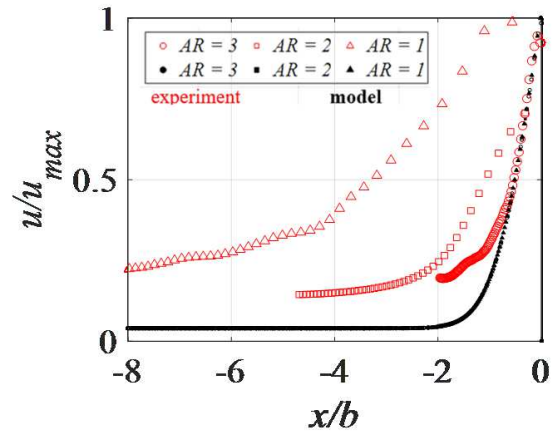
(a)



(b)



(c)



(d)

Figure 37 – axial velocity increase for channels of width, (a) $AR = 1$; (b) $AR = 2$; (c) $AR = 3$;

5.4.3 Pressure Loss characteristics

The pressure gradients in the s and n -coordinates are calculated for all the channels by applying the respective equations of motion as per the pressure calculation method described in Section 5.3. The plots are given in Figure 38(a)–(f) where the left and right columns, respectively, show the normalized streamwise and spanwise pressure gradients. The maximum pressure gradient along the corresponding streamline is used to normalize the pressure gradients. The plots can be used to compare the pressure loss characteristics in the flow field in localized as well as generalized perspectives.

From Figure 38(a)–(c) it is seen that the highest pressure loss always occurs along the central streamlines. These streamlines also have the maximum rate of change compared to the ones away from the centerline. It can be seen that the minimum pressure gradient occurs along the streamlines farther from the centerline. The higher the distance of a streamline from the centerline, the shorter distance it takes to reach the value at the inlet of the orifice.

The streamwise pressure gradients generally have their maximum increase in the region $-4 < x/b$ since this region is also where the flow has its maximum acceleration. However, like the velocity transition, higher AR leads to higher pressure gradient closer to the entrance of the orifice. This is attributed to the effect of the orifice width, b , rather than the aspect ratio. The dominance of this parameter on flow blockage has been seen in the previous chapter also in relation to its effect on the static pressure drop. The last column of Table 4 shows that lower orifice width also means lower area ratio, i.e. higher contraction, which leads to increased pressure drop.

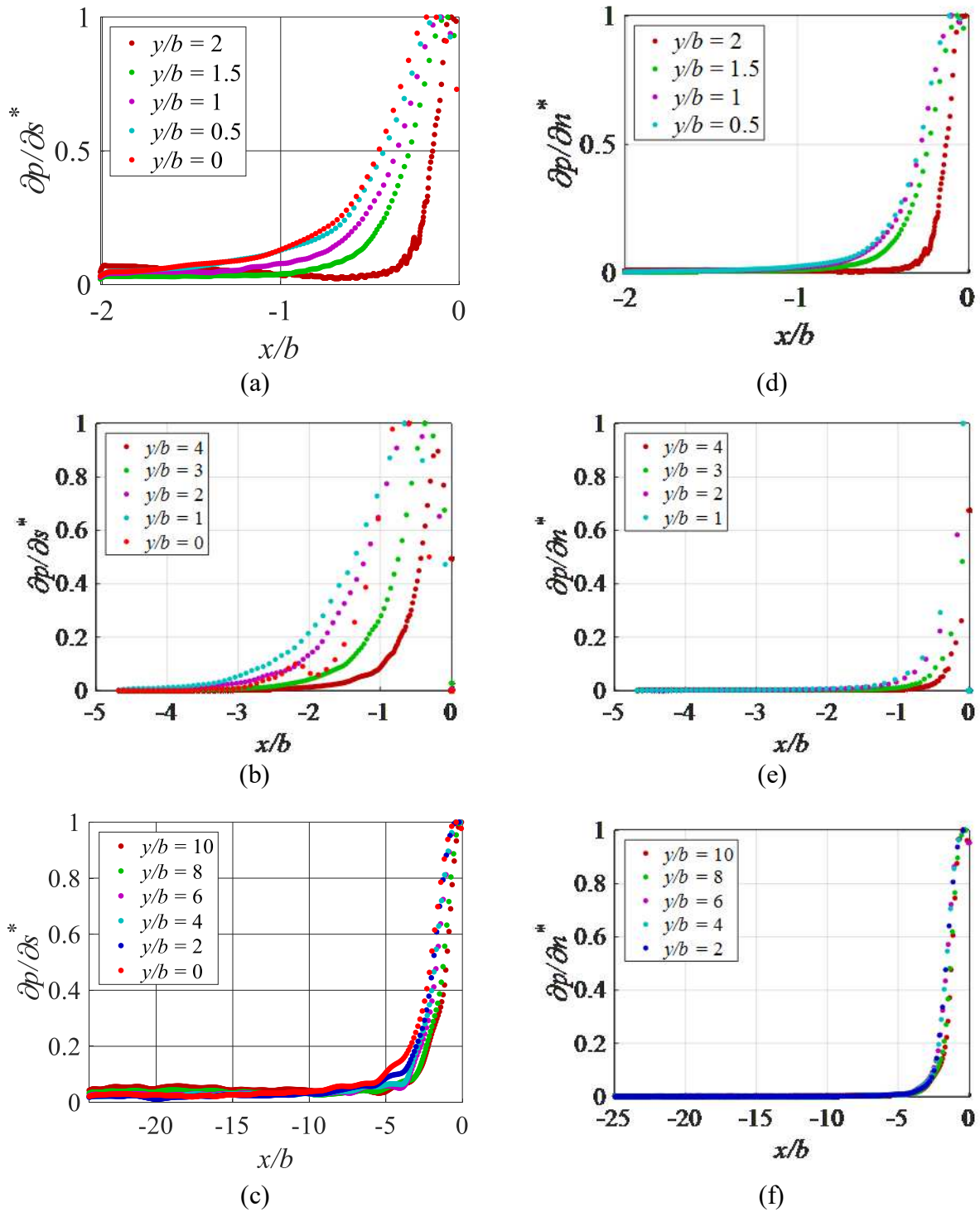


Figure 38 – Plots for normalized pressure gradient, (a)-(c) in the streamwise direction, $\frac{\partial p^*}{\partial s^*}$, and (d)-(f) in the span-wise direction, $\frac{\partial p^*}{\partial n^*}$, for (a),(d) $AR = 1$; (b),(e) $AR = 2$; and (c) (f) $AR = 3$.

The span wise pressure gradients shown in Figure 38(d)-(f) also describe the relationship established between streamline curvature and the pressure field in the literature review. The plots shown agree with the theory that the higher the curvature of the streamlines the higher the pressure gradient in the n direction. It can be seen that for all aspect ratios $AR = 1$ and $AR = 2$, the maximum span wise pressure gradients along all the plotted streamlines lies in the range $-1 < x/b < 0$ whereas for $AR = 3$ it covers $-2.5 < x/b < 0$. Comparing with the plots of streamlines given in Figure 35, it is seen that these regions are also where the streamlines undergo increased curvature.

The loss coefficient given in Eq.(35) is determined as a function of the axial distance taking advantage of point wise change in Reynolds number due to the axial change in the velocity. It is important to note here that the investigation and discussion in the development of the pressure loss coefficient model pertained to the velocity distribution along the centerline. The streamlines at $y/b = 0$ are therefore specified when plotting the loss coefficient, K . Initial estimates of, ϕ , are also fetched from the fits shown in Figure 22 to substitute in Eq.(35).

The plots showing the modeled loss coefficient as a function of x/b are given in Figure 39 for all aspect ratios. The trends show that the loss coefficient decreases as the flow approaches the entrance. In their corresponding upstream regions considered ($-\infty \leq x/b \leq 0$), the loss coefficient values range from $2.14 \times 10^5 \leq K \leq 4195$ for $AR = 1$, whereas for $AR = 2$ and 3 the ranges are $9.85 \times 10^4 \leq K \leq 1455$ and $1812 \leq K \leq 6.6$, respectively. The increase in the velocity in the flow convergence zone is considered the primary cause for the lower values of K at locations closer to the entrance of the channel. The behaviour of the streamwise and span-wise pressure distributions discussed above also support this relationship between the axial distance and the loss coefficient.

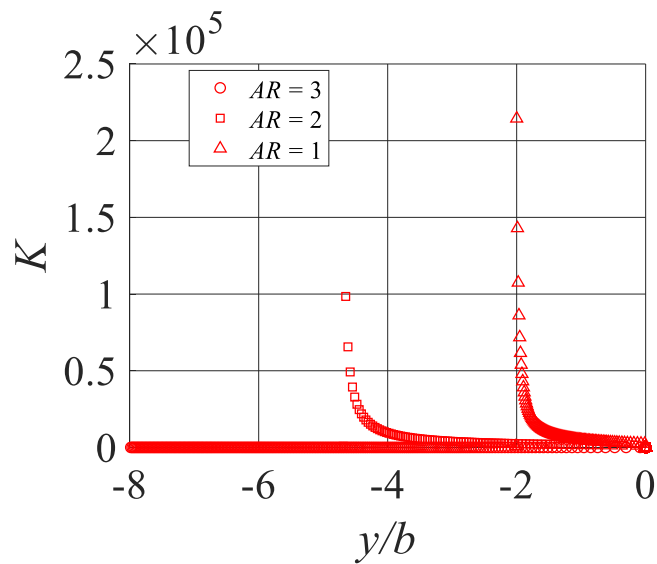


Figure 39 – The loss coefficient, K , calculated using Eq.(35) along the central streamlines for all aspect ratios for $Re = 0.1$

At all axial locations, as AR increased, the loss coefficient value decreased which also agrees with the hypothesis and the core discussion in Chapter 4. The difference in the streamline curvature phenomena in the $x - y$ plane is affected by AR which is varied by changing the width, b . The dominating effect from the width, b translates to the extent of contraction hence convergence. For lower AR the higher convergence causes the velocity transition to cover a larger distance than for higher AR as shown in Figure 37.

5.5. Conclusion

The flow convergence phenomenon in the flow through rectangular channels was investigated using a 2D measurement technique. The PIV experiments measured the velocity field in the flow domain which were used to calculate the streamlines. The variation in the parameter $d\theta$, which describes the local curvature per unit increment in streamwise distance was used to deduce about the curvature properties of the streamlines as a function of axial distance. In general, it was seen that the curvature of streamlines for the flow through the lower aspect ratio orifice occurs in a longer distance than for higher AR . Comparing the progression of flow convergence, it was

observed that the streamline curvature in the flow through the orifice with $AR = 1$ reaches maximum farther away from the inlet face. The streamlines in the case of $AR = 3$ orifice, however, have their maximum curvature at closer locations to the inlet of the orifice.

Compared to the flow domain in the configuration of the pressure measurement experiments, the flow channels in the velocimetry experiments exclude convergence in x - z plane because of the windows in the flow cell assemblies. Flow convergence thus occurring in the x - y plane has been a strong function of the width b of the orifice which is also used to normalize the position vectors. This dominance of b also aligns with the definition of the asymptotic velocity transition phenomenon given by Eq. (21) which normalizes the axial distance using the same dimension.

The pressure loss and velocity transition properties reflected the streamline curvature behavior. The comparison of the plots showed that the streamwise pressure gradient and the velocity transition reflect the same behaviours as the local angle of curvature. The resulting impact is a strong influence of AR of the rate of increase for both the velocity and the streamwise pressure gradient. The pressure gradient in the transverse direction was dominantly dictated by the curvature of streamlines as per the theory in streamline coordinate.

The pressure loss coefficient, K , calculated based on the developed relation also confirmed the effect of AR observed in Chapter 4 where higher AR led to lower value of K . This observation verifies the conclusion from the previous chapter in regards to the varying convergence phenomenon due to changing AR which result in the loss coefficient behaviour.

Chapter 6 A Pressure drop relation for the viscous flow through a rectangular orifice with a porous upstream region³

6.1. Introduction

For a coupled geometry consisting of a porous media and an orifice, approaches reviewed in the literature has shown that the pressure loss was determined by first writing the loss models for each domain separately [34], [44], [117]. Taking the sum of the corresponding losses have typically yielded the flow rate, Q , as a function of the pressure drop, ΔP , in the form of a quadratic equation. The respective coefficients in these models represented effects from the porous media and the inertia of the flow [117], [128].

To further analyse the interface phenomena and account for their effects, the modeling becomes much more complex and a system of partial differential equations needs to be solved [34], [42]. A system of differential equations containing conservation laws and constitutive equations for the Darcy- and Navier-Stokes regions describes the loss characteristics in the domain. The so-called Navier-Stokes (or non-Darcy) regions may represent free stream of fluid, an open space of exit [34], [42], or an orifice [44], [117]. The capacity of such models to predict the losses have been verified through comparisons with results from numerical simulations of the same flow domains [117], and experiments [117], [128].

Given the flow configuration in the SAGD process investigated in this study, modeling at the interfacial level is of less interest than relating the volumetric flow rate with the pressure loss at for the flow through the rectangular orifice. Fortunately, the pressure loss characteristics and

³ A version of this chapter has been published as:
Yusuf Y., Kinsale L., Ansari S., Nobes D. S. (2019) “The convergent path of streamlines for the flow approaching a rectangular orifice through a porous region” *Proceedings of the 4th Thermal and Fluids Engineering Conference (TFEC)*, April 14–17, 2019, Las Vegas, NV, USA;

streamline properties which have been covered in the previous chapters lay a solid foundation to begin accounting for effects from porous media. The model given in Eq. (28) is applied to write the loss through the rectangular orifice whereas Darcy's law is used as the model for the loss through the porous region.

Experiments have been undertaken measure the pressure drop across the coupled domain for three different aspect ratios using the same facility described in Figure 6. The results are compared with the loss predicted analytically using the derived model. Using Eq. (28) to represent the loss through the rectangular orifice allowed the parameter, ϕ , to be kept maintaining quantitative representation of the role of flow convergence. The behaviour of streamlines in a coupled media is also highlighted for a single case of AR for varying Reynolds numbers to better visualize the convergence phenomenon.

The derivation of the pressure drop relation in the coupled media is presented in the following section. The methods followed to analyse experimental data are described in Sections 6.2 and Section 6.3 discusses the results. Section 6.4 closes the chapter by stating the major conclusions drawn.

6.2. Pressure loss model for flow through the coupled media

In this study, the total pressure loss through the coupled media, ΔP_c , is taken as the sum of the losses due to the porous medium, ΔP_{pm} , and the orifice, ΔP_o , i.e. Eq. (11). The first step taken in deriving ΔP_c is thus to re-write Eq. (28) so as to express the loss through the rectangular orifice as a function of the volume flow Q . It enables to maintain the same form as Eq. (9) for the loss through porous media. Eq.(28) can be re-written by using substitution to transform the velocity term into the volumetric flow rate, Q . The resulting equation can be rearranged to give the quadratic equation in terms of Q such that:

$$\left(\frac{1}{A_o^2} - \frac{1}{A_{pipe}^2}\right)Q^2 + \left[\frac{4\phi}{\sqrt{\pi} \cdot \rho D_h}\right] \left[\frac{2AR}{AR+1}\right] \left(\frac{1}{A_o} - \frac{1}{A_{pipe}}\right)Q - \frac{2\Delta P_o}{\rho} = 0 \quad (46)$$

where A_o and A_{pipe} are the area of the orifice and the pipe, respectively. The loss through the bed of porous media placed in the upstream section of the pipe can be given as:

$$\frac{B}{gA_{pipe}^2}Q^2 + \frac{A}{\rho g A_{pipe}}Q - \frac{\Delta P_{pm}}{L} = 0 \quad (47)$$

where A and B are the hydraulic and inertial resistance coefficients, respectively, as definitions given by Eq. (10) in Section 2.4. The above two equations can be rearranged to express the corresponding pressure drop terms so that the total pressure loss through the coupled media can be found from the summation:

$$\begin{aligned} \Delta P_c &= \Delta P_o + \Delta P_{pm} \\ \Delta P_o &= \left(\frac{1}{A_o^2} - \frac{1}{A_{pipe}^2}\right) \frac{\rho Q^2}{2} + \left[\frac{4\phi}{\sqrt{\pi} \cdot D_h}\right] \left[\frac{AR}{AR+1}\right] \left(\frac{1}{A_o} - \frac{1}{A_{pipe}}\right)Q \\ \Delta P_{pm} &= \frac{B}{gA_{pipe}^2}LQ^2 + \frac{A}{\rho g A_{pipe}}LQ \end{aligned} \quad (48)$$

where the subscripts c , o , and pm signify the pressure loss as due to the coupled media, the orifice, or the porous media, respectively. The resulting final expression for the loss through the coupled domain thus becomes:

$$\Delta P_c = \left[\frac{B}{gA_{pipe}^2}L + \frac{\rho}{2}\left(\frac{1}{A_o^2} - \frac{1}{A_{pipe}^2}\right)\right]Q^2 + \left[\frac{A}{\rho g A_{pipe}}L + \left(\frac{4\phi}{\sqrt{\pi} \cdot D_h}\right)\left(\frac{AR}{AR+1}\right)\left(\frac{1}{A_o} - \frac{1}{A_{pipe}}\right)\right]Q \quad (49)$$

It can be recognized that this is a quadratic equation describing the pressure loss through the coupled media as a function of the volumetric flow rate. Exact solutions for Q can be sought by applying the quadratic formula to Eq. (49) which can be generically written as:

$$c_1 Q^2 + c_2 Q + c_3 = 0$$

where,

$$c_1 = \left[\frac{B}{gA_{pipe}^2} L + \frac{\rho}{2} \left(\frac{1}{A_o^2} - \frac{1}{A_{pipe}^2} \right) \right] \quad (50)$$

$$c_2 = \left[\frac{A}{\rho g A_{pipe}} L + \left(\frac{4\phi}{\sqrt{\pi} \cdot D_h} \right) \left(\frac{AR}{AR + 1} \right) \left(\frac{1}{A_o} - \frac{1}{A_{pipe}} \right) \right]$$

$$c_3 = -\Delta P_c$$

The relative significance of each term can be determined by evaluating the ratio $c_2^2/(-4c_1c_3)$ [117]. The quadratic term can be ignored for higher values of the ratio (typically >5 [117]) resulting in $Q = -(c_3/c_2)$. In physical terms, this case represents the scenario where the viscous resistance of the porous bed, represented by A in the coefficient c_2 , is much higher than its inertial resistance, B in c_1 . A linear relationship between the flow rate and the pressure loss also implies that the driving pressure gradient is low enough which leads to low velocities everywhere in the field. The pressure loss in this case can be represented by writing Darcy's law alone [33], [117].

The square function $Q^2 = c_3/c_1$ is taken as the solution when the value of the ratio is low (typically $< 10^{-3}$ [117]). In this case, inertial phenomena are dominating in the flow field contributing to approximately all the losses. This results if the driving pressure difference is high enough and the porous media properties, mainly its porosity and size and geometry of the particles, lead to flow acceleration, fluidization, and/or other inertia-dominated phenomena [117], [125].

The pressure drop across the coupled domain is plotted as a function of the volume flow rate in Figure 40 for the three aspect ratios considered. The porosity of the porous media has been maintained at 40% which resulted in the values for Ergun's coefficient, $A = 1.2 \times 10^6$ and $B = 69.7$. The dominance of the linear part of the relation which corresponds to the coefficient A is clearly seen from the figure. Comparing the plots for each AR shows that higher AR leads to

higher ΔP across the domain. This relationship is attributed to increasing flow blockage effects at higher AR which leads to higher acceleration and increased pressure loss in the system. This observation also agrees with what is found in literature where smaller diameters led to higher pressure drop for different porous media properties [116], [117].

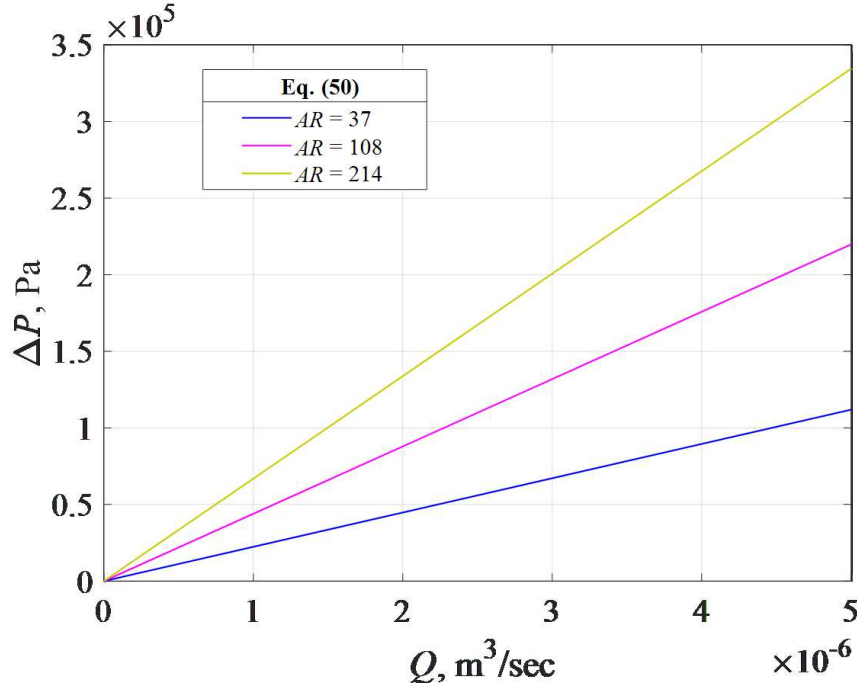


Figure 40 – ΔP as a function of Q plotted based on the developed relation given in Eq. (49). Even though this study maintained the quadratic term in Eq. (49), the plots show a linear relationship between the flow rate and pressure drop for all AR . The physical interpretation of this observation suggests that the pressure loss characteristics in the coupled domain are still affected by convergence effects in the presence of the porous media. Considering the surface properties of the glass beads used as the porous media particles, the coefficient of viscous resistance, A , may also be expected to play less role than B in determining the pressure drop across the media. In that case, the dominating role of flow convergence is reflected in the coefficient c_2 given in Eq. (50) which closely resembles the loss coefficient model expression developed for the open slot scenario.

The linear $\Delta P - Q$ relationship also leads to less pronounced effect from the porous bed as the pressure loss is mainly due to the effect of the orifice which relates to the near-entrance convergence phenomenon. The role of this dominating loss from the orifice can also be inferred from the terms accounting for its contribution. The presence of the flow convergence parameter, ϕ , along with the hydraulic diameter, D_h , and aspect ratio, AR in the coefficient of the linear term, strongly indicates minimal effects to be seen from the inclusion of the porous bed to the open slot scenario.

6.3. Results and discussion

6.3.1 Pressure loss characteristics in the coupled flow domain

The results from pressure drop measurement experiments for the coupled domain are given in Figure 41. The figure also compares the experimental results with those predicted using Eq. (49). The comparison instantly shows that the measured relationship between the pressure drop and the flow rate followed a quadratic-like behavior. There are also discernible deviations between the predicted values and the measured values for all aspect ratios.

The deviation, however, increased as AR increased with the maximum observed difference of 30% for $AR = 214$. The predicted pressure drop for $AR = 37$, were different from the measured by 25% difference. The minimum deviation was for the orifice having $AR = 108$ which was 12%.

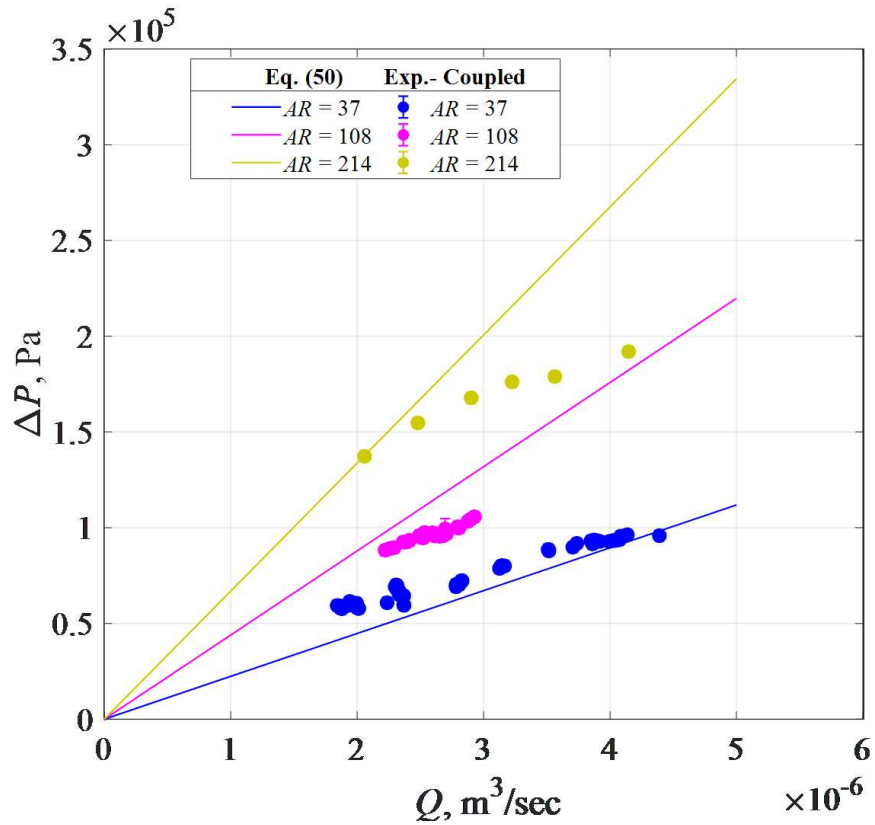


Figure 41 – The change in ΔP as a function of Q plotted using the developed relation given in Eq. (49) and data from experiment

The plot of ΔP measured for the flow through the open slot and the coupled scenarios are compared in Figure 42. The figure also includes plots for the ΔP – Q relationship given by the developed expression given in Eq. (49). In both cases, an increase in AR led to a significant increase in the pressure drop. The plots show that the porous media and the orifice subdomains had different contributions to the overall pressure drop in the system. The results indicate that the rectangular orifice had much larger contribution than the porous region. This observation comes in line with expectations based on the effect of porous media particles having smooth surfaces such as the glass beads used in the experiments [117].

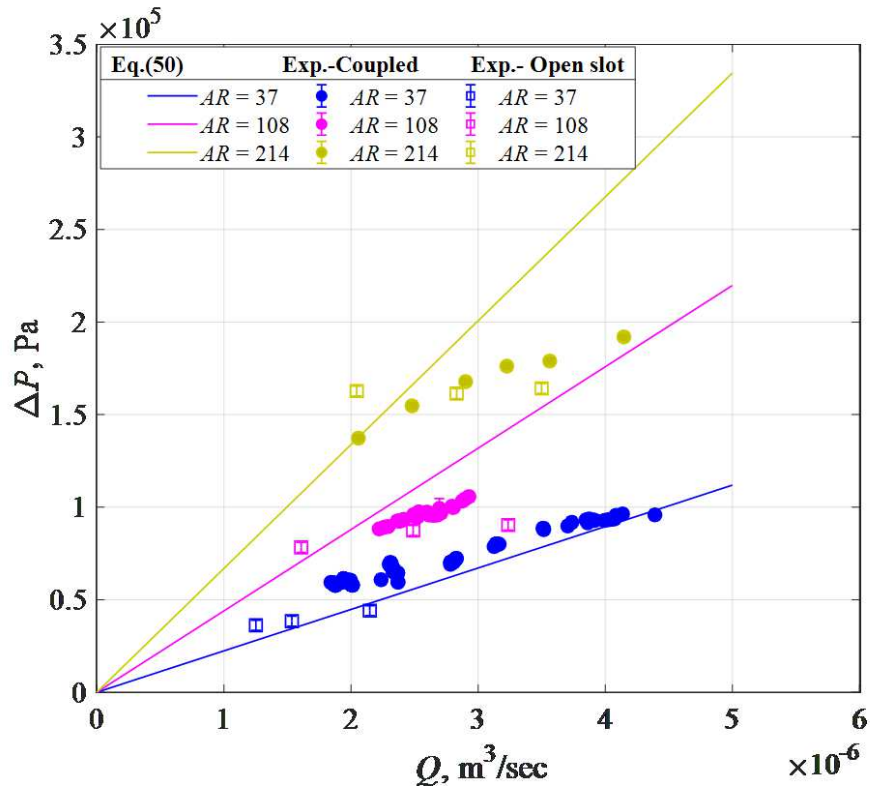
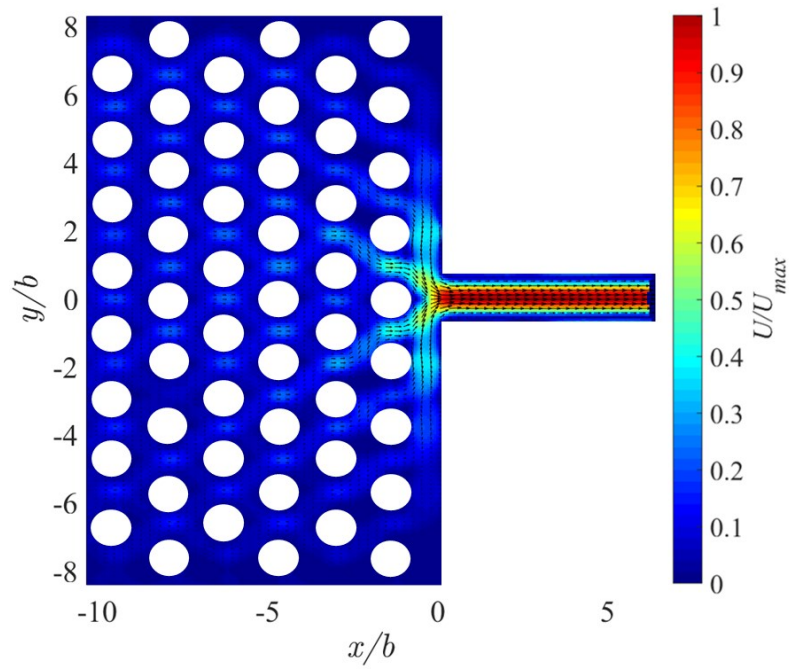


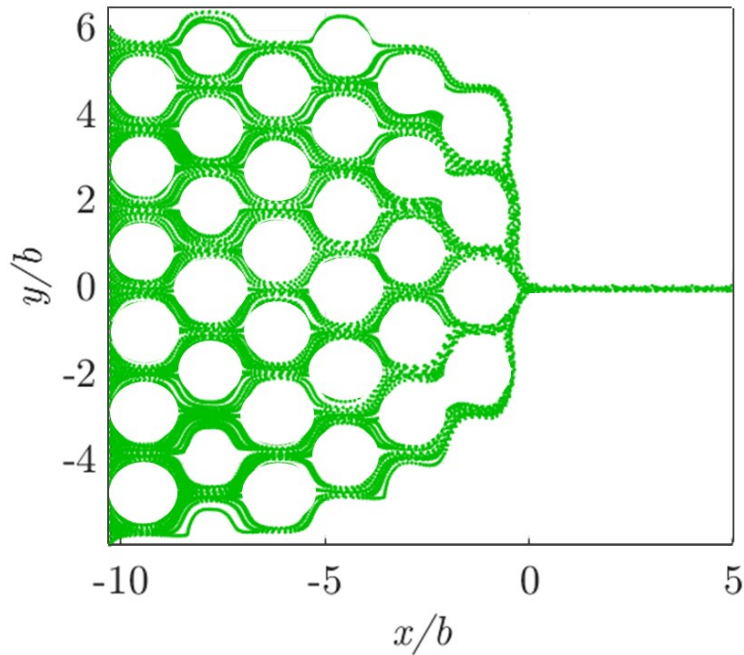
Figure 42 – The change in ΔP as a function of Q plotted using the developed relation given in Eq. (49) and data from experiment

6.3.2 Streamlines

PIV experiments were also used to investigate the flow which includes the upstream tortuous path. The velocity field and the behavior of the streamlines in the flow through an orifice with $AR = 3$ was studied. The upstream region of the flow channel assemble consisted of an arrangement of circular pillars representative of a pore-matrix (Figure 17). The diameter of the pillars was 1 mm with 1.5 mm of spacing between centers of adjacent pillars. The arrangement resulted in a region with porosity of 0.4 while the rectangular orifice had a width of 1 mm. The size of the field of view to cover the region of interest in the experiments was $15 b \times 12 b$.



(a)



(b)

Figure 43 – Streamlines in the pore matrix generated using data from PIV measurement of the flow through porous media

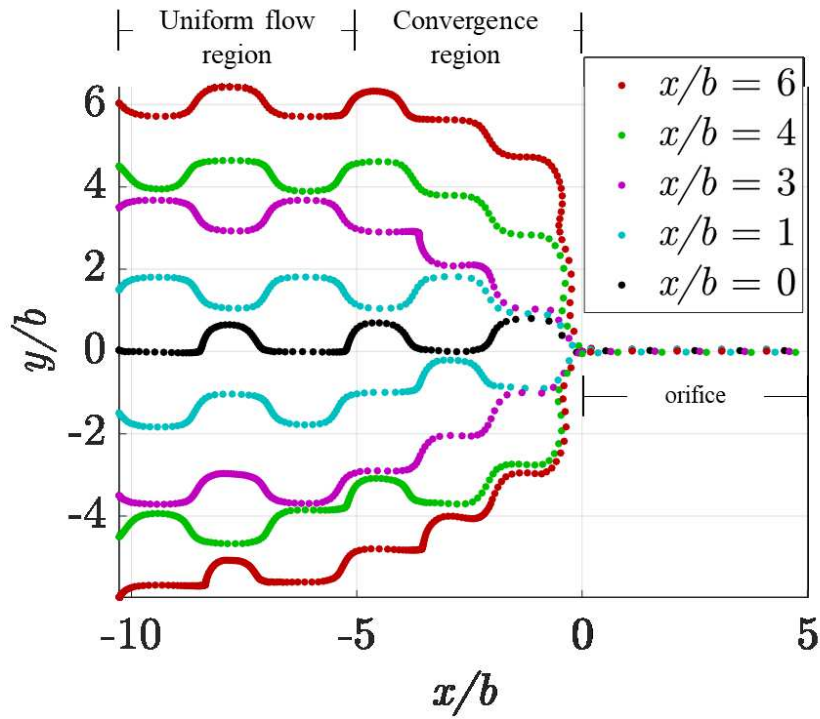
The streamlines through the porous network were calculated by using the same approach described in Section 5.2. The goal was to determine the different tortuosity phenomenon at different locations

in the flow field to identify their effect on streamline curvature, hence the pressure loss. Based on the relationship between tortuosity and the permeability coefficient as per Eq. (12), it can be expected that as the tortuosity increases the pressure drop also increases. Similar trend of the pressure gradient in the transverse direction might be expected due to the location of the orifice relative to the channel walls.

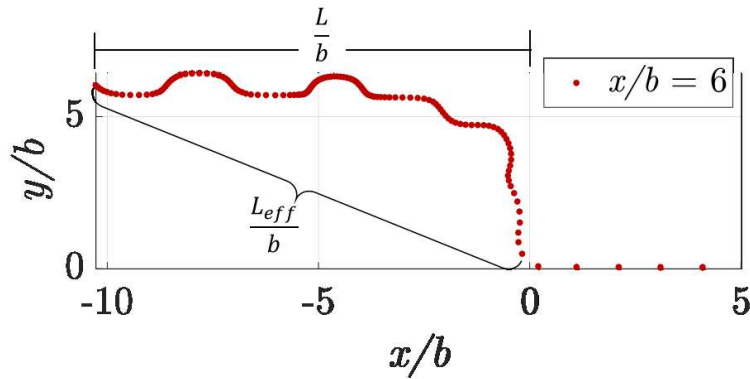
The results from the velocity field measurement are given in Figure 43. Figure 43(a) shows the colormap of the velocity field processed using 500 images and an interrogation window size of $128 \text{ pixel} \times 128 \text{ pixel}$. In Figure 43(b) the tortuous path of the fluid particles can be seen from the streamlines calculated.

From Figure 43(a), the theoretical behavior of the flow is confirmed following the velocity distribution depicted by the color map. It can be seen that the velocity goes through local maxima as the flow passes through the pore throats. The local decrease in the cross sectional area leads to the velocity to increase in the pore spaces where inertial effects dominate. The figure also gives a macroscopic view of the flow convergence phenomenon as the flow approaches the orifice inlet. The transition of the flow velocity as it increases to reach its global maximum at the inlet of the orifice is also observed [26].

The spatial distribution of the flow can be inferred from the streamlines in Figure 43(b). The region far upstream is characterized by parallel streamlines leading to a uniform velocity distribution in the y direction. As the flow enters the pore space between the particles, a localized flow acceleration and streamline curvature is seen. Because of the low Reynolds number in this region local curvature effects do not lead to any significant pressure gradient affecting the overall flow distribution. After the flow enters the convergence zone, however, the velocity increase becomes high enough resulting in prevailing streamline curvature in this region.



(a)



(b)

Figure 44 – Plots showing (a) streamlines at specified location in the flow field; and (b) the calculation of tortuosity demonstrated by the streamline at $y/b =$

One of the advantages of the implemented streamlines calculation method is that, for porous media experiments, it enabled the tortuosity to be calculated for any path in the flow field. This application is demonstrated in Figure 44 which shows the tortuous path in the porous originating from specified distances from the centerline of the domain. The elongation of the path taken by the fluid is evident from the streamlines in Figure 44(a). The streamlines also indicate the locations where they are parallel which is mostly the region $x/b \leq -5$ in the experimented case. The

relationship here is also seen for streamlines passing through adjacent pore spaces especially in the uniform flow zone.

As x/b increases, the tortuosity also increased since the fluid has to travel longer distance to enter the orifice. The definition of the non-dimensional length parameters required for the calculation of tortuosity is given in Figure 44(b). The tortuous distance L_{eff} is found by calculating the arc length of the streamline [119], [120], [123]. The tortuosity is then calculated by taking the ratio of the calculated distance to the constant straight line-length of L .

The tortuosity can then be used to calculate the pressure drop along the flow direction. If Darcy's relation in streamline coordinates, Eq. (8) in Section 2.4, is used, the viscous resistance coefficient, A , is determined using Ergun's relation given in Eq. (10). Alternatively, the Kozeny-Carman relation, Eq. (13), can be applied to calculate the permeability coefficient, κ , followed by Darcy's law to determine ΔP . It is important to note here that using the latter approach requires an averaged value of the tortuosity to be used which also leads to obtain a corresponding average ΔP across the flow field [119].

Calculating the pressure gradient along the streamlines, however, is relatively straight-forward. The results from calculating the pressure along the streamline calculated from PIV experiments is shown in Figure 45. Ergun's coefficient, A , determined using the porous media properties remains constant for all streamlines at the different y/b locations. It can be seen from Figure 45 that higher tortuosity leads to higher pressure gradient agreeing with expectations based on theory [119].

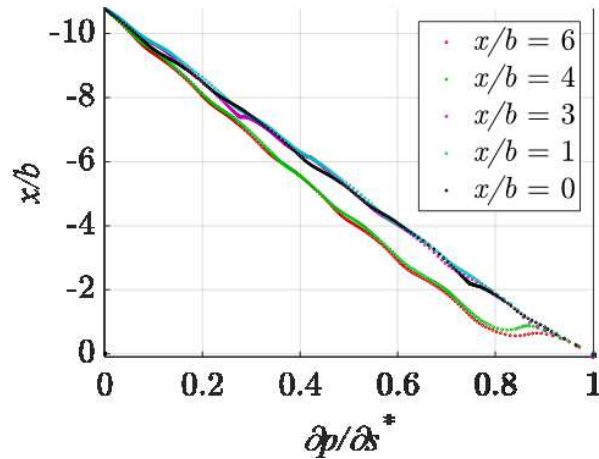


Figure 45 – Plots showing the streamwise pressure gradient $\partial p/\partial s$ calculated along the corresponding streamlines as per Eq. (8)

The varying slopes of the dp/ds curves show higher slopes for the streamlines farther from the centerline which indicate the increased rate of the pressure gradient. The result indicate the influence from tortuosity on the streamwise pressure gradient. This relationship also implies that higher pressure losses can be expected in regions with higher streamline curvatures which lead to higher elongation of the path due to tortuosity.

6.4. Conclusion

The pressure measurement experiments conducted for the coupled flow scenario automatically confirm the flow blockage effects which is shown by higher ΔP for higher AR . The additional effects from flow convergence could not be directly affirmed by the pressure measurement results. The solution of the quadratic equation, however, strongly indicates the significant role of the flow convergence through the maintained flow convergence factor, ϕ , in the final $\Delta P-Q$ function. The dominance of the convergence properties vis-à-vis streamline curvature also signify the importance of tortuosity in determining the pressure drop through the coupled system.

Based on the discussion the thesis so far, it is expected that the tortuosity is directly affected by the change in AR due to its effect on the relative distances travelled by the fluid to enter the orifice.

Lower AR will hence lead to increased tortuosity to the higher elongation of the flow path leading to the inlet. The streamlines calculated using the data from the PIV experiments for the flow through the coupled media also visualize this effect.

The streamline calculation introduced in Section 5.2 was applied to determine the tortuous path through the pore matrix as the flow approached the orifice. The corresponding streamwise pressure gradients determined from theory. The result showed that the pressure gradient is highly affected by the tortuosity factor in the flow field. The pressure loss along streamlines at the different transverse locations was compared and it was seen that the farther a streamline is from the centerline, the higher the streamwise pressure gradient due to higher tortuosity.

Chapter 7 Conclusions and Recommendations

7.1. Conclusions

The research has presented a loss coefficient model which is developed based on the 1D Navier-Stokes equation and a unique Gaussian distribution of velocity as the constitutive equation to represent the velocity transition behavior in the flow convergence. It has been shown that the length of this convergence zone is affected by the aspect ratio of the rectangular orifice. The orifice aspect ratio also affects the nature of the 2-D convergence phenomenon since the extent and location of streamline curvature is directly affected.

The developed model describes a non-dimensional pressure loss coefficient as a function of the flow Reynolds number in the creeping regime $0.01 \leq Re \leq 0.1$. The definition of the convergence parameter, ϕ , has been incorporated to the velocity transition model. This parameter plays a significant role in determining the axial distribution of the velocity in the convergence zone. Being a strong function of AR itself, ϕ , describes how much farther or closer the velocity transition begins as the flow accelerates to enter the orifice.

The pressure loss coefficient, K increases as AR decreases reflecting the idea of dominating contribution from upstream 2-D effects for low AR orifices. Experiments measured the static pressure loss, ΔP , and the calculated the pressure loss coefficient, K , to verify the model. Experiments showed that as AR increased, ΔP also increased which is attributed to flow blockage effects. An increase in Re leads to an increase in ΔP due to increasing inertia of the flow which has to be balanced by a drop in the static pressure..

An angular deviation from the model data was seen in the experimental results. This deviation is attributed to the strong 1D nature of both the experimentation and modeling techniques whereas

the convergence phenomenon ϕ is naturally 2D. The investigation led to remediating the deviation by applying the factor rotation method.

The model used was also verified by plotting the velocity transition curves showing the gradient in the convergence zone as a function of AR and Re . It has thereby been shown that ϕ from experiment can be used to describe not only the axial velocity gradient in the near inlet region but also the relative length of the convergence region. The flow convergence phenomenon was also studied using a velocimetry experiments. PIV experiments were used to measure the velocity distribution from which the streamlines in the flow field were determined.

The flow convergence occurring in the x - y plane was studied using the PIV results showing the effect of the AR by changing the width b of the rectangular orifice. Aligning with the definition of the asymptotic velocity transition phenomenon given by Eq. (21), b , was used to normalize the dimensions in the flow domain. The results showed that streamwise velocity transition and pressure loss behaviors followed the curvature properties. This resulted in varying pressure gradient and velocity transition trends among streamlines as a function of the distance or their origins from the center line.

The upstream convergence region for lower AR is larger than that for lower AR . The increased distance of velocity transition is also reflected in the higher rate of the increase of the streamwise pressure gradient. The centerline streamline in all channels has the highest rate of increase in streamwise pressure loss and zero pressure gradient in the transverse direction. The relationship between the loss coefficient and AR presented in the model developed in Chapter 4 is also confirmed by the PIV experiments confirming that higher convergence in lower AR orifices leading to higher loss coefficient, K .

The pressure measurement experiments conducted for the coupled media showed that ΔP increased as AR increases due to flow blockage effects. The dominant effects from flow convergence is representing by a dominant linear term containing ϕ in the quadratic equation for the coupled system. The strong influence from flow convergence vis-à-vis streamline curvature signify the importance of tortuosity in determining the pressure drop through the coupled system.

PIV experiments were conducted to measure the velocity field through the coupled media to determine the tortuous path of the flow using the streamline calculation method developed in Section 5.2. By calculating the pressure gradient along the tortuous path through the pore matrix, it was shown that as the maximum rate of the pressure gradient occurs along the streamline with maximum tortuosity, i.e. maximum distance from the centerline.

7.2. Recommendations

The direction of future research related to the topics covered in this thesis can be oriented towards strengthening the work in the realms of the SAGD process, and the fundamental knowledge regarding flow through rectangular orifices. In the SAGD scope, future works may aim at investigating the application of the developed model in the design of orifices found on slotted liners and other components of downhole tooling. Researchers who look to solve the issue of slot failure by modifying the slot geometry, such as its aspect ratio might also test the performance of the model and its suitability when incorporated in the package of solution tools used at present.

The refinement of the analytical model presented in Chapter 4 may also be considered in future works. Representation of the velocity transition model using the skew-Normal distribution can be pursued to bring the model even closer to the physics by accounting for the effect of hydraulic entrance length. Further enhancement to encompass the coupled flow domain might also be considered by using the multivariate skew-Normal model. It is anticipated that this would allow

the proper inclusion of an additional parameter in the velocity transition model that would account for the tortuosity undergone by the flow as highlighted in Chapter 6.

The optical diagnosis part of the research has the potential to allow the investigation of additional parameters and conditions. For instance, the experimentation and analysis can be enhanced to investigate the effects from interactions between orifices in the presence of adjacent orifices [112]. The effect of neighboring orifices on the convergence phenomenon can be studied in the linear and radial arrangement of the orifices. The study of the radial flow configuration requires the analysis and discussion in Chapter 5 to move into the cylindrical coordinate system which has the potential to produce a new model for the flow configuration. Studying the effect of having the upstream tortuous path can also be advanced by using actual particles than the mimic cylindrical pillars presented in Section 3.3. The particles must be of a transparent material the refractive index of which is matched with the working fluid.

References

- [1] C. Shen, “SAGD for Heavy Oil Recovery,” in *Enhanced Oil Recovery Field Case Studies*, First Edit., J. J. Sheng, Ed. Waltham: Gulf Professional Publishing, 2013, pp. 413–445.
- [2] J. M. Dealy, “Rheological properties of oil sand bitumens,” *Can. J. Chem. Eng.*, vol. 57, no. 6, pp. 677–683, 1979.
- [3] J. Sharma and I. D. Gates, “Multiphase flow at the edge of a steam chamber,” *Can. J. Chem. Eng.*, vol. 88, no. 3, pp. 312–321, 2010.
- [4] S. Ansari, R. Sabbagh, Y. Yusuf, and D. S. Nobes, “The Role of Emulsions in Steam Assisted Gravity Drainage (SAGD) Oil Production Process : A Review,” *SPE*, no. March, pp. 1–21, Dec. 2019.
- [5] I. D. Gates, “Oil phase viscosity behaviour in Expanding-Solvent Steam-Assisted Gravity Drainage,” *J. Pet. Sci. Eng.*, vol. 59, no. 1–2, pp. 123–134, 2007.
- [6] J. J. Sheng, *Enhanced Oil Recovery - Field Case Studies*. Elsevier, 2013.
- [7] R. M. Butler and D. J. Stephens, “The Gravity Drainage of Steam-Heated Heavy Oil to Parallel Horizontal Wells,” *J. Can. Pet. Technol.*, vol. 20, no. 2, pp. 90–96, 1981.
- [8] Q. Chen, “Assessing and Improving Steam-Assisted Gravity Drainage: Reservoir Heterogeneities, Hydraulic Fractures, and Mobility Control Foams,” no. May, p. 217, 2009.
- [9] W. Renpu, *Advanced Well Completion Engineering*, 3rd ed. Waltham: Gulf Professional Publishing, 2011.
- [10] R. M. Butler, “Steam-assisted Gravity Drainage: Concept, Development, Performance, and Future,” *J. Can. Pet. Technol.*, vol. 33, no. 2, pp. 44–50, 1994.
- [11] C. Holly, S. Soni, M. Mader, and J. Toor, “Alberta Energy Oil Sands Production Profile

2004-2014,” vol. 0, 2016.

- [12] L.-B. Ouyang and B. Huang, “An Evaluation of Well Completion Impacts on the Performance of Horizontal and Multilateral Wells,” in *SPE Annual Technical Conference and Exhibition held in Dallas, Texas, U.S.A., 9 – 12 October 2005*, 2005.
- [13] S. D. Joshi, *Horizontal Well Technology*. Tulsa; PennWell Books, 1991.
- [14] D. B. Bennion, S. Gupta, S. Gittins, and D. Hollies, “Protocols for slotted liner design for optimum SAGD operation,” *J. Can. Pet. Technol.*, vol. 48, no. 11, pp. 21–26, 2009.
- [15] RGL Reservoir Management Inc., “Flow Control Solutions,” <https://www.rglinc.com/>, 2019. [Online]. Available: <https://www.rglinc.com/solutions/flow-control/>.
- [16] Y. Yusuf, A. Baldygin, R. Sabbagh, M. Leitch, P. R. Waghmare, and D. S. Nobes, “Effect of Aspect Ratio on Pressure Loss and Characteristics of Low Reynolds Number Flow Through Narrow Slots,” in *Proceedings of the 2nd Thermal and Fluid Engineering Conference, TFEC2017 4th International Workshop on Heat Transfer, IWHT2017*, 2017.
- [17] K. Furui, D. Zhu, and A. D. Hill, “A Comprehensive Skin-Factor Model of Horizontal-Well Completion Performance,” *SPE Prod. Oper.*, vol. 20, no. 3, pp. 207–220, 2005.
- [18] M. Sivagnanam, J. Wang, and I. D. Gates, “On the fluid mechanics of slotted liners in horizontal wells,” *Chem. Eng. Sci.*, vol. 164, pp. 23–33, 2017.
- [19] V. LA Kaiser TMV, Wilson S, “Inflow Analysis and Optimization off slotted liners,” *SPE Drill. Complet.*, pp. 200–209, 2000.
- [20] S. P. Taubner, M. G. Lipsett, A. Keller, and T. M. V Kaiser, “Gravity Inflow Performance Relationship for SAGD Production Wells,” in *SPE Canada Heavy Oil Technical Conference*, 2016, pp. 1–18.

- [21] K. Furui, D. Zhu, and a. Hill, "A New Skin-Factor Model for Perforated Horizontal Wells," *SPE Drill. Complet.*, vol. 23, no. October 2004, pp. 205–215, 2008.
- [22] V. A. Moises *et al.*, "A new method for noninvasive estimation of ventricular septal defect shunt flow by Doppler color flow mapping: Imaging of the laminar flow convergence region on the left septal surface," *J. Am. Coll. Cardiol.*, vol. 18, no. 3, pp. 824–832, 1991.
- [23] J. G. Myers, J. F. Fox, A. M. Elmahdi, G. J. Perry, and A. S. Anayiotos, "Evaluation of the Proximal Flow Field to Circular and Noncircular Orifices of Different Aspect Ratios," *J. Biomed. Eng.*, vol. 119, no. August, pp. 349–356, 1997.
- [24] U. G. Romanova, "The Plugging Mechanisms of Sand Control Media in Thermal Heavy Oil and Bitumen Recovery Operations," in *Presentation at SPE Calgary Technical Luncheon*, 2014.
- [25] A. Saifelnasr, K. Kamal, and A. Lila, "Calcium Carbonate Scale Formation , Prediction and Treatment (Case Study Gumry Oilfield-PDOC)," *Int. Lett. Chem. Phys. Astron.*, vol. 12, pp. 47–58, 2013.
- [26] S. Ansari, "Visualization of fines migration in the flow entering apertures through the near-wellbore porous media," *Soc. Pet. Eng. Therm. Well Integr. Des. Symp.*, 2018.
- [27] Q. Guan *et al.*, "Integrated One-Dimensional Modeling of Asphaltene Deposition in Wellbores / Pipelines," in *Seventh International Conference on Modeling, Simulation and Applied Optimization*, 2017.
- [28] G. H. Goldsztein, "Volume of suspension that flows through a small orifice before it clogs," *SIAM J. Appl. Math.*, vol. 66, no. 1, pp. 228–236, 2005.
- [29] U. G. Romanova, M. Piwowar, and T. Ma, "Sand Control for Unconsolidated Heavy Oil

- Reservoirs: A Laboratory Test Protocol and Recent Field Observations,” in *International Symposium of the Society of Core Analysts, St. John’s, Newfoundland and Labrador, Canada*, 2015, pp. 1–6.
- [30] T. Clemo, “Flow in Perforated Pipes: A Comparison of Models and Experiments,” *SPE Prod. Oper.*, vol. 21, no. 2, pp. 302–311, 2006.
- [31] O. Vetter and V. Kandarpa, “Prediction of CaCO₃ scale under downhole conditions,” in *SPE Fifth International Symposium on Oilfield and Geothermal Chemistry*, 1980.
- [32] T. Cheung and M. Scheck, “Novel Scale Remediation for Steam Assisted Gravity Drainage (SAGD) Operations,” in *SPE International Symposium on Oilfield Chemistry*, 2013, pp. 1–10.
- [33] S. Whitaker, “Flow in Porous Media I: A Theoretical Derivation of Darcy’s Law,” *Transp. Porous Media*, vol. 1, p. 3, 1986.
- [34] M. Discacciati and A. Quarteroni, “Navier-Stokes/darcy coupling: modeling, analysis, and numerical approximation,” *Rev. Matemática Complut.*, vol. 22, no. 2, pp. 315–426, 2009.
- [35] L. Wang, “Flows through Porous Media : A Theoretical Development at Macroscale,” *Transp. Porous Media*, pp. 1–24, 2000.
- [36] I. F. Macdonald, M. S. El-Sayed, K. Mow, and F. a L. Dullien, “Flow through Porous Media-the Ergun Equation Revisited,” *Ind. Eng. Chem. Fundam.*, vol. 18, no. 3, pp. 199–208, 1979.
- [37] M. Dong and F. A. L. Dullien, “Porous Media Flows,” in *Multiphase Flow Handbook*, Taylor & Francis Group, LLC, 2006, pp. 10–1 to 10–55.
- [38] C. M. Fontanazza, V. Notaro, V. Puleo, P. Nicolosi, and G. Freni, “Contaminant intrusion

- through leaks in water distribution system: Experimental analysis,” *Procedia Eng.*, vol. 119, no. 1, pp. 426–433, 2015.
- [39] J. Xie, S. W. Jones, C. M. Matthews, B. T. Wagg, P. Parker, and R. Ducharme, “Slotted liner design for SAGD wells,” *World Oil*, pp. 67–75, 2007.
- [40] M. Ehrhardt, “An Introduction to Fluid-Porous Interface Coupling An Introduction to Fluid-Porous Interface Coupling,” *Angew. Math. und Numer. Math.*, no. October, pp. 1–10, 2010.
- [41] W. J. Layton, F. Schieweck, and I. Yotov, “Coupling fluid flow with porous media flow,” *SIAM J. Numer. Anal.*, vol. 40, no. 6, pp. 2195–2218, 2002.
- [42] M. Discacciati, “Coupling free and porous-media flows: modeling, analysis and numerical approximation,” 2011.
- [43] R. Collins and J. Boxall, “Influence of Ground Conditions on Intrusion Flows through Apertures in Distribution Pipes,” *J. Hydraul. Eng.*, vol. 139, no. October, pp. 1052–1061, 2012.
- [44] R. Collins, J. Boxall, M. C. Besner, S. Beck, and B. Karney, “Intrusion Modelling and the Effect of Ground Water Conditions,” in *Water Distribution System Analysis 2010*, 2010, pp. 585–594.
- [45] Z. Dagan, S. Weinbaum, and R. Pfeffer, “An infinite series solution for the creeping motion through an orifice of finite length,” *J. Fluid Mech.*, vol. 115, no. FEB, pp. 505–523, 1982.
- [46] R. D. Grose, “Orifice Contraction Coefficient for Inviscid Incompressible Flow,” *J. Fluids Eng.*, vol. 107, no. 1, pp. 36–43, 1985.
- [47] P. K. Kundu, I. M. Cohen, and D. R. Dowling, *Fluid Mechanics*, 5th ed. Oxford: Academic Press, Elsevier, 2012.

- [48] Y. Yusuf, R. Sabbagh, and D. S. Nobes, “Semi-empirical pressure loss model for viscous flow through high aspect ratio rectangular orifices,” *Phys. Fluids*, vol. 31, no. 7, p. (073603)1-14, 2019.
- [49] R. A. Sampson, “On Stoke’s Current Function,” *Philos. Trans. A*, vol. 1, pp. 449–518, 1890.
- [50] F. . C. Johansen, “Flow through pipe orifice at low Reynolds numbers,” *Proc. R. Soc. London. Ser. A, Contain. Pap. aMathematical Phys. Character*, vol. 126, no. 801, pp. 231–245, 1930.
- [51] H. Hasimoto, “On the flow of a viscous fluid past a thin screen at small Reynolds numbers,” *Journal of the Physical Society of Japan*, vol. 13, no. 6. pp. 633–639, 1958.
- [52] R. D. Grose, “Orifice flow at low Reynolds number,” *J. Pipelines*, vol. 3, no. 1, pp. 207–214, 1983.
- [53] W. R. Quinn, “Turbulent free jet flows issuing from sharp-edged rectangular slots: The influence of slot aspect ratio,” *Exp. Therm. Fluid Sci.*, vol. 5, pp. 203–215, 1992.
- [54] V. Zivkovic, P. Zerna, Z. T. Alwahabi, and M. J. Biggs, “A pressure drop correlation for low Reynolds number Newtonian flows through a rectangular orifice in a similarly shaped micro-channel,” *Chem. Eng. Res. Des.*, vol. 91, no. 1, pp. 1–6, 2012.
- [55] J. T. Jeong, “Two-dimensional Stokes flow through a slit in a microchannel with slip,” *J. Phys. Soc. Japan*, vol. 75, no. 9, pp. 7–11, 2006.
- [56] B. A. Finlayson *et al.*, “Microcomponent Flow Characterization,” *Micro Instrum. High Throughput Exp. Process Intensification-a Tool PAT*, no. 1, pp. 181–208, 2007.
- [57] A. H. Shapiro, “Pressure fields and fluid acceleration,” *Illustration of fluid dynamics experiments*. Massachusetts Institute of Technology, pp. 39–46, 1963.

- [58] R. M. Butler, “Steam-assisted Gravity Drainage : Concept , Development , Performance and Future,” *J. Can. Pet. Technol.*, vol. 33, no. 2, pp. 44–50, 1994.
- [59] Y. Yusuf, L. Kinsale, S. Ansari, and D. S. Nobes, “The Convergent Path of Streamlines in the Viscous flow Approaching a Rectangular Orifice through a Porous Region,” in *4th Thermal and Fluids Engineering Conference (TFEC) April 14-17, 2019*.
- [60] D. Plaines, L. Clark, and W. H. Page, “United States patent,” 1985.
- [61] W. Rudd, “Method and apparatus for manufacturing an expandable slotted tube,” 2003.
- [62] V. Fattahpour, S. Azadbakht, M. Mahmoudi, Y. Guo, and A. Nouri, “SPE-182507-MS Effect of Near Wellbore Effective Stress on the Performance of Slotted Liner Completions in SAGD Operations,” 2016.
- [63] D. Matanovic, M. Cikes, and B. Moslavac, *Sand control in well construction and operation*. Springer Science & Business Media, 2012.
- [64] T. V Tran, F. Civan, and I. Robb, “SPE 126310 Correlating Flowing Time and Condition for Plugging of Rectangular Openings , Natural Fractures , and Slotted Liners by Suspended Particles,” no. 1981, 2010.
- [65] H. Li, Y. Liu, J. Ma, and X. Wei, “Fluid Resistance Analysis of Sand Control Slotted Liner with Compound Cavity Based on Fluent,” *2010 Int. Conf. Meas. Technol. Mechatronics Autom.*, pp. 300–304, 2010.
- [66] K. Chung and R. M. Butler, “Geometrical Effect Of Steam Injection On The Formation Of Emulsions Nn The Steam-Assisted Gravity Drainage Process.pdf,” 1987.
- [67] Y. Yusuf and Y. Ma, “Design of a Simulation Tool for Sagd Based on the Concept of Unified Feature Modeling Scheme,” *J. Mech. Eng. Autom.*, 2016.

- [68] M. Leitch, Y. Yusuf, and Y. Ma, “Interdisciplinary semantic model for managing the design of a steam-assisted gravity drainage tooling system,” *J. Comput. Des. Eng.*, vol. 5, no. 1, 2018.
- [69] X. Shi and R. Okuno, “Analytical solution for steam-assisted gravity drainage with consideration of temperature variation along the edge of a steam chamber,” *Fuel*, vol. 217, no. March, pp. 262–274, 2018.
- [70] R. W. Miller, *Flow Measurement Engineering Handbook*, 3rd ed. New York: McGraw Hill, 1996.
- [71] R. W. Miller and O. Kneisel, “a Comparison Between Orifice and Flow Nozzle Laboratory Data and Published Coefficients.,” *J. Fluids Eng. Trans. ASME*, vol. 96, no. 2, 1974.
- [72] E. J. Gutmark and F. F. Grinstein, “Flow control with noncircular jets,” *Annu. Rev. Fluid Mech.*, vol. 31, pp. 239–272, 1999.
- [73] L. K. Bohra, “Flow and pressure drop of highly viscous fluids in small aperture orifices,” Georgia Institute of Technology, 2004.
- [74] D. A. McNeil, J. Addlesee, and A. Stuart, “An experimental study of viscous flows in contractions,” *J. Loss Prev. Process Ind.*, vol. 12, no. 4, pp. 249–258, 1999.
- [75] X. Liu and J. Katz, “Instantaneous pressure and material acceleration measurements using a four-exposure PIV system,” *Exp. Fluids*, vol. 41, no. 2, pp. 227–240, 2006.
- [76] S. H. Alvi, K. Sridharan, and N. S. L. Rao, “Loss characteristics of orifices and nozzles,” *J. Fluids Eng.*, vol. 100, no. 3, pp. 299–307, 1978.
- [77] Sætre and Johansen, “Discharge Coefficient Performance of Venturi, Standard Concentric Orifice Plate, V-Cone and Wedge flow Meters at Low Reynolds Numbers,” *J. Pet. Sci. Eng.*,

- vol. 78, pp. 559–566, 2011.
- [78] F. Kusmanto, E. L. Jacobsen, and B. A. Finlayson, “Applicability of continuum mechanics to pressure drop in small orifices,” *Phys. Fluids*, vol. 16, no. 11, pp. 4129–4134, 2004.
- [79] C. Mishra and Y. Peles, “An investigation of single-phase incompressible flows through rectangular micro-constriction elements,” *ICMM 2005, Proc. 3rd Int. Conf. Microchannels Minichannels, Pt A*, pp. 333–341, 2005.
- [80] M. S. N. Oliveira, M. A. Alves, F. T. Pinho, and G. H. McKinley, “Viscous flow through microfabricated hyperbolic contractions,” *Exp. Fluids*, vol. 43, no. 2–3, pp. 437–451, 2007.
- [81] M. S. N. Oliveira, L. E. Rodd, G. H. McKinley, and M. A. Alves, “Simulations of extensional flow in microrheometric devices,” *Microfluid. Nanofluidics*, vol. 5, no. 6, pp. 809–826, 2008.
- [82] L. K. Bohra, “Flow and Pressure Drop of Highly Viscous Fluids in Small,” no. June, 2004.
- [83] R. K. Shah and A. L. London, “Parallel Plates,” *Laminar Flow Forced Convect. Ducts*, vol. 2, no. 260, pp. 153–195, 1978.
- [84] R. B. Bird, W. E. Stewart, and E. N. Lightfoot, *Transport phenomena*, Revised ed. New York; New York: John Wiley & Sons, 2007.
- [85] W. Dong and J. H. Lienhard, “Contraction Coefficients for Borda Mouthpieces,” vol. 1081377, no. September, pp. 2–4, 1986.
- [86] T. A. Jankowski, E. N. Schmierer, F. C. Prenger, and S. P. Ashworth, “A Series Pressure Drop Representation for Flow Through Orifice Tubes,” *J. Fluids Eng.*, vol. 130, no. 5, p. 051204, 2008.
- [87] T. Hasegawa, A. Ushida, T. Narumi, and M. Goda, “Is the water flow more or less than that

- predicted by the Navier-Stokes equation in micro-orifices?,” *Phys. Fluids*, vol. 28, no. 9, 2016.
- [88] X. Xia and K. Mohseni, “Far-field momentum flux of high-frequency axisymmetric synthetic jets,” *Phys. Fluids*, vol. 27, no. 11, 2015.
- [89] S. G. Kandlikar, D. Schmitt, A. L. Carrano, and J. B. Taylor, “Characterization of surface roughness effects on pressure drop in single-phase flow in minichannels,” *Phys. Fluids*, vol. 17, no. 10, 2005.
- [90] T. Hasegawa, A. Ushida, and T. Narumi, “A simple expression for pressure drops of water and other low molecular liquids in the flow through micro-orifices,” *Phys. Fluids*, vol. 27, no. 12, 2015.
- [91] W. R. Quinn, “Turbulent free jet flows issuing from sharp-edged rectangular slots: the influence of slot aspect ratio,” *Exp. Therm. Fluid Sci.*, vol. 5, no. 2, pp. 203–215, 1992.
- [92] M. A. I. Rashid, “An Investigation of the Pressure Loss Characteristics for Highly Viscous Fluid Flow Through Narrow Slots,” University of Alberta, 2016.
- [93] R. C. Deo, J. Mi, and G. J. Nathan, “The influence of nozzle aspect ratio on plane jets,” *Exp. Therm. Fluid Sci.*, vol. 31, no. 8, pp. 825–838, 2007.
- [94] M. S. N. Oliveira, M. A. Alves, F. T. Pinho, and G. H. McKinley, “Viscous flow through microfabricated hyperbolic contractions,” *Exp. Fluids*, vol. 43, no. 2–3, pp. 437–451, 2007.
- [95] M. A. I. Rashid, “An investigation of the pressure loss characteristics for highly viscous fluid flow through narrow slots,” University of Alberta, 2015.
- [96] S. Abarbanel, S. Bennett, A. Brandt, and J. Gillis, “Velocity Profiles of Flow at Low Reynolds Numbers,” *Trans. ASME*, pp. 2–4, 1970.

- [97] R. D. Grose, "Orifice Contraction Coefficient for Inviscid Incompressible Flow," *J. Fluids Eng.*, vol. 107, no. 1, p. 36, 1985.
- [98] G. Astarita and G. Greco, "Excess Pressure Drop in Laminar Flow through Sudden Contraction. Newtonian Liquids," *Ind. Eng. Chem. Fundam.*, vol. 7, no. 1, pp. 27–31, 1968.
- [99] T. Hasegawa, M. Suganuma, and H. Watanabe, "Anomaly of excess pressure drops of the flow through very small orifices," *Phys. Fluids*, vol. 9, no. 1, pp. 1–3, 1997.
- [100] T. Utsunomiya *et al.*, "Doppler color flow 'proximal isovelocity surface area' method for estimating volume flow rate: Effects of orifice shape and machine factors," *J. Am. Coll. Cardiol.*, vol. 17, no. 5, pp. 1103–1111, 1991.
- [101] S. Liu and A. Afacan, "A New Pressure Drop Model for Flow-Through Orifice Plates," *Can. J. Chem. Eng.*, vol. 79, no. February, pp. 100–106, 2001.
- [102] A. A. Sonin, "Equation of Motion in Streamline Coordinates," *2.25 Adv. Fluid Mech. Fall*, 2013.
- [103] M. Pathak, A. Dewan, and A. K. Dass, "An assessment of streamline curvature effects on the mixing region of a turbulent plane jet in crossflow," *Appl. Math. Model.*, vol. 29, no. 8, pp. 711–725, 2005.
- [104] H. J. De Vriend, "Streamline curvature and bed resistance in shallow water flow," Delft, 1979.
- [105] H. Babinsky, "How do wings work?," *Phys. Educ.*, vol. 38, no. 6, pp. 497–503, 2003.
- [106] D. L. Darmofal, "Lift Generation and Streamline Curvature," *Massachusetts Inst. Technol. MIT OpenCourseWare*, 2005.
- [107] A. Ahmed and M. Demoulin, "Turbulence Modelling in the Automotive Industry," in

- Engineering Turbulence Modelling and Experiments 5*, W. Rodj and N. Fueyo, Eds. Elsevier Science Ltd., 2002, pp. 29–42.
- [108] R. A. Novak, “Streamline Curvature Computing Procedures for Fluid-Flow Problems,” *J. Eng. Power*, no. October, pp. 478–490, 1967.
- [109] T. Utsunomiya *et al.*, “Calculation of volume flow rate by the proximal isovelocity surface area method: Simplified approach using color Doppler zero baseline shift,” *J. Am. Coll. Cardiol.*, vol. 22, no. 1, pp. 277–282, 1993.
- [110] T. Utsunomiya *et al.*, “Doppler color flow ‘proximal isovelocity surface area’ method for estimating volume flow rate: Effects of orifice shape and machine factors,” *J. Am. Coll. Cardiol.*, vol. 17, no. 5, pp. 1103–1111, 1991.
- [111] S. Scharnowski and C. J. Kähler, “On the effect of curved streamlines on the accuracy of PIV vector fields,” *Exp. Fluids*, vol. 54, no. 1, 2013.
- [112] Y. Yusuf, S. Ansari, and D. S. Nobes, “Pressure field calculation from streamline behavior in the flow through adjacent rectangular orifices,” in *13th International Symposium on Particle Image Velocimetry – ISPIV 2019 July 22-24*, 2019.
- [113] P. Chadwick, *Continuum mechanics: concise theory and problems*. Courier Corporation, 2012.
- [114] M. Miorali, *Borehole radar for oil production monitoring*. 2012.
- [115] W. J. Layton, F. Schieweck, and I. Yotov, “Coupling fluid flow with porous media flow,” *SIAM J. Numer. Anal.*, vol. 40, no. 6, pp. 2195–2218, 2002.
- [116] R. Collins, J. Boxall, M. C. Besner, S. Beck, and B. Karney, “Intrusion Modelling and the Effect of Ground Water Conditions,” *Proceeding Water Distrib. Syst. Anal. - WDSA2010*

- Conf.*, pp. 585–594, 2010.
- [117] R. Collins and J. Boxall, “Influence of Ground Conditions on Intrusion Flows through Apertures in Distribution Pipes,” *J. Hydraul. Eng.*, vol. 139, no. 10, pp. 1052–1061, 2013.
- [118] R. a Waoding, A. M. Division, N. Zealand, and F. Collins, “Multiphase Fluid Flow,” pp. 233–274, 1976.
- [119] M. Matyka and Z. Koza, “How to calculate tortuosity easily?,” *AIP Conf. Proc.*, vol. 1453, no. 1, pp. 17–22, 2011.
- [120] A. Duda, Z. Koza, and M. Matyka, “Hydraulic tortuosity in arbitrary porous media flow,” *Phys. Rev. E - Stat. Nonlinear, Soft Matter Phys.*, vol. 84, no. 3, pp. 1–8, 2011.
- [121] H. Hægland, “Streamline methods with application to flow and transport in fractured media,” University of Bergen, 2009.
- [122] J. L. Kou *et al.*, “Tortuosity for streamlines in porous media,” *Chinese Phys. B*, vol. 21, no. 4, 2012.
- [123] M. Matyka, A. Khalili, and Z. Koza, “Tortuosity-porosity relation in porous media flow,” *Phys. Rev. E - Stat. Nonlinear, Soft Matter Phys.*, vol. 78, no. 2, pp. 1–8, 2008.
- [124] C.-T. Hsu, “Dynamic Modeling of Convective Heat Transfer in Porous Media,” in *Handbook of Porous Media*, 2nd ed., Kambiz Vafai, Ed. Boca Raton, FL: Taylor & Francis Group, LLC, 2005, pp. 40–78.
- [125] I. F. Macdonald, M. S. El-Sayed, K. Mow, and F. A. L. Dullien, “Flow through porous media-the Ergun equation revisited,” *Ind. Eng. Chem. Fundam.*, vol. 18, no. 3, pp. 199–208, 1979.
- [126] K. Furui and D. Zhu, “A comprehensive skin-factor model of horizontal-well completion

- performance,” *SPE Prod. Facil.*, vol. 20, no. 3, pp. 207–220, 2005.
- [127] G. S. Beavers and D. D. Joseph, “Boundary conditions at a naturally permeable wall,” *Journal of Fluid Mechanics*, vol. 30, no. 01. p. 197, 1967.
- [128] S. Fox, W. Shepherd, R. Collins, and J. Boxall, “Experimental proof of contaminant ingress into a leaking pipe during a transient event,” *Procedia Eng.*, vol. 70, pp. 668–677, 2014.
- [129] E. E. Petersen, “Diffusion in a pore of varying cross section,” *AIChE J.*, vol. 4, no. 3, pp. 343–345, 1958.
- [130] L. Shen and Z. Chen, “Critical review of the impact of tortuosity on diffusion,” *Chem. Eng. Sci.*, vol. 62, no. 14, pp. 3748–3755, 2007.
- [131] P. B. Lorenz, “Tortuosity in Porous Media,” *Nature*, vol. 189, no. 4762, pp. 386–387, 1961.
- [132] Y. Yusuf, R. Sabbagh, A. Baldygin, and D. S. Nobes, “Flow of viscous fluid through a rectangular slot Motivation Steam assisted gravity drainage (SAGD),” in *67th Canadian Chemical Engineering Conference, EDMONTON, AB, OCTOBER 22-25, 2017.*, 2017.
- [133] R. Shandas, M. Gharib, and D. J. Sahn, “Nature of flow acceleration into a finite-sized orifice: Steady and pulsatile flow studies on the flow convergence region using simultaneous ultrasound Doppler flow mapping and laser Doppler velocimetry,” *J. Am. Coll. Cardiol.*, vol. 25, no. 5, pp. 1199–1212, 1995.
- [134] Y. Yusuf, R. Sabbagh, and D. S. Nobes, “Flow convergence model for flow through long aspect ratio rectangular orifices,” in *Okanagan Fluid Dynamics Meeting, August 21-24, 2017, Kelowna, British Columbia, Canada, 2017*, pp. 145–152.
- [135] D. C. Montgomery, *Design and Analysis of Experiments*, 8th ed. Hoboken, N.J.: John Wiley & Sons, Inc., 2013.

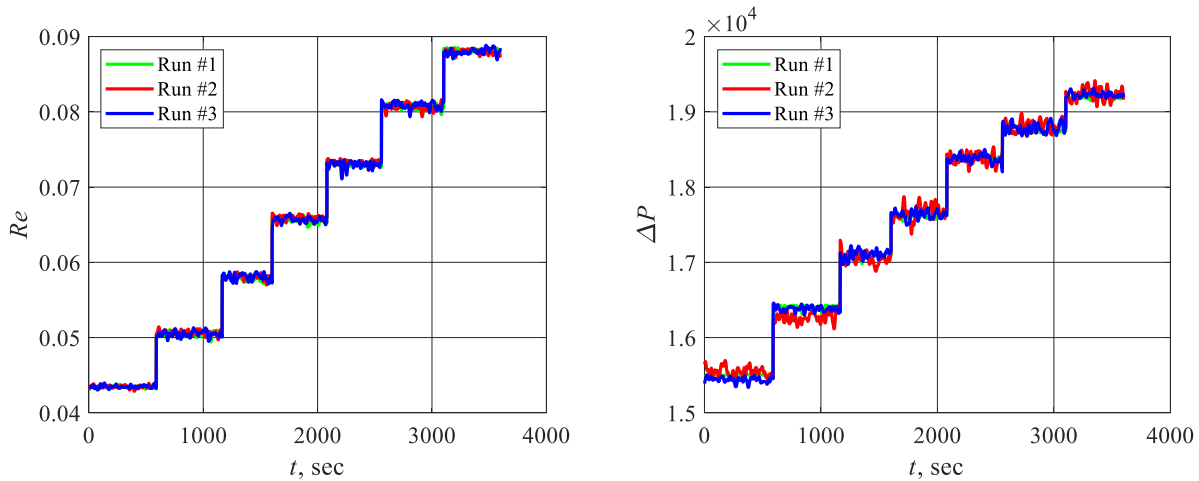
- [136] A. J. Wheeler and A. R. Ganji, *Introduction to Engineering Experimentations*, 3rd ed. Upper Saddle River: Pearson Higher Education, 2010.
- [137] The American Society of Mechanical Engineers, *Test Uncertainty*, 2006th ed. New York: The American Society of Mechanical Engineers, 2006.
- [138] M. Raffel, C. Willert, S. Wereley, and J. Kompenhans, *Particle Image Velocimetry: A Practical Guide*, vol. 2nd. New York: Springer, 2007.
- [139] Y. Yusuf, S. Ansari, M. Bayans, R. Sabbagh, M. El Hassan, and D. S. Nobes, “Study of Flow Convergence in Rectangular Slots using Particle Shadowgraph Velocimetry,” *Proc. 5th Int. Conf. Exp. Fluid Mech. – ICEFM 2018 Munich, Munich, Ger. July 2-4, 2018*, 2018.
- [140] S. Ansari, Y. Yusuf, R. Sabbagh, and D. S. Nobes, “Determining the pressure distribution of a multi-phase flow through a pore space using velocity measurement and shape analysis,” *Meas. Sci. Technol.*, vol. 30, no. 5, 2019.
- [141] S. T. Wereley and C. D. Meinhart, “Second-order accurate particle image velocimetry,” *Exp. Fluids*, vol. 31, no. 3, pp. 258–268, Sep. 2001.
- [142] D. Garcia, “A fast all-in-one method for automated post-processing of PIV data,” *Exp. Fluids*, vol. 50, no. 5, pp. 1247–1259, 2011.
- [143] B. Wieneke, “PIV uncertainty quantification from correlation statistics,” *Meas. Sci. Technol.*, vol. 26, no. 7, 2015.
- [144] A. Sciacchitano and B. Wieneke, “PIV uncertainty propagation,” *Meas. Sci. Technol.*, vol. 27, no. 8, 2016.
- [145] G. L. Morrison, “Euler Number Based Orifice Discharge Coefficient Relationship,” *J. Fluids Eng.*, vol. 125, pp. 189–202, 2003.

- [146] A. Azzalini, “A class of distributions which includes the normal ones,” *Scand. J. Stat.*, pp. 171–178, 1985.
- [147] H. K. Moffatt, “Viscous and resistive eddies near a sharp corner,” *J. Fluid Mech.*, vol. 18, no. 1, pp. 1–18, 1964.
- [148] P. Tryfos, “Factor Analysis,” in *Methods for Business Analysis and Forecasting: Text & Cases*, New Y: Wiley, 2001, p. 22.
- [149] R. A. Darton, “Rotation in Factor Analysis,” *J. R. Stat. Soc. Ser. D (The Stat.)*, vol. 29, no. 3, pp. 167–194, 1980.
- [150] J. W. Osborne, “What is rotating in exploratory factor analysis?,” *Pract. Assessment, Res. Eval.*, vol. 20, no. 2, p. 7, 2015.
- [151] H. Abdi, “Factor Rotations in Factor Analyses,” *Encyclopedia of Social Sciences Research Methods*. Thousand Oaks (CA): Sage, pp. 1–8, 2003.
- [152] K. Taira *et al.*, “Modal Analysis of Fluid Flows: An Overview,” *AIAA J.*, vol. 55, no. 12, pp. 4013–4041, 2017.
- [153] G. Terzakis, P. Culverhouse, G. Bugmann, and S. Sharma, “A Recipe on the Parameterization of Rotation Matrices for Non-Linear Optimization using Quaternions,” 2012.
- [154] B. van Oudheusden, “PIV-based pressure measurement,” *Meas. Sci. Technol.*, vol. 24, 2013.
- [155] N. J. Neeteson, S. Bhattacharya, D. E. Rival, D. Michaelis, D. Schanz, and A. Schröder, “Pressure-field extraction from Lagrangian flow measurements: first experiences with 4D-PTV data,” *Exp. Fluids*, vol. 57, no. 6, pp. 1–18, 2016.

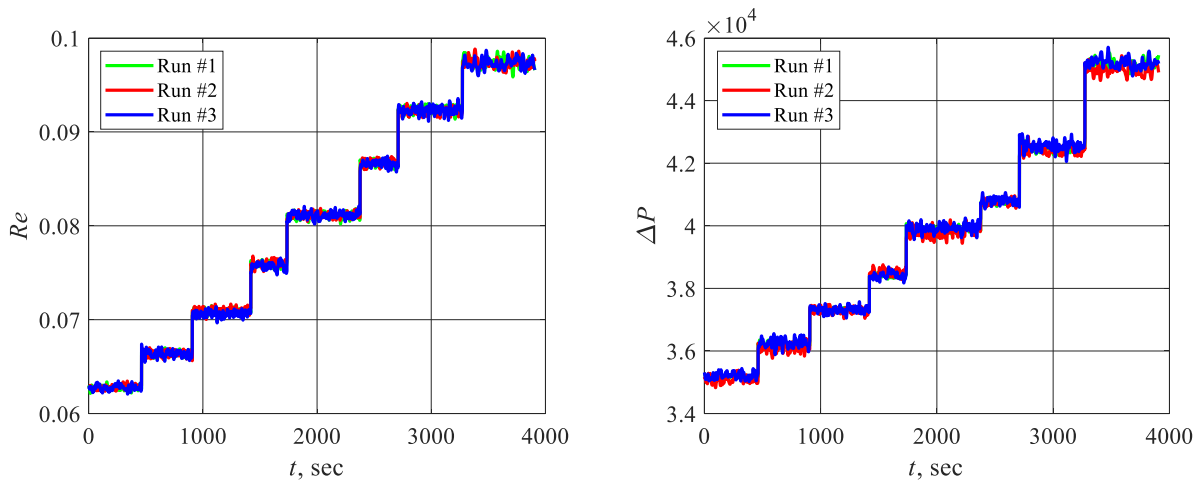
Appendices

A. Raw data for pressure measurement

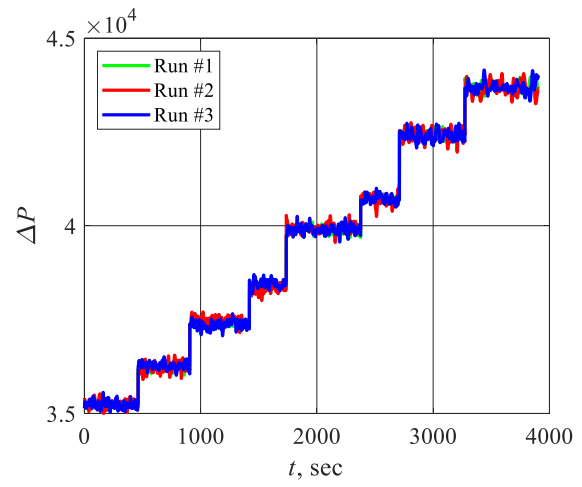
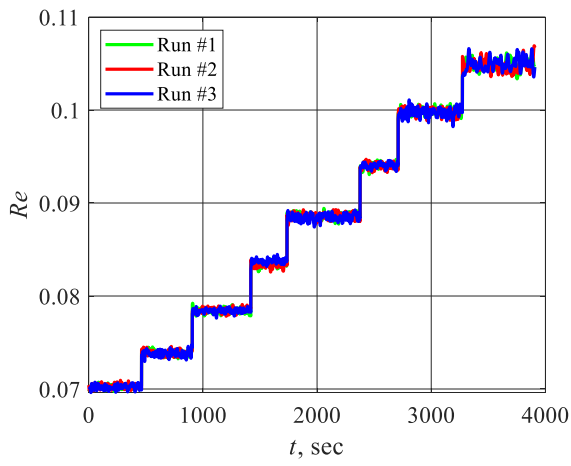
The raw data from obtained from the pressure measurement experiment for the open-slot scenario are given in Figure 46 below for each AR . The various values of Re used for the experiments are shown in the left column whereas the right column presents the corresponding measurement of the static pressure. It is noted here that for data presentation and clearer comparison, the measurement obtained from all the three runs are plotted on the same plot. Inconsistencies in the durations, corresponding to a given Re have also been avoided by limiting the corresponding limit at a given Re to the minimum among the cases of AR .



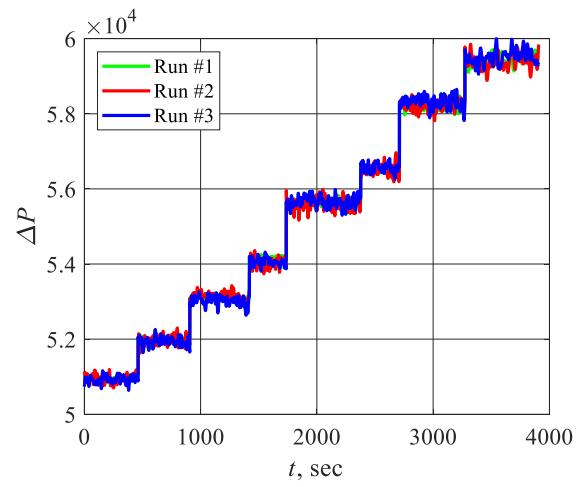
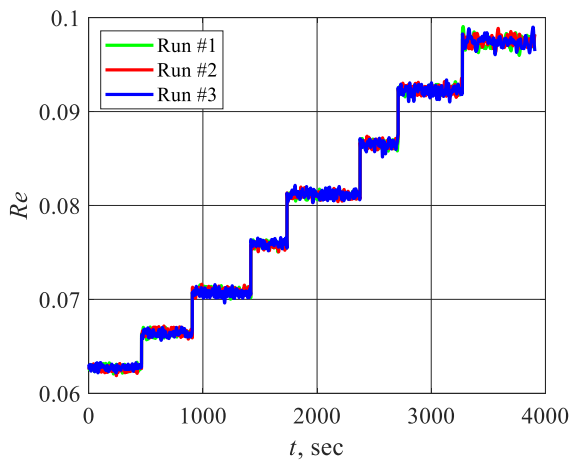
(i). $AR = 1$



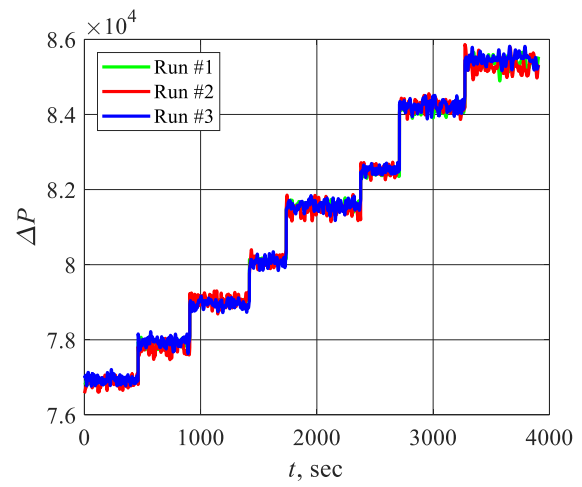
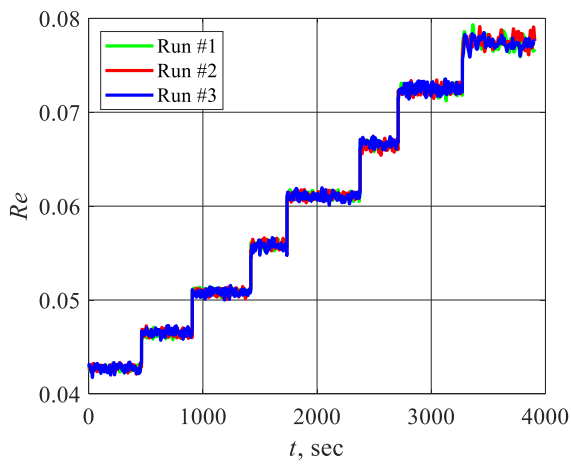
(ii). $AR = 37$



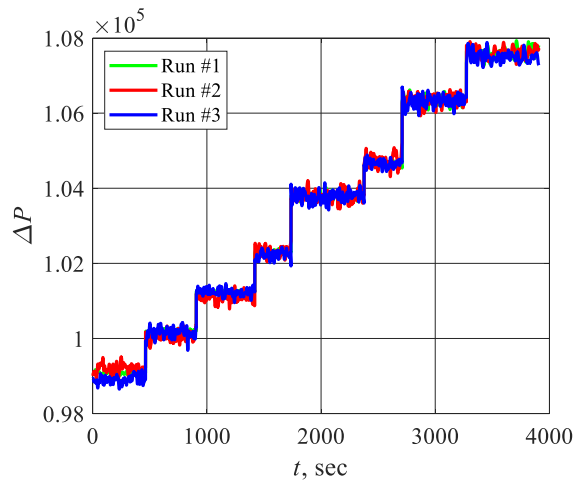
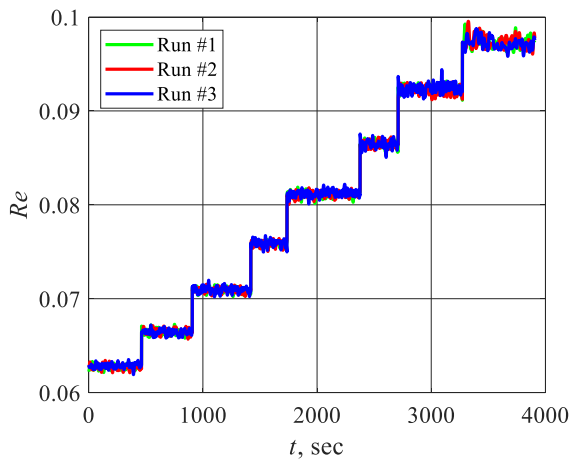
(iii). $AR = 50$



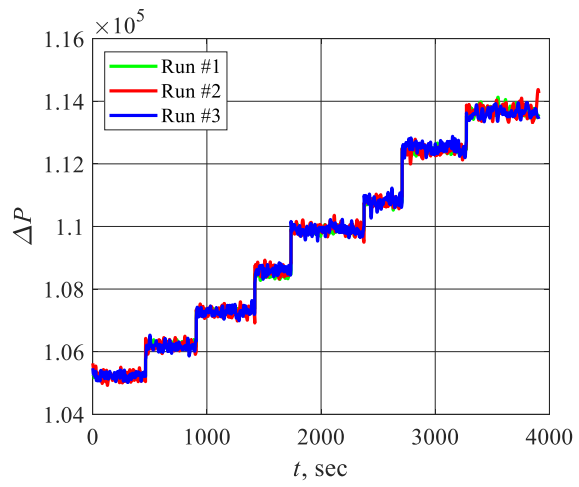
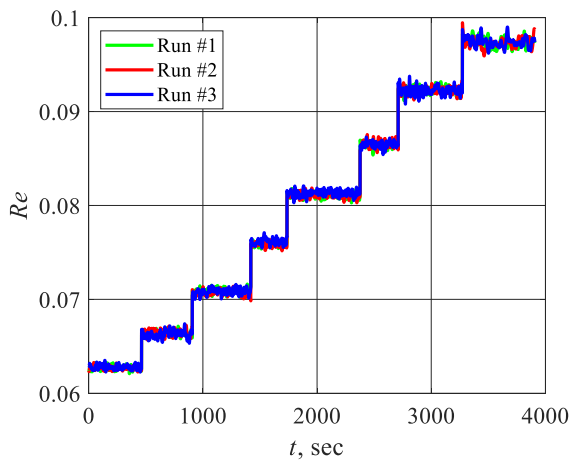
(iv). $AR = 72$



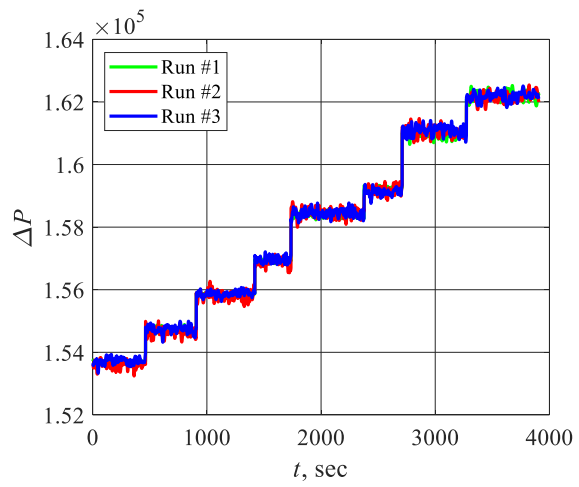
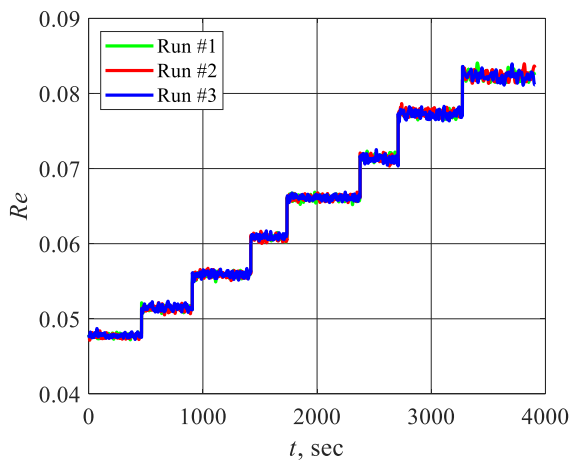
(v). $AR = 108$



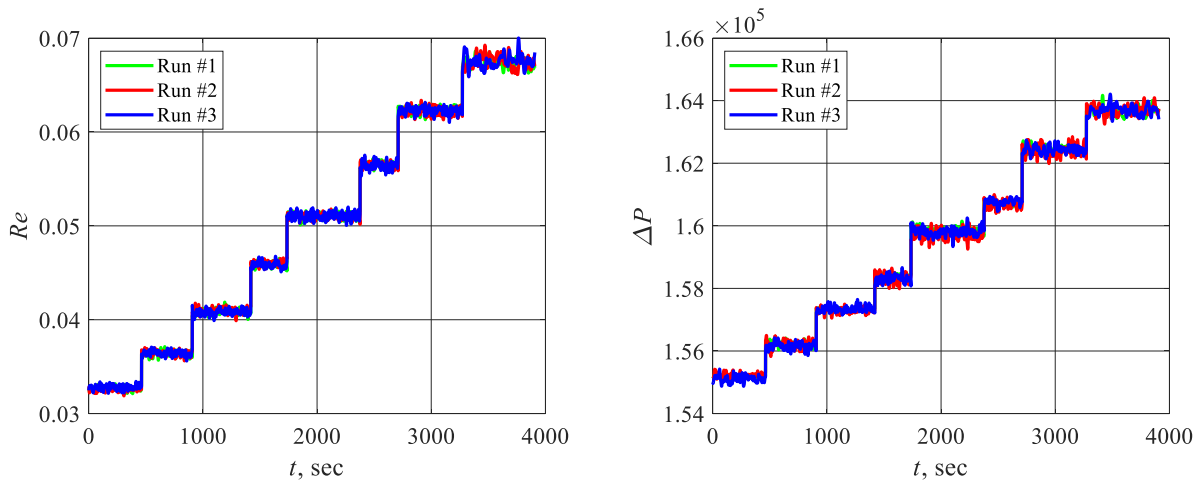
(vi). $AR = 143$



(vii). $AR = 179$



(viii). $AR = 214$



(ix). $AR = 250$

Figure 46 (i)–(ix) Raw data from the pressure measurement experiments in the open slot scenario for $AR = 1$ to $AR = 250$, correspondingly

B. Source codes for data acquisition software and data processing programs

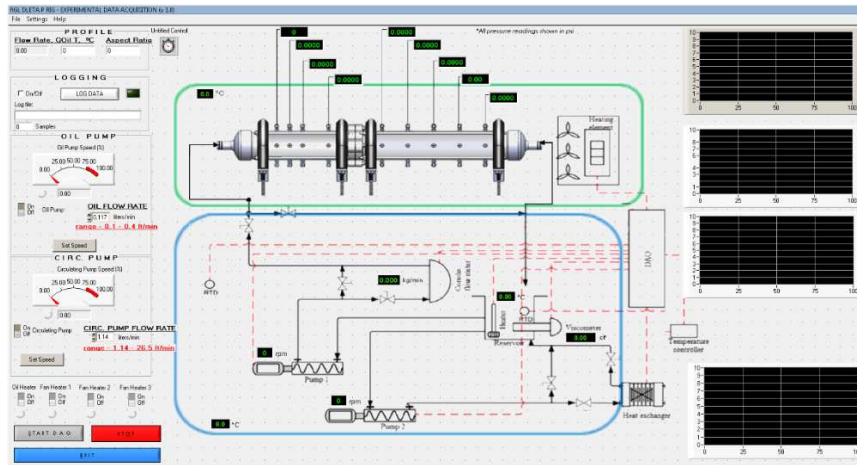
(i). Data acquisition and monitoring software for pressure measurement experiments

The program with graphical user interface for data acquisition, monitoring and logging process parameters was built in a commercial integrated development environment (LabWindows/CVI 2010, National Instruments). The program achieved reading from and writing to all channels that correspond to the instruments in the system.

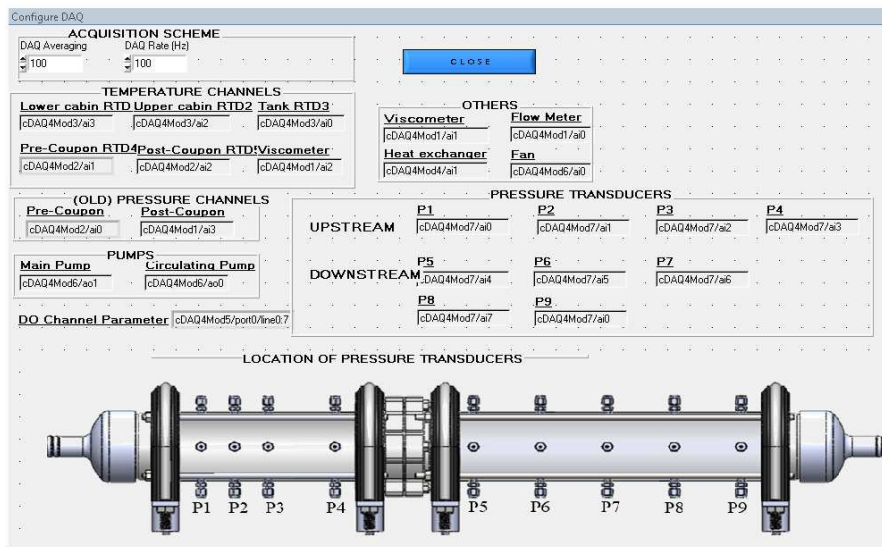
The developed software actively involves the user for inputs and interactions to provide settings and specifications for the data acquisition from the instruments. The components of the graphical user interfaces (GUI) used by the software are given in Figure 47. As it can be seen from the left hand side of the main interface shown Figure 47(a), it allows the user to set the directory path for the log file, specify the pump speeds, and turn the heaters in the system on/off. The interface is also equipped with indicators display controls for live monitoring of the parameters. The specification of the channels that are connected to the data acquisition system are initially provided by the user by selecting the respective option from the menu. From Figure 47(b) it is seen that the specification of the physical channel corresponding to the connection of each instrument is specified along with the general parameters for averaging of readings, and setting the acquisition rate. The menu to be used to setup the graphing task of the software is shown in Figure 47(c) which enables the user to specify the parameters to be plotted (from the drop-down menu). The scale and limits of the axes can also be set manually or left in auto mode for the default display settings to apply.

The development of this software has made references the software programs written by Aleksey Baldygin for emulsion flooding experiments, and by Reza Sabbagh for experiments using hydro-cyclone which were both for different flow rigs but written in the same development environment (LabWindows/CVI 2010, National Instruments). The software also uses codes

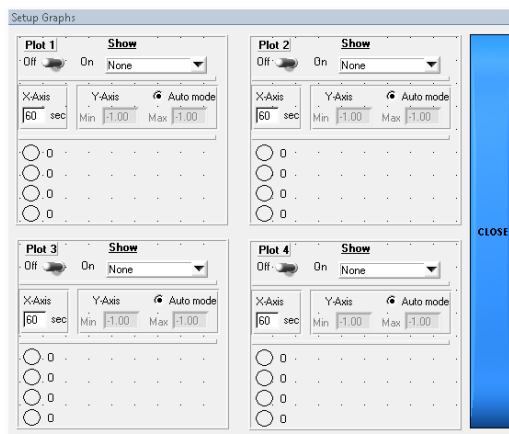
written by David S. Nobes especially for functions accomplishing the data logging task. The credits for these contributions are recognized in the “About” panel shown in Figure 47(d).



(a)



(b)



(c)



(d)

Figure 47 – GUIs developed for (a) live monitoring and control, and to configure settings for (b) data acquisition, (c) strip charts, and (d) showing credits

(ii). Processing and plotting of pressure measurement data

A multi-paradigm computing environment (Matlab 2018a, MathWorks) is used to write the scripts to achieve reading, processing, and analysis of data from the pressure measurement experiments.

The codes read the raw data, performed error calculations, conducted the averaging, plotted and rotated curves of the loss coefficient curves from the model.

```

%
% %%%%%%%%%%%%%%%%%%%%%%%%%%%%%%%%%%%%%%%%%%%%%%%%%%%%%%%%%%%%%%%%%%%%%%%%%
% % what : 1. Primary import of raw data to generate diagnosis plots
% %       2. Initial averaging of data based on Reynolds number to obtain
% %         local averages.
% %       3. Define error sources and determine the coefficients to
% %         calculate random and bias uncertainty levels.
% %       4. Error function analysis to determine the velocity transition
% %         plots from pressure drop measurement data and application of the
% %         developed model in Yusuf et al. (2019, Physics of Fluids) paper.
% %
% % who   : Yishak Yusuf
% % when  : v1 (April, 2017)
% %       v2 (February, 2018)
% %       v3 (December, 2018)
% %
% %update: January, 2019
% %%%%%%%%%%%%%%%%%%%%%%%%%%%%%%%%%%%%%%%%%%%%%%%%%%%%%%%%%%%%%%%%%%%%%%%%%

close all
clear all
clc
Font = 'Times';
Font_size = 22;
Line_w = 1.25;
set(0, 'DefaultAxesFontName', Font);
set(0, 'DefaultUIControlFontName', Font);
set(0, 'defaultUitableFontName', Font);
set(0, 'defaultTextFontName', Font);
set(0, 'defaultUipanelFontName', Font);
set(0, 'defaultTextFontSize', Font_size);
set(0, 'DefaultLineLinewidth',Line_w)
% set(0, 'defaulttextinterpreter','tex');
set(gcf,'Color','w')
set(findall(gcf,'type','text'),'FontSize',Font_size)
Interpreter = 'tex';

AR_clr = [0 0 0; 0 0 255; 0 128 0;...
          255 0 0; 255 0 255; 119 136 153;...
          204 204 0; 0 255 0; 210 105 30]./255;

%%=====
%          READING FROM LOG FILE
%%=====

% prompt = uigetdir('G:\My Drive\03_POF(SemiEmpirical_DeltaP_Model)\02_Plot_and_Process\',
'Select a folder');
prompt = ('A R =');
syms Re_c
% prompt = ('Select Folder containing all 9 files');
% title = 'Aspect_Ratio';
% AR_in = cell2mat(inputdlg(prompt,title));
Re_c = 0.005;          %Default Criterion for averaging based on Re
st = 7;              % starting point to skip log file header and

```

```

% data logged while heating
% file = uigetfile({'*.xlsx'}, 'Select log file');
% folder = uigetdir('G:\My
Drive\03_POF(SemiEmpirical_DeltaP_Model)\02_Plot_and_Process\Average_of_Repeats_Data\',...
% 'Select a folder');
folder = 'G:\My
Drive\03_POF(SemiEmpirical_DeltaP_Model)\02_Plot_and_Process\Average_of_Repeats_Data\Checked_PASS
';
files = dir(fullfile(folder,'*.xlsx'));
AR_pts = [1 37 50 72 108 143 179 214 250];

% figure()
% saveas(gcf,'Phi_erf_fit.fig')

sav_data = 0;
i0_all = 1:length(AR_pts); %loop goes through ALL_ARS
i0_a = [1 2 3 4]; %loop goes through AR = [1 37 50 72]
i0_b = [4 5 6 7]; %loop goes through AR = [72 108 143 179]
i0_c = [7 8 9]; %loop goes through AR = [179 214 250]
for i0= 1

% for i0= 1:length(AR_pts)
file = files(i0);
s_loc = strfind(file.name, '_');
AR_file = file.name(s_loc(1)+3:s_loc(2)-1);
AR_in = AR_file;
% if ((i0==1) & (AR_in ~='001'))||(i0==2 && AR_in ~='037'))
% return
% end

% if file == 0
% msgbox('Log file not selected','Error','Error')
% return
% elseif strcmp(AR_file, AR_in)==0
% msgbox('Selected file does not match entered aspect ratio')
% return
% end %location of underscore in the file name
fname1 = 'Averaged_Summary_AR';
fname2 = file.name(s_loc(1)+3:s_loc(2)-1) ; %extracting the locatoion of 'AR###' based
on location of
fname3 = file.name(s_loc(2):s_loc(3)-1); % '_'for file name to save averaged data
fname4 = 'PvsQData_AR';
fname6 = 'Averaged_DeltaPs_AR';
fname8 = 'Uncertainty_DeltaP_AR';
fname10 = 'P_Profile_AR';

if strcmp(AR_in,'000')
a = 76.2/1000;
b = 76.2/1000;
Re_c = 1e-6;

elseif strcmp (AR_in,'001')
a = 3/1000;
b = 3/1000;

```

```

Re_c = 0.0025;
fin_pt = 3968;
elseif strcmp (AR_in,'037')
a = 18.1/1000;
b = 0.5/1000;
Re_c = 0.0025;
%   fin_pt = 6563;
elseif strcmp (AR_in,'050')
a = 21.21/1000;
b = 0.424/1000;
Re_c = 0.0025;
%   fin_pt = 6102;
elseif strcmp (AR_in,'072')
a = 25.5/1000;
b = 0.35/1000;
Re_c = 0.0025;
%   fin_pt = 7234;
elseif strcmp (AR_in,'108')
a = 31.1/1000;
b = 0.29/1000;
Re_c = 0.0025;
st = 1130;
elseif strcmp (AR_in,'143')
a = 35.9/1000;
b = 0.25/1000;
Re_c = 0.005;
%   st = 226;
elseif strcmp (AR_in,'179')
a = 40.1/1000;
b = 0.22/1000;
Re_c = 0.00125;
elseif strcmp (AR_in,'214')
a = 43.9/1000;
b = 0.2/1000;
Re_c = 0.005;
%   st = 1197;
elseif strcmp (AR_in,'250')
a = 47.5/1000;
b = 0.19/1000;
Re_c = 0.005;
st = st+1;
else
msgbox('Undefined Aspect ratio')
return
end

D   = 76.2/1000;           %diameter of pipe, m
d_h = (4*a*b) / (2*(a+b)); %hydraulic diameter, m
L   = 10/1000;           %length of orifice (thickness of coupon), m
L2  = L/(2*a);          %length scale parameter for Dagan equation, m
mu  = 1.8;               %Pa.s
rho = 884.3;             %kg/m3
beta = d_h/D;           %beta ratio
A_o = a*b;               %m2

```



```

A_p = pi*D^2/4;           %m2
if strcmp(AR_in,'000')
    A_o = A_p;
end
alpha = A_o/A_p;         %area ratio
AR = a/b;                %aspect ratio

% fname1 = 'Averaged_Summary_REEP_AR';
% fname2 = file(s_loc(1)+3:s_loc(2)-1) ;           %extracting the locatoion of 'AR###' based on
location of
% fname3 = file(s_loc(2):s_loc(3)-1);           %'_'for file name to save averaged data
% fname4 = 'PvsQData_REEP_AR';
% fname6 = 'Averaged_DeltaPS_REEP_AR';
% fname8 = 'Uncertainty_DeltaP_REEP_AR';
% fname10 = 'P_Profile_REEP_AR';

if strcmp (AR_in,'1') || strcmp (AR_in,'37') || strcmp (AR_in,'50')|| strcmp (AR_in,'72')
    fname_pre = '0';
    fname = strcat(fname1, fname_pre, fname2, fname3);
    fname5 = strcat(fname4, fname_pre, fname2, fname3);
    fname7 = strcat(fname6, fname_pre, fname2, fname3);
    fname9 = strcat(fname8, fname_pre, fname2, fname3);
    fname11 = strcat(fname10, fname_pre, fname2, fname3);
else
    fname = strcat(fname1, fname2, fname3);
    fname5 = strcat(fname4, fname2, fname3);
    fname7 = strcat(fname6, fname2, fname3);
    fname9 = strcat(fname8, fname2, fname3);
    fname11 = strcat(fname10, fname2, fname3);
end

all_data = xlsread(strcat(file.folder, '\', file.name));           %nbr_data - all
numbers in the file. Text and empty cells shown as "NaN"
%txt_data - all text in the log file.
%data - the log file as is. Empty cells sh

    m_dot_a = all_data(st:end,16);           %volumetric flow rate in liters per minute set as pump
speed
    P1_raw = all_data(st:end,2);           %Pressure at location 1, psi
    P2_raw = all_data(st:end,3);           %Pressure at location 2, psi_ADP
    P3_raw = all_data(st:end,4);           %Pressure at location 3, psi_ADP
    P4_raw = all_data(st:end,5);           %Pressure at location 4, psi
    P5_raw = all_data(st:end,6);           %Pressure at location 5, psi
    P6_raw = all_data(st:end,7);           %Pressure at location 6, psi
    P7_raw = all_data(st:end,8);           %Pressure at location 7, psi
    P8_raw = all_data(st:end,9);           %Pressure at location 8, psi
    P9_raw = all_data(st:end,10);          %Pressure at location 9, psi
    Oil_T = all_data(st:end,13);           %Oil temperature in deg_C from RTD in the tank
    Visc = all_data(st:end,14);           %viscosity in cP from viscometer
    r = size(all_data);
    t = 0:1:r(1)-st;

```

```

%*****
%                CORRECTING TRANSDUCER ERRORS (The commented part can be used for calibration)
%*****
%First Transducer upstream (P2 @ 2.5D)
% P2_act = [0 0.01 0.5 0.87 1 4.4 5 10 15 16.6 20 22.1 30 37.4 40 50 60 70 80];
%transducer offset corrections.
% P2_read = [0.11 0.22 0.59 1.07 1.09 4.55 5.03 9.99 14.91 16.61 19.84 22.04 29.75 37.16 39.66
49.63 59.65 69.7 79.82];    %Calibrated on July 14, 2018
% P2_fit = fitlm(P2_read,P2_act);
% P2 = table2array(P2_fit.Coefficients(2,1))*P2_raw - table2array(P2_fit.Coefficients(1,1));

FS_P2 = 78*6894.76;    %bias error of transducer based on the full scale (psi*conversion) of
the diaphragm installed
errB_P2 = (0.25/100)*FS_P2;

%Second Transducer upstream (P3 @ 2D)
% P3_act = [0 0.5 1 5 10 15 20 30 40 50 60 70 80];
% P3_read = [0.9 1.38 1.88 5.86 10.8 15.73 20.67 30.62 40.56 50.51 60.58 70.66 80.81];
% P3_fit = fitlm(P3_read,P3_act);
% P3 = table2array(P3_fit.Coefficients(2,1))*P3_raw - table2array(P3_fit.Coefficients(1,1));

FS_P3 = 78*6894.76;    %bias error of transducer based on the full scale of the diaphragm
installed
errB_P3 = (0.25/100)*FS_P3;

%Third Transducer upstream (P4 @ 1D)
% P4_act = [0 0.5 1 5 10 15 20 30 40 50 60 70 80];
% P4_read = [1.02 1.49 2.00 5.98 10.94 15.89 20.84 30.76 40.70 50.69 60.69 70.73 80.85];
% P4_fit = fitlm(P4_read,P4_act);
% P4 = table2array(P4_fit.Coefficients(2,1))*P4_raw - table2array(P4_fit.Coefficients(1,1));
FS_P4 = 78*6894.76;    %bias error of transducer based on the full scale of the diaphragm
installed
errB_P4 = (0.25/100)*FS_P4;

%First Transducer downstream (P5 @ 1D)
% P5_act = [0 0.05 0.25 0.5 0.75 1 1.5 2.5 5 7.5 10 11.5 12.5];
% P5_read = [0.03 0.08 0.27 0.52 0.77 1.01 1.51 2.51 5.09 7.6 10.12 11.63 12.66];
% P5_fit = fitlm(P5_read,P5_act);
% P5 = table2array(P5_fit.Coefficients(2,1))*P5_raw - table2array(P5_fit.Coefficients(1,1));
FS_P5 = 12.5*6894.76;    %bias error of transducer based on the full scale of the diaphragm
installed
errB_P5 = (0.25/100)*FS_P5;

%Second Transducer downstream (P6 @ 2D)
% P6_act = [0 0.05 0.25 0.5 0.75 1 1.5 2.5 5 7.5 10 11.5 12.5];
% P6_read = [-0.07 -0.01 0.18 0.43 0.67 0.92 1.42 2.43 4.95 7.45 9.95 11.46 12.48];
% P6_fit = fitlm(P6_read,P6_act);
% P6 = table2array(P6_fit.Coefficients(2,1))*P6_raw - table2array(P6_fit.Coefficients(1,1));
FS_P6 = 12.5*6894.76;    %bias error of transducer based on the full scale of the diaphragm
installed
errB_P6 = (0.25/100)*FS_P6;

%Third Transducer downstream (P7 @ 3D)

```

```

% P7_act = [0 0.05 0.25 0.5 0.75 1 1.5 2.5 5 7.5 10 11.5 12.5];
% P7_read = [-0.09 0.0 0.33 0.72 1.14 1.57 2.39 4.04 8.13 12.24 16.35 18.82 20.49];
% P7_fit = fitlm(P7_read,P7_act);
% P7 = table2array(P7_fit.Coefficients(2,1))*P7_raw - table2array(P7_fit.Coefficients(1,1));
FS_P7 = 20*6894.76;      %bias error of transducer based on the full scale of the diaphragm
installed
errB_P7 = (0.25/100)*FS_P7;

%Last Transducer downstream (P9 @ 5D)
% P9_act = [-0.91 -0.72 -0.53 -0.31 -0.11 0 0.05 0.11 0.25 0.31 0.5 0.53 0.72 0.75 0.91 1 1.5 2.5
5 7.5 10 11.5 12.5];
% P9_read = [-1.06 -0.82 -0.56 -0.28 -0.01 0.09 0.15 0.29 0.4 0.53 0.73 0.79 1.06 1.07 1.3 1.4
2.05 3.37 6.62 9.84 12.39 12.54 12.63];
% P9_fit = fitlm(P9_read,P9_act);
% P9 = table2array(P9_fit.Coefficients(2,1))*P9_raw - table2array(P9_fit.Coefficients(1,1));
FS_P9 = 12.5*6894.76;      %bias error of transducer based on the full scale of the diaphragm
installed
errB_P9 = (0.25/100)*FS_P9;
% % P_idx = [2 3 4 5 6 7 9];

P2 =P2_raw; P3 =P3_raw;P4 = P4_raw-0.1450;P5 =P5_raw;P6 =P6_raw;P7 =P7_raw;P9 =P9_raw;
%Volume flow
Q_a = sort(m_dot_a./(rho*60));
%Saving Data for future analysis

%Velocity through orifice
u_d_a = Q_a/A_o;
%Velocity through pipe
u_u_a = Q_a/A_p;
%Reynolds numbers
Re_oa = (2*m_dot_a)/(60*mu*(a+b));
if strcmp(AR_in,'000')
    Re_oa =(4*m_dot_a)./(60*pi*D*mu);
end
%Across-coupon_DeltaPs, in Pa
dP1 = (P2-P5)*6894.76;
dP2 = (P2-P6)*6894.76;
dP3 = (P2-P7)*6894.76;
dP4 = (P2-P9)*6894.76;

%UPStream_DeltaPs, in Pa
USdP1 = (P2-P4)*6894.76;
USdP2 = (P2-P3)*6894.76;
USdP3 = (P3-P4)*6894.76;

%Downstream_DeltaPs, in Pa
DSdP1 = (P5-P9)*6894.76;
DSdP2 = (P5-P7)*6894.76;
DSdP3 = (P5-P6)*6894.76;
DSdP4 = (P6-P7)*6894.76;
DSdP5 = (P6-P9)*6894.76;
DSdP6 = (P7-P9)*6894.76;
S_dP4= expsmooth(dP4, 1, 1000000);

```

```

%for Dagan et al. (1982)
% P = (16*L2/pi)+3;
% Dp = (P.*Q_a.*mu)/(a^3);
%check if the experiment is for empty pipe
if strcmp(AR_in,'000')
    A_o = pi*D^2/4;
end

Q = m_dot/(rho*60);
u_d = Q/A_o;
%Velocity through pipe
u_u = Q/A_p;
Re_p = (4*m_dot)/(60*pi*D*mu);
du= u_d - u_u;
S_Re_o= expsmooth(Re_o, 1, 10000);
KE_term = (0.5*rho*(u_d.^2));
K = dP4./(0.5*rho*(u_d.^2)); %Pressure loss coefficient
phi_m = (((sqrt(pi)*Re_o)/4).*(K-(1-alpha^2)))./((1-alpha).*((2*AR)/(AR+1)));
% if strcmp(AR_in,'250')
% phi_m = (((sqrt(pi)*Re_o)/4).*(K-(1-alpha^2)))./((1-alpha).*((2*AR)/(AR+1)));
% elseif strcmp(AR_in,'214')
% phi_m = (((sqrt(pi)*Re_o)/4).*(K-(1-alpha^2)))./((1-alpha).*((2*AR)/(AR+1)));
% % phi_Re_AR;
% end

%for Dagan et al. (1982)
P = (16*L2/pi)+3;
Dp = (P.*Q_a.*mu)/(a^3);
LD =3*D;
R = D;
QPois= USdP3*(pi*(R^4))/(8*mu*LD);
%Gaussian Check
normplot(dP4)
if(sav_data ==1)
save(['G:\My Drive\work from home\Open_Slot_Experiments\Pressure_vs_Flowrate_Data\'
fname5'],'P2','P3','P4','P5','P6','P7','P9','Q_a','dP4','Re_o')
end
figure('Name','Averaging_Thesis');
plot(t,Re_o,'.','Color',[0 0 0]);
xlabel({'\it{t}, sec'],'FontSize',Font_size, 'Interpreter', Interpreter)
ylabel({'\it{Re}'],'FontSize',Font_size, 'Interpreter', Interpreter)
% ylim([0.05 0.1])
hold on
yyaxis right
for j =1:length(dP4)-1
    b_raw(j) = abs(t(j)-t(j+1));
    a_prime_raw (j) = abs(dP4(j)-dP4(j+1));
    c_raw(j) = sqrt(a_prime_raw (j)^2 + b_raw (j)^2);
    a_raw (j) = sqrt(c_raw (j)^2 - b_raw (j)^2);
    dP4_raw(j) = dP4(j)+a_raw (j) ;

plot(t(j),dP4_raw(j),'.','color',[1 0 0]);
end
ylabel({'\it{\Delta P}'],'FontSize',Font_size, 'Interpreter', Interpreter)

```

```

% set(gca,'XDir','reverse')
set(gca,'FontSize',Font_size);
set(gcf,'Color','w')
grid on
xlim([0 6500])

legend({'\it{Re}','\it{\Delta P}','Interpreter','Latex'});

figure('Name','Q Compare')
plot(t,Q/max(Q),'o',t,QPois/max(QPois),'+');
xlabel('\it{t}')
ylabel('\it{Q/Q_{max}}')
legend('Experiment','Poiseuille flow profile')
set(gca,'FontName',Font,'FontSize',Font_size)

figure('Name','Summary');
plot(t,m_dot/60,t,Q,t,Re_o);
hold on
yyaxis right
plot(t,dP4)
legend('massflow,kg/s ','Q [m3/sec]','Re_{orifice}','Re_{act}','DeltaP');
set(gca,'FontName',Font,'FontSize',Font_size)
grid on

figure('Name','Velocities')
plot(t,u_u,'o',t,QPois,'+');
ylim([0 max(u_d)])
hold on
yyaxis right

plot(max(t)+1:2*max(t)+1,u_d,'. ');
ylim([min(u_u) max(u_d)])
legend('upstream velocity, [m/s]','downstream velocity, [m/s]');
set(gca,'FontName',Font,'FontSize',Font_size)
K_s = smooth(K,5,'moving');
figure('Name','LossCoefficient')
plot(t,K);
set(gca,'FontName',Font,'FontSize',Font_size)
%SORTING Re_vs_K
Re_k = horzcat(Re_o,K,P2,P3,P4,P5,P6,P7,P9,m_dot,t');
[~,idx] = sort(Re_k(:,1)); % sort just the first column
sortedRe = Re_k(idx,:);
Re_k2 = unique(Re_k,'rows');
fit_type = fitype('a/x');
fit_typeL = fitype('a*x + b');
[K_Fit, other]=fit(Re_k2(:,1),Re_k2(:,2),fit_type);
[K_Fit_2, other2] = fit(Re_k2(:,1),Re_k2(:,2),fit_type);
[P2_Fit,P2_other] = fit(Re_k2(:,1),Re_k2(:,3),fit_typeL);
[P3_Fit,P3_other] = fit(Re_k2(:,1),Re_k2(:,4),fit_typeL);
[P4_Fit,P4_other] = fit(Re_k2(:,1),Re_k2(:,5),fit_typeL);
[P5_Fit,P5_other] = fit(Re_k2(:,1),Re_k2(:,6),fit_typeL);
[P6_Fit,P6_other] = fit(Re_k2(:,1),Re_k2(:,7),fit_typeL);
[P7_Fit,P7_other] = fit(Re_k2(:,1),Re_k2(:,8),fit_typeL);
[P9_Fit,P9_other] = fit(Re_k2(:,1),Re_k2(:,9),fit_typeL);

```

```

[MD_Fit,MD_other] = fit(Re_k2(:,1),Re_k2(:,10),fit_typeL);
[t_Fit,t_other]   = fit(Re_k2(:,11),Re_k2(:,1),fit_typeL);
K_Stokes = ((12*pi)./(Re_k2(:,1))) + (64*L)./((Re_k2(:,1)).*d_h);
K_Stokes_2 = ((12*pi)./(Re_k2(:,1))) + ((64*L)./((Re_k2(:,1)).*d_h));
% K_Fit.c = abs(K_Fit.c);
figure('Name','Reynolds number vs. K: Experiment')
plot((K_Fit),abs(Re_k2(:,1)),abs(Re_k2(:,2)),'bs');
hold on
% plot()
yyaxis left
set(gca,'YColor','k')
xlim([0.01 0.1]);
ylim([0 150000]);
xlabel('\it {Re}');
ylabel('\it {K} (Experiment)');
% set(gca,'TickLabelInterpreter','latex');
set(gca,'FontName',Font,'FontSize',Font_size)
hold on
% figure('Name','Reynolds number vs. K: Stokes Flow')
plot(abs(Re_k2(:,1)), abs(K_Stokes), '-b')
yyaxis right

set(gca,'YColor','b')
grid on
% legend('Original data','Moving Average','Location','NW')
xlim([0.01 0.1]);
ylim([0 150000]);
xlabel('\it {Re}');
ylabel('\it {K} (Stokes flow)');
% set(gca,'TickLabelInterpreter','latex');
set(gca,'FontName',Font,'FontSize',Font_size)
legend({'Experiment','Fit Eq.(3)','Stokes Flow Eq. (4)'},'Interpreter','Latex')

% figure('Name','Reynolds number vs. K: Experiment_unsorted')
% yyaxis left
% plot(K_Fit,Re_k2(:,1),Re_k2(:,2),'bs');
% set(gca,'YColor','k')
% % xlim=[0.04 0.12];
% xlabel('\it {Re}');
% ylabel('\it {K} (Experiment)');
% % set(gca,'TickLabelInterpreter','latex');
% set(gca,'FontName',Font,'FontSize',Font_size)
% hold on
% % figure('Name','Reynolds number vs. K: Stokes Flow')
% yyaxis right
% plot(Re_k2(:,1), K_Stokes_2, '-b')
% set(gca,'YColor','b')
% grid on
% % legend('Original data','Moving Average','Location','NW')
% % xlim=[0.04 0.12];
% xlabel('\it {Re}');
% ylabel('\it {K} (Stokes flow)');
% % set(gca,'TickLabelInterpreter','latex');

```

```

% set(gca,'FontName',Font,'FontSize',Font_size)
% legend({'Experiment','Fit Eq.(3)','Stokes Flow Eq. (4)'})

figure('Name','Pressure transducer #1');
semilogy(t,P2, t,Q)
xlabel('\it{t}, sec');
legend ('\it{P}_{#2}, psi','\it{Q}, m^{3}/sec')
grid on
set(gca,'FontName',Font,'FontSize',Font_size)

figure('Name','\Delta P between different segments in the pipe')
semilogy(t,m_dot,'-', t, dP1, '--', t, dP2, '--', t,dP3, '-.',t,dP4, '--',t, Dp,'-');
legend('mass flow, kg/min', '\Delta P_1, Pa', '\Delta P_conv,Pa', '\Delta P_3,Pa','\Delta
P_4,Pa','\Delta P from Dagan et al. (1981)');
xlabel('t, sec')
grid on
set(gca,'FontName',Font,'FontSize',Font_size)

figure('Name','\Delta P exponentially smoothed');
plot(t,dP4, '--r',t,s_dP4, '-k');
legend('\Delta P_4,Pa', 'Smoothed \Delta P_4,Pa ');
xlabel('t, sec')
ylabel('\Delta P, Pa')
grid on
set(gca,'FontName',Font,'FontSize',Font_size)

figure('Name','\phi calculated from the model');
plot(t, phi_m)
legend('\phi_y')
set(gca,'FontName',Font,'FontSize',Font_size)
grid on

%=====
%           AVERAGING
%=====
k = size(Re_o);
d_Re = zeros(k(1)-1,1);
for i2 = 1:k(1)-1
    d_Re(i2) = abs(Re_o(i2+1)-Re_o(i2));
end
Re_loc = find(d_Re>Re_c);
s = size(Re_loc);

Re_ave = zeros(s(1),1); Phi_ave = zeros(s(1),1); K_ave = zeros(s(1),1);
m_dot_ave = zeros(s(1),1); u_d_ave = zeros(s(1),1); u_u_ave = zeros(s(1),1);
P2_ave = zeros(s(1),1); P3_ave = zeros(s(1),1); P4_ave = zeros(s(1),1);
P5_ave = zeros(s(1),1); P6_ave = zeros(s(1),1); P7_ave = zeros(s(1),1);
P9_ave = zeros(s(1),1);

DP1_ave = zeros(s(1),1); DP2_ave = zeros(s(1),1); DP3_ave = zeros(s(1),1);
DP4_ave = zeros(s(1),1);

US_DP1_ave = zeros(s(1),1); US_DP2_ave = zeros(s(1),1); US_DP3_ave = zeros(s(1),1);

```

```

DS_DP1_ave = zeros(s(1),1); DS_DP2_ave = zeros(s(1),1); DS_DP3_ave = zeros(s(1),1);
DS_DP4_ave = zeros(s(1),1); DS_DP5_ave = zeros(s(1),1); DS_DP6_ave = zeros(s(1),1);

errP_P2_ave = zeros(s(1),1); errP_P3_ave = zeros(s(1),1); errP_P4_ave = zeros(s(1),1);
errP_P5_ave = zeros(s(1),1); errP_P6_ave = zeros(s(1),1); errP_P7_ave = zeros(s(1),1);
errP_P9_ave = zeros(s(1),1); errP_MDot_ave = zeros(s(1),1); errP_DP_ave = zeros(s(1),1);
errP_K_ave = zeros(s(1),1); errP_Phi_ave = zeros(s(1),1); errP_Re_ave = zeros(s(1),1);

SC_K_DP = zeros(s(1),1); SC_K_m_dot = zeros(s(1),1); SC_K_A_o = zeros(s(1),1);
SC_Phi_Re = zeros(s(1),1); SC_Phi_DP = zeros(s(1),1); SC_Phi_alpha = zeros(s(1),1);

U95_DP = zeros(s(1),1); U95_K = zeros(s(1),1); U95_Phi = zeros(s(1),1);

n=1;
for j2 = 1:s(1)
    %Re, Phi, and K
    Re_ave(j2)=mean(Re_o(n:Re_loc(j2)-1));
    Phi_ave(j2)=mean(phi_m(n:Re_loc(j2)-1));
    K_ave(j2)=mean(K(n:Re_loc(j2)-1));
    m_dot_ave(j2)=mean(m_dot(n:Re_loc(j2)-1));
    u_d_ave(j2)=mean(u_d(n:Re_loc(j2)-1));
    u_u_ave(j2)=mean(u_u(n:Re_loc(j2)-1));
    %Pressure readings to plot pressure profile along the flow channel
    P2_ave(j2)=mean(P2(n:Re_loc(j2)-1));           %(-2.5D)
    P3_ave(j2)=mean(P3(n:Re_loc(j2)-1));           %(-2D)
    P4_ave(j2)=mean(P4(n:Re_loc(j2)-1));           %(-D)
    P5_ave(j2)=mean(P5(n:Re_loc(j2)-1));           %(+D)
    P6_ave(j2)=mean(P6(n:Re_loc(j2)-1));           %(+2D)
    P7_ave(j2)=mean(P7(n:Re_loc(j2)-1));           %(+3D)
    P9_ave(j2)=mean(P9(n:Re_loc(j2)-1));           %(+5D)

    %Across-slot differential pressures, + represents downstream location
    DP1_ave(j2)=mean(dP1(n:Re_loc(j2)-1));         %(-2.5D) - (+D)
    DP2_ave(j2)=mean(dP2(n:Re_loc(j2)-1));         %(-2.5D) - (+2D)
    DP3_ave(j2)=mean(dP3(n:Re_loc(j2)-1));         %(-2.5D) - (+3D)
    DP4_ave(j2)=mean(dP4(n:Re_loc(j2)-1));         %(-2.5D) - (+5D) (the main loss)

    %Pre-slot differential pressures, - represents upstream location
    US_DP1_ave(j2) = mean(USdP1(n:Re_loc(j2)-1));  %(-2.5D) - (-D)
    US_DP2_ave(j2) = mean(USdP2(n:Re_loc(j2)-1)); %(-2.5D) - (-2D)
    US_DP3_ave(j2) = mean(USdP3(n:Re_loc(j2)-1)); %(-2D) - (-D)

    %Post-slot differential pressures
    DS_DP1_ave(j2) = mean(DSdP1(n:Re_loc(j2)-1)); %(+D) - (+5D)
    DS_DP2_ave(j2) = mean(DSdP2(n:Re_loc(j2)-1)); %(+D) - (+3D)
    DS_DP3_ave(j2) = mean(DSdP3(n:Re_loc(j2)-1)); %(+D) - (+2D)
    DS_DP4_ave(j2) = mean(DSdP4(n:Re_loc(j2)-1)); %(+2D) - (+3D)
    DS_DP5_ave(j2) = mean(DSdP5(n:Re_loc(j2)-1)); %(+2D) - (+5D)
    DS_DP6_ave(j2) = mean(DSdP6(n:Re_loc(j2)-1)); %(+3D) - (+5D)

    %+++++
    %ERROR CALCULATION FOR UNCERTAINTY
    %+++++

```



```

%Sensitivity coefficients to calculate uncertainty of results
SC_K_DP(j2) = 2*rho*(A_o^2)/((m_dot_ave(j2)./60).^2);
SC_K_m_dot(j2) = -4*rho*(A_o^2).*DP4_ave(j2)./((m_dot_ave(j2)./60).^3);
SC_K_A_o(j2) = 4*rho*(A_o^2).*DP4_ave(j2)/((m_dot_ave(j2)/60).^3);
SC_Phi_Re(j2)=(sqrt(pi)/4).*((K_ave(j2)-(1-alpha^2))./(2*AR/(AR+1))*(1-alpha)));
SC_Phi_DP(j2) = (sqrt(pi)/4).*Re_ave(j2).*((2*AR/(AR+1))*(1-alpha)*(u_d(j2)^2))^(-1);
SC_Phi_alpha(j2) = ((sqrt(pi)/4).*Re_ave(j2)./(2*AR/(AR+1))).*((K_ave(j2)-alpha^2-1)./(1-alpha)^2);
%Precision errors (std.dev)
errP_P2_ave(j2)=((std(P2(n:Re_loc(j2)-1)))/sqrt(size(P2(n:Re_loc(j2)-1),1)))*6894.76;
%(-2.5D)
errP_P3_ave(j2)=((std(P3(n:Re_loc(j2)-1)))/sqrt(size(P3(n:Re_loc(j2)-1),1)))*6894.76;
%(-2D)
errP_P4_ave(j2)=((std(P4(n:Re_loc(j2)-1)))/sqrt(size(P4(n:Re_loc(j2)-1),1)))*6894.76;
%(-D)
errP_P5_ave(j2)=((std(P5(n:Re_loc(j2)-1)))/sqrt(size(P5(n:Re_loc(j2)-1),1)))*6894.76;
%(+D)
errP_P6_ave(j2)=((std(P6(n:Re_loc(j2)-1)))/sqrt(size(P6(n:Re_loc(j2)-1),1)))*6894.76;
%(+2D)
errP_P7_ave(j2)=((std(P7(n:Re_loc(j2)-1)))/sqrt(size(P7(n:Re_loc(j2)-1),1)))*6894.76;
%(+3D)
errP_P9_ave(j2)=((std(P9(n:Re_loc(j2)-1)))/sqrt(size(P9(n:Re_loc(j2)-1),1)))*6894.76;
%(+5D)
errP_MDot_ave(j2)=((std(m_dot(n:Re_loc(j2)-1)))/sqrt(size(m_dot(n:Re_loc(j2)-1),1)));
errP_Re_ave(j2)=((std(Re_o(n:Re_loc(j2)-1)))/sqrt(size(Re_o(n:Re_loc(j2)-1),1)));
errP_DP_ave(j2)= sqrt((errP_P2_ave(j2)^2)+ errP_P9_ave(j2)^2)/sqrt(size(P2(n:Re_loc(j2)-1),1));
errP_K_ave(j2)= sqrt(abs(((SC_K_DP(j2)*errP_DP_ave(j2))^2)+
((SC_K_m_dot(j2)*errP_MDot_ave(j2)^2))));
errP_Phi_ave(j2)= sqrt(((SC_Phi_DP(j2)*errP_DP_ave(j2))^2)+
((SC_Phi_Re(j2)*errP_Re_ave(j2)^2)))/sqrt(size(P2(n:Re_loc(j2)-1),1));

n = Re_loc(j2);
end

DP_ave = DP4_ave;
errB_corFM = 0.001; %coriolis flow meter accuracy
errB_A_o = 0.01; %accuracy area of slots
errB_DP_ave = sqrt(errB_P2^2 + errB_P9^2);
errB_K_ave = sqrt(((SC_K_DP*errB_DP_ave).^2) + ((SC_K_m_dot*errB_corFM).^2) +
((SC_K_A_o*errB_A_o).^2));
errB_Re = 0.02; %C H E C K
errB_alpha = 0.01;
errB_Phi_ave = sqrt(((SC_Phi_Re*errB_Re).^2) + ((SC_Phi_DP*errB_DP_ave).^2) +
((SC_Phi_alpha*errB_alpha).^2));
for i3 = 1:size(errP_DP_ave,1)
    U95_DP(i3) = 2.*(sqrt(errP_DP_ave(i3).^2 + errB_DP_ave^2));
end

for i4 = 1:size(errP_K_ave,1)
    U95_K(i4) = 2.*(sqrt(errP_K_ave(i4).^2 + errB_K_ave(i4).^2));
end

```

```

for i5 = 1:size(errP_Phi_ave,1)
    U95_Phi(i5) = 2.*(sqrt(errP_Phi_ave(i5).^2 + errB_Phi_ave(i5).^2));
end
if(sav_data ==1)
save(['G:\My Drive\work from home\Open_Slot_Experiments\Averaged_Summary\'
fname], 'Re_ave', 'DP_ave', 'Phi_ave', 'K_ave', 'K_Fit', 'other', 'K_Fit_2', 'Re_k2', 'Re_k')
save(['G:\My Drive\work from home\Open_Slot_Experiments\Averaged_Summary\'
fname7], 'DP1_ave', 'DP2_ave', 'DP3_ave', 'DP4_ave', ...
    'US_DP1_ave', 'US_DP2_ave', 'US_DP3_ave', ...
    'DS_DP1_ave', 'DS_DP2_ave', 'DS_DP3_ave', 'DS_DP4_ave', 'DS_DP5_ave', 'DS_DP6_ave')
save(['G:\My Drive\work from home\Open_Slot_Experiments\Averaged_Summary\'
fname9], 'errP_P2_ave', 'errP_P3_ave', 'errP_P4_ave', ...

'errP_P5_ave', 'errP_P6_ave', 'errP_P7_ave', 'errP_P9_ave', 'errP_DP_ave', 'errB_DP_ave', 'U95_DP', 'U95
_K', 'U95_Phi')

%=====
%   PRESSURE DISTRIBUTION ALONG THE PIPE
%=====
X_Locs = [1 2 3 4 5 6 7];
data_str2 = [2 3 4 5 6 7 9];
X_Loc_plot = [2.5 3 4 6.13 7.13 8.13 10.13];
data_str3 = '_ave';
data_str4 = '_raw';
font_n = 'Times';
font_s = 16;
marker_s = 5;
line_w = 1.5;

for i6 = 1:size(X_Locs,2)
    ave_Pdata_string = strcat('P', num2str(data_str2(1,X_Locs(i6))), data_str3);
    ave_p_Data(:,i6) = (eval(ave_Pdata_string)*6894.76)+101325;
    Pdata_string = strcat('P', num2str(data_str2(1,X_Locs(i6))), data_str4);
    p_Data(:,i6) = (eval(Pdata_string)*6894.76)+101325;
end

for j3=1:length(u_d_ave)
    norm_p_Data(j3,:) = p_Data(j3,:)/(mu*u_d(j3,:));
    ave_norm_p_Data(j3,:) = ave_p_Data(j3,:)/(mu*u_d_ave(j3,:));
    norm_p_Data_2(j3,:) = p_Data(j3,:)/(0.5*(u_d_ave(j3,:).^2)*rho); % normalized by KE
    ave_norm_p_Data_2(j3,:) = ave_p_Data(j3,:)/(0.5*(u_d_ave(j3,:).^2)*rho);
end

for i7= 1:size(X_Locs,2)
    X_loc_array(:,i7) = repelem(X_Loc_plot(i7),size(p_Data,1));
    X_loc_array_ave(:,i7) = repelem(X_Loc_plot(i7),size(ave_p_Data,1));
    np_X_loc_array(:,i7) = repelem(X_Loc_plot(i7),size(norm_p_Data,1));
    np2_X_loc_array(:,i7) = repelem(X_Loc_plot(i7),size(norm_p_Data_2,1));
    anp_X_loc_array(:,i7) = repelem(X_Loc_plot(i7),size(ave_norm_p_Data,1));
    anp2_X_loc_array(:,i7) = repelem(X_Loc_plot(i7),size(ave_norm_p_Data_2,1));
end
save(['G:\My Drive\work from home\Open_Slot_Experiments\Averaged_Summary\'
fname11], 'X_loc_array', 'X_loc_array_ave', 'anp2_X_loc_array', ...

```

```

        'anp_X_loc_array', 'ave_norm_p_Data', 'ave_norm_p_Data_2', 'ave_p_Data',
        'norm_p_Data', 'norm_p_Data_2', 'np2_X_loc_array', 'np_X_loc_array', 'p_Data')
end

```

```

%=====
%-----PHI FIT FOR erf (29/Dec/2018) -----
%=====

% openfig('Phi_erf_fit.fig')
%
% if((i0==1))||(i0==4)||(i0==7))
%     clf
% end

% Re_dist= floor(length(Re_loc)/2)-1;
% Re_dist= 100;
% %=====
% %Re points 1
% %=====
% %
% Re_points = [0.05; 0.06; 0.05 ;...
%             0.07 ; 0.05; 0.07;...
%             0.04; 0.05; 0.075];

%=====
%Re points 2
%=====
% Re_points = [0.05 0.075; 0.06 0.075 ; 0.05 0.075 ;...
%             0.07 0.08 ; 0.05 0.075 ; 0.07 0.08 ;...
%             0.04 0.05 ; 0.05 0.075 ; 0.05 0.075 ];
% %=====
% %Re points 3
% % %=====
Re_points = [0.05 0.075 0.09; 0.06 0.075 0.09; 0.05 0.075 0.08;...
            0.07 0.08 0.1; 0.05 0.075 0.1; 0.07 0.08 0.1;...
            0.04 0.05 0.07; 0.05 0.075 0.09; 0.05 0.075 0.08];

% Re_points_nom = [1 2 3];
% Re_points = 0.05:0.005:0.08;
Re_points_nom = 1:1:length(Re_points);
Re_points = repmat(Re_points',1,9);
AR_names = cell(length(Re_points(:,i0)),1);
Re_names = cell(length(Re_points(:,i0)),1);
figure()
for i6 = 1:length(Re_points(:,i0))
    AR_names{i6} = strcat('AR_',num2str(AR_pts(i0)));
    Re_names{i6} = strcat('Re_',num2str(Re_points_nom(i6)));
    DRe_ind.(Re_names{i6}) = abs(Re_o - Re_points(i6,i0));
    if (i0==1)
        DRe_crit = 0.00175;
    elseif(i0==2)
        DRe_crit = 0.01;
    end
end

```

```

DRe_crit = 0.002;
Re_ind.(Re_names{i6}) = find((DRe_ind.(Re_names{i6})) < (DRe_crit));
phi_c1= Re_ind.(Re_names{i6})(1);
phi_c2 = Re_ind.(Re_names{i6})(end);
Re_mean.(Re_names{i6}) = mean(Re_o(phi_c1:phi_c2));
Le.(Re_names{i6}) = Re_mean.(Re_names{i6})*0.05*d_h;
u_u_data.(Re_names{i6})= (u_u(phi_c1:phi_c2));
u_d_data.(Re_names{i6})= (u_d(phi_c1:phi_c2));
du_i.(Re_names{i6})= u_d_data.(Re_names{i6})- u_u_data.(Re_names{i6});
number_of_points.(Re_names{i6})= size(u_d_data.(Re_names{i6}),1);
x_c_1 = -5*b;
%       x_c_2 = 0;
x_c_2 = Le.(Re_names{i6})/b;
x_czone = linspace(x_c_1, x_c_2, (number_of_points.(Re_names{i6})))';
%       phi_converge(:,i6)= mean(phi_m(phi_c1:phi_c2))*ones(length(x_czone),1);
avg_phi.(Re_names{i6})= mean((phi_m(phi_c1:phi_c2)/max(phi_m(phi_c1:phi_c2))));
%
ph_epsilon.(Re_names{i6}) = (avg_phi.(Re_names{i6})/b)*(x_czone);
%       ph_epsilon.(Re_names{i6}) =
ph_epsilon.(Re_names{i6})/max(ph_epsilon.(Re_names{i6}));

u_d_u.(Re_names{i6}) =(u_u_data.(Re_names{i6})./(u_d_data.(Re_names{i6})));
u_d_u.(Re_names{i6}) = u_d_u.(Re_names{i6})/max(u_d_u.(Re_names{i6}));

fit_options = fitoptions('Method','NonlinearLeastSquares');
fit_type = fitype('1-a*erf(x)', 'options', fit_options);

start = 0;

[Phi_erf_fit,erf_fit_other] = fit(ph_epsilon.(Re_names{i6}),u_d_u.(Re_names{i6}),
fit_type, 'StartPoint',start);
%       [Phi_erf_fit,erf_fit_other] = fit(ph_epsilon.(Re_names{i6}),0.5*u_d_u.(Re_names{i6}),
fit_type)
u_x_fit.(Re_names{i6}) = u_u_data.(Re_names{i6}).*(Phi_erf_fit
(ph_epsilon.(Re_names{i6})));
%       (u_u_data.(Re_names{i6})./u_d_data.(Re_names{i6}))
%       u_x_fit.(Re_names{i6}) = u_x_fit.(Re_names{i6})*du_i.(Re_names{i6});
u_x_exp.(Re_names{i6}) = (u_u_data.(Re_names{i6})./u_d_data.(Re_names{i6}))...
+
(du_i.(Re_names{i6})./u_d_data.(Re_names{i6})).*erf((ph_epsilon.(Re_names{i6})));
%       u_x_exp.(Re_names{i6}) = 0.5* u_x_exp.(Re_names{i6});
%=====
%Calculate PDF from CDF

%       erf_slope = 2.*exp((- Phi_erf_value1(:,i6)).^2)./sqrt(pi);
%       L_e(:,i6) = (avg_phi(:,i6)/b)*(0.05*d_h*mean(Re_o(phi_c1:phi_c2)));
%       mu(:,i6) = mean(L_e(:,i6)./max(L_e(:,i6)));
%       sigma(:,i6) = .11*mu(:,i6);
%       delta (:,i6) = ph_epsilon(:,i6);
%       CDF(:,i6) = .5*[mean(u_u(phi_c1:phi_c2))+mean(du_i(:,i6))...
%       *erf((delta(:,i6)-mu(:,i6))/(sqrt(2*sigma(:,i6).^2)))]);
%=====

```

```

        PDF_exp.(Re_names{i6}) = diff(u_x_exp.(Re_names{i6})) ./
diff(ph_epsilon.(Re_names{i6}));
        PDF_fit.(Re_names{i6}) = diff(u_x_fit.(Re_names{i6})) ./
diff(ph_epsilon.(Re_names{i6}));
        new_fipsilon.(Re_names{i6}) = ph_epsilon.(Re_names{i6})(1:end-1) +
diff(ph_epsilon.(Re_names{i6}))./2;
%         figure()
%         plot(delta(:,i6),CDF(:,i6))

%         xlim([x_c_1, 0])
%         u_pts = 300;
%         u_exp_pts = 5;
AR_clr = [0 0 0; 0 0 255; 0 128 0;...
          255 0 0; 255 0 255; 119 136 153;...
          204 204 0; 0 255 0; 210 105 30]./255;
%     end
    if i0==1
        line = 'o';
    elseif i0==2
        line = 'o';
    elseif i0==3
        line = 'x';
    elseif i0==4
        line = '^';
    elseif i0==5
        line='v';
    elseif i0==6
        line='>';
    elseif i0==7 %|| (i0==7)
        line='<';
    elseif i0==8
        line = 'd';
    elseif i0==9
        line = 's';
    end

%         ylabel('\it{u}(x): cdf(x)','Interpreter','tex')
%         legend('\it{u}(\epsilon): experiment','\it{u}(\epsilon): erf fit(\epsilon)')

%

plot(ph_epsilon.(Re_names{i6}),((1+u_x_exp.(Re_names{i6}))./max(1+u_x_exp.(Re_names{i6}))),'-'.
, (avg_phi.(Re_names{i6}))*x_c_2, mean(u_d_data.(Re_names{i6})./max(u_d_data.(Re_names{i6}))), 's'
...
        , 'Color', AR_clr(i0,:), 'Linewidth', 1.5)
vline(x_c_2)
xlabel('\it{\epsilon}','Interpreter','tex')
ylabel('\bar{u}(x)','Interpreter','Latex')
legend('\it{u}(\epsilon): experiment','\it{u}(\epsilon): erf fit(\epsilon)'...
        , 'Location', 'Northwest')
    hold on
% %         saveas(gcf, 'YY_fig_u(x)_CDF.fig')

```

```

%
% %           openfig('YY_fig_u(x)_PDF.fig')
%           hold on
%           plot(new_fips1on.(Re_names{i6}),PDF_exp.(Re_names{i6}),'-'. ...
%               , 'Color', AR_clr(i0,:), 'Linewidth', 1.5);
%           xlabel('\it{\epsilon}', 'Interpreter', 'tex')
%           ylabel('\bar{u}(x)', 'Interpreter', 'Latex')
%           legend('\it{u}(\epsilon): experiment', '\it{u}(\epsilon): erf fit(\epsilon)' ...
%               , 'Location', 'NorthWest')
%           saveas(gcf, 'YY_fig_u(x)_PDF.fig')
end

% saveas(gcf, 'Phi_erf_fit.fig')
% if((i0==4)||(i0==7)||(i0==9))
%   sav_string = strcat('Phi_erf_fit_below_AR', num2str(AR_in));
%   saveas(gcf, sav_string)
% end
min(Re_o)
max(Re_o)
max(t)
% close all
clc
i0
AR_in
% if(sav_data==1)
% clearvars -except Font Font_size Linewidth st Re_c folder files sav_data Line_w AR_pts
% end

% openfig('Phi_erf_fit.fig')
end
% tilefigs()

```

```

%
% %%%%%%%%%%
% % what : 1. Plot Log(Re) vs Log(K).from experimental data and developed model
% %      2. Perform the Factor Rotation Analysis to correct for the angular deviation
% %
% % who : Yishak Yusuf
% % when : v1 (Decempber, 2017)
% %      v2 (February, 2018)
% %%%%%%%%%%

```

```

close all
clear all
clc

```

```

%=====
%-----VARIABLES FOR PLOT SETTINGS -----
%=====

```

```

Font = 'Times';
Font_size = 22;
Font_legend = 16; %for llegend
Line_w = 1.5;
m_size = 1.4;
x_plot_range= [0.01 0.1];
y_plot_range= [-inf inf];
sho_legend = 1;
% x_plot_range= [0.01 0.1];
% y_plot_range = [0 1e6];
% scale = 'linear';
% scale = 'log';

```

```

set(0, 'DefaultAxesFontName', Font);
set(0, 'DefaultUIControlFontName', Font);
set(0, 'defaultuitableFontName', Font);
set(0, 'defaultTextFontName', Font);
set(0, 'defaultuipanelFontName', Font);
set(0, 'defaultTextFontSize', Font_size);
set(0, 'DefaultLineLinewidth',Line_w)
set(0, 'DefaultLineMarkerSize',m_size)
% set(0, 'defaulttextinterpreter','tex');
set(gcf,'Color','w')
% set(findall(gcf,'type','text'),'FontSize',Font_size)

```

```

%=====
%-----LOADING SAVED FILES-----
%=====

```

```

AR1_1 = load('G:\My Drive\work from
home\Open_Slot_Experiments\Averaged_Summary\Averaged_Summary_AR001_R2.mat'); %OK
AR37_1 = load('G:\My Drive\work from
home\Open_Slot_Experiments\Averaged_Summary\Averaged_Summary_AR037_R2.mat');
AR50_1 = load('G:\My Drive\work from
home\Open_Slot_Experiments\Averaged_Summary\Averaged_Summary_AR050_R2.mat');
AR72_1 = load('G:\My Drive\work from
home\Open_Slot_Experiments\Averaged_Summary\Averaged_Summary_AR072_RPT.mat');

```

```

AR108_1 = load('G:\My Drive\work from
home\Open_Slot_Experiments\Averaged_Summary\Averaged_Summary_AR108_R3.mat');
AR143_1 = load('G:\My Drive\work from
home\Open_Slot_Experiments\Averaged_Summary\Averaged_Summary_AR143_R3.mat');
AR179_1 = load('G:\My Drive\work from
home\Open_Slot_Experiments\Averaged_Summary\Averaged_Summary_AR179_R1.mat');
AR214_1 = load('G:\My Drive\work from
home\Open_Slot_Experiments\Averaged_Summary\Averaged_Summary_AR214_R2.mat');
AR250_1 = load('G:\My Drive\work from
home\Open_Slot_Experiments\Averaged_Summary\Averaged_Summary_AR250_R2.mat');

errAR1 = load('G:\My Drive\work from
home\Open_Slot_Experiments\Averaged_Summary\Uncertainty_DeltaP_AR001_R2.mat');
errAR37 = load('G:\My Drive\work from
home\Open_Slot_Experiments\Averaged_Summary\Uncertainty_DeltaP_AR037_R2.mat');
errAR50 = load('G:\My Drive\work from
home\Open_Slot_Experiments\Averaged_Summary\Uncertainty_DeltaP_AR050_R2.mat');
errAR72 = load('G:\My Drive\work from
home\Open_Slot_Experiments\Averaged_Summary\Uncertainty_DeltaP_AR072_RPT.mat');
errAR108= load('G:\My Drive\work from
home\Open_Slot_Experiments\Averaged_Summary\Uncertainty_DeltaP_AR108_R3.mat');
errAR143 = load('G:\My Drive\work from
home\Open_Slot_Experiments\Averaged_Summary\Uncertainty_DeltaP_AR143_R3.mat');
errAR179 = load('G:\My Drive\work from
home\Open_Slot_Experiments\Averaged_Summary\Uncertainty_DeltaP_AR179_R1.mat');
errAR214 = load('G:\My Drive\work from
home\Open_Slot_Experiments\Averaged_Summary\Uncertainty_DeltaP_AR214_R2.mat');
errAR250 = load('G:\My Drive\work from
home\Open_Slot_Experiments\Averaged_Summary\Uncertainty_DeltaP_AR250_R2.mat');

%=====
%-----GLOBAL VARIABLES-----
%=====
Re_range = [0.01 0.1];
b = [3 0.5 0.424 0.35 0.29 0.25 0.22 0.2 0.19]./1000; %widths of slots
a = [3 18.1 21.21 25.5 31.1 35.9 40.1 43.9 47.5]./1000; %lengths of slots
% AR = [1 37 50 72 108 143 179 214 250];
AR_pts = [1 37 50 72 108 143 179 214 250];

%a= [63.5 63.5 63.5 63.5 63.5 63.5]./1000;
Dh = (2.*b.*a)./(b+a); %hydraulic diameters
D = 76/1000; %diameter of pipe
L = 10/1000;
% alpha = (a.*b)/(pi*D^2/4); %area ratio
alpha = 0.002;
rho = 884.3; %density (kg/m3)
mu = 1.8; % viscosity (Pa.s)
Dh = (2.*b.*a)./(b+a); %hydraulic diameters
D= 76/1000; %diameter of pipe
TD = T./Dh; %thickness to diameter ratio
beta=Dh./D; % "beta ratio" ratio of hydraulic diamter to diameter of the pipe
a_p = (pi*D^2/4); %pipe area
alpha = (a.*b)/(pi*D^2/4); %area ratio

```



```

AR = a./b; % aspect ratio
s=size(AR);
% AR_pts = [1 37 50 72 108 143 179 214 250];
mu = 1.8; %Pa.s
rho = 884.3; %kg/m3
nu = mu/rho;

%parameters to plot the model
Re_range = [0.01 0.1];
Re_points = 1000;
Re =(linspace(Re_range(1), Re_range(end),Re_points))';
r=size(Re);
ud=zeros(r(2),size(AR,2));
uu=zeros(r(2),size(AR,2));
phi_m = zeros(r(2),size(AR,2));
phi_m2 = zeros(r(2),size(AR,2));
erf_arg = zeros(r(2),size(AR,2));
x_location = -2.5*D;
xu=x_location;
xd=0;
% erf_DP_term = -2*DP/rho;
erf_DP_term = -10;
dx = xd-xu;
% dx = 0.0057;

for j0=1:1:size(AR,2)
    DP(:,j0) = (29736.30554+(415.4395163.*AR(j0))); %from simplified linear approximation of
    DP vs. AR from Fig.5 PoF paper.
    % phi_m2(:,j0) = (0.018166*AR(j0)^2) - 6.1303* AR(j0) + 506.1669; % from the phi_fit in
    YY_AUTO_Plot_Data_and_phi_FIT...
    % phi_m2(:,j0)= (0.01844*AR(j0)^2) - 6.2738* AR(j0) + 523.3247; % from the phi_fit in
    YY_AUTO_Plot_Data_and_phi_FIT...
    % phi_m2(:,j0)= (0.0073313*AR(j0)^2) - 0.30697* AR(j0) + 58.851; % (R2=0.86 for Re=0.05) from
    the phi_fit in YY_AUTO_Plot_Data_and_phi_FIT...
    % phi_m2(:,j0)= (0.017823*AR(j0)^2) - 6.2484* AR(j0) + 546.4179; % (R2=0.86 for Re=0.05)
    % phi_m2(:,j0) = (391.2241/AR(j0)^2) - 0.0143868*AR(j0) + 41.6847; (R2=0.99)
    % phi_m2(:,j0) = (600/AR(j0)^2) - 0.05*AR(j0) + 50; %(R2=0.99412 for Re = 0.1)
    phi_m2(:,j0) = (30/AR(j0)^2) + (365.3/AR(j0)) + 34.82; %(R2=0.99822)
    phi_m2(:,j0) = 33*((2*(AR(j0))/(AR(j0)+1))^(-2) + 330*((2*(AR(j0))/(AR(j0)+1))^(-1) + 33;
    %(R2=0.99822)
    phi_m2_a(:,j0) = 33*((2*(AR(j0))/(AR(j0)+1))^(-2); %(R2=0.99822)
    phi_m2_b(:,j0) = 330*((2*(AR(j0))/(AR(j0)+1))^(-1); %(R2=0.99822)
    phi_m2(:,j0) = 33*(AR(j0)^(-2) + 330*(AR(j0)^(-1) + 33; %(R2=0.99822)

end

%%%%%%%%%%%%%%%%%%%%%%%%%%%%%%%%%%%%%%%%%%%%%%%%%%%%%%%%%%%%%%%%%%%%%%%%
%*****Phi - Analytical*****
%%%%%%%%%%%%%%%%%%%%%%%%%%%%%%%%%%%%%%%%%%%%%%%%%%%%%%%%%%%%%%%%%%%%%%%%
for j=1:1:size(AR,2)
    for i = 1:1:r(1)
        ud(i,j) = Re(i,1).*(nu./(Dh(1,j)));
        uu(i,j) = Re(i,1).*(nu/D);
        du(i,j) = ud(i,j)-uu(i,j);
    end
end

```

```

erf_DP_term(i,j) = (2/rho).*(DP(1,j));
%   erf_DP_term(i,j) = -100;

erf_arg(i,j)= (ud(i,j)- uu(i,j)).*((erf_DP_term(i,j) -(2*nu.*((du(i,j))/dx)))^-1/2);
erf_arg_RHS_a(i,j) = (du(i,j));
erf_arg_RHS_b(i,j) = ((erf_DP_term(i,j) -(2*nu.*((du(i,j))/dx)))^-1/2);
erf_arg_RHS_b2(i,j) = ((du(i,j))/dx);
erf_arg_RHS_b1(i,j) = -(2*nu.*((du(i,j))/dx));

phi_m(i,j) = (b(1,j)/dx).*erfinv(erf_arg(i,j));   %erfinv(-1)= -inf; erfinv(0)   =0
erfinv(1)=inf
%   phi_m(i,j) = (b(1,j)/dx).*(AR(j)^-2)+ (AR(j)^-1);
%       phi_m_RHS_a(i,j) = ((b(1,j)/dx);
%       phi_m_RHS_b(i,j) = erfinv(erf_arg(i,j));
%   inv_erf(i,j) = sqrt((1/0.7182)*log(1.557/erf(erf_arg(i,j)))); %approxiamtion of erfinv
Greene (1989 p. 226)
%   phi_m(i,j) = (b(1,j)/dx).*inv_erf(i,j);
%

end
end

```

```

for j2 = 1:1:size(AR,2)
    for i2=1:1:r(1)
        if (j2<5)
%           NDP_Yishak(i2,j2) =((1-
alpha(j2).^2)+(((4*((phi_m(i2,j2))))/(sqrt(pi).*Re(i2))))*(2*((AR(j2))/(AR(j2)+1)).*(1-
alpha(j2))))); %alpha, area ratio = area of slot/ area of pipe
%           NDP_Yishak(i2,j2) =((1-
alpha(j2).^2)+(((4*((phi_m(i2,j2))))/(sqrt(pi).*Re(i2)^2))))*(2*((AR(j2))/(AR(j2)+1)).*(1-
alpha(j2))))); %alpha, area ratio = area of slot/ area of pipe
            NDP_Yishak(i2,j2) =((1-
alpha(j2).^2)+(((4*((phi_m2(1,j2))))/(sqrt(pi).*Re(i2))))*(2*((AR(j2))/(AR(j2)+1)).*(1-
alpha(j2))))); %alpha, area ratio = area of slot/ area of pipe
        else
%           NDP_Yishak(i2,j2) =((1-
alpha(j2).^2)+(((4*((phi_m(i2,j2))))/(sqrt(pi).*Re(i2))))*(2*((AR(j2))/(AR(j2)+1)).*(1-
alpha(j2))))); %alpha, area ratio = area of slot/ area of pipe
%           NDP_Yishak(i2,j2) =((1-
alpha(j2).^2)+(((4*((phi_m(i2,j2))))/(sqrt(pi).*Re(i2)^2))))*(2*((AR(j2))/(AR(j2)+1)).*(1-
alpha(j2)))));
            NDP_Yishak(i2,j2) =((1-
alpha(j2).^2)+(((4*((phi_m2(1,j2))))/(sqrt(pi).*Re(i2))))*(2*((AR(j2))/(AR(j2)+1)).*(1-
alpha(j2))))); %alpha, area ratio = area of slot/ area of pipe
        end
        NDP_RHS_a(i2,j2) =0.5*(1-alpha(j2).^2);   %ok
        NDP_RHS_b(i2,j2) = (4*((phi_m(i2,j2))))/(sqrt(pi).*Re(i2));

        NDP_RHS_c(i2,j2) = 0.5*(2*(AR(j2)))/(AR(j2)+1);   %ok 1<= NDP_RHS_c <= 1.992

        NDP_RHS_d(i2,j2)= 0.5*(1-alpha(j2));   %ok
        NDP_Euler (i2, j2) = (abs(DP(1,j2))/(0.5*rho.*ud(i2,j2)^2));
    end
end

```

```

end
close all
figure('Name','Re vs. K: Model')
% box on
% scale = 'linear';
scale = 'log';
plot(Re, (NDP_Yishak(:,1)),'-k') %AR1_ReK(:,1),AR1_ReK(:,2))
hold on
plot(Re, (NDP_Yishak(:,2)),'-b')%AR37_ReK(:,1),AR37_ReK(:,2))
plot(Re, (NDP_Yishak(:,3)),'-', 'Color',[0 128 0]/255)%AR50_ReK(:,1),AR50_ReK(:,2))
plot(Re, (NDP_Yishak(:,4)),'-r')%AR72_ReK(:,1),AR72_ReK(:,2))
plot(Re, (NDP_Yishak(:,5)),'-m')%AR108_ReK(:,1),AR108_ReK(:,2));
plot(Re, (NDP_Yishak(:,6)),'-', 'Color',[119 136 153]/255)%AR143_ReK(:,1),AR143_ReK(:,2));
plot(Re, (NDP_Yishak(:,7)),'-', 'Color',[204 204 0]/255)%AR179_ReK(:,1),AR179_ReK(:,2));
plot(Re, (NDP_Yishak(:,8)),'-g')%AR214_ReK(:,1),AR214_ReK(:,2));
plot(Re, (NDP_Yishak(:,9)),'-', 'Color',[210 105 30]/255)%AR250_ReK(:,1),AR250_ReK(:,2));

grid on
set(gca,'XScale',scale);
set(gca,'YScale',scale);

xlabel('log({\it{Re}})');
ylabel('log({\it{K}})');
xlim(x_plot_range)
ylim(y_plot_range)
grid on
if sho_legend == 1
legend({'{\it{AR}}= 1 ', '{\it{AR}} = 37', '{\it{AR}} = 50', ...
      '{\it{AR}} = 72', '{\it{AR}} = 108', '{\it{AR}}= 143', ...
      '{\it{AR}} = 179', '{\it{AR}} = 214', '{\it{AR}} = 250'}, ...
      'Orientation','Vertical','FontSize',Font_legend)
end

set(gca,'TickLabelInterpreter','latex');
set(gca,'FontName',Font,'FontSize',Font_size)
set(gcf,'units','inches','position',[0,0,4,4.5])
% hold all
dk=0;
AR_clr = [0 0 0; 0 0 255; 0 128 0; 255 0 0; 255 0 255; ...
          119 136 153; 204 204 0; 0 255 0; 210 105 30]/255;
figure('Name','log(K)=mlog(Re)+k')
scale = 'linear'
for ii=1:length(AR_pts)
    AR_names{ii} = strcat('AR',num2str(AR_pts(ii)));
    logfit_model(:,ii)= polyfit(log10(Re), log10(NDP_Yishak(:,ii)),1);
    logfit_exp(:,ii) = polyfit(log10(eval(strcat('AR',num2str(AR_pts(ii)),'_Re'))),
    log10(eval(strcat('AR',num2str(AR_pts(ii)),'_K'))),1);
    mlog_model(:,ii) = logfit_model(1,ii);
    mlog_exp(:,ii) = logfit_exp(1,ii);
    klog_model(:,ii) = logfit_model(2,ii);
    klog_exp(:,ii) = logfit_exp(2,ii);
    KLine_model(:,ii) = (mlog_model(:,ii)).*log10(Re)+ log10(klog_model(:,ii));
    KLine_exp(:,ii) = (mlog_exp(:,ii)).*log10(Re)+ log10(klog_exp(:,ii));
%     DK (:,ii) = abs((KLine_exp(:,ii)- KLine_model(:,ii))./KLine_exp(:,ii))*100;

```

```

DK(:,ii)          = ((KLine_exp(:,ii))-KLine_model(:,ii));
%   DK(:,ii)      = (((KLine_exp(:,ii)- KLine_model(:,ii))));
Avg_DK(:,ii)     = mean(KLine_exp(:,ii)- KLine_model(:,ii));
%Notice the multiplication by 1/ln(10), seen in Stuve (2004)
semilogy(10.^(log10(Re)),10.^(log10(DK(:,ii)))./log(10),'-', 'color',AR_clr(ii,:))
xlabel('\it{Re}');
ylabel('\it{\epsilon}_{raw}', 'Interpreter','Tex');
set(gca,'XScale',scale);
set(gca,'YScale',scale);
xlim([0.01 0.1])
ylim([0 1])
grid on
if (sho_legend==1)
legend('mean difference','Linear fit')
end
set(gca,'FontName',Font,'FontSize',Font_size)
% plot(log10(Re), KLine_exp(:,ii)- KLine_model(:,ii),'+')
hold on
end

if sho_legend == 1
legend({'\it{AR} = 1 ', '\it{AR} = 37', '\it{AR} = 50', ...
        '\it{AR} = 72', '\it{AR} = 108', '\it{AR} = 143', ...
        '\it{AR} = 179', '\it{AR} = 214', '\it{AR} = 250'}, ...
        'Orientation','Vertical','FontSize',Font_legend)
end

%+++++
%                               THE ROTATION
%+++++
for i4=1:length(AR_pts)
    AR_names{i4} = strcat('AR',num2str(AR_pts(i4)));
    const(:,i4) = polyfit(log10(Re), log10(nDP_Yishak(:,i4)),1);
    %   const(:,i4) = polyfit((Re), (nDP_Yishak(:,i4)),1);
    const2(:,i4) = polyfit(log10(eval(strcat('AR',num2str(AR_pts(i4)),'_1.Re_k2(:,1)'))),
log10(eval(strcat('AR',num2str(AR_pts(i4)),'_1.Re_k2(:,2)'))),1);
    m(:,i4) = const(1,i4);
    m2(:,i4) = const2(1,i4);
    k(:,i4) = const(2,i4);
    k2(:,i4) = const2(2,i4);
    LnDP_Yishak(:,i4) = (m(:,i4)).*log10(Re)+(k(:,i4));
    %   LK_exp.(AR_names{i4}) =
    (eval(strcat('AR',num2str(AR_pts(i4)),'_1.Re_k2(:,1)'))).^m2(:,i4).*10^(k2(:,i4));
    LK_exp.(AR_names{i4}) =
m2(:,i4).*log10(eval(strcat('AR',num2str(AR_pts(i4)),'_1.Re_k2(:,1)')))+(k2(:,i4));
    L1.(AR_names{i4})= horzcat(log10(Re), log10(nDP_Yishak(:,i4)));
    %   L1.(AR_names{i4}) = horzcat(eval(strcat('log10(AR',num2str(AR_pts(i4)),'_1.Re_k2(:,1)'))),
LK_exp.(AR_names{i4}));
    L2.(AR_names{i4}) =horzcat(log10(eval(strcat('AR',num2str(AR_pts(i4)),'_1.Re_k2(:,1)'))),
log10(eval(strcat('AR',num2str(AR_pts(i4)),'_1.Re_k2(:,2)'))));
    Intersection.(AR_names{i4})= InterX(L1.(AR_names{i4}),L2.(AR_names{i4}));
    m = abs(m);
    m2 = abs(m2);
    slope_ratio(i4)= ((m2(:,i4)-m(:,i4)))/(1-(m(:,i4).*m2(:,i4)));

```

```

theta_raw.(AR_names{i4}) = atan(slope_ratio(i4))*pi./180;
theta_factor = 20;
model_theta.(AR_names{i4}) = theta_factor*theta_raw.(AR_names{i4});

ARtheta(i4) = model_theta.(AR_names{i4}) ;
ARtheta_raw(i4) = theta_raw.(AR_names{i4}) ;

%
V.(AR_names{i4}) = horzcat(L1.(AR_names{i4}), zeros(length(L1.(AR_names{i4})),1));
V_centre.(AR_names{i4}) = mean(V.(AR_names{i4}),1); % C H K?
V_c.(AR_names{i4}) = V.(AR_names{i4})-
ones(length(V.(AR_names{i4})),1)*V_centre.(AR_names{i4});
Vc.(AR_names{i4})=V.(AR_names{i4})-
ones(length(V.(AR_names{i4}')),1)*V_centre.(AR_names{i4}); %Centering coordinates
E.(AR_names{i4}) = [0 0 model_theta.(AR_names{i4})]; %Euler angles for X,Y,Z-axis rotations

% %Direction Cosines (rotation matrix) construction
Rx.(AR_names{i4})=[1      0      0;...
                  0      cos(E.(AR_names{i4})(1)) -sin(E.(AR_names{i4})(1));...
                  0      sin(E.(AR_names{i4})(1))  cos(E.(AR_names{i4})(1))]; % x-axis
rotation
Ry.(AR_names{i4})=[cos(E.(AR_names{i4})(2))  0      sin(E.(AR_names{i4})(2));...
                  0      1      0;...
                  -sin(E.(AR_names{i4})(2))  0      cos(E.(AR_names{i4})(2))]; % y-axis
rotation
Rz.(AR_names{i4})=[cos(E.(AR_names{i4})(3)) -sin(E.(AR_names{i4})(3)) 0;...
                  sin(E.(AR_names{i4})(3))  cos(E.(AR_names{i4})(3)) 0;...
                  0      0      1]; % z-axis
rotation

R.(AR_names{i4})=Rx.(AR_names{i4})*Ry.(AR_names{i4})*Rz.(AR_names{i4}); %Rotation matrix
Vrc.(AR_names{i4})=[R.(AR_names{i4})*V_c.(AR_names{i4})]'; %Rotating centred coordinates
Vruc.(AR_names{i4})=[R.(AR_names{i4})*V.(AR_names{i4})]'; %Rotating un-centred coordinates
Vr.(AR_names{i4})=Vrc.(AR_names{i4}) + ones(size(V.(AR_names{i4}),1),1)*V_centre.(AR_names{i4});
%Shifting back to original location
% Vr.(AR_names{i4})=Vruc.(AR_names{i4})+
ones(size(V.(AR_names{i4}),1),1)*V_centre.(AR_names{i4}); %Shifting back to original location
end

```

```

x_plot_range= [-inf inf];
y_plot_range= [-inf inf];
%Checking Rodriques' equation and trend in Theta
ARtheta = 0.5*ARtheta;
for j3=1:length(ARtheta)
EE.(AR_names{j3}) = 0.5*[E.(AR_names{j3})*E.(AR_names{j3})]';
skew_theta.(AR_names{j3})=[0 model_theta.(AR_names{j3}) 0 ;model_theta.(AR_names{j3}) 0 0; 0 0 0
];
R_theta.(AR_names{j3}) = eye(3) +
((sin(model_theta.(AR_names{j3}))/model_theta.(AR_names{j3}))*skew_theta.(AR_names{j3})) + (((1-
cos(model_theta.(AR_names{j3}))/model_theta.(AR_names{j3})^2))*(EE.(AR_names{j3})- eye(3)));
K_chk.(AR_names{j3}) = [R_theta.(AR_names{j3})*V_c.(AR_names{j3})]';
K_chk.(AR_names{j3}) =
K_chk.(AR_names{j3})+ones(size(V.(AR_names{j3}),1),1)*V_centre.(AR_names{j3});
end

```

```

figure('Name','log10(Re) vs. log10(K):Model+Exp (Raw)')
% box on
hold on
% scale = 'linear';
scale = 'log';
plot(10.^(log10(Re)), 10.^(log10(nDP_Yishak(:,1))), '-k') %AR1_ReK(:,1),AR1_ReK(:,2))
plot(10.^(log10(Re)), 10.^(log10(nDP_Yishak(:,2))), '-b')%AR37_ReK(:,1),AR37_ReK(:,2))
plot(10.^(log10(Re)), 10.^(log10(nDP_Yishak(:,3))), '-', 'color',[0 128
0]./255)%AR50_ReK(:,1),AR50_ReK(:,2))
plot(10.^(log10(Re)), 10.^(log10(nDP_Yishak(:,4))), '-r')%AR72_ReK(:,1),AR72_ReK(:,2))
plot(10.^(log10(Re)), 10.^(log10(nDP_Yishak(:,5))), '-m')%AR108_ReK(:,1),AR108_ReK(:,2));
plot(10.^(log10(Re)), 10.^(log10(nDP_Yishak(:,6))), '-', 'color',[119 136
153]./255)%AR143_ReK(:,1),AR143_ReK(:,2));
plot(10.^(log10(Re)), 10.^(log10(nDP_Yishak(:,7))), '-', 'color',[204 204
0]./255)%AR179_ReK(:,1),AR179_ReK(:,2));
plot(10.^(log10(Re)), 10.^(log10(nDP_Yishak(:,8))), '-g')%AR214_ReK(:,1),AR214_ReK(:,2));
plot(10.^(log10(Re)), 10.^(log10(nDP_Yishak(:,9))), '-', 'color',[210 105
30]./255)%AR250_ReK(:,1),AR250_ReK(:,2));
grid on
hold on
plot(10.^(log10(AR1_1.Re_k2(:,1))),10.^(log10(AR1_1.Re_k2(:,2))), 'ko')
plot(10.^(log10(AR37_1.Re_k2(:,1))),10.^(log10(AR37_1.Re_k2(:,2))), 'bo')
plot(10.^(log10(AR50_1.Re_k2(:,1))),10.^(log10(AR50_1.Re_k2(:,2))), 'x','color',[0 128 0]./255)
plot(10.^(log10(AR72_1.Re_k2(:,1))),10.^(log10(AR72_1.Re_k2(:,2))), 'r^')
plot(10.^(log10(AR108_1.Re_k2(:,1))),10.^(log10(AR108_1.Re_k2(:,2))), 'mv')
plot(10.^(log10(AR143_1.Re_k2(:,1))),10.^(log10(AR143_1.Re_k2(:,2))), '>', 'color',[119 136
153]./255)
plot(10.^(log10(AR179_1.Re_k2(:,1))),10.^(log10(AR179_1.Re_k2(:,2))), '<', 'color',[204 204
0]./255)
plot(10.^(log10(AR214_1.Re_k2(:,1))),10.^(log10(AR214_1.Re_k2(:,2))), 'gd')
plot(10.^(log10(AR250_1.Re_k2(:,1))),10.^(log10(AR250_1.Re_k2(:,2))), 's', 'color',[210 105
30]./255)

set(gca,'xscale',scale);
set(gca,'yscale',scale);
% % Re_range,nDP_Yishak(:,2),'--k',Re_range,nDP_Yishak(:,3),'-',Re_range,nDP_Yishak(:,4),'-
',Re_range,nDP_Yishak(:,5),'-',...
% % Re_range,nDP_Yishak(:,6),'-',Re_range,nDP_Yishak(:,7),'-',Re_range,nDP_Yishak8,'-
',Re_range,nDP_Yishak9,'-')
% % set(axes,'LineStyleorder',{'-k','-b','-c','-r','-m','-y','-g','-k',':b'});
% hold all
xlabel('\it {Re}');
ylabel('\it {K}');
xlim(x_plot_range)
ylim(y_plot_range)
grid on
if sho_legend == 1
leg=legend({'\it{AR} = 1 ','\it{AR} = 37','\it{AR} = 50',...
'\it{AR} = 72','\it{AR} = 108','\it{AR} = 143',...
'\it{AR} = 179','\it{AR} = 214','\it{AR} = 250'},...
'Oriantation','Vertical','FontSize',Font_legend);
title(leg,'Eq(13) and experiment')
end

```

```

%set(gca,'TickLabelInterpreter','latex');
set(gca,'FontName',Font,'FontSize',Font_size)

AR_clr = [0 0 0; 0 0 255; 0 128 0; 255 0 0; 255 0 255;...
          119 136 153; 204 204 0; 0 255 0; 210 105 30]/255;
Re_offset=1;
K_offset=[0.2 0.259 0.1 0.2120 0.2 0.1 0.158 0.178 0.12];
figure()
scale = 'linear'
for ii=1:length(AR_pts)
    AR_names{ii} = strcat('AR',num2str(AR_pts(ii)));
    logfit_model(:,ii)= polyfit(log10(Re), log10(nDP_Yishak(:,ii)),1);
    logfit_exp(:,ii) = polyfit(log10(eval(strcat('AR',num2str(AR_pts(ii)),'_Re'))),
log10(eval(strcat('AR',num2str(AR_pts(ii)),'_K'))),1);
    mlog_model(:,ii) = logfit_model(1,ii);
    mlog_exp(:,ii) = logfit_exp(1,ii);
    klog_model(:,ii) = logfit_model(2,ii);
    klog_exp(:,ii) = logfit_exp(2,ii);
    KLine_model(:,ii) = (mlog_model(:,ii)).*log10(Re)+(klog_model(:,ii));
    KLine_exp(:,ii) = (mlog_exp(:,ii)).*log10(Re)+(klog_exp(:,ii));
    DK_rotated(:,ii) = (KLine_exp(:,ii)- Vr.(AR_names{ii})(:,2));

    Avg_DK(:,ii) = mean(KLine_exp(:,ii)- KLine_model(:,ii));
    semilogy(10.^(log10(Re)),10.^(log10(DK_rotated(:,ii)))/log(10),'-', 'color', AR_clr(ii,:))
    xlabel('\it {Re}');
    ylabel('\it{\epsilon}_{rotated}', 'Interpreter','Tex');
    xlim([0.01 0.1])
    ylim([0 1])
set(gca,'XScale',scale);
set(gca,'YScale',scale);
grid on
if(sho_legend==1)
legend('mean difference','Linear fit')
end
set(gca,'FontName',Font,'FontSize',Font_size)
% plot(log10(Re), KLine_exp(:,ii)- KLine_model(:,ii),'+')
hold on
end

if sho_legend == 1
Legend({'\it{AR}= 1 ', '\it{AR} = 37', '\it{AR} = 50',...
        '\it{AR} = 72', '\it{AR} = 108', '\it{AR}= 143',...
        '\it{AR} = 179', '\it{AR} = 214', '\it{AR} = 250'},...
        'Orientation','Vertical','FontSize',Font_legend)
end
figure('Name','log10(Re) vs. log10(K):Model+Exp (Rotated)')
% box on
hold on
% scale = 'linear';
scale = 'log';
Re_offset=1;
K_offset=[0.2 0.259 0.1 0.2120 0.2 0.1 0.158 0.178 0.12];
% K_offset = zeros(1,length(AR));

```

```

plot(10.^(Vr.AR1(:,1))*Re_offset, 10.^(Vr.AR1(:,2))+K_offset(:,1)),'-.k')
%AR1_ReK(:,1),AR1_ReK(:,2))
plot(10.^(Vr.AR37(:,1))*Re_offset,10.^(Vr.AR37(:,2))+K_offset(:,2)),'-
.b')%AR37_ReK(:,1),AR37_ReK(:,2))
plot(10.^(Vr.AR50(:,1))*Re_offset, 10.^(Vr.AR50(:,2))+K_offset(:,3)),'-.','color', [0 128
0]./255)%AR72_ReK(:,1),AR72_ReK(:,2))
plot(10.^(Vr.AR72(:,1))*Re_offset, 10.^(Vr.AR72(:,2))+K_offset(:,4)),'-
.r')%AR72_ReK(:,1),AR72_ReK(:,2))
plot(10.^(Vr.AR108(:,1))*Re_offset,10.^(Vr.AR108(:,2))+K_offset(:,5)),'-.m')
plot(10.^(Vr.AR143(:,1))*Re_offset,10.^(Vr.AR143(:,2))+K_offset(:,6)),'-.','color',[119 136
153]./255)
plot(10.^(Vr.AR179(:,1))*Re_offset, 10.^(Vr.AR179(:,2))+K_offset(:,7)),'-.','color',[204 204
0]./255)
plot(10.^(Vr.AR214(:,1))*Re_offset, 10.^(Vr.AR214(:,2))+K_offset(:,8)),'-.g')
plot(10.^(Vr.AR250(:,1))*Re_offset, 10.^(Vr.AR250(:,2))+K_offset(:,9)),'-.','color',[210 105
30]./255)

hold on
plot(10.^(log10(AR1_1.Re_k2(:,1))),10.^(log10(AR1_1.Re_k2(:,2))), 'ko')
plot(10.^(log10(AR37_1.Re_k2(:,1))),10.^(log10(AR37_1.Re_k2(:,2))), 'bo')
plot(10.^(log10(AR50_1.Re_k2(:,1))),10.^(log10(AR50_1.Re_k2(:,2))), 'x','color', [0 128 0]./255)
plot(10.^(log10(AR72_1.Re_k2(:,1))),10.^(log10(AR72_1.Re_k2(:,2))), 'r^')
plot(10.^(log10(AR108_1.Re_k2(:,1))),10.^(log10(AR108_1.Re_k2(:,2))), 'mv')
plot(10.^(log10(AR143_1.Re_k2(:,1))),10.^(log10(AR143_1.Re_k2(:,2))), '>','color',[119 136
153]./255)
plot(10.^(log10(AR179_1.Re_k2(:,1))),10.^(log10(AR179_1.Re_k2(:,2))), '<','color',[204 204
0]./255)
plot(10.^(log10(AR214_1.Re_k2(:,1))),10.^(log10(AR214_1.Re_k2(:,2))), 'gd')
plot(10.^(log10(AR250_1.Re_k2(:,1))),10.^(log10(AR250_1.Re_k2(:,2))), 's','color',[210 105
30]./255)
if sho_legend == 1
leg=legend({'{\it{AR}} = 1 ', '{\it{AR}} = 37', '{\it{AR}} = 50', ...
' {\it{AR}} = 72', '{\it{AR}} = 108', '{\it{AR}} = 143', ...
' {\it{AR}} = 179', '{\it{AR}} = 214', '{\it{AR}} = 250'}, ...
'Orientation', 'Vertical', 'FontSize', Font_legend);
title(leg, 'rotated Eq(13) and experiment ');
end

set(gca, 'XScale', scale);
set(gca, 'YScale', scale);
xlabel('\it {Re}');
ylabel('\it {K}');
xlim(x_plot_range)
ylim(y_plot_range)
grid on
%set(gca, 'TickLabelInterpreter', 'latex');
set(gca, 'FontName', Font, 'FontSize', Font_size)

% tilefigs()

```



```

%
% %%%%%%%%%%%%%%%%%%%%%%%%%%%%%%%%%%%%%%%%%%%%%%%%%%%%%%%%%%%%%%%%%%%%%%%%%
% % what : 1. Plot averaged data and uncertainty bands for DP,K,and Phi
% %      2. Non-linear least square fit for Phi

% % who  : Yishak Yusuf
% % when : v1 (Decempber, 2017)
% %      v2 (February, 2018)
% %%%%%%%%%%%%%%%%%%%%%%%%%%%%%%%%%%%%%%%%%%%%%%%%%%%%%%%%%%%%%%%%%%%%%%%%%

close all
clear all
clc
font_n = 'Times';
font_s = 20;
font_l = 16; %for llegend
marker_s = 10;
line_w = 2;
angle_tick = 60;
% xtickangle(angle_tick);
b = [3 0.5 0.424 0.35 0.29 0.25 0.22 0.2 0.19]./1000; %widths of slots
a = [3 18.1 21.21 25.5 31.1 35.9 40.1 43.9 47.5]./1000; %lengths of slots
AR = [1 37 50 72 108 143 179 214 250];
AR_pts = [1 37 50 72 108 143 179 214 250];

%a= [63.5 63.5 63.5 63.5 63.5 63.5]./1000;
Dh = (2.*b.*a)./(b+a); %hydraulic diameters
D = 76/1000; %diameter of pipe
L = 10/1000;
% alpha = (a.*b)/(pi*D^2/4); %area ratio
alpha = 0.002;
rho = 884.3; %density (kg/m3)
mu = 1.8; % viscosity (Pa.s)

%---LOADING SAVED FILES
AR1_1 = load('G:\My Drive\work from
home\Open_Slot_Experiments\Averaged_Summary\Averaged_Summary_AR001_R2.mat'); %OK
AR37_1 = load('G:\My Drive\work from
home\Open_Slot_Experiments\Averaged_Summary\Averaged_Summary_AR037_R2.mat');
AR50_1 = load('G:\My Drive\work from
home\Open_Slot_Experiments\Averaged_Summary\Averaged_Summary_AR050_R2.mat');
AR72_1 = load('G:\My Drive\work from
home\Open_Slot_Experiments\Averaged_Summary\Averaged_Summary_AR072_RPT.mat');
AR108_1 = load('G:\My Drive\work from
home\Open_Slot_Experiments\Averaged_Summary\Averaged_Summary_AR108_R3.mat');
AR143_1 = load('G:\My Drive\work from
home\Open_Slot_Experiments\Averaged_Summary\Averaged_Summary_AR143_R3.mat');
AR179_1 = load('G:\My Drive\work from
home\Open_Slot_Experiments\Averaged_Summary\Averaged_Summary_AR179_R1.mat');
AR214_1 = load('G:\My Drive\work from
home\Open_Slot_Experiments\Averaged_Summary\Averaged_Summary_AR214_R2.mat');
AR250_1 = load('G:\My Drive\work from
home\Open_Slot_Experiments\Averaged_Summary\Averaged_Summary_AR250_R2.mat');

```

```

AR1_DP = load('G:\My Drive\work from
home\Open_Slot_Experiments\Averaged_Summary\Averaged_DeltaPs_AR001_R2.mat'); %OK
AR37_DP = load('G:\My Drive\work from
home\Open_Slot_Experiments\Averaged_Summary\Averaged_DeltaPs_AR037_R2.mat');
AR50_DP = load('G:\My Drive\work from
home\Open_Slot_Experiments\Averaged_Summary\Averaged_DeltaPs_AR050_R2.mat');
AR72_DP = load('G:\My Drive\work from
home\Open_Slot_Experiments\Averaged_Summary\Averaged_DeltaPs_AR072_RPT.mat');
AR108_DP = load('G:\My Drive\work from
home\Open_Slot_Experiments\Averaged_Summary\Averaged_DeltaPs_AR108_R3.mat');
AR143_DP = load('G:\My Drive\work from
home\Open_Slot_Experiments\Averaged_Summary\Averaged_DeltaPs_AR143_R3.mat');
AR179_DP = load('G:\My Drive\work from
home\Open_Slot_Experiments\Averaged_Summary\Averaged_DeltaPs_AR179_R1.mat');
AR214_DP = load('G:\My Drive\work from
home\Open_Slot_Experiments\Averaged_Summary\Averaged_DeltaPs_AR214_R2.mat');
AR250_DP = load('G:\My Drive\work from
home\Open_Slot_Experiments\Averaged_Summary\Averaged_DeltaPs_AR250_R2.mat');

errAR1 = load('G:\My Drive\work from
home\Open_Slot_Experiments\Averaged_Summary\Uncertainty_DeltaP_AR001_R2.mat');
errAR37 = load('G:\My Drive\work from
home\Open_Slot_Experiments\Averaged_Summary\Uncertainty_DeltaP_AR037_R2.mat');
errAR50 = load('G:\My Drive\work from
home\Open_Slot_Experiments\Averaged_Summary\Uncertainty_DeltaP_AR050_R2.mat');
errAR72 = load('G:\My Drive\work from
home\Open_Slot_Experiments\Averaged_Summary\Uncertainty_DeltaP_AR072_RPT.mat');
errAR108 = load('G:\My Drive\work from
home\Open_Slot_Experiments\Averaged_Summary\Uncertainty_DeltaP_AR108_R3.mat');
errAR143 = load('G:\My Drive\work from
home\Open_Slot_Experiments\Averaged_Summary\Uncertainty_DeltaP_AR143_R3.mat');
errAR179 = load('G:\My Drive\work from
home\Open_Slot_Experiments\Averaged_Summary\Uncertainty_DeltaP_AR179_R1.mat');
errAR214 = load('G:\My Drive\work from
home\Open_Slot_Experiments\Averaged_Summary\Uncertainty_DeltaP_AR214_R2.mat');
errAR250 = load('G:\My Drive\work from
home\Open_Slot_Experiments\Averaged_Summary\Uncertainty_DeltaP_AR250_R2.mat');

p = size(AR,2);
Re_pts = 3;
% Re_ave=zeros(Re_pts,p);
% figure('Name','Raw Pressure Data')

for i0=1:p
    Re_string = strcat('AR',num2str(AR(i0)),'_1.Re_ave');
    Re_data = unique (sort(eval(Re_string)), 'rows');
    DP_string = strcat('AR',num2str(AR(i0)),'_1.DP_ave');
    DP_data = eval(DP_string);
    DP_Raw_string = strcat('AR',num2str(AR(i0)),'_1.Re_k'); %Re_k =
    horzcat(Re_o,K,P2,P3,P4,P5,P6,P7,P9,m_dot,t');
    Raw_data = eval(DP_Raw_string);
    US_DP_string = strcat('AR',num2str(AR(i0)),'_DP.US_DP1_ave');

```

```

US_DP_data = eval(US_DP_string);
US_DP2_string = strcat('AR',num2str(AR(i0)),'_DP.US_DP2_ave');
US_DP2_data = eval(US_DP2_string);
US_DP3_string = strcat('AR',num2str(AR(i0)),'_DP.US_DP3_ave');
US_DP3_data = eval(US_DP3_string);
%   P2_Raw.(strcat('AR',num2str(AR_pts(i0)))) = Raw_data(:,3)*6894.76;
%   P9_Raw.(strcat('AR',num2str(AR_pts(i0)))) = Raw_data(:,9)*6894.76;
%   DP_Raw.(strcat('AR',num2str(AR_pts(i0)))) = (Raw_data(:,3)-Raw_data(:,9))*6894.76;
%   t.(strcat('AR',num2str(AR_pts(i0))))= Raw_data(:,11);
K_string = strcat('AR',num2str(AR(i0)),'_1.K_ave');
K_data = (eval(K_string));
Phi_string = strcat('AR',num2str(AR(i0)),'_1.Phi_ave');
Phi_data = (eval(Phi_string));
err_DP_string = strcat('errAR',num2str(AR(i0)),'.U95_DP');
err_DP_data= (eval(err_DP_string));
err_K_string = strcat('errAR',num2str(AR(i0)),'.U95_K');
err_K_data= (eval(err_DP_string));
err_Phi_string = strcat('errAR',num2str(AR(i0)),'.U95_Phi');
err_Phi_data= (eval(err_Phi_string));
Re_pts = 3;
pts_per_Re = 20;
t_pts = Re_pts*pts_per_Re;
n = ceil((length(Raw_data)/t_pts)+1);
%plot(t,P2,'r>',t,P9,'b<',t, DP,'ks')
%
loglog(Raw_data(:,11),Raw_data(:,3)*6894.76,'r>',Raw_data(:,11),Raw_data(:,9)*6894.76,'b<',...
%   Raw_data(:,11),(Raw_data(:,3)-
Raw_data(:,9))*6894.76,'ks',Raw_data(:,11),Raw_data(:,1),'mo')
%   hold on
%   xlabel('\it{t}')
%   ylabel('Raw Pressures, Pa')
%   legend({'Upstream','Downstream','\it
{\Delta P}','Orientation','Horizonta1','FontSize',font_l,'Interpreter','Latex'})
%   grid on
%   set(gca,'FontName',font_n,'FontSize',font_s)

AR_names{i0} = strcat('AR',num2str(AR_pts(i0)));
floor(length(Re_data)/Re_pts)
Re_chunk.(AR_names{i0}) = mat2tiles(Re_data,[floor(length(Re_data)/Re_pts), 1]);
DP_chunk.(AR_names{i0}) = mat2tiles(DP_data,[floor(length(DP_data)/Re_pts), 1]);
US_DP_chunk.(AR_names{i0}) = mat2tiles(US_DP_data,[floor(length(US_DP_data)/Re_pts), 1]);
US_DP2_chunk.(AR_names{i0}) = mat2tiles(US_DP2_data,[floor(length(US_DP2_data)/Re_pts), 1]);
US_DP3_chunk.(AR_names{i0}) = mat2tiles(US_DP3_data,[floor(length(US_DP3_data)/Re_pts), 1]);
K_chunk.(AR_names{i0}) = mat2tiles(K_data,[floor(length(K_data)/Re_pts), 1]);
Phi_chunk.(AR_names{i0}) = mat2tiles(Phi_data,[floor(length(Phi_data)/Re_pts), 1]);
err_DP_chunk.(AR_names{i0}) = mat2tiles(err_DP_data,[floor(length(err_DP_data)/Re_pts), 1]);
err_K_chunk.(AR_names{i0}) = mat2tiles(err_K_data,[floor(length(err_K_data)/Re_pts), 1]);
err_Phi_chunk.(AR_names{i0}) = mat2tiles(err_Phi_data,[floor(length(err_Phi_data)/Re_pts), 1]);
for i1=1:Re_pts
    Re_ave.(AR_names{i0})(i1) = mean(cell2mat(Re_chunk.(AR_names{i0})(i1)));
    DP_ave.(AR_names{i0})(i1) = mean(cell2mat(DP_chunk.(AR_names{i0})(i1)));
    US_DP_ave.(AR_names{i0})(i1) = mean(cell2mat(US_DP_chunk.(AR_names{i0})(i1)));
    US_DP2_ave.(AR_names{i0})(i1)= mean(cell2mat(US_DP2_chunk.(AR_names{i0})(i1)));
    US_DP3_ave.(AR_names{i0})(i1)= mean(cell2mat(US_DP3_chunk.(AR_names{i0})(i1)));

```

```

K_ave.(AR_names{i0})(i1) = mean(cell2mat(K_chunk.(AR_names{i0})(i1)));
Phi_ave.(AR_names{i0})(i1) = mean(cell2mat(Phi_chunk.(AR_names{i0})(i1)));
err_DP.(AR_names{i0})(i1) = mean(cell2mat(err_DP_chunk.(AR_names{i0})(i1)));
err_K.(AR_names{i0})(i1) = mean(cell2mat(err_K_chunk.(AR_names{i0})(i1)));
err_Phi.(AR_names{i0})(i1) = mean(cell2mat(err_Phi_chunk.(AR_names{i0})(i1)));
Q_ave.(AR_names{i0})(i1) = (Re_ave.(AR_names{i0})(i1).*mu.*(a(i0)+b(i0)))./(2*rho);
US_DP1_HagP.(AR_names{i0})(i1) = (8*mu*1.5*D*(Q_ave.(AR_names{i0})(i1)))./(pi*(D^4/64));
US_DP2_HagP.(AR_names{i0})(i1) = (8*mu*0.5*D*(Q_ave.(AR_names{i0})(i1)))./(pi*(D^4/64));
US_DP3_HagP.(AR_names{i0})(i1) = (8*mu*1.0*D*(Q_ave.(AR_names{i0})(i1)))./(pi*(D^4/64));
end

end
save(['X:\01_Current_Students\Yishak\03_Publications\04_Journals\06{EIF(Flow_through_coupled_medium)\02_Plot_and_Process\' strcat('openSlot averages')],...
'DP_ave','err_DP','Q_ave','US_DP_ave')

```

```

%=====
%FIGURE 6:Plot of static pressure drop vs. aspect ratio for different Reynolds numbers
%=====
figure('Name', 'AR vs. DP : ALL_Re')
Re_clr = [0 128 0; 220 20 60; 0 0 255;]./255; %green (Re_lo); red(Re_mid); blue(Re_max)

for i2=1:length(AR)
    for j0 = 1:Re_pts
        errorbar(AR(i2),DP_ave.(AR_names{i2})(:,j0),err_DP.(AR_names{i2})(:,j0),...
            'o','MarkerSize',marker_s,'Linewidth',line_w,'Color',Re_clr(j0,:)); hold on
    end
end
grid on
legend({strcat('{\it{Re}} = 0.05'), strcat('{\it{Re}} = 0.075'), strcat('{\it{Re}} = 0.1')}, 'Orientation', 'Horizonatal', 'FontSize', font_l);
xlabel('\it {AR}')
xticks(AR);
% xticklabels({ num2str(AR(1)),num2str(AR(2)),num2str(AR(3)), num2str(AR(4)), num2str(AR(5)),
num2str(AR(6)), num2str(AR(7)), num2str(AR(8))})
xticklabels({ num2str(AR(1)),num2str(AR(2)),num2str(AR(3)), num2str(AR(4)), num2str(AR(5)),
num2str(AR(6)), num2str(AR(7)), num2str(AR(8)), num2str(AR(9))})
xtickangle(angle_tick);
% ylabel('{\Delta}\it{P}}, Pa');
set(gca, 'FontName', font_n, 'FontSize', font_s)
set(gca, 'TickLabelInterpreter', 'tex');
ylabel('{\it{\Delta P}}, Pa', 'Interpreter', 'tex');

```

```

figure('Name', 'AR vs. US_DP : ALL_Re')
Re_clr = [0 128 0; 220 20 60; 0 0 255;]./255; %green (Re_lo); red(Re_mid); blue(Re_max)

for i2=1:length(AR)
    for j0 = 1
        errorbar(AR(i2),abs(US_DP_ave.(AR_names{i2})(:,j0)),0.5*err_DP.(AR_names{i2})(:,j0),...
            'o','MarkerSize',marker_s,'Linewidth',line_w,'Color',Re_clr(j0,:)); hold on
        plot(AR(i2),1000*US_DP1_HagP.(AR_names{i2})(:,j0),...
            's','MarkerSize',marker_s,'Linewidth',line_w,'Color',Re_clr(j0,:))
    end
end
end

```

```

grid on
legend({strcat('{\it{Re}} = 0.05'), strcat('{\it{Re}} = 0.075'), strcat('{\it{Re}} =
0.1')},'Orientation','Horizontata1','FontSize',font_1);
xlabel('\it {AR}')
xticks(AR);
% xticklabels({ num2str(AR(1)),num2str(AR(2)),num2str(AR(3)), num2str(AR(4)), num2str(AR(5)),
num2str(AR(6)), num2str(AR(7)), num2str(AR(8))})
xticklabels({ num2str(AR(1)),num2str(AR(2)),num2str(AR(3)), num2str(AR(4)), num2str(AR(5)),
num2str(AR(6)), num2str(AR(7)), num2str(AR(8)), num2str(AR(9))})
xtickangle(angle_tick);
% ylabel('{\Delta}\it{P}}, Pa');
set(gca,'FontName',font_n,'FontSize',font_s)
set(gca,'TickLabelInterpreter','tex');
ylabel('{\it{P}_1 - P_3}}, Pa','Interpreter','tex');

figure('Name', 'AR vs. US_DP2 : ALL_Re')
for i2=1:length(AR)
    for j0 = 1
        errorbar(AR(i2),abs(US_DP2_ave.(AR_names{i2})(:,j0)),err_DP.(AR_names{i2})(:,j0),...
            'o','MarkerSize',marker_s,'Linewidth',line_w,'Color',Re_clr(j0,:)); hold on
        plot(AR(i2),1000*US_DP2_HagP.(AR_names{i2})(:,j0),...
            's','MarkerSize',marker_s,'Linewidth',line_w,'Color',Re_clr(j0,:))
    end
end
grid on
legend({strcat('{\it{Re}} = 0.05'), strcat('{\it{Re}} = 0.075'), strcat('{\it{Re}} =
0.1')},'Orientation','Horizontata1','FontSize',font_1);
xlabel('\it {AR}')
xticks(AR);
% xticklabels({ num2str(AR(1)),num2str(AR(2)),num2str(AR(3)), num2str(AR(4)), num2str(AR(5)),
num2str(AR(6)), num2str(AR(7)), num2str(AR(8))})
xticklabels({ num2str(AR(1)),num2str(AR(2)),num2str(AR(3)), num2str(AR(4)), num2str(AR(5)),
num2str(AR(6)), num2str(AR(7)), num2str(AR(8)), num2str(AR(9))})
xtickangle(angle_tick);
% ylabel('{\Delta}\it{P}}, Pa');
set(gca,'FontName',font_n,'FontSize',font_s)
set(gca,'TickLabelInterpreter','tex');
ylabel('{\it{P}_1 - P_2}}, Pa','Interpreter','tex');

figure('Name', 'AR vs. US_DP3 : ALL_Re')
for i2=1:length(AR)
    for j0 = 1
        errorbar(AR(i2),abs(US_DP3_ave.(AR_names{i2})(:,j0)),err_DP.(AR_names{i2})(:,j0),...
            'o','MarkerSize',marker_s,'Linewidth',line_w,'Color',Re_clr(j0,:)); hold on
        plot(AR(i2),1000*US_DP3_HagP.(AR_names{i2})(:,j0),...
            's','MarkerSize',marker_s,'Linewidth',line_w,'Color',Re_clr(j0+1,:))
    end
end
grid on
legend({'Measured', 'Hagen-Poiseuille-Eq.(31)'},'Orientation','Horizontata1','FontSize',font_1);
xlabel('\it {AR}')
xticks(AR);
% xticklabels({ num2str(AR(1)),num2str(AR(2)),num2str(AR(3)), num2str(AR(4)), num2str(AR(5)),
num2str(AR(6)), num2str(AR(7)), num2str(AR(8))})

```

```

xticklabels({ num2str(AR(1)),num2str(AR(2)),num2str(AR(3)), num2str(AR(4)), num2str(AR(5)),
num2str(AR(6)), num2str(AR(7)), num2str(AR(8)), num2str(AR(9))})
xtickangle(angle_tick);
% ylabel('\Delta\it{P}}, Pa');
set(gca, 'FontName', font_n, 'FontSize', font_s)
set(gca, 'TickLabelInterpreter', 'tex');
ylabel('\it{P}_2 - P_3}}, Pa', 'Interpreter', 'tex');

%=====
%FIGURE 7:Plot of K vs. aspect ratio for different Reynolds numbers
%=====
figure('Name', 'AR vs. K : ALL_Re')
for i3=1:length(AR)
    for j1 = 1:Re_pts
        % ones(length(DP_ave.(AR_names{i2})),1);*V_centre.(AR_names{i4})
        errorbar(AR(i3),K_ave.(AR_names{i3})(:,j1),...

err_K.(AR_names{i3})(:,j1), 'o', 'MarkerSize',marker_s, 'Linewidth',line_w, 'Color',Re_clr(j1,:));
hold on
% errorbar(AR,DP_ave(2,:),err_DP(2,:), 'b^', 'MarkerSize',marker_s, 'Linewidth',line_w); hold on
% errorbar(AR,DP_ave(3,:),err_DP(3,:), 'ks', 'MarkerSize',marker_s, 'Linewidth',line_w);

% errorbar(AR,DP_ave(4,:),err_DP(4,:), 'ys', 'MarkerSize',marker_s, 'Linewidth',line_w);
% errorbar(AR,DP_ave(5,:),err_DP(5,:), 'gs', 'MarkerSize',marker_s, 'Linewidth',line_w);

%plot(AR,DP_ave(1,:), 'ko',AR,DP_ave(2,:), 'k^',AR,DP_ave(3,:), 'ks', 'MarkerSize',marker_s, 'Linewidth',line_w);
end
end
grid on
legend({strcat('\it{Re}} = 0.05'), strcat('\it{Re}} = 0.075'), strcat('\it{Re}} = 0.1')}, 'Orientation', 'Horizontal', 'FontSize', font_1);
xlabel('\it {AR}')
xticks(AR);
% xticklabels({ num2str(AR(1)),num2str(AR(2)),num2str(AR(3)), num2str(AR(4)), num2str(AR(5)),
num2str(AR(6)), num2str(AR(7)), num2str(AR(8))})
xticklabels({ num2str(AR(1)),num2str(AR(2)),num2str(AR(3)), num2str(AR(4)), num2str(AR(5)),
num2str(AR(6)), num2str(AR(7)), num2str(AR(8)), num2str(AR(9))})
xtickangle(angle_tick);
ylabel('\it{k}');
set(gca, 'FontName', font_n, 'FontSize', font_s)
set(gca, 'TickLabelInterpreter', 'tex');

```

```

%=====
%FIGURE 8:Plot of phi vs. aspect ratio for different Reynolds numbers
%=====
figure('Name', 'AR vs. Phi')

for i4=1:length(AR)
    for j2 = 1:Re_pts
        % ones(length(DP_ave.(AR_names{i2})),1);*V_centre.(AR_names{i4})

errorbar(AR(i4),Phi_ave.(AR_names{i4})(:,j2), (err_Phi.(AR_names{i4})(:,j2)./max(Phi_ave.(AR_names{i4})(:,j2))),...

```

```

        'o','MarkerSize',marker_s,'Linewidth',line_w,'Color',Re_clr(j2,:)); hold on
%     errorbar(AR,DP_ave(2,:),err_DP(2,:),'b^','MarkerSize',marker_s,'Linewidth',line_w); hold on
%     errorbar(AR,DP_ave(3,:),err_DP(3,:),'ks','MarkerSize',marker_s,'Linewidth',line_w);

% errorbar(AR,DP_ave(4,:),err_DP(4,:),'ys','MarkerSize',marker_s,'Linewidth',line_w);
% errorbar(AR,DP_ave(5,:),err_DP(5,:),'gs','MarkerSize',marker_s,'Linewidth',line_w);

%plot(AR,DP_ave(1,:),'ko',AR,DP_ave(2,:),'k^',AR,DP_ave(3,:),'ks','MarkerSize',marker_s,'Linewidth',line_w);
end
end

% plot(AR,Phi_ave(1,:),'ro','MarkerSize',marker_s,'Linewidth',line_w); hold on
% plot(AR,Phi_ave(2,:),'b^','MarkerSize',marker_s,'Linewidth',line_w); hold on
% plot(AR,Phi_ave(3,:),'ks','MarkerSize',marker_s,'Linewidth',line_w);
% plot(AR,Phi_ave(4,:),'ys','MarkerSize',marker_s,'Linewidth',line_w);
% plot(AR,Phi_ave(5,:),'gs','MarkerSize',marker_s,'Linewidth',line_w);
%
plot(AR,Phi_ave(1,:),'o',AR,Phi_ave(2,:),'^',AR,Phi_ave(3,:),'s','MarkerSize',marker_s,'Linewidth',line_w);
grid on
legend({'\it{Re}} = 0.05', '\it{Re}} = 0.075', '\it{Re}} = 0.1'}, 'Orientation','Horizontal', 'FontSize',font_1);
xlabel('\it {AR}')
xticks(AR);
% xticklabels({ num2str(AR(1)),num2str(AR(2)),num2str(AR(3)), num2str(AR(4)), num2str(AR(5)),
num2str(AR(6)), num2str(AR(7)), num2str(AR(8))})
xticklabels({ num2str(AR(1)),num2str(AR(2)),num2str(AR(3)), num2str(AR(4)), num2str(AR(5)),
num2str(AR(6)), num2str(AR(7)), num2str(AR(8)), num2str(AR(9))})
xtickangle(angle_tick);
ylabel('\it{\phi}');
set(gca, 'FontName', font_n, 'FontSize', font_s)
set(gca, 'TickLabelInterpreter', 'tex');
%=====
%-----
%=====
%
%                               FITTING PHI
%=====
%-----
%=====
number_of_points = 300;
number_of_data = size(Phi_ave,2);
fit_options = fitoptions('Method','NonlinearLeastSquares');
% fit_type = fitype('a*((2*x)/(x+1))^2 + b*((2*x)/(x+1)) + c ','options',fit_options);
fit_type = fitype('a*(x^2) + b*(x-1) + c ','options',fit_options);
% fit_type = fitype('a*(x^2) + b*(x) + c ','options',fit_options);
start = [0;0;0];

for j3=1:length(AR)
    for i5=1:Re_pts
        Phi_Ave_data(i5,j3) = (Phi_ave.(AR_names{j3}))(:,i5));
    end
end
end

```

```

[equation1,other1] = fit(AR',Phi_Ave_data(1,:)','fit_type, 'StartPoint',start);           %Phi for
1st Re
[equation2,other2] = fit(AR',Phi_Ave_data(2,:)','fit_type, 'StartPoint',start);           %Phi for
2nd Re
[equation3,other3] = fit(AR',Phi_Ave_data(3,:)','fit_type, 'StartPoint',start);           %Phi for
3rd Re

AR_value = linspace(1, max(AR),number_of_points);
Phi_ave_value1 = equation1 (AR_value);
Phi_ave_value2 = equation2 (AR_value);
Phi_ave_value3 = equation3 (AR_value);
x_loc = 10;
y_loc1 = 95;
y_loc2 = 85;

%---Phi fit plot for 1st Reynolds number
% figure('Name','Phi plot for Re = 0.05');
% plot (AR_value,Phi_ave_value1,'-r', AR, Phi_ave(1,:), 'b*');
% legend('Fit ','Experimental');
% xlabel('\it {AR}');
% ylabel('\phi');
% set(gca,'Ylim',[0 100]);
% set(gcf,'Color','w')
% set(gca,'FontName',font_n,'FontSize',font_s)
% format short
C11 = num2str(equation1.a);
C12 = num2str(equation1.b);
C13 = num2str(equation1.c);
% text(x_loc, y_loc1, strcat('\phi= ',C11, '\it{AR}^2$', ' + ', C12,'\it{AR}', ' + ',
C13),'Interpreter','Latex');
% text(x_loc, y_loc2, strcat('R^2 = ', num2str(other1.rsquare), '),'Interpreter','Latex');
% grid on
% box on

%---Phi fit plot for 2nd Reynolds number
% figure('Name','Phi plot for Re = 0.075');
% plot (AR_value,Phi_ave_value2,'-r', AR, Phi_ave(2,:), 'b*');
% legend('Fit ','Experimental');
% xlabel('\it {AR}');
% ylabel('\phi','Interpreter','Latex');
% grid on
% set(gca,'Ylim',[0 100]);
% set(gcf,'Color','w')
% format short
C21 = num2str(equation2.a);
C22 = num2str(equation2.b);
C23 = num2str(equation2.c);
% hold on
% text(x_loc, y_loc1, strcat('\phi= ',C21, '\it{AR}^2$', ' + ', C22,'\it{AR}', ' + ',
', C23), 'Interpreter','Latex');
% text(x_loc, y_loc2, strcat('R^2 = ', num2str(other2.rsquare), '),'Interpreter','Latex');
%
% box on

```



```

%---Phi fit plot for 3rd Reynolds number
% figure('Name','Phi plot for Re = 0.1')
% plot (AR_value,Phi_ave_value3,'-r', AR, Phi_ave(3,:), 'b*');
% legend('Fit','Experimental');
% xlabel('\it {AR}$','Interpreter','Latex');
% ylabel('\phi$','Interpreter','Latex');
% grid on
% set(gca,'Ylim',[0 100]);
% set(gcf,'Color','w')
% format short
C31 = num2str(equation3.a);
C32 = num2str(equation3.b);
C33 = num2str(equation3.c);
% text(x_loc, y_loc1, strcat('\phi= $',C31, '\it{AR}^2$', ' + ', C32,'\it{AR}}', ' + ',
C33),'Interpreter','Latex');
% text(x_loc, y_loc2, strcat('R^2 = $', num2str(other3.rsquare), '),'Interpreter','Latex');

%--- Plot all phi fits for comparison'
a1 = strcat('\phi= $',c11, '\it{AR^2}}$', ' - ', c12,'\it{AR}}', ' + ', c13);
a2 = strcat('R^2 = $', num2str(other1.rsquare), ' ');
b1 = strcat('\phi= $',c21, '\it{AR^2}}$', ' - ', c22,'\it{AR}}', ' + ', c23);
b2 = strcat('R^2 = $', num2str(other2.rsquare), ' ');
c1 = strcat('\phi= $',c31, '\it{AR^2}}$', ' - ',c32,'\it{AR}}', ' + ', c33);
c2 = strcat('R^2 = $', num2str(other3.rsquare), ' ');
figure('Name','Phi fit comparison')
plot (AR_value,Phi_ave_value1,'-', 'Color', Re_clr(1,:))
hold on
plot(AR_value,Phi_ave_value2,'-', 'Color', Re_clr(2,:))
plot(AR_value,Phi_ave_value3,'-', 'Color', Re_clr(3,:));
hold on
% plot (AR,Phi_ave(1,:), 'r*',AR,Phi_ave(2,:), 'b*',AR,Phi_ave(3,:), 'k*');
for i6=1:length(AR)
    for j4=1:Re_pts
        errorbar(AR(i6),Phi_ave.(AR_names{i6})(:,j4),(err_Phi.(AR_names{i6})(:,j4)./max(Phi_ave.(AR_names
{i6})(:,j4))), 'o', ...
            'MarkerSize',marker_s, 'Linewidth',line_w, 'Color',Re_clr(j4,:));
    end
end
grid on
set(gca,'Ylim',[-50 700]);
set(gca,'Xlim',[0 250])
legend({strcat('\it{Re}} = 0.05'), strcat('\it{Re}} = 0.075'), strcat('\it{Re}} =
0.1')}, 'Orientation','Horizontal', 'FontSize',font_1);
% legend({strcat('\it{Re} = 0.05}', a1, a2), strcat('\it{Re} = 0.075}', b1, b2), strcat('\it{Re} =
0.1}', c1, c2)}, 'Interpreter','Latex');
% legend({strcat('\it{Re}} = 0.05'), strcat('\it{Re}} = 0.075'), strcat('\it{Re}} =
0.1')}, 'Orientation','Horizontal', 'FontSize',font_1);
[lgd, icons, plots, txt] = legend('show');
xlabel('\it {AR}')
xticks(AR);
% xticklabels({ num2str(AR(1)),num2str(AR(2)),num2str(AR(3)), num2str(AR(4)), num2str(AR(5)),
num2str(AR(6)), num2str(AR(7)), num2str(AR(8))})
xticklabels({ num2str(AR(1)),num2str(AR(2)),num2str(AR(3)), num2str(AR(4)), num2str(AR(5)),

```

```
num2str(AR(6)), num2str(AR(7)), num2str(AR(8)), num2str(AR(9)))}
xtickangle(angle_tick);
ylabel('\it{\phi}');
set(gca, 'FontName', font_n, 'FontSize', font_s)
set(gca, 'TickLabelInterpreter', 'tex');

% tilefigs()
```

(iii). *Streamline calculation*

The streamline calculation algorithm is also implemented in a multi-paradigm computing environment (Matlab 2018a, MathWorks). The program achieved the goal by first taking the data for the velocity vector field to calculate the streamlines in the flow field. Obtaining the streamlines yielded the path for the streamwise calculation of the parameters of interest such as the local curvature, velocity transition, and pressure gradients. The code for the channel having $AR = 2$ is given below as an example. The exact same lines with the only alteration of the source file for the velocity vector field and the factors for the pixel-to-mm conversion.

```

%
% %%%%%%%%%%
% % what : Get .vc7 PIV data and calculate streamlines
% % who  : Yishak Yusuf and Shadi Ansari
% % when : March 2018/January 2019
% % Aim  : Plotting streamlines/Calculate the
% %       radius of curvature and streamwise pressure
% %update: April 2019, June 2019
% %%%%%%%%%%
close all
clear all
clc

FSize = 22;
set(0, 'DefaultAxesFontName', 'Times New Roman');
set(0, 'DefaultUIControlFontName', 'Times New Roman');
set(0, 'defaultUitableFontName', 'Times New Roman');
set(0, 'defaultTextFontName', 'Times New Roman');
set(0, 'defaultUipanelFontName', 'Times New Roman');
Interpreter = 'tex';
msize = 2.5;
msizep = 2.5;
L_width = 2;
calc_P = 0;
% %%%%%%%%%%
% % what : Define file loading/saving parameters
% %%%%%%%%%%

Re_clr = [1 0 0; 0 1 0; 1 0 1; 0 1 1; 1/0.75 0 0; 0 1 1; 1 0 1; 0 1 0; 1 0 0];
Re_clr = Re_clr*0.75;

sho_plot =1;

for R0 = 2
%R0 = 2, 3, and 4 refer to Reynolds number 0.1, 0.5, 1 respectively
    if(R0==2)
        v_File = 'Re0p1_3mm_a.vc7';
    elseif(R0==3)
        v_File = 'Re0p5_3mm_a.vc7';
    elseif(R0==4)
        v_File = 'Re1_3mm_a.vc7';
    end
    VEC = loadvec(v_File);

% Scaling/flipping .vc7 data to match flow direction and keep alignment

if(R0==2)
    x_start = 1;
    x_end = length(VEC.x);
    y_start = 1;
    y_end = length(VEC.y);
    pixel_to_mm = 210;

```

```

x_offset = 4.8; y_offset = 3.8;

% VEC.x=flip1r(VEC.x);
VEC.y=flip1r(VEC.y);
VEC.vx=flip1r(VEC.vx);
VEC.vy=flip1r(VEC.vy);
frameRate =3;
dt =15;
elseif(R0==3)
x_end = length(VEC.x)-1;
y_start = 2;
y_end = length(VEC.y)-1;
pixel_to_mm = 210;
x_offset = 4.8; y_offset =3.8;

% VEC.x=flip1r(VEC.x);
VEC.y=flip1r(VEC.y);
VEC.vx=flip1r(VEC.vx);
VEC.vy=flip1r(VEC.vy);
frameRate =0.09;
dt =200;
elseif(R0==4)
x_start = 2;
x_end = length(VEC.x)-1;
y_start = 2;
y_end = length(VEC.y)-1;
pixel_to_mm = 210;
x_offset = 4.8; y_offset =4.8;

% VEC.x=flip1r(VEC.x);
VEC.y=flip1r(VEC.y);
VEC.vx=flip1r(VEC.vx);
VEC.vy=flip1r(VEC.vy);
frameRate = 0.09;
dt =200;
end

% convert from pixels to mm and apply offset to set the origin at the orifice inlet
VEC.x= VEC.x(x_start:x_end);
VEC.y= VEC.y(y_start:y_end);
VEC.x= (VEC.x/pixel_to_mm)-x_offset;
VEC.y= (VEC.y/pixel_to_mm)- y_offset;
VEC.vx= (VEC.vx(x_start:x_end,y_start:y_end)/pixel_to_mm)*frameRate;
VEC.vy= (VEC.vy(x_start:x_end,y_start:y_end)/pixel_to_mm)*frameRate;

%=====
%===== SMOOTHENING =====
%=====
% VEC = struct('x',VEC.x,'y',VEC.y,'vx',VEC.vx,'vy',VEC.vy);
% w_size = 10;
% VEC.x = smoothdata(VEC.x,1,'gaussian',w_size);
% VEC.y = smoothdata(VEC.y,1,'gaussian',w_size);
% VEC.vx = smoothdata(VEC.vx,1,'gaussian',w_size);

```

```

% VEC.vy = smoothdata(VEC.vy,1,'gaussian',w_size);

%====Figure(1): vector plot of original data of PIVMAT
% figure(1)
% showvec(VEC,'background','off','Streamline')

% %=====
% %===== DRAWING COLOR MAPS =====
% %=====
% if(R0==1)
%     header='3mm_a_Re0p01';
% elseif(R0==2)
%     header='3mm_b_Re0p1';
% elseif(R0==3)
%     header='3mm_c_Re0p5';
% elseif(R0==4)
%     header='3mm_c_Re1';
% end
figure()
Vnorm = vec2scal(VEC,'norm');
vvv = Vnorm.w;
vvv_masked = vvv;
vvv_masked = imrotate(vvv_masked,-90);
if(R0==2)||(R0==3)||(R0==4)
    IMoffx = -0.7;
    IMoffy = -0.4;
end
% if(R0==1)||(R0==2)||(R0==3)||(R0==4)
% vvv_masked = imrotate(vvv_masked,4);
% end

%     h = imagesc(VEC.x-IMoffx,VEC.y-IMoffy,vvv_masked/max(max(vvv_masked))); % plot this scalar
field

    colormap('jet'); % Have a contoured color map
    c = colorbar;
    ylabel(c,'\itu/U_{max}','FontSize',FSize-2, 'Interpreter', Interpreter)
    hold on
% VEC.y = -1*VEC.y;
img = showvec(VEC,...
    'scalearrow',20, 'spacing',[2,4]);
ax = gca;
arrow = ax.Children(1,1);
arrow.Color = [0 0 0];
colormap('jet(50)'); % Have a contoured color map
c = colorbar;
ylabel(c,'\itu/U_{max}','FontSize',FSize-2, 'Interpreter', Interpreter)
%     xlim([-4, 4])
%     ylim([-4, 4])
xlabel('\ity/b','FontSize',FSize, 'Interpreter', Interpreter)
ylabel('\it{x/b}','FontSize',FSize, 'Interpreter', Interpreter)

```

```

        set(gca,'FontSize',30);
%     view([90 90]);
%     set(gca,'Ydir','reverse')
% % axis equal
vv = sqrt(VEC.vx.^2+VEC.vy.^2);
figure(2)
plot(-1*VEC.y(2:end-1)',vv(87,2:end-1)/max(max(vv)),'-o','Color',[1 0 0])
hold on
xlabel('\it{x/b}','FontSize',FSize, 'Interpreter', Interpreter)
ylabel('\it{U/U_{max}}','FontSize',FSize, 'Interpreter', Interpreter)
set(gca,'FontSize',FSize);
set(gcf,'Color','w')
legend({'\it{y/b} = 0'},strcat('\it{y/b} = 2'),strcat('\it{y/b} =
4')},'Interpreter','Latex');

grid on
figure(3)
hold on
plot(VEC.x',vv(:,80)/max(max(vv)),'o','Color',[1 0 0])
xlim([-3.8, 3.8])
xlabel('\it{y/b}','FontSize',FSize, 'Interpreter', Interpreter)
ylabel('\it{U/U_{max}}','FontSize',FSize, 'Interpreter', Interpreter)
set(gca,'FontSize',FSize);
set(gcf,'Color','w')
legend({'\it{x/b} = 0'},strcat('\it{x/b} = 2'),strcat('\it{x/b} =
4')},'Interpreter','Latex');
grid on
box on
ual=1;                % initiating the streamline/position "tag" or "number"
% figure
% %%%%%%%%%%%
% % START: STREAMLINE CALCULATION
% %%%%%%%%%%%
sline_tag = cell(1,1); eqline_tag = cell(1,1);
X_Start_position1 = zeros(1,1);
X = zeros(1,1);      %Allocate space for position and velocity data that are going to
be calculated
Y = zeros(1,1);
VY = zeros(1,1);
VX = zeros(1,1);
d_theta = zeros(1,1);
V = zeros(1,1);
V_model =zeros(1,1);
V_model_Re = zeros(1,1);
rho = 1257.7/(1e3);
dp_ds=zeros(1,1);
dp_dn=zeros(1,1);
DP = zeros(1,1);
dV_ds = zeros(1,1);
dV = zeros(1,1);
S = zeros(1,1);
ds = zeros(1,1);
r_curv = zeros(1,1);
Re = zeros(1,1);

```

```

K = zeros(1,1);
K_2 = zeros(1,1);
Eu = zeros(1,1);
alpha = 0.02;
AR = 3/6.35;
phi= 100;
% Re =1;
Dh=4*(1*6.35)/(2*(1+6.35));
% mu = 0.90568/(1e6); %viscosity in Ns/mm2
mu = 0.001;
del_phi = zeros(length(VEC.x),length(VEC.y));
Sline_location = delaunayn(VEC.x');
if(R0==2)
x_loc = 1*[3.5 3 2 1 0];
% x_loc = -3:0;
% x_loc = horzcat(x_loc,flip(-1*x_loc(1:length(x_loc)-1),2));
Y_0 = 2;
elseif(R0==3)
% x_loc =[0,1,2,4,6,8];
x_loc = -8:0.5:8;
Y_0 = 2;
elseif(R0==4)
x_loc = -7:0.5:7;
% x_loc = min(VEC.x):0.1:max(VEC.x);
Y_0 = 2;
end
for jj=1:length(x_loc)
X_Start_position1(jj) = dsearchn(VEC.x',Sline_location,x_loc(jj));
end

% fig_s1=open('Munich2019_Streamlines.fig');
% fig_press=open('Munich2019_dp_ds.fig');
for X_Start_position= 1:length(X_Start_position1)
X_ArreyStart = X_Start_position1(X_Start_position);
Y_ArreyStart = Y_0;
x = VEC.x(1,X_ArreyStart);
y = VEC.y(1,Y_ArreyStart);
vx0 = VEC.vx(X_ArreyStart,Y_ArreyStart);
vy0 = VEC.vy(X_ArreyStart,Y_ArreyStart);

i=1;
X(1,ua1) = x;
Y(1,ua1) = y;
YDelta_in_loadedmatrix = zeros(1,1);
XDelta_in_loadedmatrix = zeros(1,1);

vx(1,ua1)=vx0;
vy(1,ua1)=vy0;
d_theta(1,ua1)=atand(vx(1,ua1)/vy(1,ua1));
V(1,ua1) = sqrt((vy(1,ua1).^2)+(vx(1,ua1).^2));
A = (150*mu*(1-0.427)^2)/(rho*9.8*1000*(0.427)^3);
dv(1,ua1) = 0;
dv_ds(1,ua1) = 0;
dp_ds(1,ua1) = 0;

```



```

dp_dn(1,ua1) = 0;
DP(1,ua1) = sqrt((dp_ds(1,ua1).^2)+(dp_dn(1,ua1).^2));
ds(1,ua1) = 0;
center = [0 0];%./pixel_to_mm;
r_curv(1,ua1)= sqrt(((center(:,1)-Y(1,ua1))^2)+((center(:,2)-X(1,ua1))^2));
Re(1,ua1) = (V(1,ua1))*Dh*rho/mu;
K(1,ua1) = (1-alpha^2)+((4*phi)/(sqrt(pi)*Re(1,ua1))*(1-alpha));
K_2(1,ua1)=( dp_ds(1,ua1))/(mu*V(1,ua1)/(3/1000)^2);
Eu(1,ua1) = dp_ds(1,ua1)/(0.5*rho*V(1,ua1)^2);
V_model_Re(1,ua1) = alpha +((1-alpha))*erf(Y(1,ua1)/(Re(1,ua1)));
V_model(1,ua1) = alpha +((1-alpha))*erf(Y(1,ua1));

while (abs(y))> min(abs(VEC.y))&&(VX(i,ua1)~=0 || VY(i,ua1)~=0) && i < 1000
    x=(X(i,ua1)+VX(i,ua1)*dt);
    y=(Y(i,ua1)+VY(i,ua1)*dt);

    X(i+1,ua1)=x;
    Y(i+1,ua1)=y;

    for n = 1:length(VEC.y)
        YDelta_in_loadedmatrix(1,n)=(Y(i+1,ua1)-VEC.y(1,n));
    end
    for m=1:length(VEC.x)
        XDelta_in_loadedmatrix(1,m)=(X(i+1,ua1)-VEC.x(1,m));
    end
    Y_delta_closest=min(abs(YDelta_in_loadedmatrix));
    [i1,j1]=find(abs(YDelta_in_loadedmatrix)==Y_delta_closest);
    X_delta_closest=min(abs(XDelta_in_loadedmatrix));
    [i2,j2]=find(abs(XDelta_in_loadedmatrix)==X_delta_closest);
    YDelta_in_loadedmatrix(i1,j1);
    XDelta_in_loadedmatrix(i2,j2);
    Y_closest=y-YDelta_in_loadedmatrix(i1,j1);
    X_closest=x-XDelta_in_loadedmatrix(i2,j2);
    [i3,j3]=find(VEC.x==X_closest);
    [i4,j4]=find(VEC.y==Y_closest);
    VX(i+1,ua1)=VEC.vx(j3,j4);
    VY(i+1,ua1)=VEC.vy(j3,j4);
    d_theta(i+1,ua1)= (atand(VX(i+1,ua1)/VY(i+1,ua1)));
    V(i+1,ua1)= sqrt((VY(i+1,ua1).^2)+(VX(i+1,ua1).^2));

    ds(i+1,ua1) = arclength(Y(i:i+1,ua1),X(i:i+1,ua1));
    dV_ds(i+1,ua1)= ((VX(i+1,ua1)^2));
    dp_ds(i+1,ua1) = 0.5*rho*dV_ds(i+1,ua1);
    r_curv(i+1,ua1)= sqrt(((center(:,1)-Y(i+1,ua1))^2)+((center(:,2)-X(i+1,ua1))^2));
    dp_dn(i+1,ua1) = rho*((V(i+1,ua1)^2))/(r_curv(i+1,ua1));
    DP(i+1,ua1) = DP(i,ua1)+sqrt((dp_ds(i+1,ua1)^2)+(dp_dn(i+1,ua1)^2));
    Re(i+1,ua1) = (V(i+1,ua1))*Dh*rho/mu;
    K(i+1,ua1) = (1-alpha^2)+(4*phi/(sqrt(pi)*mean(Re(:,ua1)))*(1-alpha));
    K_2(i+1,ua1)=( dp_ds(i+1,ua1))/(mu*V(i+1,ua1)/(3/1000)^2);
    Eu(i+1,ua1) = DP(i+1,ua1)/(0.5*rho*(V(i+1,ua1)^2));
    V_model(i+1,ua1) = alpha +((1-alpha))*erf(-Y(i+1,ua1));
    V_model(i+1,ua1) = 1-abs(V_model(i+1,ua1));
    % V_skew(i+1,ua1) = alpha +((1-alpha))*erf(-Y(i+1,ua1)*phi);
    V_model_Re(i+1,ua1) = alpha +((1-alpha))*erf(-Y(i+1,ua1)/mean(Re(i+1,ua1)));

```

```

i=i+1
end
if (ua1 ==5)
Y(:,ua1) = smoothdata(Y(:,ua1),2,'movmean',5);
end
% figure('Name','Stream(TortuosPath)Lines')
if(R0==4)
    X_offset = 0; Y_offset = 0;
elseif(R0==3)
    X_offset = 0;
    Y_offset = 0;
elseif(R0==1)||(R0==2)
    Y_offset = 0;
    X_offset = 0;
end

if (R0==2)||(R0==3)||(R0==4)
%====Figure(2): Streamline plot from algorithm in Yusuf et al. POF II (2019)
Y=-1*Y;
end
if(R0==1)
    figure(4)
    hold on
    plot(Y(:,ua1)+Y_offset,X(:,ua1)+X_offset
,'o','MarkerFaceColor',Re_clr(X_Start_position,:), 'MarkerEdgeColor',Re_clr(X_Start_position,:), 'M
arkerSize',msize)
elseif(R0==2)
    figure(4)
    hold on
    plot(Y(:,ua1)+Y_offset,X(:,ua1)+X_offset
,'o','MarkerFaceColor',Re_clr(X_Start_position,:), 'MarkerEdgeColor',Re_clr(X_Start_position,:), 'M
arkerSize',msize)
    % set(gca,'XDir','reverse')
elseif(R0==3)
    figure(4);
    hold on
    plot(Y(:,ua1)+Y_offset,X(:,ua1)+X_offset
,'o','MarkerFaceColor',Re_clr(X_Start_position,:), 'MarkerEdgeColor',Re_clr(X_Start_position,:), 'M
arkerSize',msize)
elseif(R0==4)
    figure(4);
    hold on
    plot(Y(:,ua1)+Y_offset,X(:,ua1)+X_offset
,'o','MarkerFaceColor',Re_clr(X_Start_position,:), 'MarkerEdgeColor',Re_clr(X_Start_position,:), 'M
arkerSize',msize)
end

xlabel({'\it{x/b}'}, 'FontSize', FSize, 'Interpreter', Interpreter)
ylabel({'\it{y/b}'}, 'FontSize', FSize, 'Interpreter', Interpreter)
% set(gca,'XDir','reverse')
set(gca,'FontSize',FSize);
set(gcf,'Color','w')
grid on
legend({strcat('\it{y/b} = 4'),strcat('\it{y/b} = 3'),strcat('\it{y/b} = 2')},

```

```

strcat('\it{y/b} = 1'),...
    strcat('\it{y/b} = 0'),'FontSize',FSize-4,
'Interpreter',Interpreter,'Location','Northwest');
figure(5)
hold on

plot(Y(:,ual)+Y_offset,abs(d_theta(:,ual)),'o','MarkerFaceColor',Re_clr(X_Start_position,:),'Mark
erEdgeColor',Re_clr(X_Start_position,:),'MarkerSize',msize)
    xlabel('\it{x/b}','FontSize',FSize,'Interpreter',Interpreter)
    ylabel('d\it{\theta}','FontSize',FSize,'Interpreter',Interpreter)
% set(gca,'XDir','reverse')
xlim([-5 0])
ylim([0 80])
    set(gca,'FontSize',FSize);
    set(gcf,'Color','w')
    grid on
    legend({strcat('\it{y/b} = 4'),strcat('\it{y/b} = 3'),strcat('\it{y/b} = 2'),
strcat('\it{y/b} = 1'),...
    strcat('\it{y/b} = 0'),'FontSize',FSize-4,
'Interpreter',Interpreter,'Location','Northwest');

    sline_tag{ual} = strcat('Steamline',num2str(ual));
% stream_fun.(sline_tag{ual}) = horzcat(Y(:,ual)+Y_offset, X(:,ual)+X_offset);
% eqline_tag{ual} = strcat('EqLine',num2str(ual));
% eq_fun.(eqline_tag{ual}) =
horzcat(VX(:,ual).*X(:,ual)+X_offset,VY(:,ual).*(Y(:,ual)+Y_offset));
% legend({strcat('\it{x/b} = 0'),strcat('\it{x/b} = 1'), strcat('\it{x/b} = 2'),...
%     strcat('\it{x/b} = 3'),strcat('\it{x/b} = 4'),strcat('\it{x/b} =
5')},'Interpreter','Latex');
% %
plot(abs((eq_fun.(eqline_tag{ual})(:,1))/max(eq_fun.(eqline_tag{ual})(:,1))),X(:,ual)+X_offset,'s
','Color',Re_clr(X_Start_position,:),'Linewidth',1.2)
% %====plot equipotential lines
% % eqp_step = 20;
% % eqp_lines = 1:eqp_step:length(Y(:,ual))
% % eqp_loc = i== eqp_lines
% %
viscircles(zeros(length(Y(1:eqp_step:end,ual)),2),abs(Y(1:eqp_step:end,ual)),'Color',Re_clr(2,:))
;
% % for eq_pot=1:length(Y(:,ual))
% %     eqp_line(i,ual)= viscircles(center,Y(:,ual),'Color','k');
% % end
% hold off
% % xlim([0 6])
% % ylim([0 4])
% % ylabel('\it{x/b}','FontSize',FSize,'Interpreter',Interpreter)
% % xlabel('\it{y/b}','FontSize',FSize,'Interpreter',Interpreter)
% % ylabel('\it{x/b}','FontSize',FSize,'Interpreter',Interpreter)
% % set(gca,'XDir','reverse')
% set(gca,'FontSize',FSize);
% set(gcf,'Color','w')
% grid on
%
% if(sho_plot==1)

```

```

%====Figure(3): dp/ds streamwise pressure drop

if(R0==1)
    figure(7)
    hold on
    plot(Y(:,ua1)+Y_offset_dp,abs((dp_ds(:,ua1))./max((dp_ds(:,ua1))))), 'o', 'MarkerFaceColor',Re_clr(X
_Start_position,:), 'MarkerEdgeColor',Re_clr(X_Start_position,:), 'MarkerSize',msizep)
    hold off
elseif(R0==2)
    figure(7)
    hold on
    plot(Y(:,ua1)+Y_offset_dp,abs((dp_ds(:,ua1))./max((dp_ds(:,ua1))))), 'o', 'MarkerFaceColor',Re_clr(X
_Start_position,:), 'MarkerEdgeColor',Re_clr(X_Start_position,:), 'MarkerSize',msizep)
    hold off
elseif(R0==3)
    figure(7)
    hold on
    plot(Y(:,ua1)+Y_offset_dp,abs((dp_ds(:,ua1))./max((dp_ds(:,ua1)))))/0.7, 'o', 'MarkerFaceColor',Re_c
lr(X_Start_position,:), 'MarkerEdgeColor',Re_clr(X_Start_position,:), 'MarkerSize',msizep)
    hold off
    % set(gca,'XDir','reverse')
elseif(R0==4)
    figure(7);
    hold on

plot(Y(:,ua1)+Y_offset_dp,abs((dp_ds(:,ua1))./max((dp_ds(:,ua1))))), 'o', 'MarkerFaceColor',Re_clr(X
_Start_position,:), 'MarkerEdgeColor',Re_clr(X_Start_position,:), 'MarkerSize',msizep)
    hold off
end

    xlim([-5 0])
% xlim([0 6])
% ylim([0 1e-5])
% ylabel({'\it{x/b}'}, 'FontSize', FSize, 'Interpreter', Interpreter)
xlabel({'\it{x/b}'}, 'FontSize', FSize, 'Interpreter', Interpreter)
ylabel({'\it{\partial p/\partial s}^*'}, 'FontSize', FSize, 'Interpreter', Interpreter)
% set(gca,'XDir','reverse')
set(gca,'FontSize',FSize);
set(gcf,'Color','w')
    legend({strcat({'\it{y/b}} = 4'),strcat({'\it{y/b}} = 3'),strcat({'\it{y/b}} = 2'),
strcat({'\it{y/b}} = 1'),...
    strcat({'\it{y/b}} = 0')}, 'FontSize', FSize-4,
'Interpreter', Interpreter, 'Location', 'Northwest');
    grid on
% savefig('Munich2019_dp_ds.fig')
% %====Figure(4): dp/dn spanwise pressure gradient
figure(8)
hold on

plot(Y(:,ua1),abs((dp_dn(:,ua1))./max((dp_dn(:,ua1))))), 'o', 'MarkerFaceColor',Re_clr(X_Start_posit
ion,:), 'MarkerEdgeColor',Re_clr(X_Start_position,:), 'MarkerSize',msizep)

    xlim([-5 0])

```

```

% xlim([0 6])
% ylim([0 1e-5])
% ylabel({'\it{y/b}}','FontSize',FSize, 'Interpreter', Interpreter)
% xlabel({'\it{x/b}}','FontSize',FSize, 'Interpreter', Interpreter)
% ylabel({'\it{\partial p/\partial n}^*','FontSize',FSize, 'Interpreter', Interpreter)
% set(gca,'XDir','reverse')
set(gca,'FontSize',FSize);
set(gcf,'Color','w')
legend({strcat('\it{y/b} = 4'),strcat('\it{y/b} = 3'),strcat('\it{y/b} = 2'),
strcat('\it{y/b} = 1'),...
strcat('\it{y/b} = 0')},'FontSize',FSize-4,
'Interpreter',Interpreter,'Location','Northwest');
grid on
%
%====Figure(5): K Pressure loss coefficient from model given in Yusuf et
%al. (2019) POF 1
% figure(5)
if(ua1==4)
openfig('K_model_ARS.fig')
hold on

plot(Y(:,ua1),(K(:,ua1)),'s','MarkerFaceColor',Re_clr(X_Start_position,:), 'MarkerEdgeColor',Re_clr(X_Start_position,:), 'MarkerSize',4.5)
% xlim([-5 0])

% xlim([0 6])
% ylim([0 1e-5])
% ylabel({'\it{y/b}}','FontSize',FSize, 'Interpreter', Interpreter)
% xlabel({'\it{x/b}}','FontSize',FSize, 'Interpreter', Interpreter)
% ylabel({'\it{K_2}}','FontSize',FSize, 'Interpreter', Interpreter)
% set(gca,'XDir','reverse')
set(gca,'FontSize',FSize);
set(gcf,'Color','w')
grid on
savefig('K_model_ARS_3mm.fig')
end
% %====Figure(6a): velocity transition plot along a streamline from experiment u/u_max vs. y/b
% %where, in the code, u = V;
w_size_V = 20;
if (ua1==4)
w_size_V = 10;
end
V(:,ua1)= smoothdata(V(:,ua1),1, 'gaussian',w_size_V);
figure(6)
hold on
temp = Y(:,ua1);
temp(temp >= 0) =nan;

plot(temp,abs((V(:,ua1))/max(max(V))), 'o', 'MarkerFaceColor',Re_clr(X_Start_position,:), 'MarkerEdgeColor',Re_clr(X_Start_position,:), 'MarkerSize',msizep)
xlim([-5 0])
% xlim([0 6])
% ylim([0 1e-5])
% ylabel({'\it{y/b}}','FontSize',FSize, 'Interpreter', Interpreter)

```

```

xlabel({'\it{x/b}'},'FontSize',FSize, 'Interpreter', Interpreter)
ylabel({'\it{V}'},'FontSize',FSize, 'Interpreter', Interpreter)
% set(gca,'XDir','reverse')
set(gca,'FontSize',FSize);
set(gcf,'Color','w')
grid on
legend({'\it{y/b} = 4'},strcat({'\it{y/b} = 3'},strcat({'\it{y/b} = 2'},
strcat({'\it{y/b} = 1'},...
strcat({'\it{y/b} = 0'}),'FontSize',FSize-4,
'Interpreter',Interpreter,'Location','Northwest');
%====Figure(6b): velocity transition plot along a streamline from model given in
% Yusuf et al. POF1. The velocity along a streamline is calculated as
%  $v_{model}(:,ua1) = \alpha + ((1-\alpha))*erf(Y(:,ua1)/(Re(:,ua1)))$ ;
hold on
%  $v_{model}=v_{model}/\max(\max(v_{model}))$ ;
plot(Y(2:end,ua1),((v_model(2:end,ua1)/\max(\max(v_model)))),'s','MarkerFaceColor',[0 0
0],'MarkerEdgeColor',[0 0 0],'MarkerSize',msizep)
xlim([-5 0])
% xlim([0 6])
% ylim([0 1e-5])
% ylabel({'\it{x/b}'},'FontSize',FSize, 'Interpreter', Interpreter)
xlabel({'\it{x/b}'},'FontSize',FSize, 'Interpreter', Interpreter)
ylabel({'\it{u/u_{max}}'},'FontSize',FSize, 'Interpreter', Interpreter)
% set(gca,'XDir','reverse')
set(gca,'FontSize',FSize);
set(gcf,'Color','w')
grid on
% legend('Experiment','Model')

% end
figure(9)
hold on
%  $v_{model}=v_{model}/\max(\max(v_{model}))$ ;

plot(Y(2:end,ua1),(v_model_Re(2:end,ua1)),'s','Color',Re_clr(X_Start_position,:),'Linewidth',1.2)
hold off
xlim([-5 0])
% xlim([0 6])
% ylim([0 1e-5])
% ylabel({'\it{x/b}'},'FontSize',FSize, 'Interpreter', Interpreter)
xlabel({'\it{x/b}'},'FontSize',FSize, 'Interpreter', Interpreter)
ylabel({'\it{V_{model}/Re_{local}}'},'FontSize',FSize, 'Interpreter', Interpreter)
% set(gca,'XDir','reverse')
set(gca,'FontSize',FSize);
set(gcf,'Color','w')
grid on

% % plot(sort(dp_ds(:,ua1)),Y(:,ua1),'s','Color',Re_clr(X_Start_position,:),'Linewidth',1)
% hold on
% % yyaxis left
%
% if(R0==1)|| (R0==4)|| (R0==5)
% xlim([-5 0])
% % ylim([0 25])

```

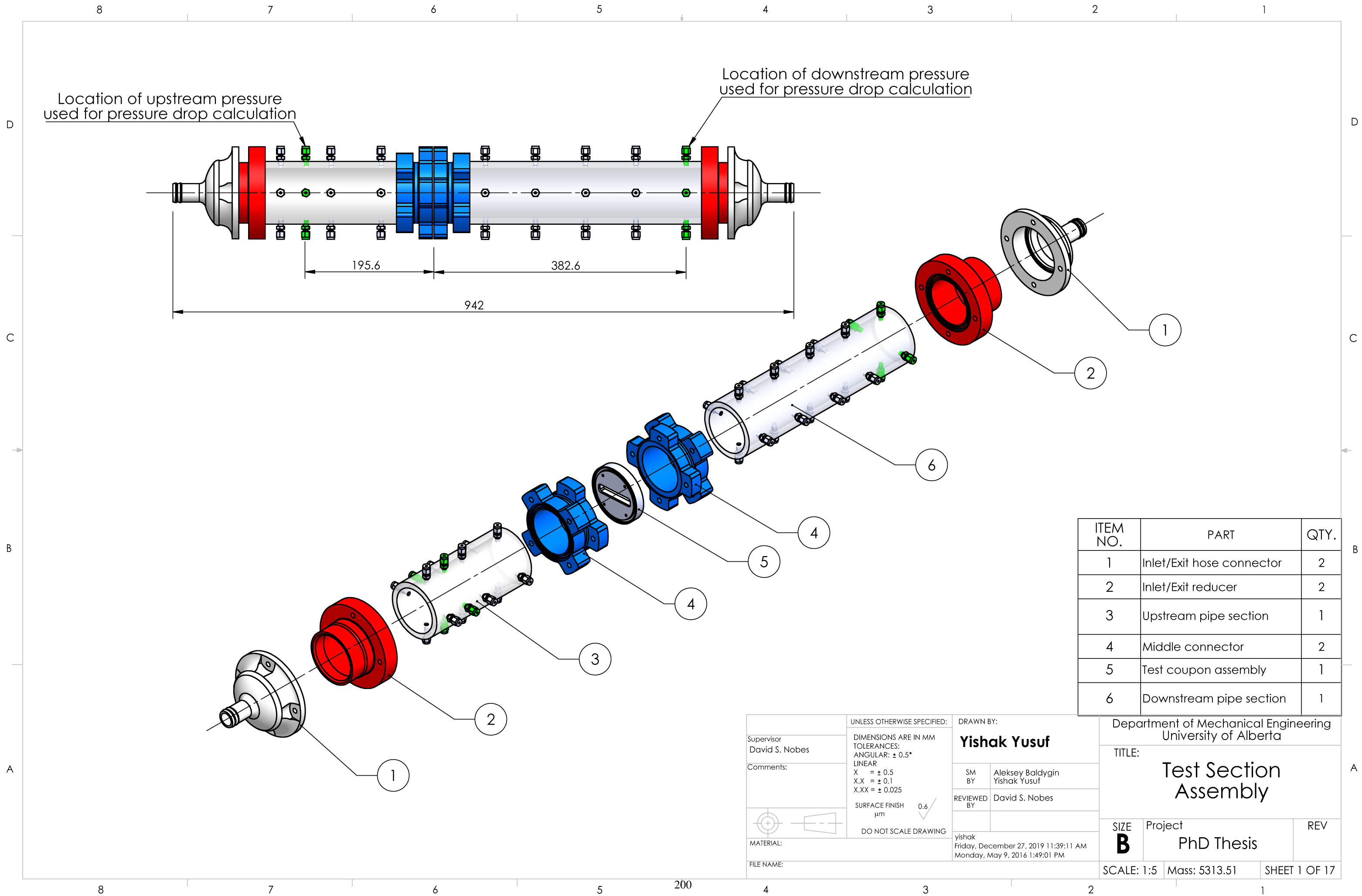
```

% end
% hold on
% set(gca,'FontSize',FSize);
% set(gcf,'Color','w')
%% xlabel('\it{x/b}','FontSize',FSize, 'Interpreter', Interpreter)
%
% legend({strcat('\it{x/b} = 0'),strcat('\it{x/b} = 1'), strcat('\it{x/b} = 2'),...
%         strcat('\it{x/b} = 3'),strcat('\it{x/b} = 4'),strcat('\it{x/b} =
5')},'Interpreter','Latex');
% set(gca,'TickLabelInterpreter','latex');
% grid on
%% if(R0==4)||(R0==5)
%%     S(:,ua1) = (arclength(Y(:,ua1),X(:,ua1)));
%% elseif(R0==3)
%%     S(:,ua1) = abs(arclength(Y(:,ua1),X(:,ua1)));
%% end
% hold on
center = [0 0];%./pixel_to_mm;
R_pts = 6; %number of points on a streamline to draw the "R" lines
d_beta = ceil(length(Y)/R_pts);
figure(4)
% hold on
% for i5=1:d_beta:length(Y)-1
%     p= ([Y(i5,ua1), X(i5,ua1)]);
%     line([p(1) center(1)], [p(2) center(2)], 'Color','r','Linewidth',1.2)
%     hold on
% end
%% xlim([-6 0])
%% set(gca,'XDir','reverse')
% grid on
figure(11)
hold on
for i7 = 1:length(Y)
    r_curv(i7,ua1) = sqrt(((center(:,1)-Y(i7,ua1))^2)+((center(:,2)-X(i7,ua1))^2));
end
% plot(Y(1:length(Y)-1,j5),ds(:,j5),'bo')
hold on
plot(Y(:,ua1),r_curv(:,ua1), 'Color',Re_clr(X_Start_position,:), 'Linewidth',1.2)
ylabel('\it{R/b}','FontSize',FSize, 'Interpreter', Interpreter)
xlim([-inf 0])
% set(gca,'XDir','reverse')
set(gca,'FontSize',FSize);
set(gcf,'Color','w')
set(gcf,'Position',[10 10 500 400])
xlabel('\it{x/b}','FontSize',FSize, 'Interpreter', Interpreter)
% legend({strcat('\it{Re} = 0.1'), strcat('\it{Re} = 0.5'), strcat('\it{Re} = 5'),
strcat('\it{Re} = 10')},'Interpreter','Latex');
set(gca,'TickLabelInterpreter','latex');
grid on
hold on
ua1=1+ua1;
end

```

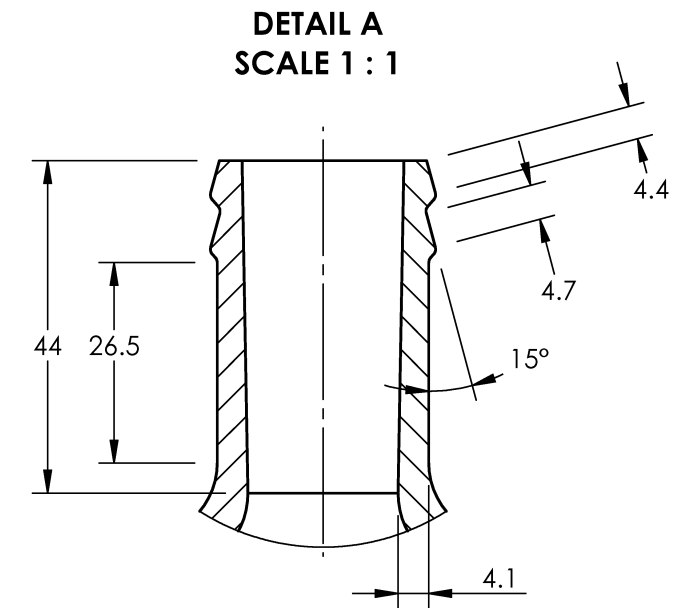
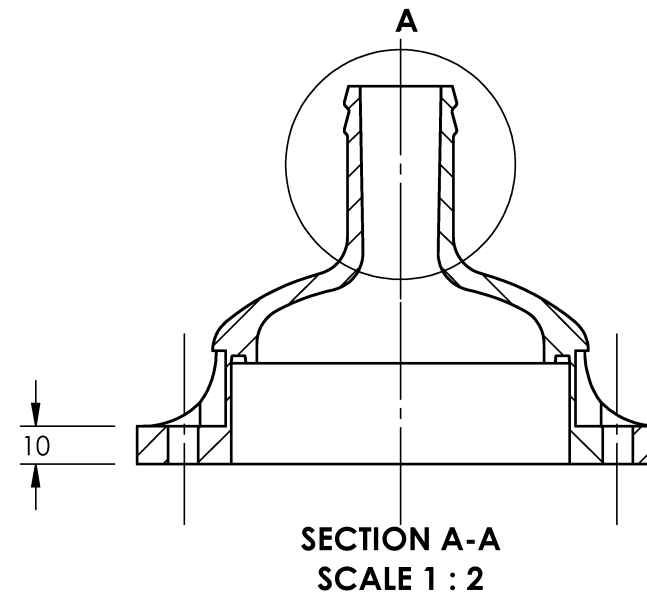
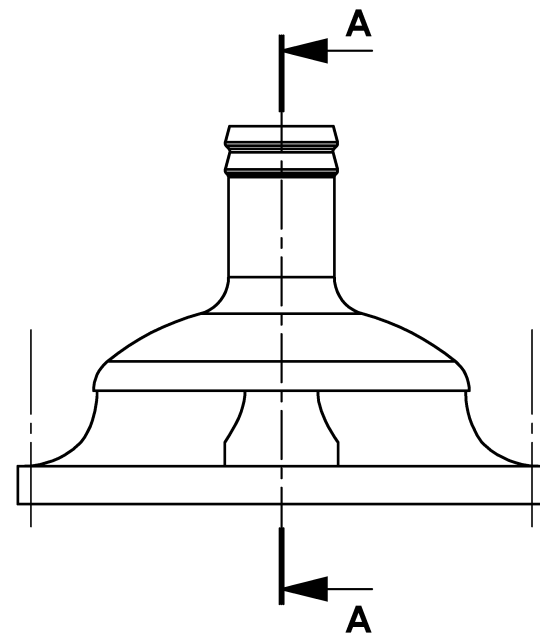
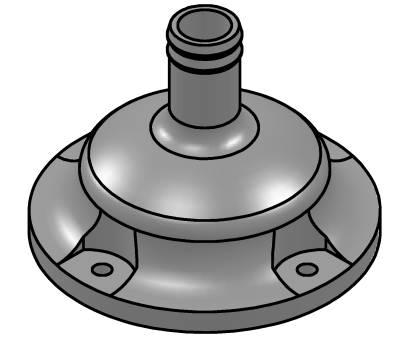
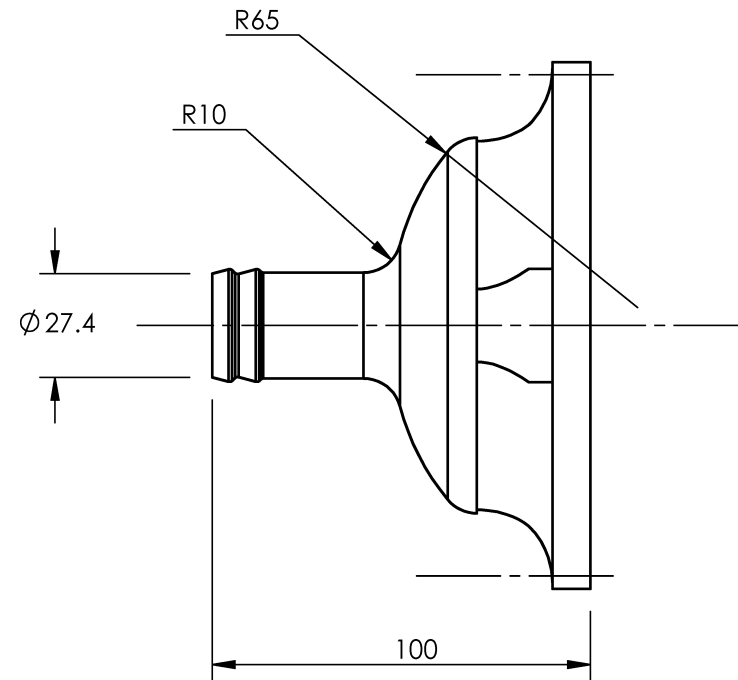
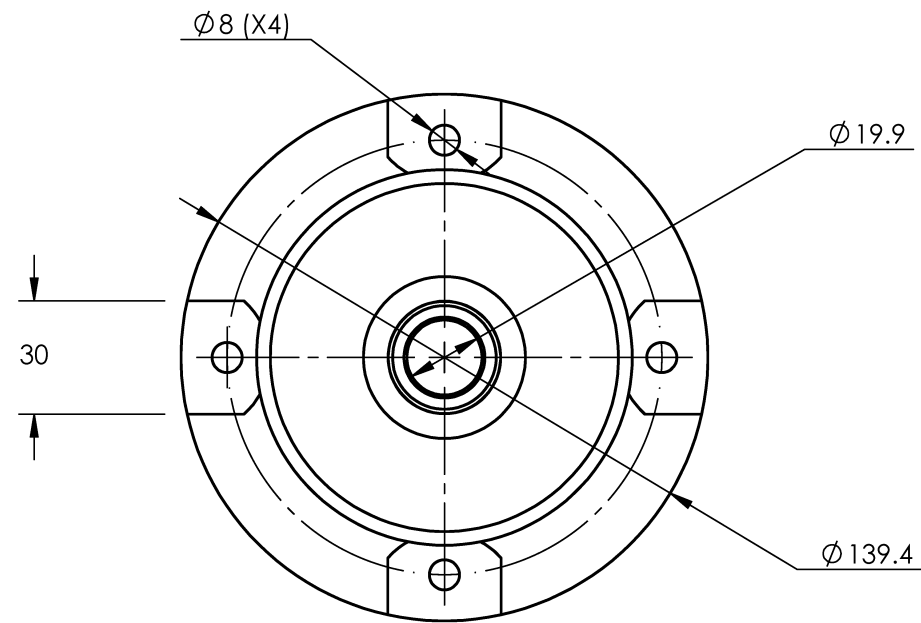
C. Detail Drawings

Designing components of the test section of the pressure measurement facility, and flow channel assemblies used in PIV experiments was required in the research to achieve the proper measurement of parameters. All the design work has been done using a commercial software package for solid modelling and simulation (SolidWorks 2018/19, Dassault Systèmes). This section provides the standard drawing sheets showing the detail designs of the components. A combination of 3D printing and laser cutting was used to manufacture the parts.



ITEM NO.	PART	QTY.
1	Inlet/Exit hose connector	2
2	Inlet/Exit reducer	2
3	Upstream pipe section	1
4	Middle connector	2
5	Test coupon assembly	1
6	Downstream pipe section	1

Supervisor David S. Nobes		UNLESS OTHERWISE SPECIFIED: DIMENSIONS ARE IN MM TOLERANCES: ANGULAR: $\pm 0.5^\circ$ LINEAR X = ± 0.5 X.X = ± 0.1 X.XX = ± 0.025		DRAWN BY: Yishak Yusuf		Department of Mechanical Engineering University of Alberta	
Comments:		SURFACE FINISH μm 0.6 ✓ DO NOT SCALE DRAWING		SM BY: Aleksey Baldygin Yishak Yusuf		TITLE: Test Section Assembly	
MATERIAL:		REVIEWED BY: David S. Nobes		yishak Friday, December 27, 2019 11:39:11 AM Monday, May 9, 2016 1:49:01 PM		SIZE Project B PhD Thesis	
FILE NAME:		200		4		SCALE: 1:5 Mass: 5313.51	
		3		2		SHEET 1 OF 17	



Supervisor David S. Nobes	UNLESS OTHERWISE SPECIFIED: DIMENSIONS ARE IN MM TOLERANCES: ANGULAR: $\pm 0.5^\circ$ LINEAR X = ± 0.5 X.X = ± 0.1 X.XX = ± 0.025 SURFACE FINISH μm 0.6 ✓ DO NOT SCALE DRAWING	DRAWN BY: Yishak Yusuf		Department of Mechanical Engineering University of Alberta	
		SM BY Yishak Yusuf	TITLE: Test Section Assembly		
Comments: Edit in SM		REVIEWED BY David S. Nobes	SIZE B	Project PhD Thesis	REV
MATERIAL: Acrylonitrile butadiene styrene (ABS)		yishak Thursday, October 31, 2019 1:23:42 PM Thursday, September 22, 2016 5:28:03 PM	SCALE: 1:5	Mass: 204.08	SHEET 2 OF 17
MANUFACTURING: Fused deposition modeling 3D printing using Ultimaker2+					

8 7 6 5 4 3 2 1

D

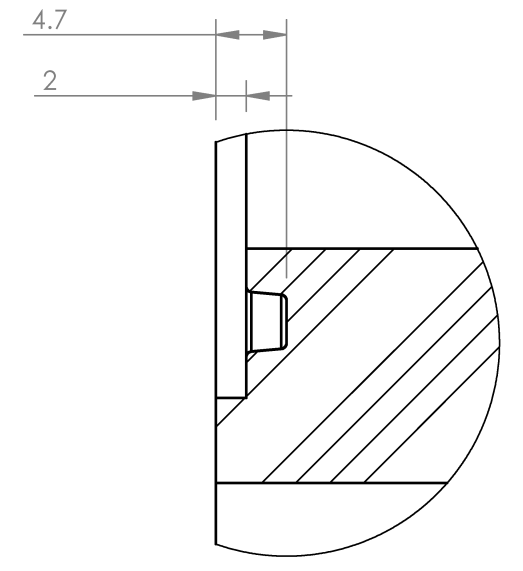
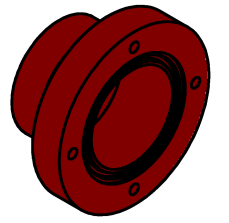
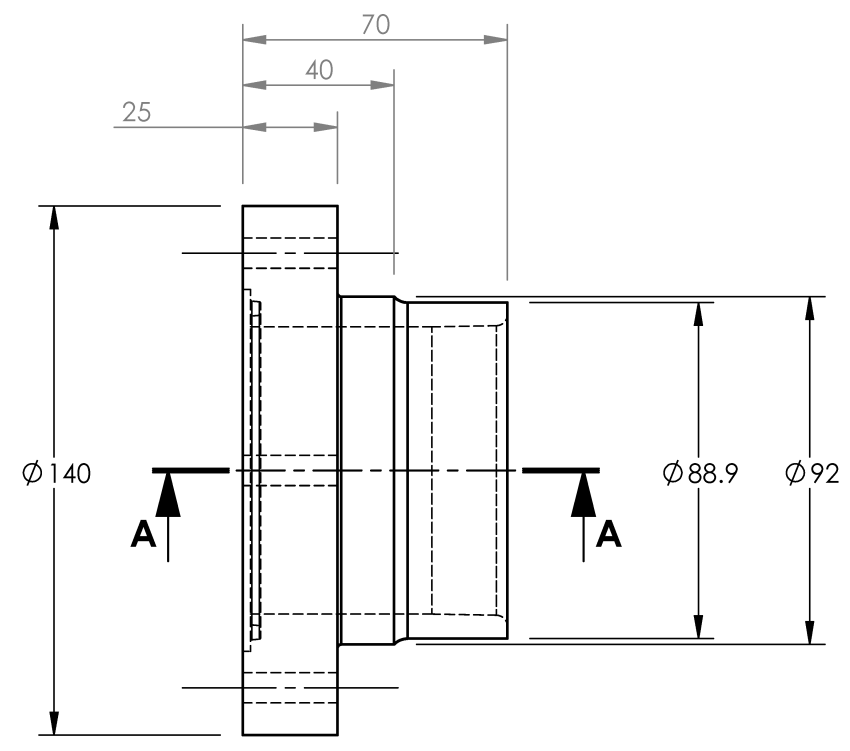
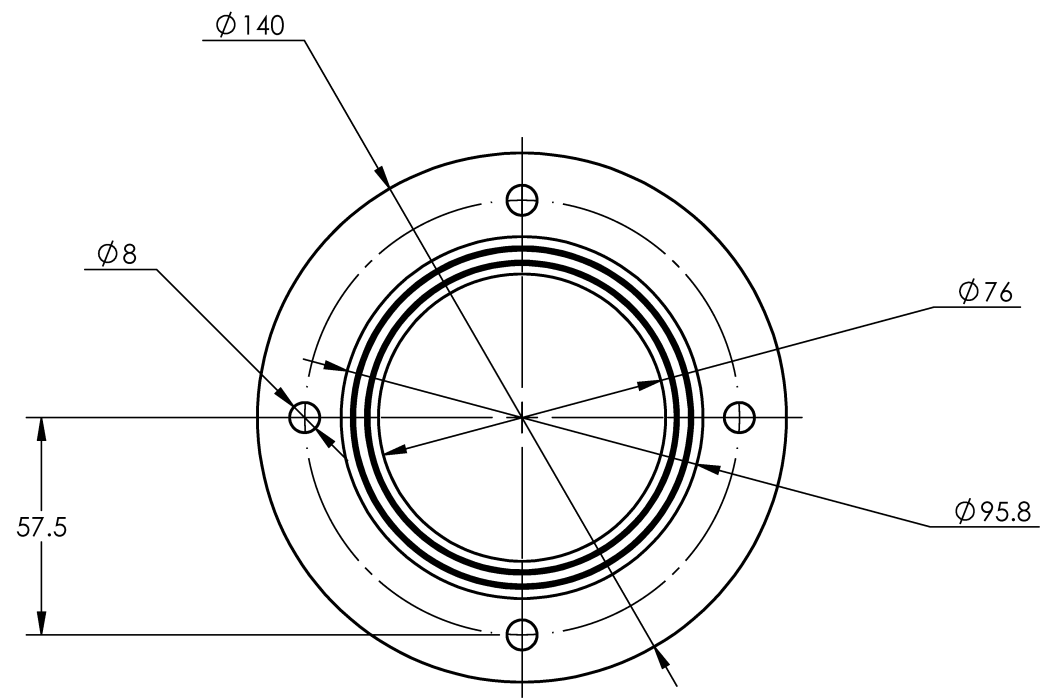
C

B

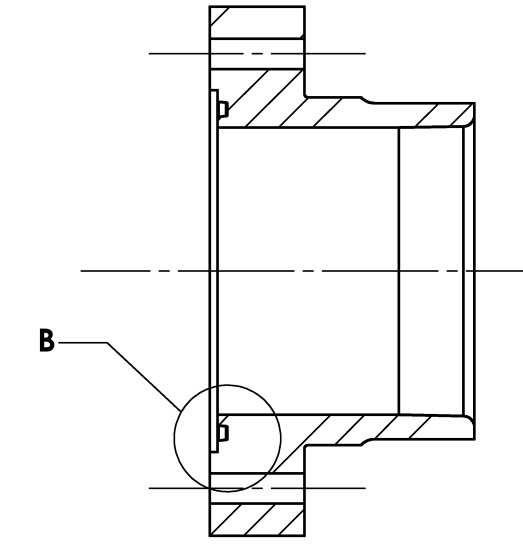
A

8 7 6 5 4 3 2 1

201

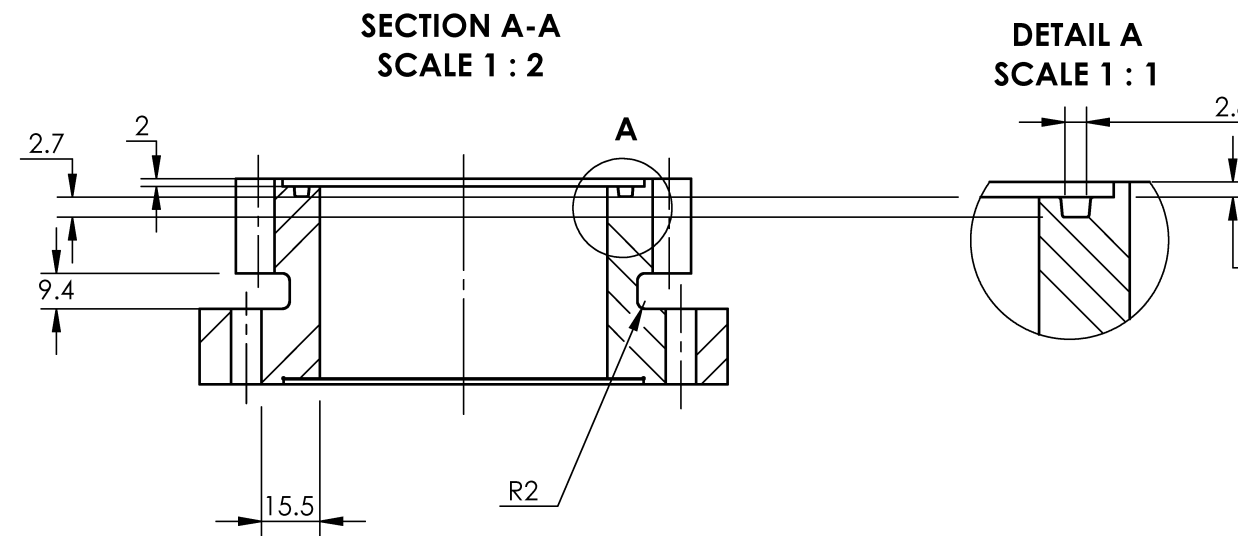
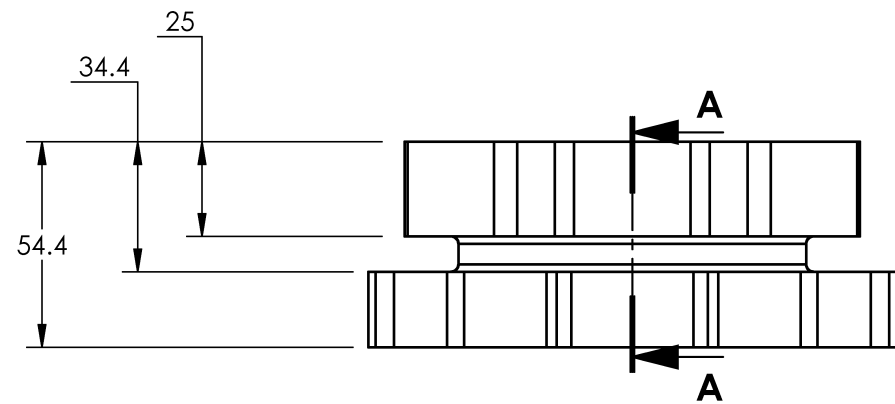
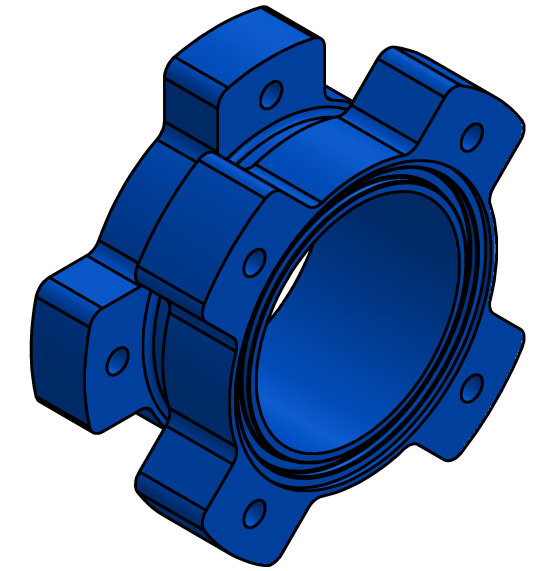
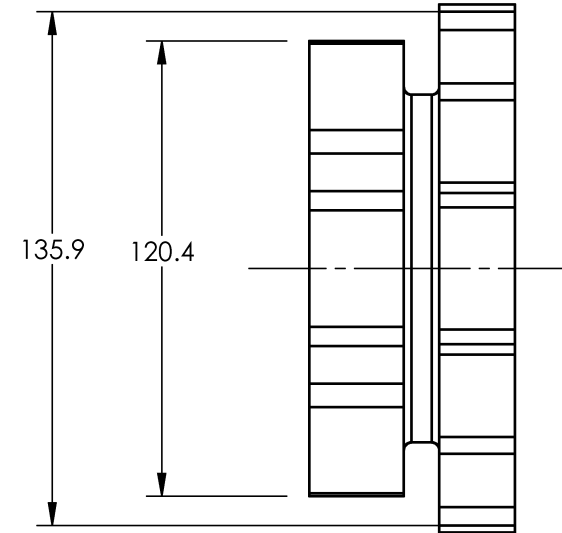
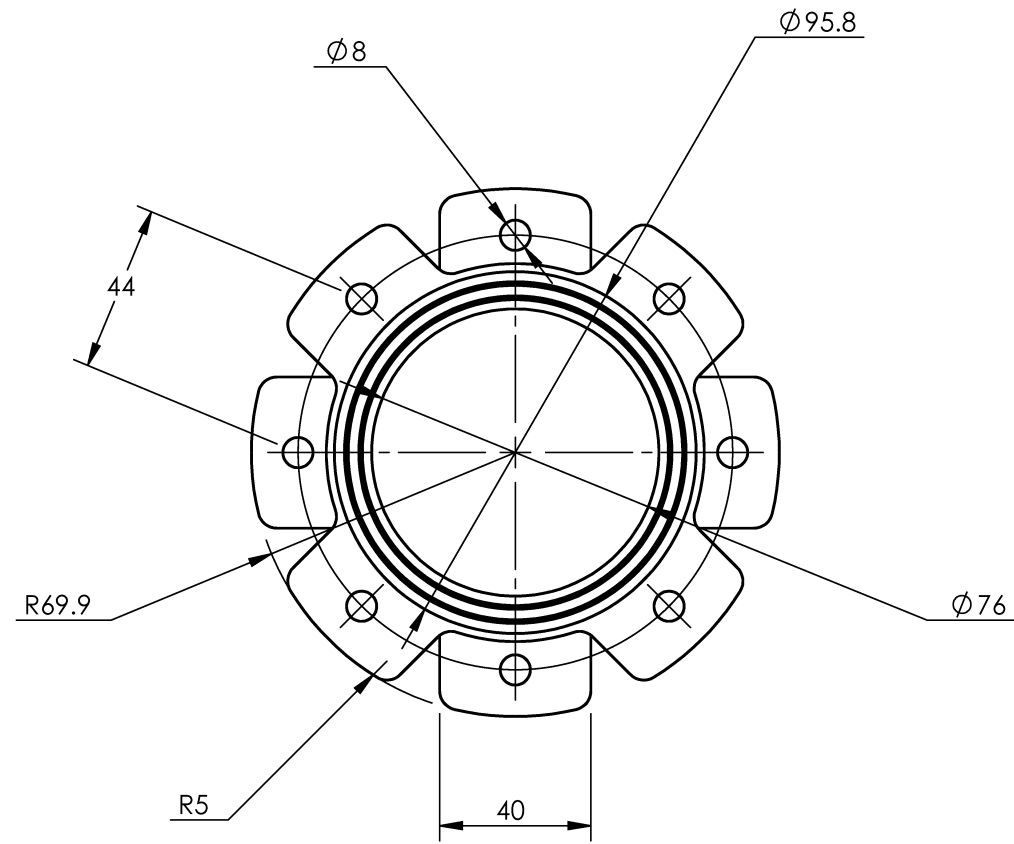


**DETAIL B
SCALE 2 : 1**



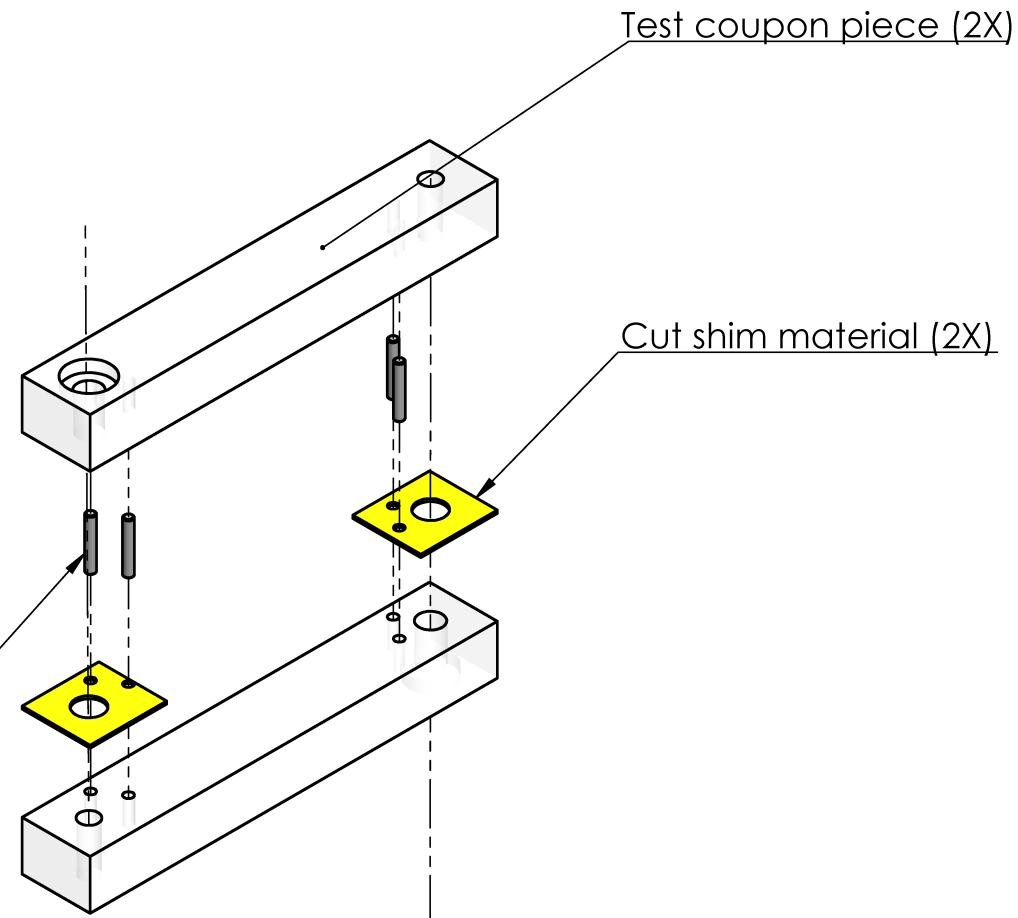
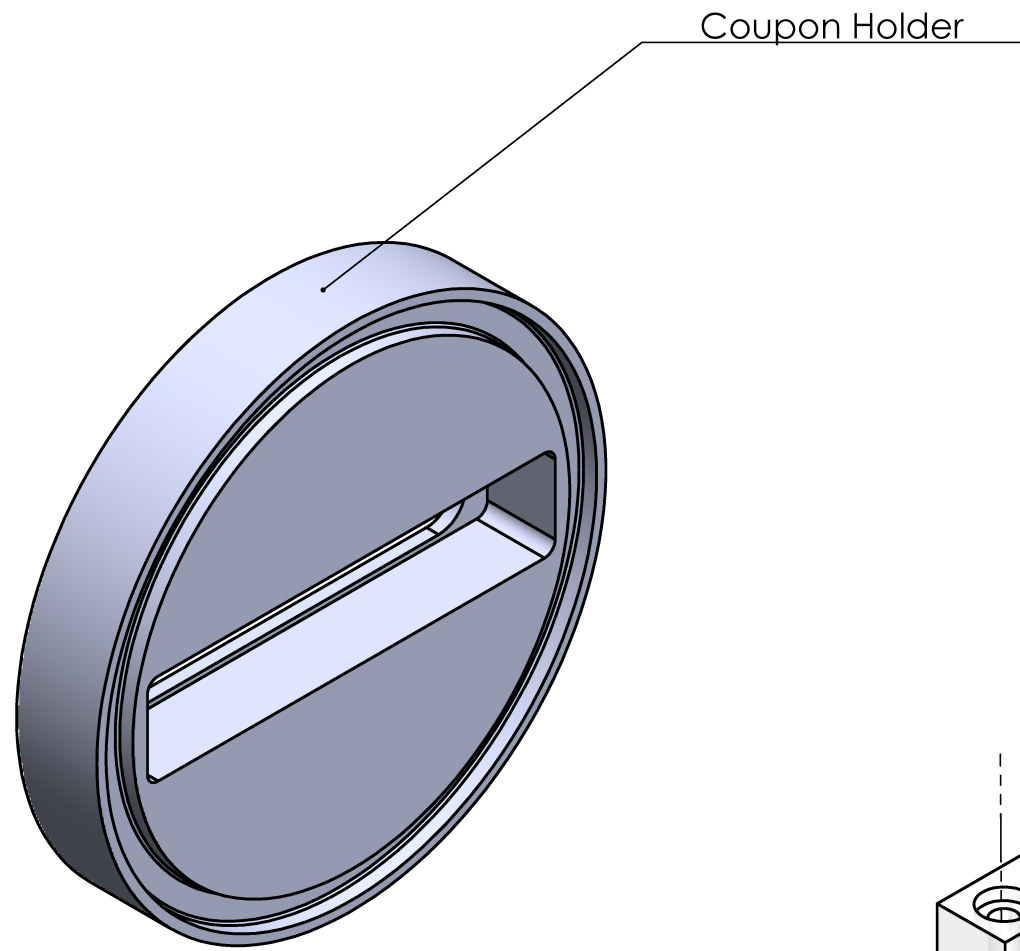
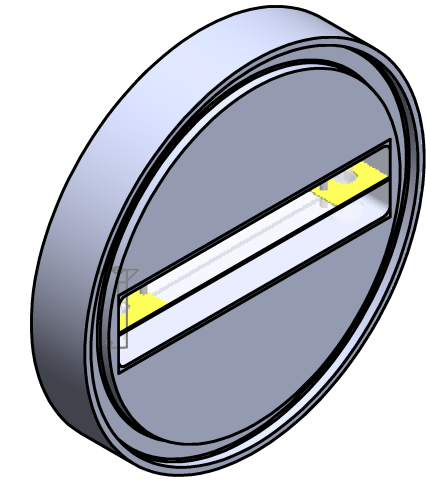
**SECTION A-A
SCALE 1 : 2**


Supervisor David S. Nobes		UNLESS OTHERWISE SPECIFIED: DIMENSIONS ARE IN MM TOLERANCES: ANGULAR: ± 0.5° LINEAR X = ± 0.5 X.X = ± 0.1 X.XX = ± 0.025		DRAWN BY: Yishak Yusuf		Department of Mechanical Engineering University of Alberta	
Comments:		SURFACE FINISH µm 0.6 ✓ DO NOT SCALE DRAWING		SM BY: Yishak Yusuf		TITLE: Inlet/Exit Reducer	
MATERIAL: Acrylonitrile butadiene styrene (ABS)		REVIEWED BY: David S. Nobes		yishak Thursday, October 31, 2019 1:33:37 PM Tuesday, August 2, 2016 9:07:51 AM		SIZE Project REV B PhD Thesis	
MANUFACTURING: Fused deposition modeling 3D printing using Ultimaker2+		SCALE: 1:5		Mass:		SHEET 3 OF 17	



Fused deposition modeling 3D printing using Ultimaker2+

Supervisor David S. Nobes		UNLESS OTHERWISE SPECIFIED: DIMENSIONS ARE IN MM TOLERANCES: ANGULAR: ± 0.5° LINEAR X = ± 0.5 X.X = ± 0.1 X.XX = ± 0.025		DRAWN BY: Yishak Yusuf		Department of Mechanical Engineering University of Alberta	
Comments:		SURFACE FINISH µm 0.6 ✓ DO NOT SCALE DRAWING		SM BY: Yishak Yusuf		TITLE: Middle Connector	
MATERIAL: Acrylonitrile butadiene styrene (ABS)		REVIEWED BY: David S. Nobes		yishak Thursday, October 31, 2019 1:19:48 PM		SIZE B	Project PhD
MANUFACTURING:		Tuesday, August 2, 2016 9:07:51 AM		SCALE: 1:5		Mass:	REV SHEET 4 OF 17



Supervisor David S. Nobes		UNLESS OTHERWISE SPECIFIED: DIMENSIONS ARE IN MM TOLERANCES: ANGULAR: $\pm 0.5^\circ$ LINEAR X = ± 0.5 X.X = ± 0.1 X.XX = ± 0.025 SURFACE FINISH μm 0.6 ✓ DO NOT SCALE DRAWING	DRAWN BY: Yishak Yusuf		Department of Mechanical Engineering University of Alberta	
Comments:			SM BY Yishak Yusuf	TITLE: Shim-based rectangular coupon holder		
 MATERIAL: Variable MANUFACTURING: Variable		REVIEWED BY David S. Nobes	SIZE B	Project PhDThesis	REV	
		yishak Thursday, October 31, 2019 1:49:06 PM Friday, February 9, 2018 1:41:10 PM	SCALE: 1:5	Mass:	SHEET 5 OF 17	

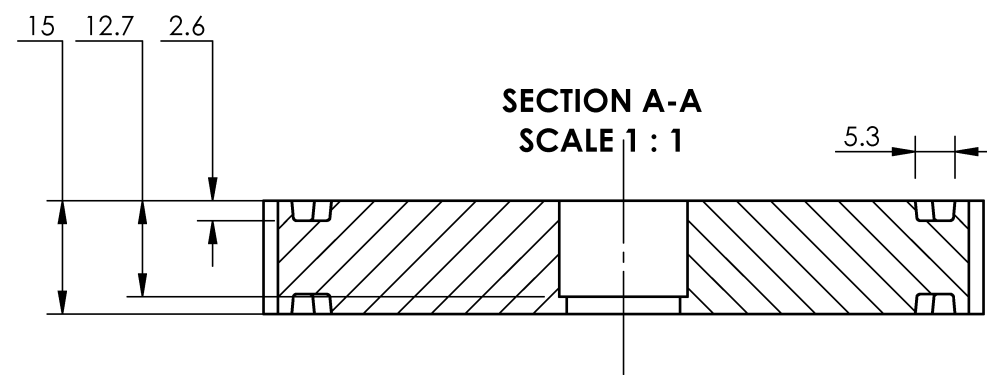
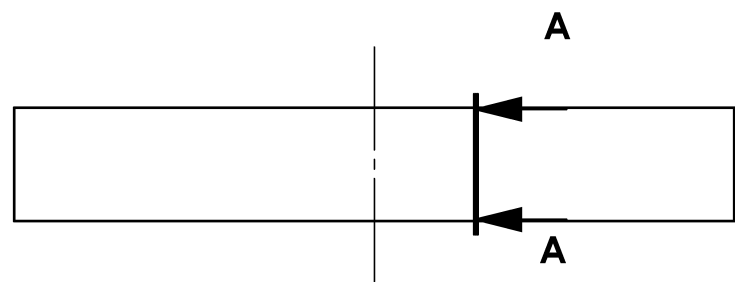
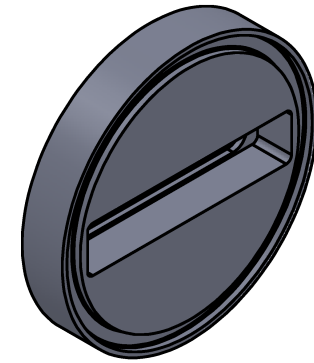
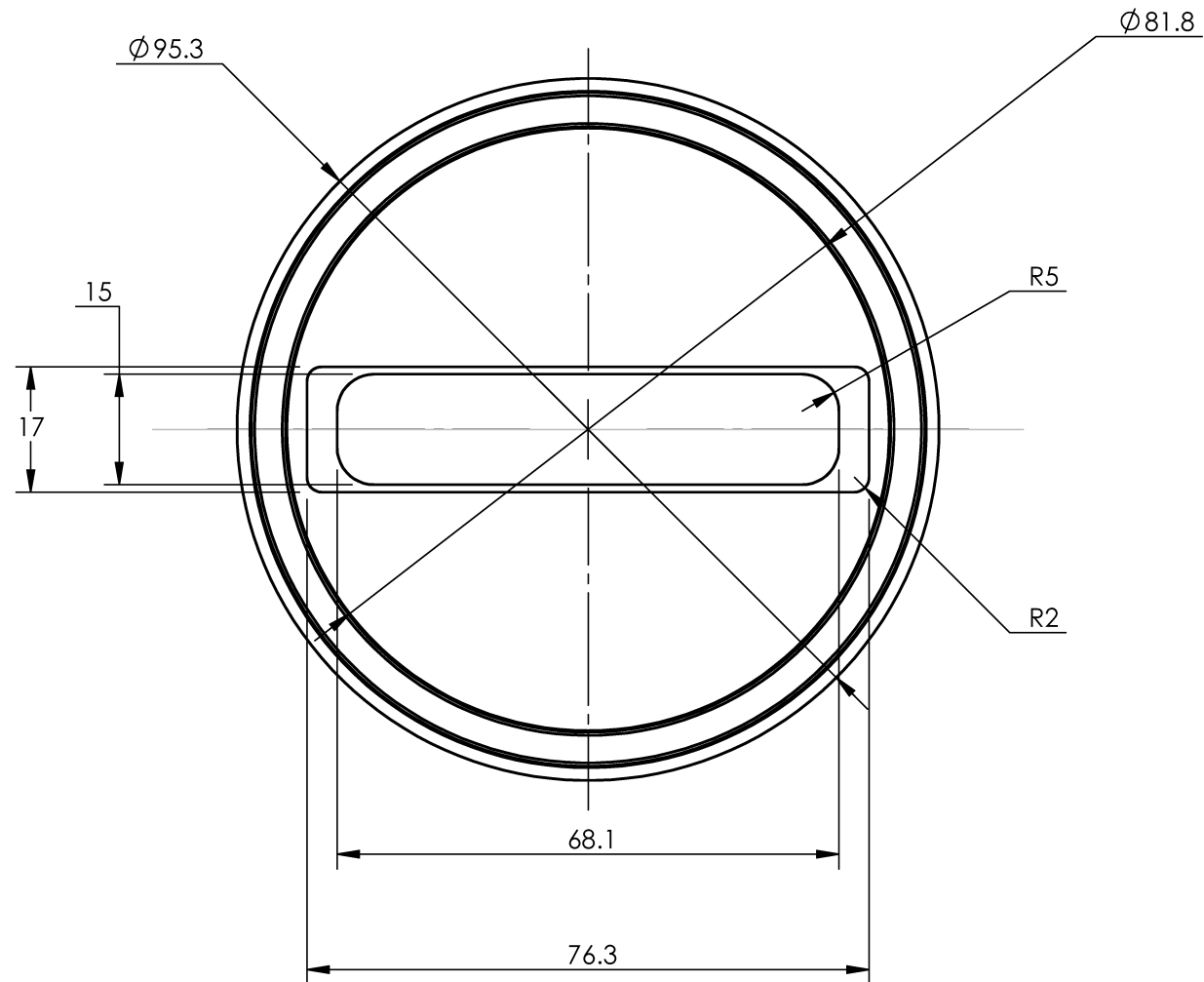
8 7 6 5 4 3 2 1

D
C
B
A

D
C
B
A

8 7 6 5 4 3 2 1

204



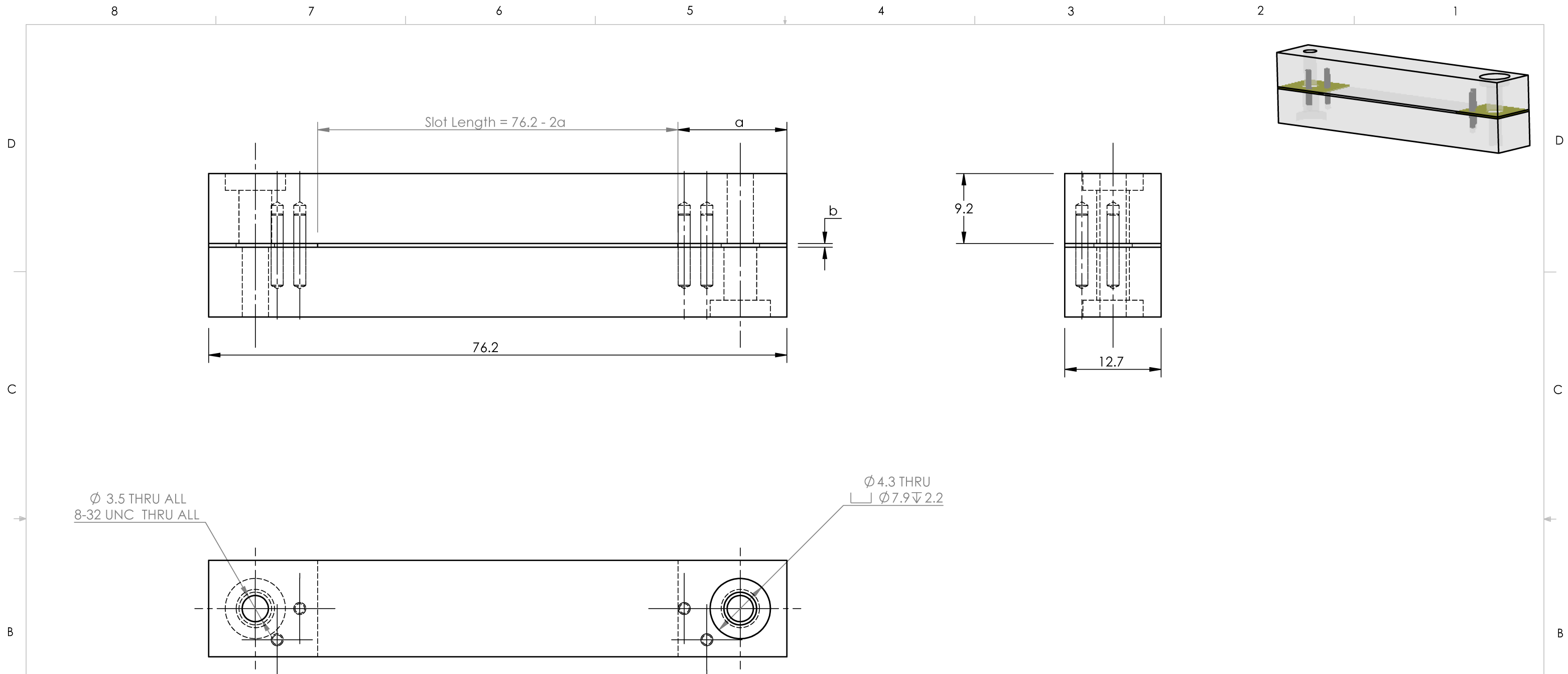
Supervisor David S. Nobes		UNLESS OTHERWISE SPECIFIED: DIMENSIONS ARE IN MM TOLERANCES: ANGULAR: $\pm 0.5^\circ$ LINEAR X = ± 0.5 X.X = ± 0.1 X.XX = ± 0.025		DRAWN BY: Yishak Yusuf		Department of Mechanical Engineering University of Alberta	
Comments:		SURFACE FINISH μm 0.6 ✓ DO NOT SCALE DRAWING		SM BY: Yishak Yusuf		TITLE: Shim-based rectangular coupon holder	
MATERIAL: Photopolymer resin		MANUFACTURING: Stereolithographic 3D printing using Form2 by Formlabs		REVIEWED BY: David S. Nobes		SIZE B Project PhD Thesis	
				yishak Thursday, October 31, 2019 1:28:48 PM Friday, September 16, 2016 1:03:01 PM		REV	
				SCALE: 1:5		Mass: SHEET 6 OF 17	

8 7 6 5 4 3 2 1

D
C
B
A

D
C
B
A

8 7 6 5 4 3 2 1



Ø 3.5 THRU ALL
8-32 UNC THRU ALL

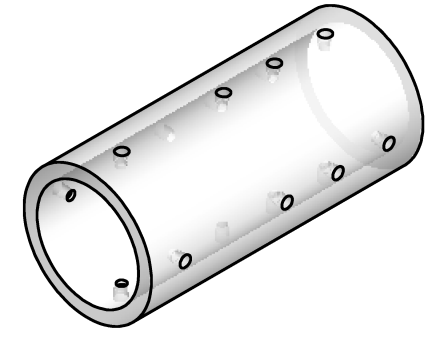
Ø 4.3 THRU
Ø 7.9 ∇ 2.2

Note: The length and width were varied to produce rectangular orifices of varying aspect ratio

a	b
36.60	3.00
28.98	0.5
27.50	0.42
25.37	0.35
22.51	0.29
20.17	0.25
18.03	0.22
16.16	0.20
14.42	0.19

Supervisor David S. Nobes	UNLESS OTHERWISE SPECIFIED: DIMENSIONS ARE IN MM TOLERANCES: ANGULAR: $\pm 0.5^\circ$ LINEAR X = ± 0.5 X.X = ± 0.1 X.XX = ± 0.025 SURFACE FINISH μm 0.6 ✓ DO NOT SCALE DRAWING	DRAWN BY: Yishak Yusuf		Department of Mechanical Engineering University of Alberta		
		SM BY Yishak Yusuf	REVIEWED BY David S. Nobes		TITLE: Shim-based rectangular coupon	
Comments:		yishak Thursday, October 31, 2019 1:49:05 PM Thursday, November 3, 2016 11:24:18 AM		SIZE B	Project PhD Thesis	REV
MATERIAL: Stainless steel		MANUFACTURING: CNC Machining		SCALE: 1:5	Mass:	SHEET 7 OF 17

8 7 6 5 4 3 2 1



D

D

C

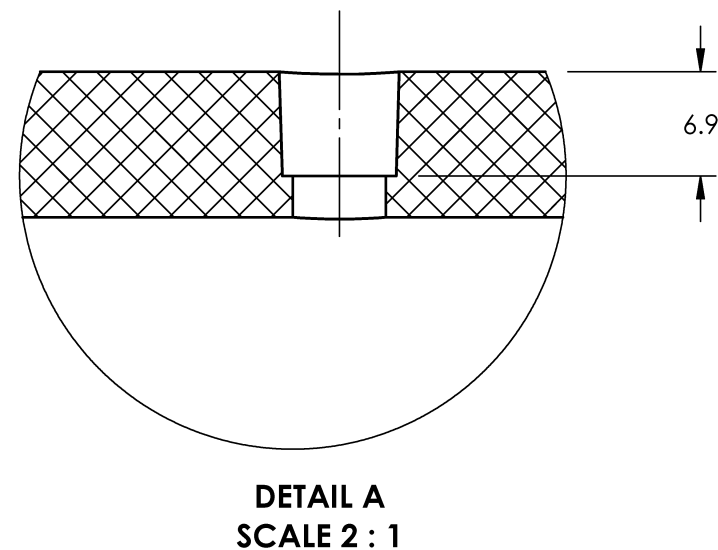
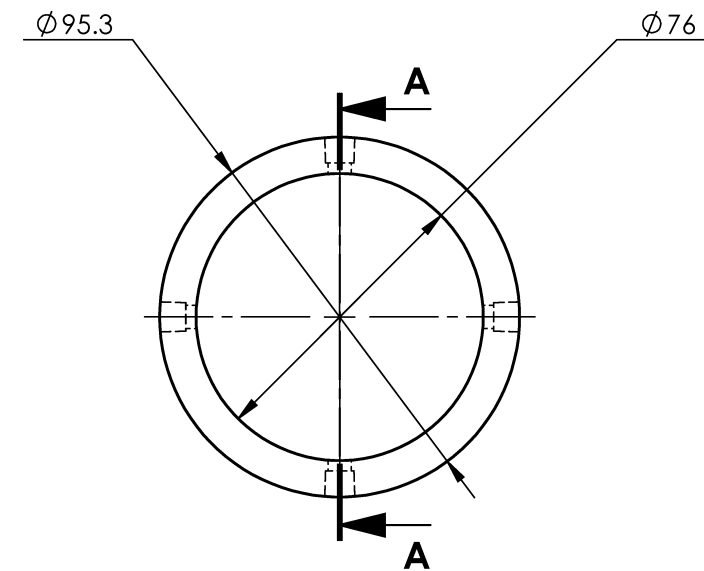
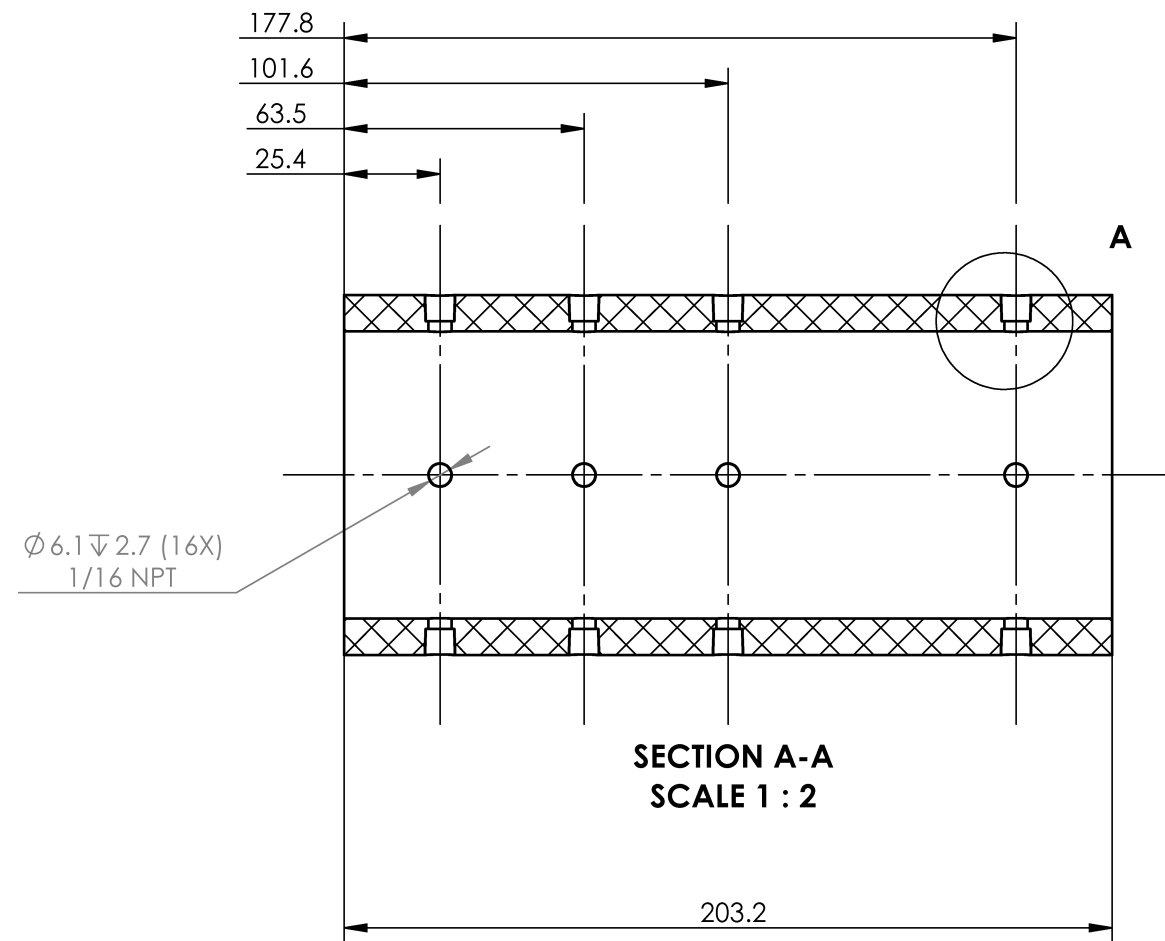
C

B

B

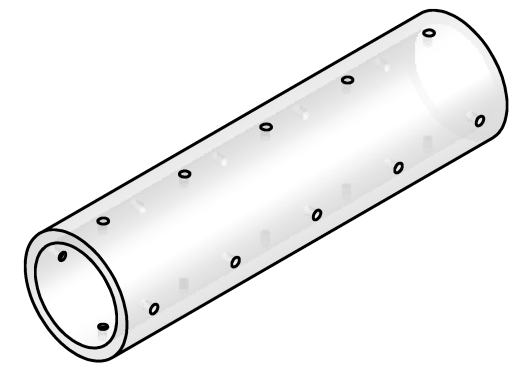
A

A

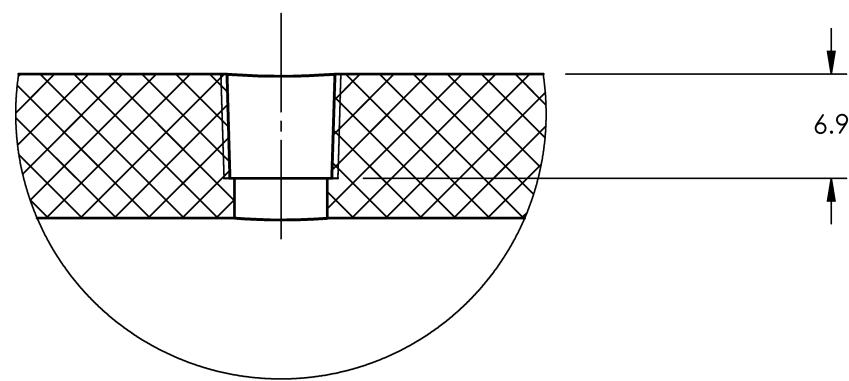
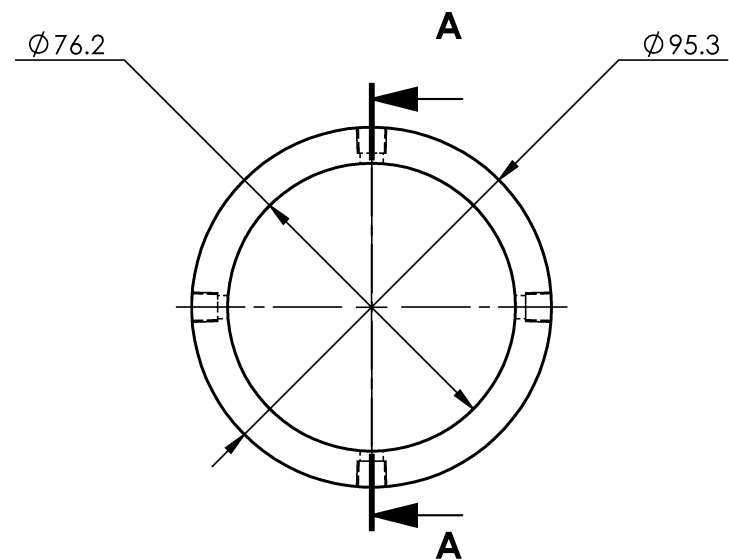
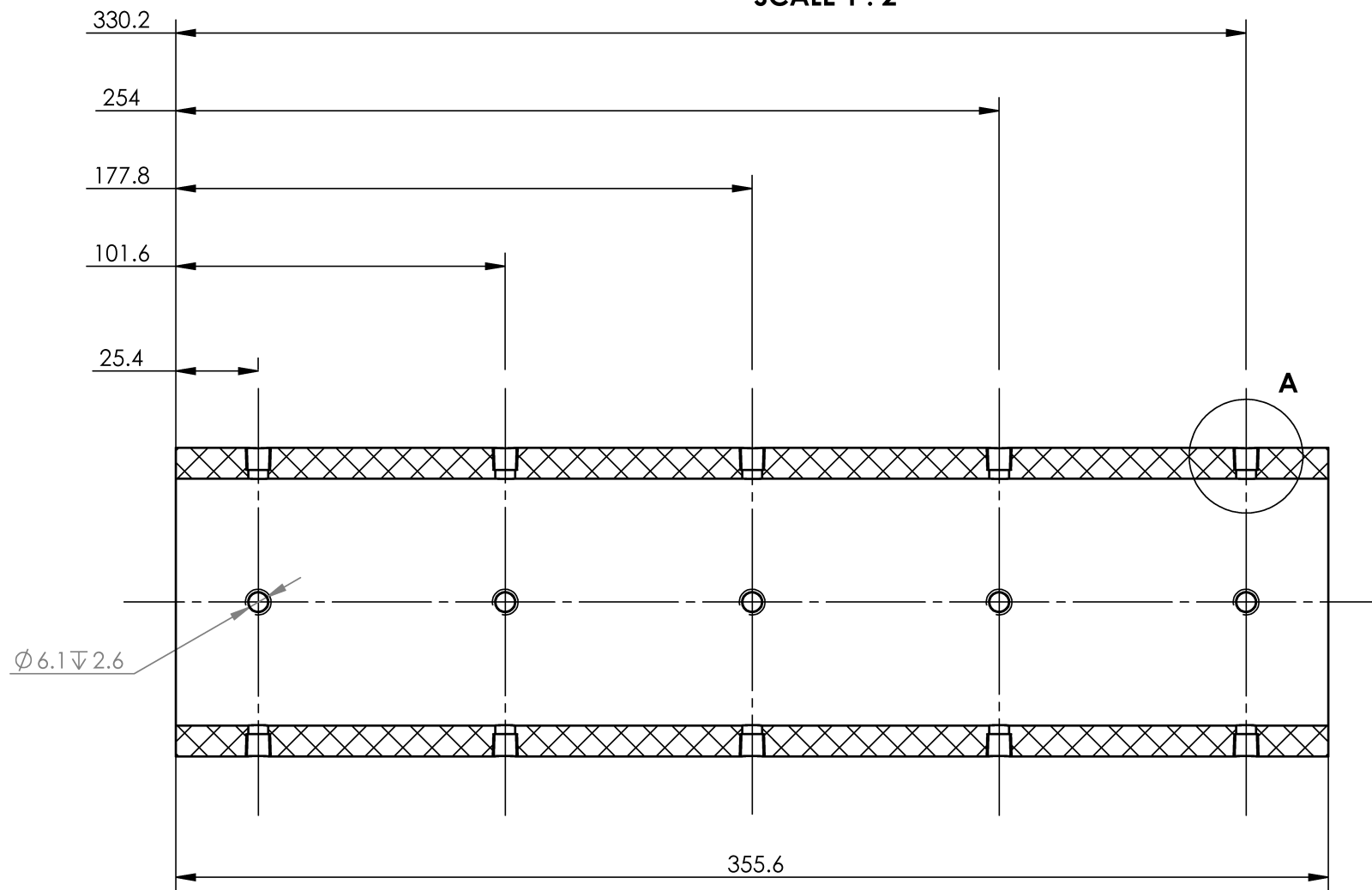


Supervisor David S. Nobes	UNLESS OTHERWISE SPECIFIED: DIMENSIONS ARE IN MM TOLERANCES: ANGULAR: ± 0.5° LINEAR X = ± 0.5 X.X = ± 0.1 X.XX = ± 0.025 SURFACE FINISH 0.6 µm ✓ DO NOT SCALE DRAWING	DRAWN BY: Yishak Yusuf		Department of Mechanical Engineering University of Alberta	
Comments:		SM BY Aleksy Baldygin Yishak Yusuf	REVIEWED BY David S. Nobes	TITLE: Upstream pipe section	
MATERIAL: Transparent acrylic tube		yishak Thursday, October 31, 2019 1:19:48 PM Monday, May 9, 2016 1:30:13 PM		SIZE B	Project PhD Thesis
MANUFACTURING: CNC Machining		SCALE: 1:5	Mass: 623.58	REV SHEET 8 OF 17	

8 7 6 5 4 3 2 1

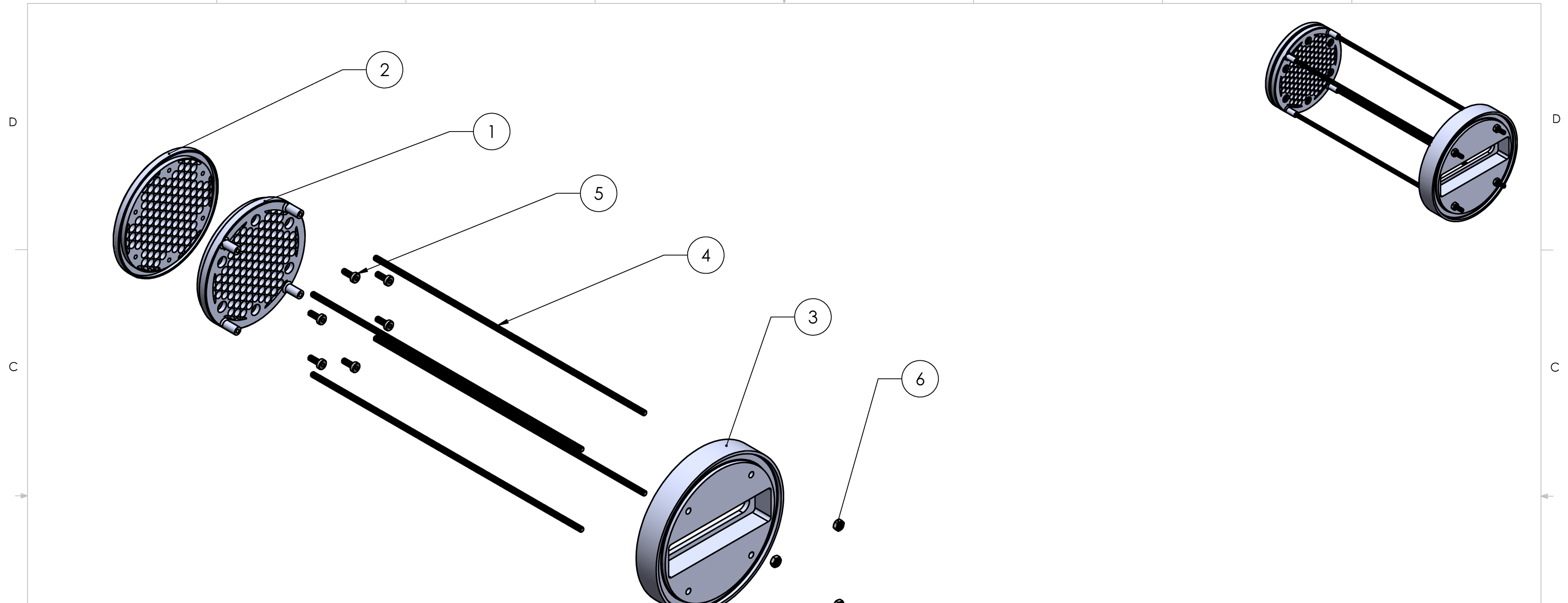


**SECTION A-A
SCALE 1 : 2**



**DETAIL A
SCALE 2 : 1**

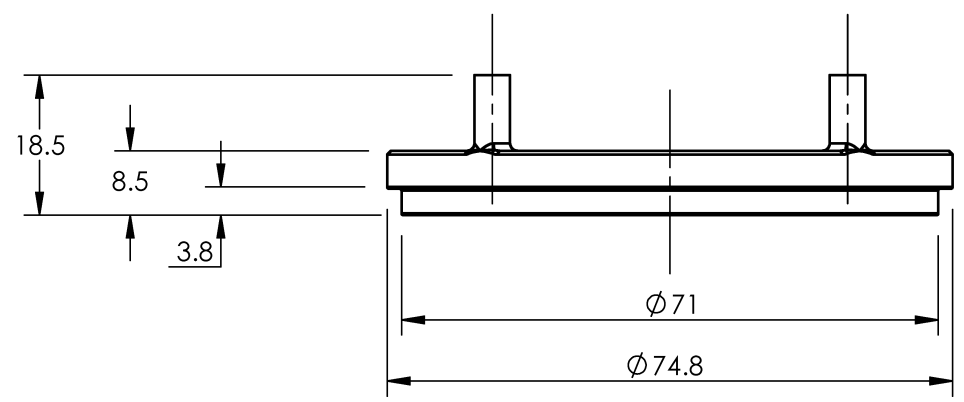
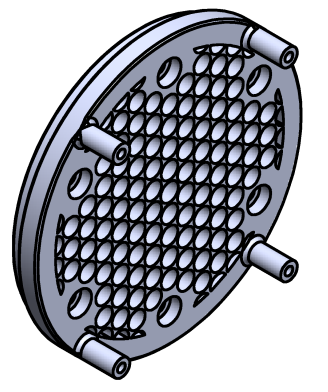
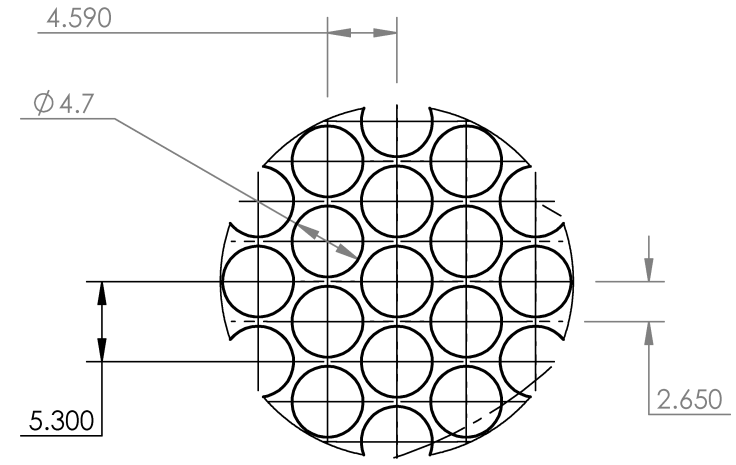
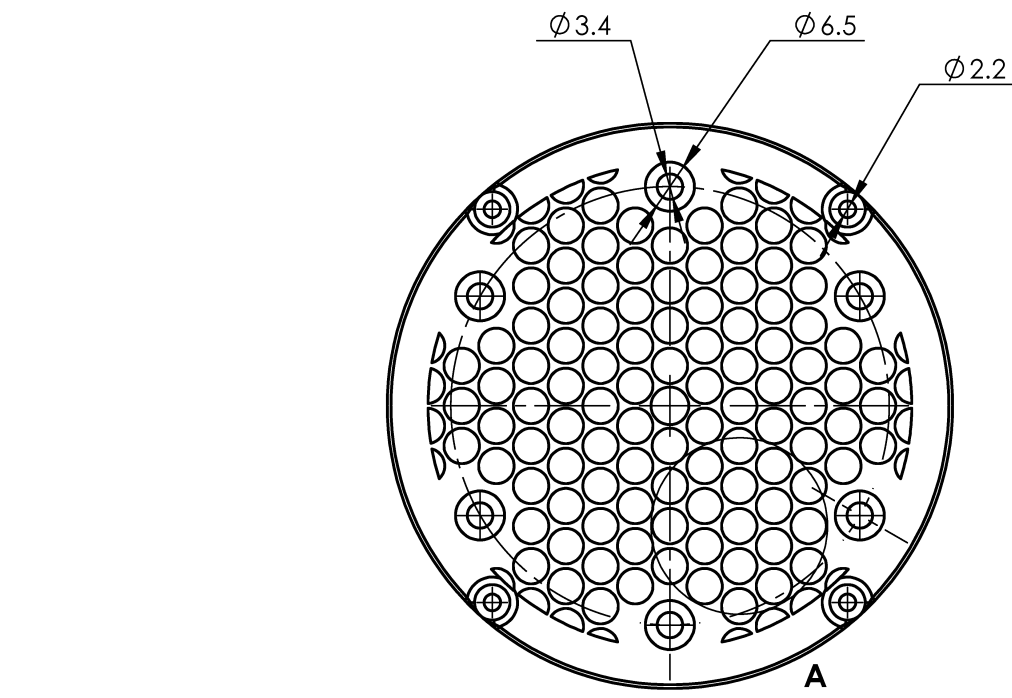
Supervisor David S. Nobes	UNLESS OTHERWISE SPECIFIED: DIMENSIONS ARE IN MM TOLERANCES: ANGULAR: ± 0.5° LINEAR X = ± 0.5 X.X = ± 0.1 X.XX = ± 0.025 SURFACE FINISH 0.6 µm ✓ DO NOT SCALE DRAWING	DRAWN BY: Yishak Yusuf		Department of Mechanical Engineering University of Alberta	
		SM BY Alekesey Baldygin Yishak Yusuf	REVIEWED BY David S. Nobes	TITLE: Downstream pipe section	
Comments:		yishak Thursday, October 31, 2019 1:19:39 PM Monday, May 9, 2016 1:30:13 PM		SIZE B	Project PhD Thesis
MATERIAL: Transparent acrylic tube		SCALE: 1:5		Mass: 1086.51	REV
MANUFACTURING: CNC Machining		208		SHEET 9 OF 17	



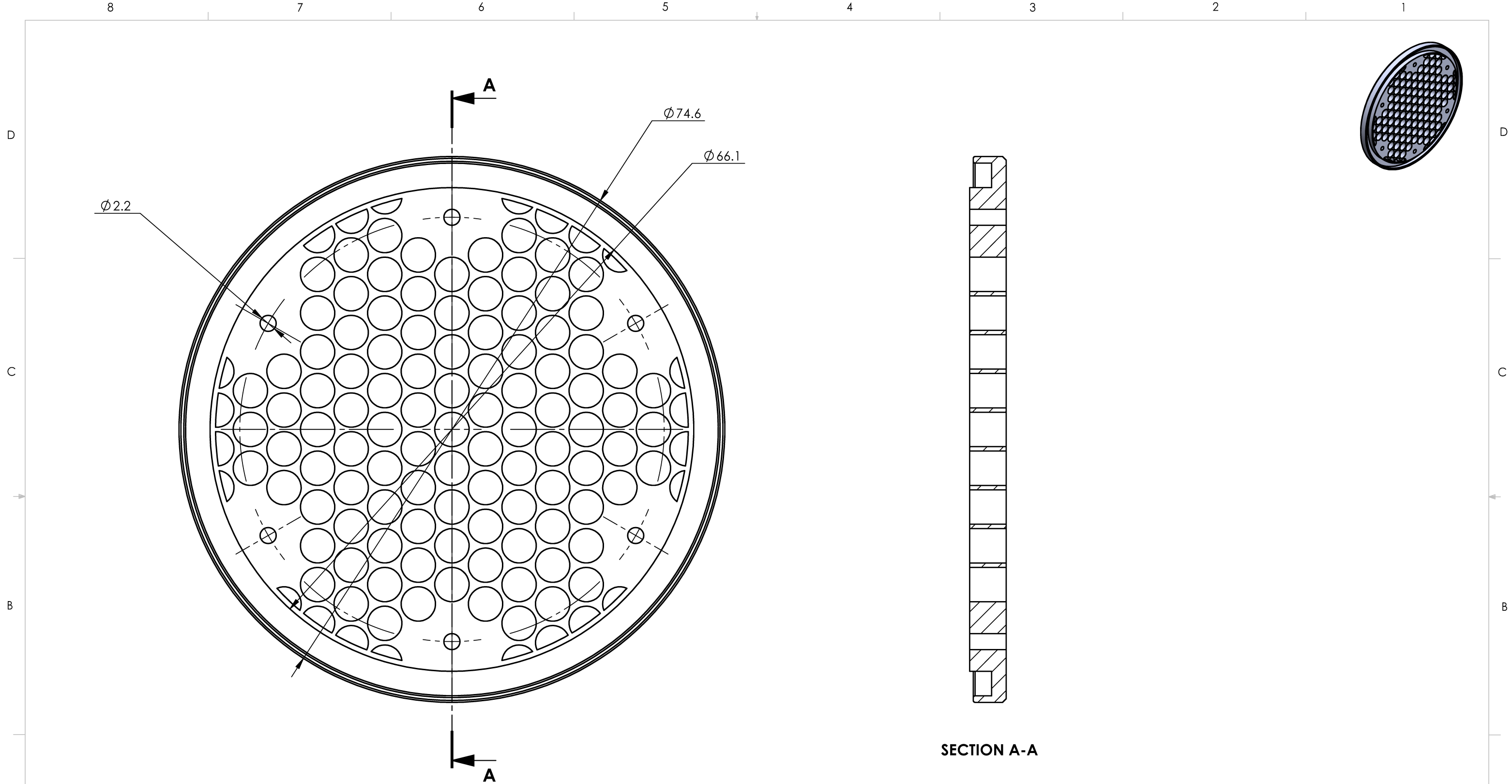
ITEM NO.	PART	QTY.
1	Front face	1
2	Back face	1
3	Test coupon assembly	1
4	M3 full thread tie rod	4
5	M3 flat head screw	6
6	M3 Hex Nuts	4

Note:
 - The assembled screen is inserted in the upstream pipe section for experiments which include the porous media.
 - The coupon holder is modified to add the four holes to fasten the tierods with hex nuts.

Supervisor David S. Nobes		UNLESS OTHERWISE SPECIFIED: DIMENSIONS ARE IN MM TOLERANCES: ANGULAR: $\pm 0.5^\circ$ LINEAR X = ± 0.5 X.X = ± 0.1 X.XX = ± 0.025		DRAWN BY: Yishak Yusuf		Department of Mechanical Engineering University of Alberta	
Comments:		SURFACE FINISH $0.6 \mu\text{m}$ ✓		SM BY: Yishak Yusuf		TITLE: Screen assembly for packing porous media	
MATERIAL: VARIABLE		DO NOT SCALE DRAWING		REVIEWED BY: David S. Nobes		SIZE Project REV	
FILE NAME:		209		yishak Thursday, October 31, 2019 1:19:29 PM Wednesday, May 30, 2018 10:07:59 AM		PhD Thesis	
		4				SCALE: 1:5 Mass: SHEET 10 OF 17	

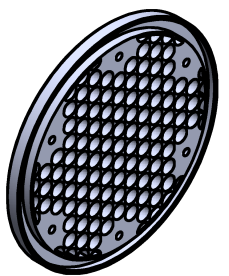


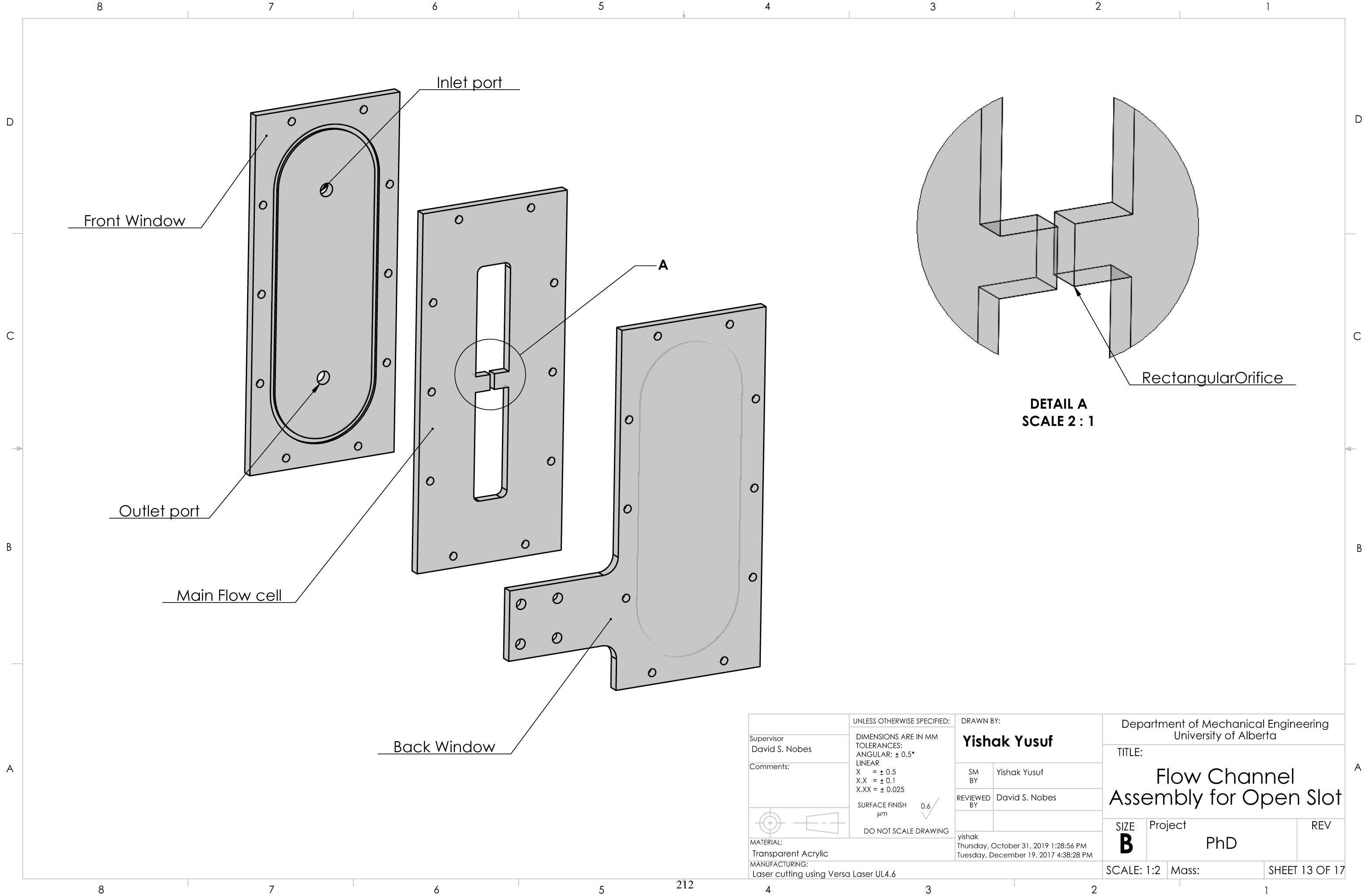
Supervisor David S. Nobes		UNLESS OTHERWISE SPECIFIED: DIMENSIONS ARE IN MM TOLERANCES: ANGULAR: $\pm 0.5^\circ$ LINEAR X = ± 0.5 X.X = ± 0.1 X.XX = ± 0.025 SURFACE FINISH μm 0.6 ✓ DO NOT SCALE DRAWING	DRAWN BY: Yishak Yusuf		Department of Mechanical Engineering University of Alberta	
Comments:			SM BY Yishak Yusuf	REVIEWED BY David S. Nobes		TITLE: Porous Media Screen Front Face
MATERIAL: Photopolymer Resin		MANUFACTURING: Stereolithographic 3D printing using Form2 by Formlabs		SIZE B	Project PhD Thesis	REV
				SCALE: 1:5	Mass:	SHEET 11 OF 17



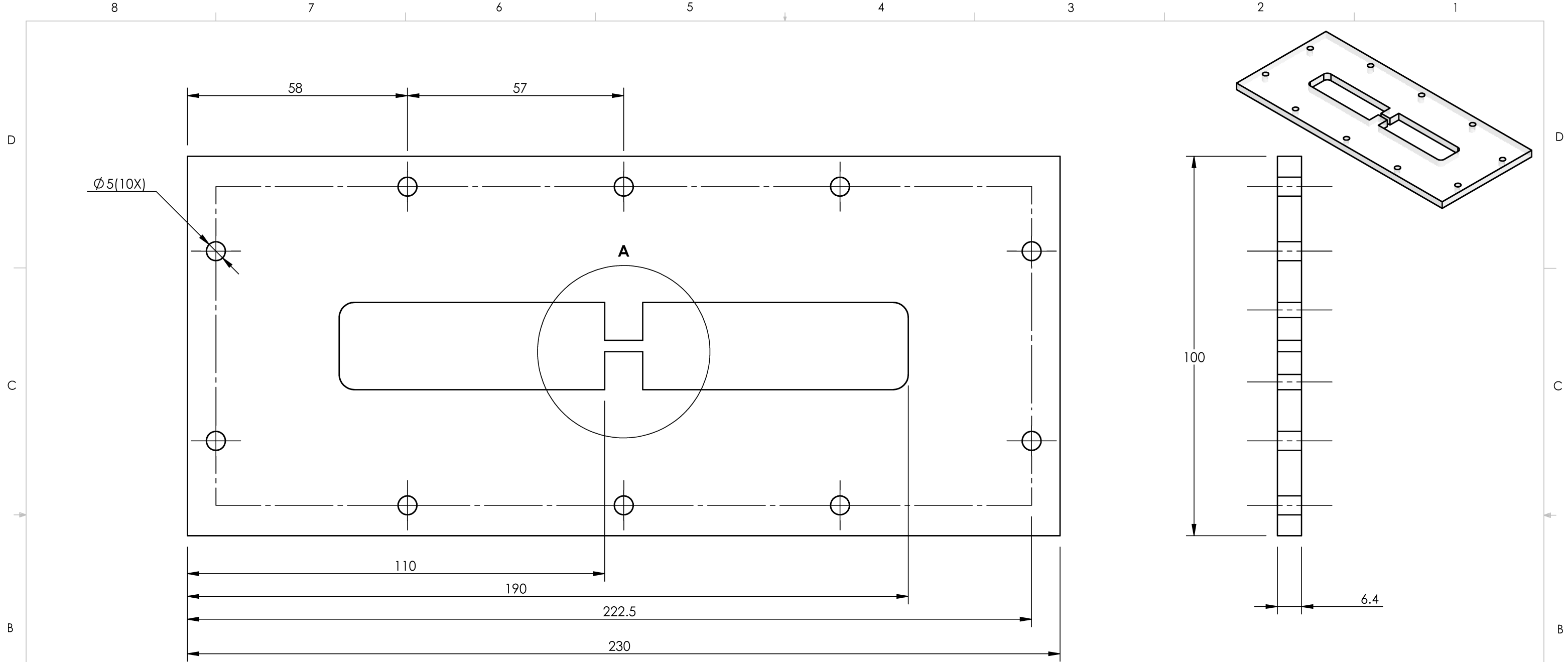
SECTION A-A

Supervisor David S. Nobes		UNLESS OTHERWISE SPECIFIED: DIMENSIONS ARE IN MM TOLERANCES: ANGULAR: ± 0.5° LINEAR X = ± 0.5 X.X = ± 0.1 X.XX = ± 0.025 SURFACE FINISH 0.6 μm ✓ DO NOT SCALE DRAWING	DRAWN BY: Yishak Yusuf		Department of Mechanical Engineering University of Alberta	
Comments:			SM BY Yishak Yusuf	REVIEWED BY David S. Nobes		TITLE: Porous Media Screen Back Face
MATERIAL: Photopolymer Resin		MANUFACTURING: Stereolithographic 3D printing using Form2 by Formlabs		SIZE B	Project PhD Thesis	REV
				SCALE: 1:5	Mass:	SHEET 12 OF 17



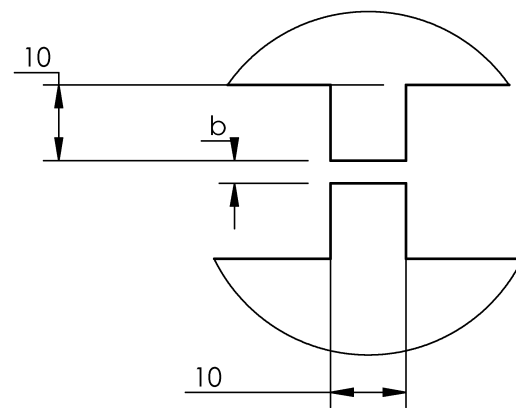


Supervisor David S. Nobes		UNLESS OTHERWISE SPECIFIED: DIMENSIONS ARE IN MM TOLERANCES: ANGULAR: $\pm 0.5^\circ$ LINEAR X = ± 0.5 X.X = ± 0.1 X.XX = ± 0.025 SURFACE FINISH μm 0.6 ✓ DO NOT SCALE DRAWING		DRAWN BY: Yishak Yusuf		Department of Mechanical Engineering University of Alberta	
Comments:		SM BY Yishak Yusuf	REVIEWED BY David S. Nobes		TITLE: Flow Channel Assembly for Open Slot		
MATERIAL: Transparent Acrylic		yishak Thursday, October 31, 2019 1:28:56 PM		SIZE B	Project PhD	REV	
MANUFACTURING: Laser cutting using Versa Laser UL4.6		Tuesday, December 19, 2017 4:38:28 PM		SCALE: 1:2	Mass:	SHEET 13 OF 17	



Note: The dimension b is varied to make orifices of different aspect ratio

b	Aspect Ratio
5	1.27
3	2.12
1	3

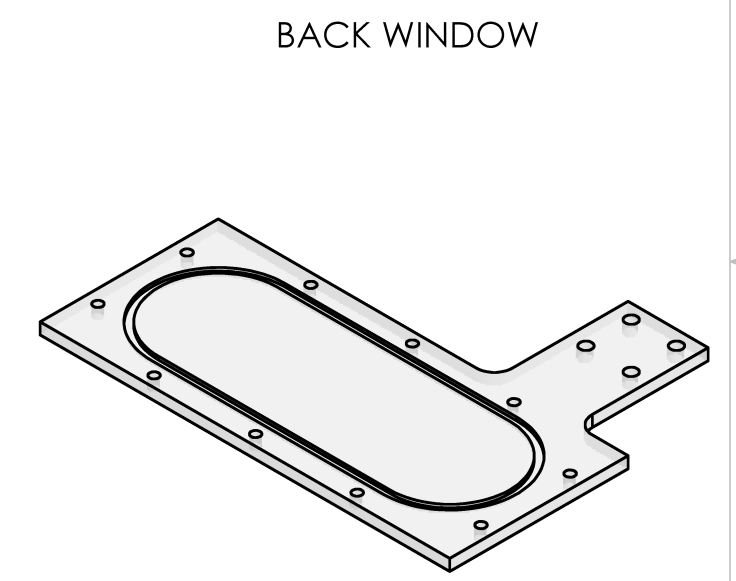
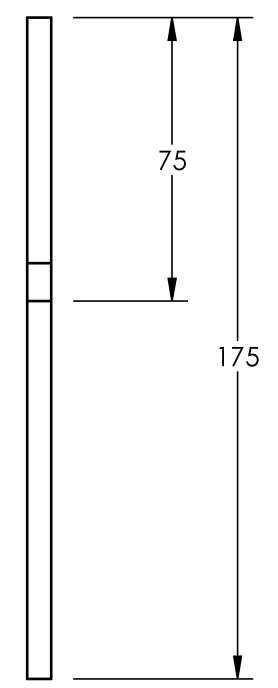
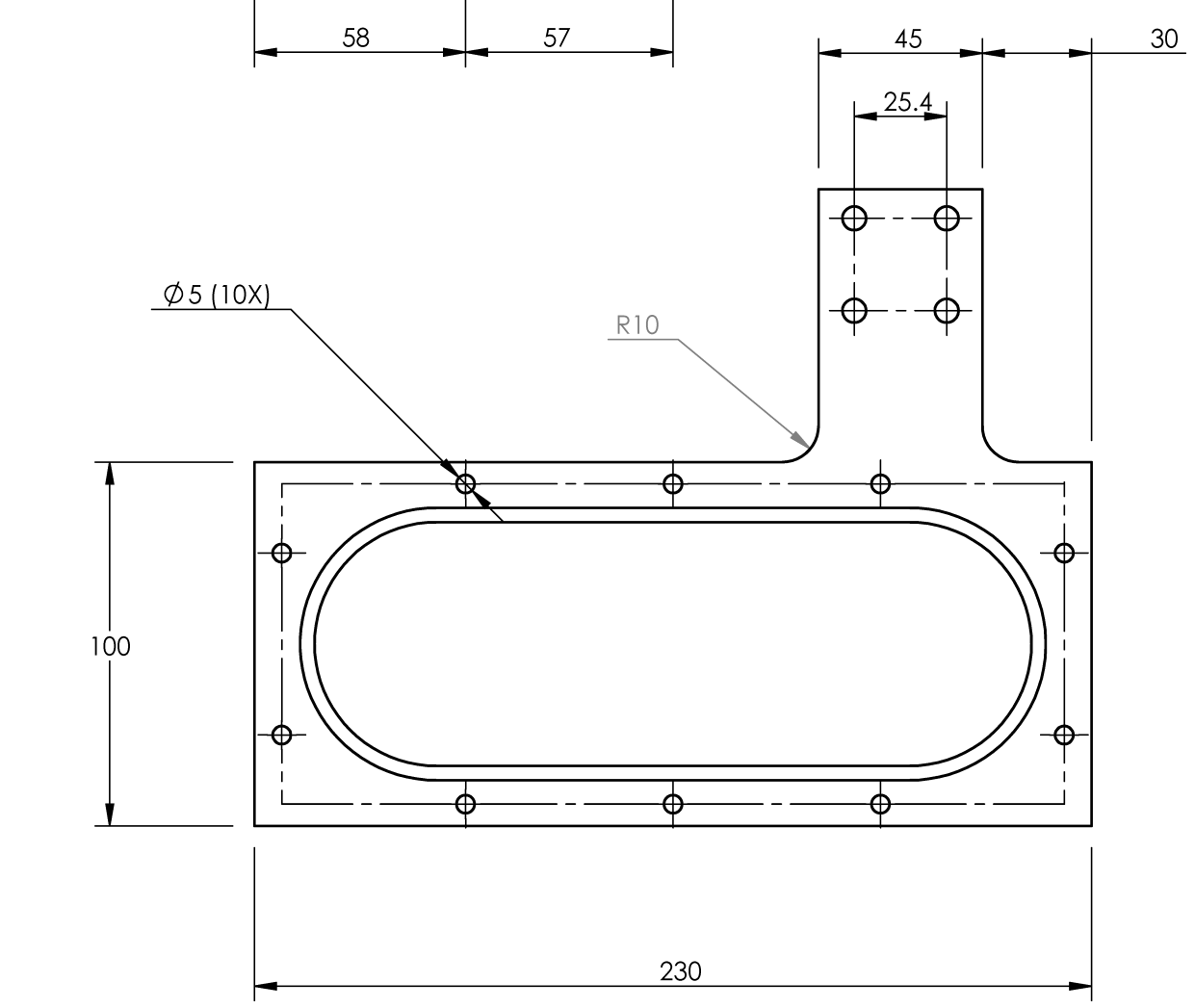
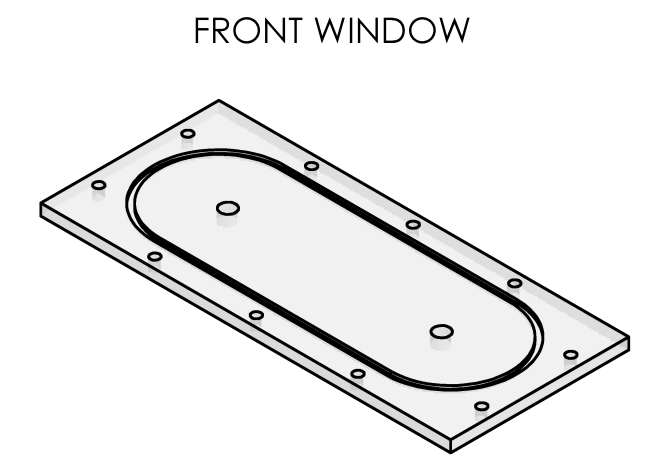
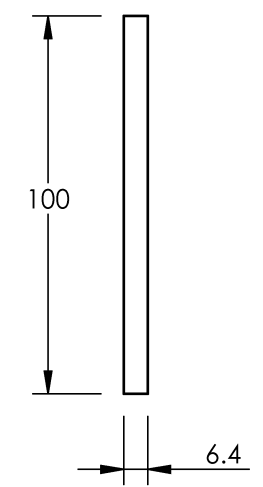
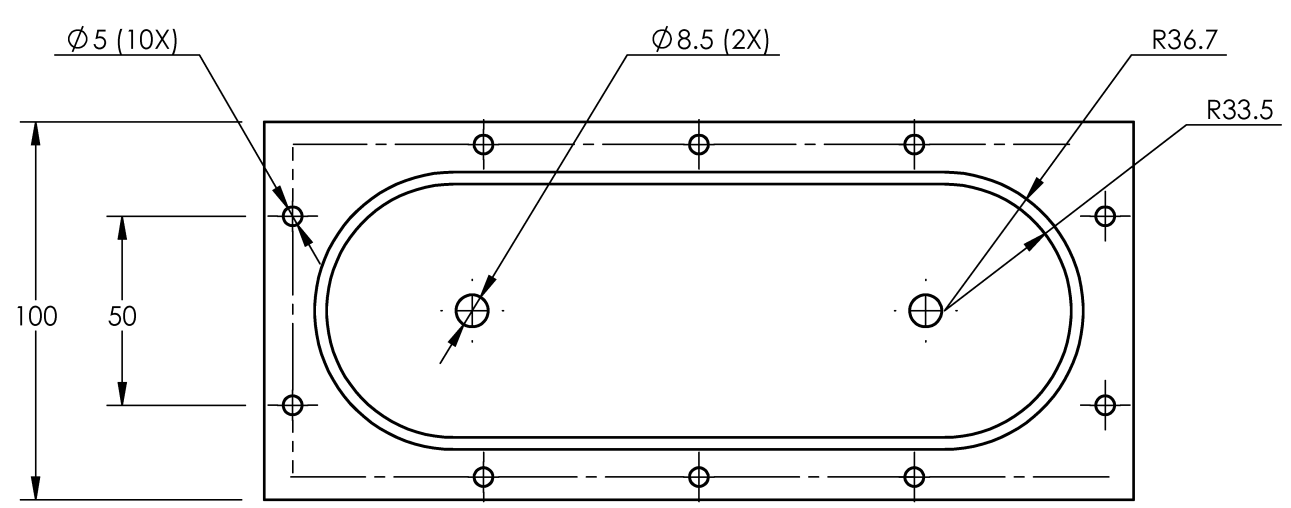


DETAIL A
SCALE 1 : 1

Supervisor David S. Nobes		UNLESS OTHERWISE SPECIFIED: DIMENSIONS ARE IN MM TOLERANCES: ANGULAR: $\pm 0.5^\circ$ LINEAR X = ± 0.5 X.X = ± 0.1 X.XX = ± 0.025		DRAWN BY: Yishak Yusuf		Department of Mechanical Engineering University of Alberta	
Comments:		SM BY: Yishak Yusuf		TITLE: Flow Cell for Open Slot			
		REVIEWED BY: David S. Nobes		SIZE B		Project PhD Thesis	
MATERIAL: Acrylic				yishak Thursday, October 31, 2019 1:28:47 PM Wednesday, July 27, 2016 8:42:25 AM		REV	
MANUFACTURING: Laser cut using Versa Laser UL4.6		DO NOT SCALE DRAWING		SCALE: 1:2		Mass: SHEET 14 OF 17	

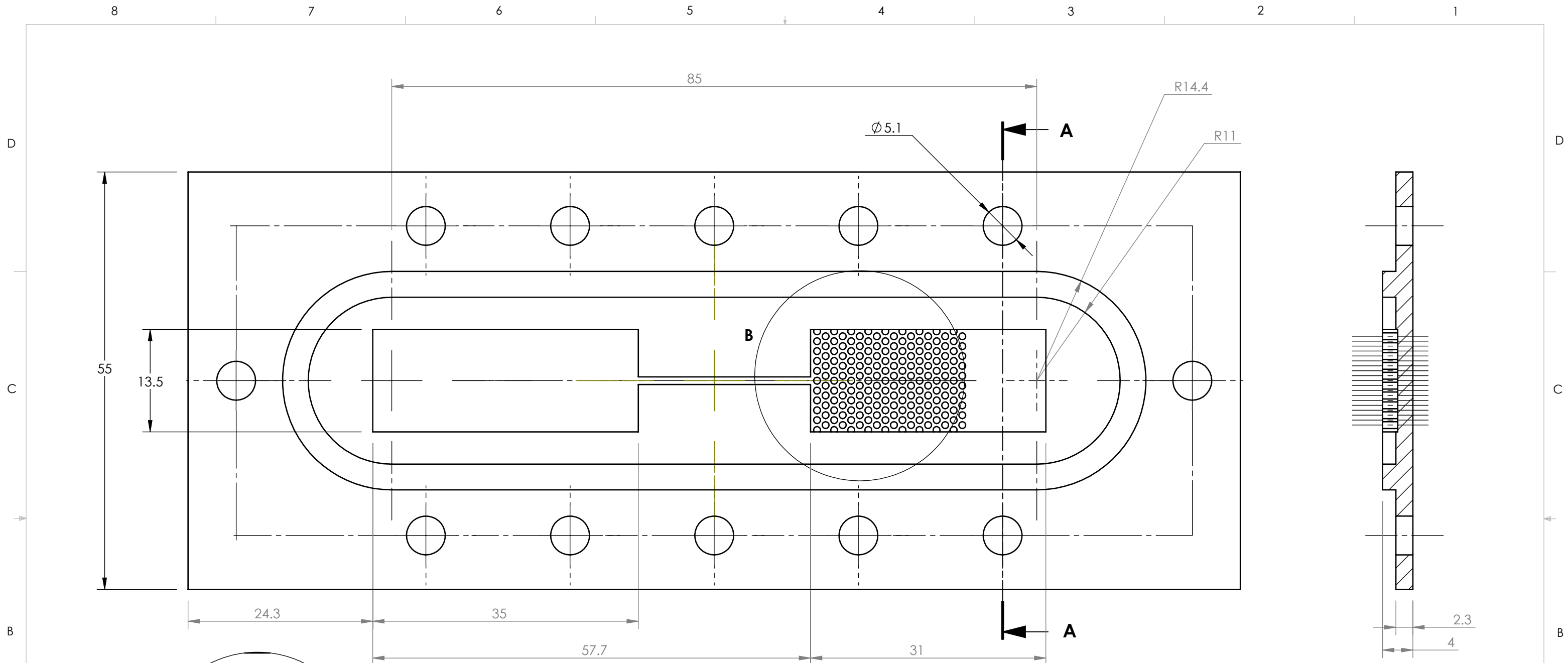
8 7 6 5 4 3 2 1

D
C
B
A

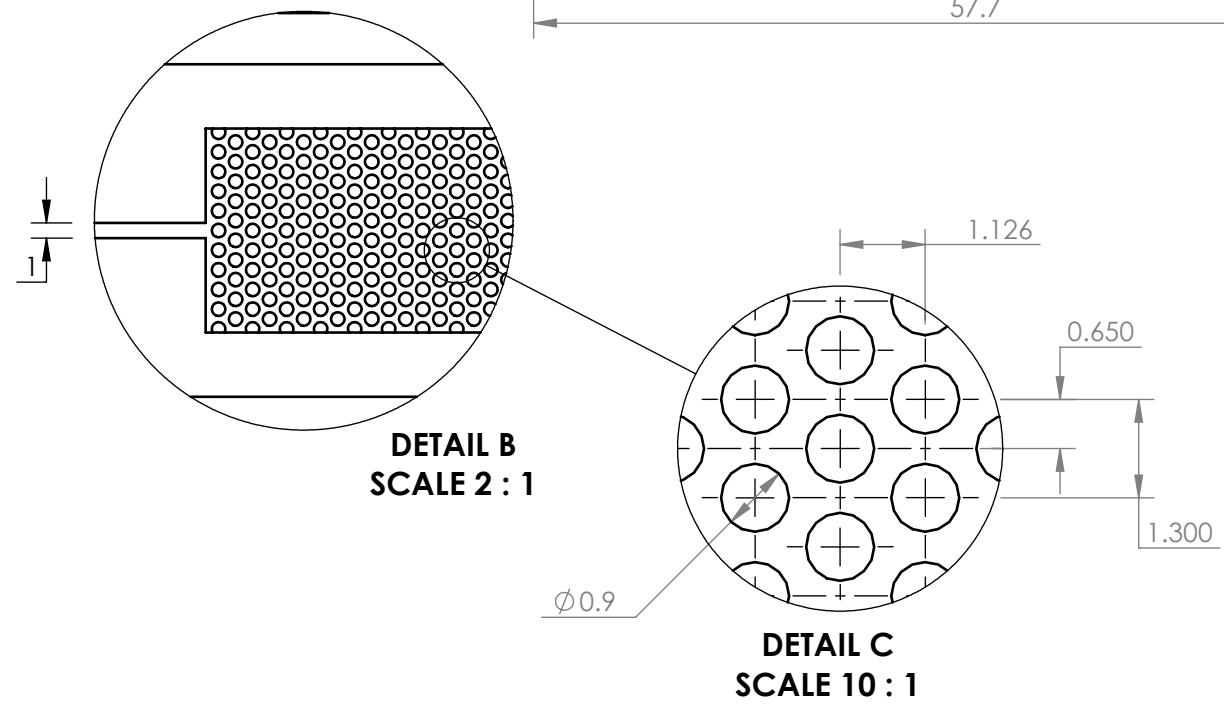


Supervisor David S. Nobes		UNLESS OTHERWISE SPECIFIED: DIMENSIONS ARE IN MM TOLERANCES: ANGULAR: ± 0.5° LINEAR X = ± 0.5 X.X = ± 0.1 X.XX = ± 0.025		DRAWN BY: Yishak Yusuf		Department of Mechanical Engineering University of Alberta	
Comments:		SURFACE FINISH µm 0.6 ✓ DO NOT SCALE DRAWING		SM BY: Yishak Yusuf		TITLE: Windows for Open Slot Flow Cell	
MATERIAL: Acrylic		MANUFACTURING: Laser cut using Versa Laser UL4.6		REVIEWED BY: David S. Nobes		SIZE Project REV	
				yishak Thursday, October 31, 2019 1:28:47 PM Wednesday, July 27, 2016 8:42:25 AM		PhD Thesis	
				SCALE: 1:2 Mass:		SHEET 15 OF 17	

8 7 6 5 4 3 2 1



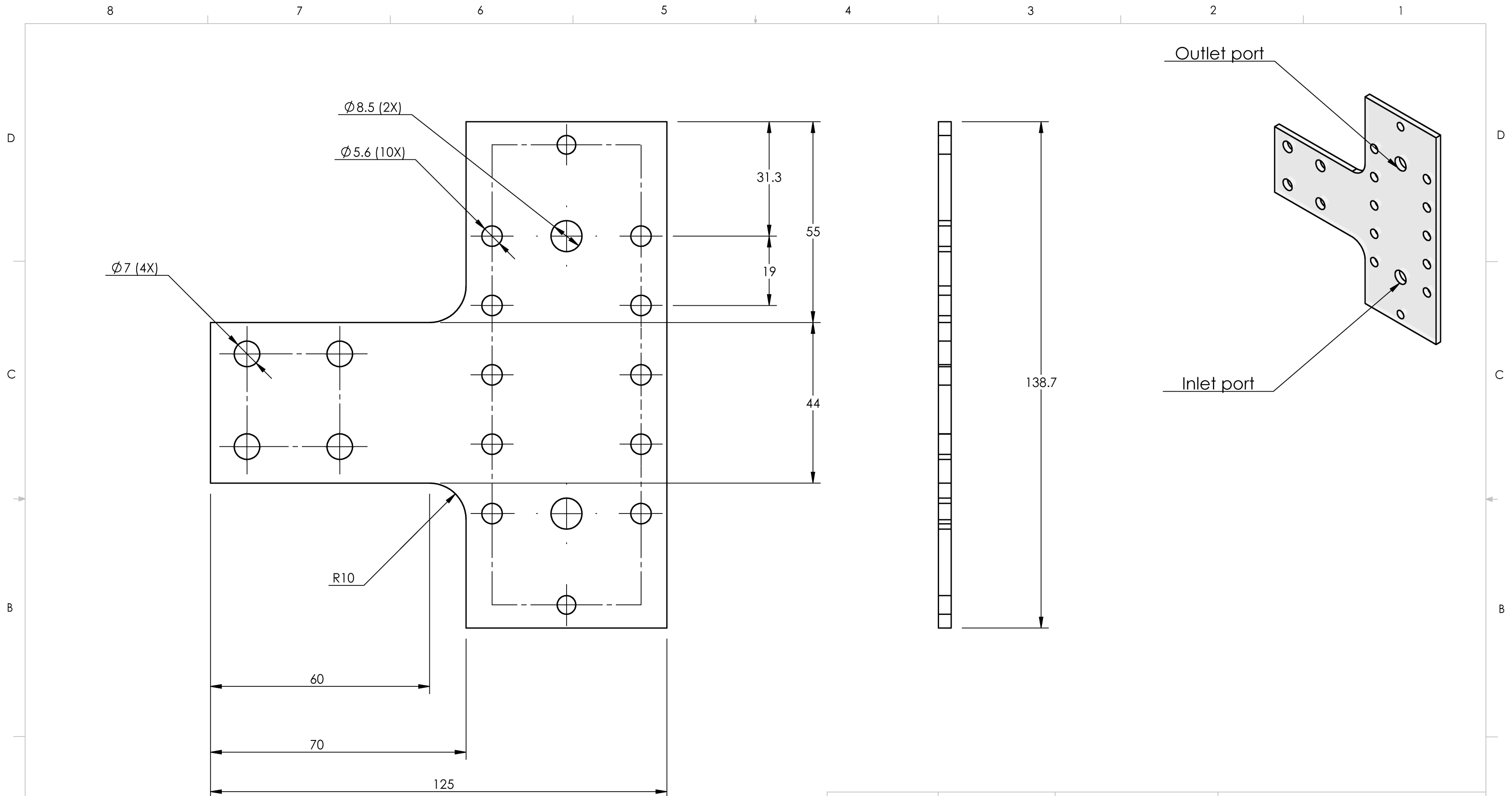
**SECTION A-A
SCALE 2 : 1**



**DETAIL B
SCALE 2 : 1**

**DETAIL C
SCALE 10 : 1**

Supervisor David S. Nobes		UNLESS OTHERWISE SPECIFIED: DIMENSIONS ARE IN MM TOLERANCES: ANGULAR: ± 0.5° LINEAR X = ± 0.5 X.X = ± 0.1 X.XX = ± 0.025		DRAWN BY: Yishak Yusuf		Department of Mechanical Engineering University of Alberta	
Comments:		SURFACE FINISH μm 0.6 ✓ DO NOT SCALE DRAWING		SM BY Yishak Yusuf	REVIEWED BY David S. Nobes		TITLE: Flow Cell for Tortuous Path
MATERIAL: Clear Photopolymer Resin		MANUFACTURING: Stereolithographic 3D printing using Form2 by Formlabs		yishak Friday, November 1, 2019 9:38:25 AM Friday, December 1, 2017 1:30:38 PM		SIZE B	Project PhD Thesis
				SCALE: 1:1		Mass:	REV SHEET 16 OF 17



Supervisor David S. Nobes		UNLESS OTHERWISE SPECIFIED: DIMENSIONS ARE IN MM TOLERANCES: ANGULAR: $\pm 0.5^\circ$ LINEAR X = ± 0.5 X.X = ± 0.1 X.XX = ± 0.025 SURFACE FINISH μm 0.6 ✓ DO NOT SCALE DRAWING		DRAWN BY: Yishak Yusuf		Department of Mechanical Engineering University of Alberta	
Comments:		SM BY: Yishak Yusuf		REVIEWED BY: David S. Nobes		TITLE: Window for flow cell with tortuous path	
MATERIAL: Acrylic		yishak Thursday, October 31, 2019 1:28:47 PM Friday, December 1, 2017 1:30:38 PM		SIZE B	Project PhD Thesis	REV	
MANUFACTURING: Laser cut using Versa Laser UL4.6		SCALE: 1:1		Mass:		SHEET 17 OF 17	